



Ca' Foscari  
University  
of Venice

Master's Degree programme

in Environmental Sciences

Second Cycle (D.M. 270/2004)

Final Thesis

**An analysis of near-surface atmospheric  
and oceanographic data over the  
equatorial Pacific Ocean with a special  
focus on the daily cycle**

**Supervisor**

Ch. Prof. Angelo Rubino

**Assistant supervisor**

Dr. Davide Zanchettin

**Graduand**

Francesco De Rovere

Matriculation Number 844701

**Academic Year**

2016 / 2017

## Preface

This thesis work is the result of both a shared and personal effort. In particular, the assessment of the diurnal cycles at the Tropics started from an idea of Professor Angelo Rubino, who recognised the TAO array as an important source of data for this purpose. The thesis work has been conducted through personal analyses of data and subsequent attempts to explain the results, which in turn solicit other analyses. During this work, I learnt from Professor Angelo Rubino and Dr. Davide Zanchettin how to reflect critically on the results of data elaborations, to elaborate the most accurate methods for future analyses and, among all, that research requires constant efforts and is an endless path. Therefore, I would like to thank my supervisors for their constant support and enthusiasm during the development of this thesis. In addition, I thank them for encouraging and giving me the opportunity to present my work in the second and third edition of THEMES, a scientific workshop dedicated to the study of marine environments.

I thank my parents, whose efforts have guaranteed me an education and allowed me to create a basis for my own future.

I thank my family and my friends for their constant patience and for their ability to render my life unpredictable and special.

I thank my grandfather and my girlfriend because they continued to believe in me.

*To us*

## Abstract

The study of the Earth's climate relies on the characterisation of the processes occurring at different time scales. The diurnal cycle is one of the most fundamental temporal modes of the global climate system, associated mainly to a well-defined variation in the solar forcing. This thesis work aims to assess the daily cycles of different near-surface atmospheric and oceanographic parameters over the Equatorial Pacific Ocean. To this purpose, an array of high-frequency (10-minutes) *in situ* observations is selected, i.e. the TAO array. The determination of the diurnal cycles is performed by assessing the daily anomalies of each parameter (except precipitation), thus removing the effect of climatic variations with periods greater than 24 hours on the mean state of the system. Instead, precipitation is inspected by determining the counts and frequency of rainfall events at each hour of the day. The variation of the daily cycles under distinct local meteorological conditions, i.e. sunny, cloudy, windy and calm days, and different "background" large-scale climatic conditions, i.e. El Niño and La Niña, is also assessed. Moreover, the evolution of the diurnal cycles over a multi-yearly scale is examined, addressing particularly the variation of the cycles under different parameters' regimes.

Frequently, the findings of this thesis work agrees with the results of previous studies as regards the entity and geographic variation of the diurnal cycles of wind speed, sea surface temperature (SST) and sea level pressure. Most of the variables are not distinctly altered by the different climatic and meteorological conditions, except the air temperature and SST.

Overall, few noteworthy and original aspects are distinguished:

- The air temperature measurements of the equatorial TAO buoys are affected by an error caused by the heating of the naturally ventilated shield covering the sensor.
- The diurnal variation of precipitation is not clearly consistent with previous results. In addition, an anomalous routine activity of the precipitation sensor is detected.
- The wind speed controls both the diurnal and annual variability of air temperature and SST mostly in the Equatorial Eastern and Central Pacific Ocean.
- The air temperature and SST are influenced by a warming process during night-time hours.

# Summary

1.	Introduction.....	5
1.1	Climate change and the study of the diurnal cycle .....	5
1.2	The Tropical Pacific Ocean .....	7
1.3	The daily cycles in the Tropical Pacific Ocean .....	11
1.3.1	Description of the datasets.....	11
1.3.2	Near-surface air temperature .....	12
1.3.3	The radiative heating error .....	13
1.3.4	Barometric Pressure.....	16
1.3.5	Wind .....	16
1.3.6	Sea Surface Temperature (SST) .....	17
1.3.7	Convection and precipitation.....	18
1.4	General aim and objectives of the thesis work .....	21
2.	Data, methods and software description .....	22
2.1	Data.....	22
2.1.1	The evolution of the TAO project .....	22
2.1.2	Moorings' specifications .....	23
2.1.3	Data used in this study.....	25
2.2	Methods .....	29
2.2.1	Data pre-processing .....	29
2.2.2	Diurnal cycle determination .....	30
2.2.3	Distinction according to the “background” climatic conditions.....	31
2.2.4	Assessment of the diurnal cycle according to different meteorological and climatological conditions.....	33
2.2.5	Assessment of the diurnal cycle variation over the long period .....	34
2.2.6	Data smoothing.....	34
2.2.7	Assessment of the relationships between physical parameters on a diurnal scale.....	35
2.3	Description of the utilised software.....	36
3.	Data elaboration.....	37
3.1	Downgoing Shortwave Radiation.....	37
3.2	Wind Velocity .....	44
3.3	Near-surface air Temperature.....	53
3.4	Sea Surface Temperature.....	65
3.5	Relative Humidity .....	73

3.6	Sea Level Pressure.....	82
3.7	Wind Direction.....	90
3.8	Precipitation.....	99
3.9	Relations between variables .....	105
4.	Discussion.....	108
4.1	The diurnal cycles of the different variables observed in the Eastern, Central and Western Equatorial Pacific .....	108
4.2	The diurnal cycles observed during the “warm” and “cold” phases of ENSO.....	114
4.3	The diurnal cycles observed under different local meteorological conditions .....	118
4.4	The variation of the diurnal cycles over the entire recorded periods.....	124
4.6	Limitations and recommendations.....	129
5.	Conclusions.....	131
6.	References.....	133
	Appendix A .....	137
	Appendix B.....	139

# 1. Introduction

This thesis provides an assessment of the observed daily cycles of different climatic parameters in the Tropical Pacific Ocean and the variability of such evolutions. The diurnal evolutions constitute fundamental information needed to estimate the long-term climatic variability of our planet. This chapter constitutes an introduction to the subject, describing the main issues and the consolidated knowledge related to this theme. It is structured as follows: Section 1.1 presents the topic of climate change and the importance of diurnal climatic studies for understanding climate's variability and implementing projections. Section 1.2 introduces the studied area, i.e. the Tropical Pacific Ocean; in particular, the focus is drawn on the main characteristics and climatic processes defining the interested region. Section 1.3 reports previous works regarding the assessment of diurnal cycles in tropical oceanic regions, with a particular focus on the Pacific Ocean. Section 1.4 details the specific purposes and the objectives of this thesis work.

## 1.1 Climate change and the study of the diurnal cycle

The Earth's climate identifies a group of average properties of a system. This system incorporates five major compartments: the atmosphere, hydrosphere, cryosphere, lithosphere and biosphere, which interact with each other by means of physical, chemical and biological processes. The synergies evolving in and among the different compartments cause the system to change its characteristics continuously at all timescales. Paleoclimate reconstructions showed the existence of a number of characteristic decadal-to-multimillennial cycles, which are linked to astronomical and natural forcings.

During the last two centuries, climate observations have reported an increase in the averaged global near surface air temperature. Moreover, since 1950s the observed variations are characterised by an *unprecedented* rate of change (Stocker et al., 2013). The atmosphere and the oceans have warmed, the sea level has risen and the volume of snow and ice have decreased. Specifically, the combined land and ocean surface temperature has increased of 0.85 [0.65-1.06] °C since 1880s (Stocker et al., 2013). Currently, the majority of climate scientists agree that the humankind's impacts on the environment are the main cause of these changes. The continuous emission of greenhouse gases and aerosols along with the change in land surface properties are affecting the Earth's energy budget (Cubasch et al., 2013). Such alteration of the mean climate has been associated with changes in different extreme weather and climatic events observed since 1950s. The occurrence of heat waves along with the frequency and intensity of heavy precipitation events have *likely* increased in different regions of the Earth (Stocker et al., 2013). On a global scale, the number of cold days and nights has decreased in favour of the number of warm days and nights. Moreover, the latter decades have been registered as the warmest in the available records (Stocker et al., 2013). Glaciers around the world have been experienced a net ice loss, estimated to be 226 [91-361] Gt/yr within the period 1971 to 2009. Moreover, the snow cover extent of the northern hemisphere has decreased since the 1950s (Stocker et al., 2013). Oceans are the storage compartment of the increased energy within the climate system. The energy stored in the oceans is estimated to account for the 90% of the total energy accumulated between 1971 and 2010. Specifically, scientists estimated that the 60% is stored in the upper 700m of the ocean, while the remaining 30% below 700m. Global warming has affected profoundly the sea surface, heating the upper 75m of the ocean by 0.11 [0.09-0.13] per decade within the period 1971-2009. It is *likely* that the ocean temperature has increased at higher depths, although the small amount of available data renders difficult to estimate this change (Stocker et al., 2013).

Climate change science is firstly devoted to the examination of long temporal variability and trends in the atmosphere and oceans. The implementation of general circulation models (GCMs) has become of major importance for dealing with these purposes. GCMs are complex mathematical models attempting to simulate climate dynamics and are largely involved in the climate change field of work. Accordingly, these models are run to examine the processes occurring in the climate system and to predict future changes in climate under several scenarios. These scenarios feature different possible future impacts resulting from human and natural drivers. The parameterisation of climatic processes occurring on a long timescale is based on the understanding and reproduction of the processes taking place on smaller time periods. The diurnal time scale is certainly among the finest time scales for the occurrence of weather-related processes. Dai and Trenberth (2004) stressed the importance of parameterising diurnal variations in surface and atmospheric layers to reproduce variations in energy's fluxes and precipitation events. Bergman and Salby (1996) highlighted the dependence of clouds on surface conditions. Furthermore, clouds strongly interact with longwave and shortwave radiation altering surface and atmospheric heating. Rainfall events are related to diurnal cycles in local atmospheric and surface conditions as well (Trenberth et al., 2008). Therefore, the improvement in the quality of climate models heavily relies on observations concerning the diurnal cycles of different physical parameters to simulate accurately long-periods phenomena. Moreover, understanding the causes and consequences of these cycles could lead to a better interpretation of the relations existing between the numerous elements composing the climate system. Nowadays, climate simulations base on coupled models of ocean and atmosphere because of the important roles of the oceans. Oceanic processes, through thermal and dynamic inertia, play a primary role in regulating climate changes on a long temporal scale (Bigg et al., 2003). Moreover, during the last three decades, IPCC's Assessment Reports emphasised the role of the ocean in understanding and predicting climate changes. Therefore, a better comprehension of diurnal cycles over the ocean is directly related to a more complete knowledge of the climatic system and its possible future changes.

## 1.2 The Tropical Pacific Ocean

This section aims to describe the general characteristics of the studied area. Figure 1.1 illustrates the geography of the Pacific Ocean.

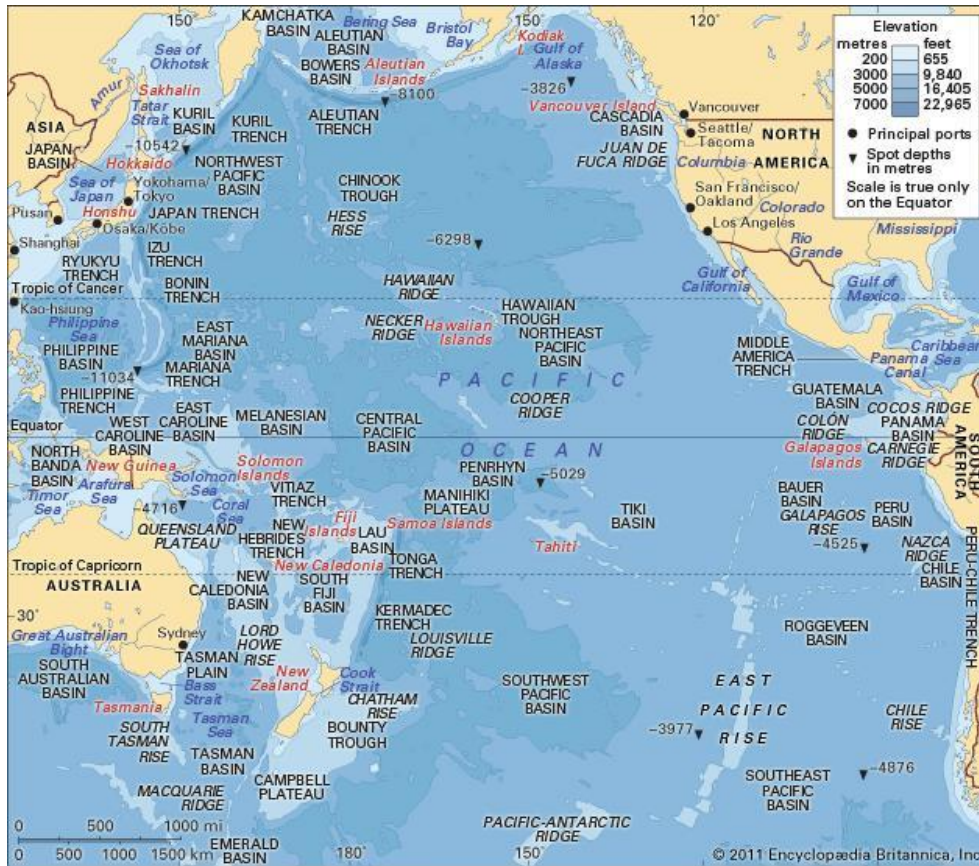


Figure 1.1: The Pacific Ocean.  
Source: Encyclopædia Britannica (2017)

The Tropical Pacific Ocean spans from 30°N to 30°S and is surrounded by the central and southern America on the eastern part and by Australia and the islands of south-east Asia on the western part. The Tropical Pacific presents just a few volcanic islands. In this region, trade winds originating at low latitudes on the margins of high pressure cells over the northeast and southeast Pacific dominates (Barry and Chorley, 2009; Encyclopædia Britannica, 2017). Trade winds have generally a constant direction and velocity. Winds blow north-westward in the southern hemisphere and south-westward in the northern hemisphere, with an average speed of about 7 m/s (Barry and Chorley, 2009). However, winds tend to be stronger in the Eastern Pacific. Air converges in the *Equatorial Trough* of low pressure promoting the enhancement of calm conditions (Encyclopædia Britannica, 2017). Trade winds in the Eastern Pacific convey cool air toward the equator, which modifies air humidity and lapse rate. In the west coast of the American continents, trade winds cause upwelling of cold waters from the ocean's bottom (Barry and Chorley, 2009; Encyclopædia Britannica, 2017). The Western equatorial Pacific features conditions of calm and sudden variable winds (Barry and Chorley, 2009). The tendency of trade winds originated in the two hemispheres to converge over the equator in the Central Pacific triggers the development of the so-called Inter-Tropical Convergence Zone (ITCZ). The ITCZ is defined by Waliser and Gautier (1993) as a "*near-solid convective cloud band encircling the*

earth near the equator". Furthermore, other studies identified the ITCZ as a tropical belt of maximum time-mean precipitations (Schneider et al., 2014). Over the Pacific Ocean the ITCZ is located north of the equator, moving seasonally between 4°N in March-April and 8°N in September. Moreover, during the boreal summer, the ITCZ becomes stronger across the Pacific Ocean (Barry and Chorley, 2009). However, the dynamics of the ITCZ and the associated rainfall intensities have not been completely understood (Schneider et al., 2014). The air convergence over the Western equatorial Pacific triggers the formation of the South-Pacific Convergence Zone (SPCZ). The SPCZ identifies an area of maximum cloudiness extending from Papua New Guinea to 30°S and shares common characteristics with the ITCZ. The SPCZ location and development exhibit seasonal and inter annual variability. During the boreal summer the SPCZ is poorly developed, while it grows during the austral summer. Moreover, after April the SPCZ moves westward and equatorward. The inter-annual variation of the SPCZ is mostly linked with the phase of the El Niño Southern Oscillation phenomenon or ENSO (Barry and Chorley, 2009). The cloud bands' variations throughout the year are shown in Figure 1.2.

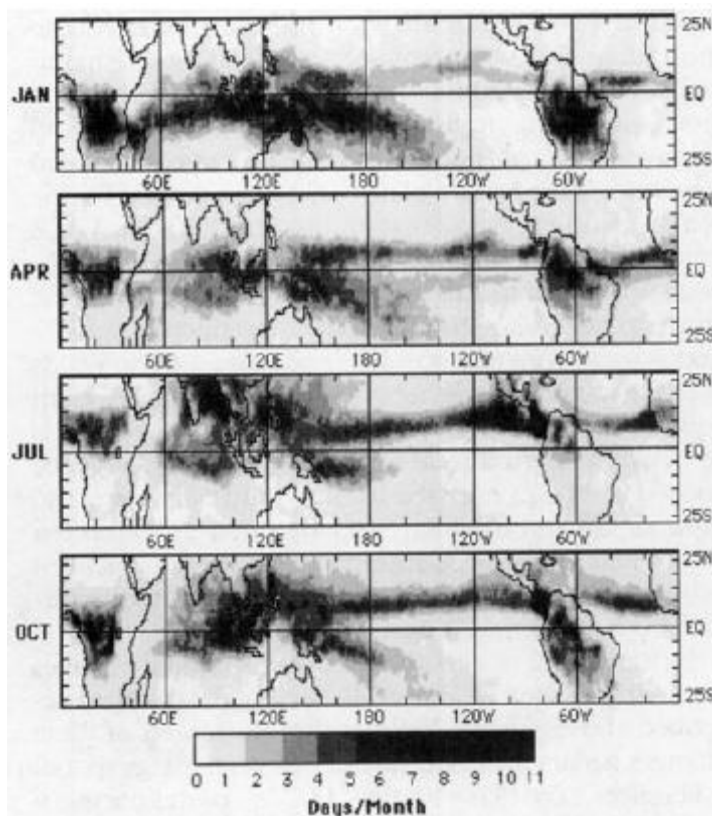


Figure 1.2: Mean monthly ITCZ and SPCZ structure for months: January, April, July, October. Values represent the number of days per months during which the given grid point was covered by large-scale deep convective system. These images were computed from 17 years of highly reflective cloud satellite images sampled once a day. Source: Waliser and Gautier (1993).

ENSO is the most important climatic phenomenon occurring in the Pacific Ocean. It consists in an irregular variation in atmospheric mass and pressure associated with exchanges of air between the subtropical high-pressure cell over the Eastern south Pacific and the west Pacific low-pressure region (Barry and Chorley, 2009). In the west coast of the American continents, trade winds cause upwelling of cold waters from the ocean's bottom (Ahrens, 2012; Encyclopædia Britannica, 2017). Starting from December of each year, warm waters directed southward substitute surface cold waters. During most of the years, this phenomenon ends after few weeks and weather patterns returns to normality (Ahrens, 2012). However, every two to seven years, warm waters interrupt entirely the oceanic upwelling. Experts agree that the weakening of Pacific trade winds caused by changes in surface atmospheric pressure patterns triggers this phenomenon. Others emphasise also the role of near-surface temperature variations in the Tropical Pacific in generating the El

Niño event (Barry and Chorley, 2009). During normal conditions, surface waters are cooler in the Eastern equatorial Pacific and warmer in the Western equatorial Pacific. In addition, trade winds move surface water westward, thus lowering the sea level in the Eastern Pacific and increasing it in the Western Pacific (Ahrens, 2012). Due to the presence of a strong upwelling, the thermocline reaches lower depths in the Eastern Pacific compared to the Western Pacific. During an El Niño event, the westward gradient of sea surface temperatures across the Pacific is inverted and a typical warm “tongue” located off South-America’s coasts and surrounding the equator is formed. The occurrence of these conditions activates a positive feedback in the atmosphere-ocean system of the Eastern Pacific, modifying the Walker circulation. Over the Western Tropical Pacific, the area of maximum sea surface temperatures tends to move eastward toward the Central Pacific due to the changes in the Walker circulation. As a result, the Western Pacific experiences lower sea surface temperatures than usual. The thermocline over the eastern Pacific is depressed, further avoiding cold waters to reach the surface. During normal conditions, rising air and associated convective activities are mostly located over the western Pacific. During El Niño conditions, rising air and convection phenomena are shifted eastward, following the change in sea surface temperature (Barry and Chorley, 2006). The atmospheric pressure increases over the Western Pacific and decreases over the Eastern Pacific. As a result, sinking air and dry conditions occur in the Western Pacific, whereas air convergence and convection phenomena occurs in the Central and Eastern Pacific. This variation in surface pressure condition at opposite sides of the Pacific Ocean is named the Southern Oscillation (Ahrens, 2012). Near the end of an El Niño event, the normal pressure gradient between west and east Pacific is restored. In addition, trade winds over the Eastern Pacific return to be stable (Ahrens, 2012). Very strong winds cause the development of La Niña. It occurs when cold waters spread along the Eastern and Central Tropical Pacific due to increased upwelling near the South American coasts and the stronger action of trade winds. Therefore, sea surface temperatures become colder in the Eastern and Central Pacific and warm waters are kept to the farthest west side of the Pacific Ocean. La Niña conditions strength the high pressure over the eastern Pacific and the convective conditions over the western Pacific (Barry and Chorley, 2009). Figure 1.3 schematises the anomalous conditions associated to El Niño and La Niña events.

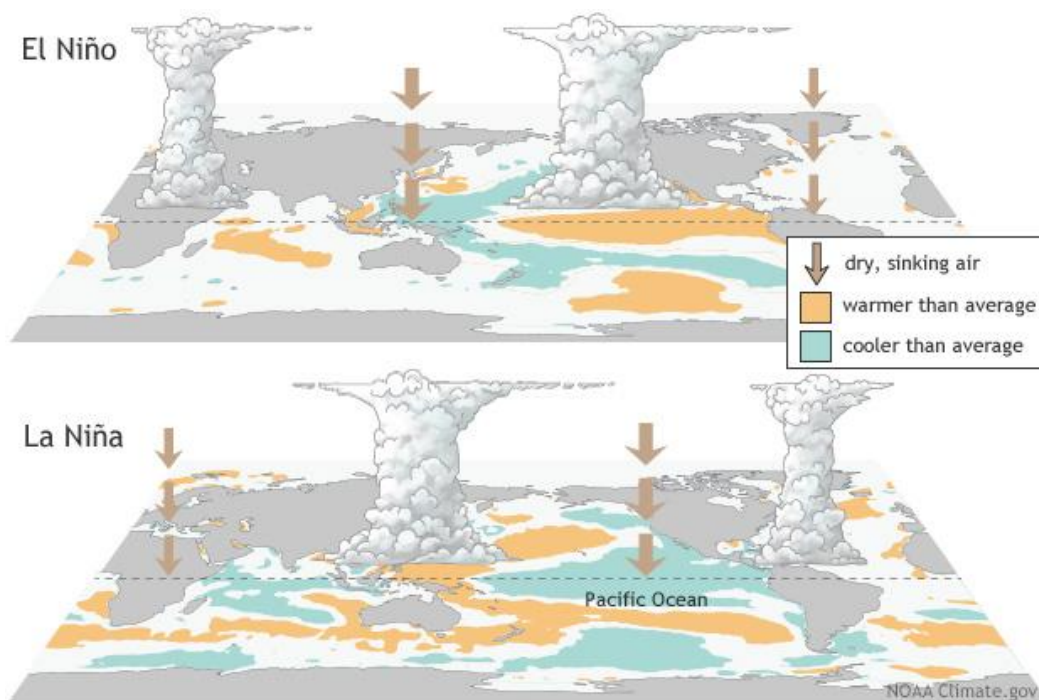


Figure 1.3: El Niño and La Niña conditions over the world.

Source: NOAA (2017a).

El Niño and La Niña are usually referred to as the “warm” and “cold” phases of ENSO, respectively. The intensity of ENSO is measured by the Southern Oscillation Index (SOI). This index is based on the comparison between the sea level pressure observed at Tahiti (Central Tropical Pacific) and Darwin (Northern Australia). Prolonged periods of negative (positive) SOI values are linked to abnormally warm (cold) ocean surface temperature over the Eastern Pacific typical of El Niño (La Niña) episodes (NOAA, 2017c). The importance of ENSO resides particularly in its effects on the global weather patterns. The ocean-atmosphere interactions between sea surface temperature and weather patterns in a distant part of the world are called “teleconnections”.

## 1.3 The daily cycles in the Tropical Pacific Ocean

In the following sub-sections, aspects of the consolidated knowledge regarding the tropical daily cycle are explained. Sub-section 1.3.1 describes the different types of measurements used by researchers to examine the tropical daily cycle during the years, among which the source of data utilised in this study. Sub-section 1.3.2 illustrates the major forcing affecting the near-surface air temperature cycle during the day. Sub-section 1.3.3 examines the presence of an error in the air temperature measurements made by naturally ventilated sensors. Sub-sections 1.3.4 to 1.3.7 present previous findings concerning the diurnal cycle of barometric pressure, wind speed and direction, sea surface temperature and convection in the Tropical Pacific. In this section, the terms “diurnal” and “daily” cycle identify a daily oscillation with a maximum and a minimum within the 24-hour period. Instead, the term “semidiurnal” cycle labels a daily oscillation with two maxima and two minima occurring within the 24-hour period.

### 1.3.1 Description of the datasets

The first observational studies on the climate in the Tropical Pacific Ocean used data coming mainly from research vessels and merchant ships in addition to measurements performed on island stations. Ships provided mainly *in situ* measurements of the ocean temperature along with weather reports describing qualitatively the weather conditions. Island stations gave detailed precipitation information. During the second part of the twentieth century, more and more climate-related data have been acquired to study the climate characterising different regions of the globe. In particular, starting mainly from late 1970s and the early 1980s, satellite observations have been utilised to examine the meteorological conditions all over the Earth’s surface. Remote sensing data became the main source of climatic and oceanographic information for the tropical Pacific. The satellite data products used in the studies illustrated in Sub-Sections 1.3.5 to 1.3.7 are described as follows. The Tropical Rainfall Measuring Mission (TRMM) is a joint mission of NASA and the Japan Aerospace Exploration Agency (JAXA) aiming to study rainfall characteristics for weather and climate research (NASA, 2017). Launched in November 1997, TRMM is equipped with a precipitation radar (PR), a microwave imager (TMI) and a visible and infrared scanner (VIRS). Another remote sensing data source is the Geostationary Operational Environmental Satellite (GOES), managed by NOAA, collecting data for weather monitoring and forecasting (NOAA, 2017). These instruments have been operating since 1974. Researchers inferred convective activities over the interested areas through different types of satellite data, such as images reporting cloud temperature, fractional cloud coverage and scattering due to presence of water droplets in the atmosphere. Remote sensing observations have different characteristics compared to *in situ* data. Satellite data are characterised by a great spatial coverage and a coarse spatial resolution (often ranging between 1° and 2° for latitude and longitude). Moreover, satellites often acquired images a few times per day. Therefore, satellite images are extremely useful for examining and comparing different areas. On the other hand, the small number of images acquired during the day limits the characterisation of the diurnal cycles. To surpass this limitation, starting from mid-1980s, researchers started using buoy data to study the surface conditions of the oceans. Buoys acquire point data at a high temporal frequency. The TOGA COARE array is one of the first observational schemes involving moored buoys acquiring weather and climate data for climate research. However, the TOGA COARE project involved other sources of data i.e. ships observations and remote sensing. After this project, other monitoring networks using moored buoys have been designed such as the Tropical Atmosphere Ocean (TAO) monitoring scheme developed in the Tropical Pacific. Nowadays, the most important buoy dataset is the Global Tropical Moored Buoy Array (GTMB)

involving three monitoring programs distributed over the tropical oceans: the TAO array, the PIRATA array in the Atlantic Ocean and the RAMA array in the Indian Ocean. This study uses data retrieved by the TAO array. A description of the GTMBA and TAO arrays is provided in section 2.1. A large part of the studies reported in sections 3.1.2 to 3.1.7 uses remote sensing data to infer the daily cycles of different parameters over a large spatial area. Instead, *in situ* observations depict only the local conditions, which may be different from the large scale conditions. Bowman et al. (2006) performed a comparison between the convection-related parameters of buoy (TAO array) and satellite (TRMM instruments) sources. They analysed time-averaged values from buoys' data and time and space-averaged satellite data to obtain two comparable datasets. Results show a greater correlation as the time window average of buoy data increases around the time of satellite image acquisition. The correlation between the two data sources is strongest when satellite data of  $1^{\circ} \times 1^{\circ}$  and buoy data averaged over a period between 2 and 10 hours are considered. Instead, taking into account coarser time and spatial averages results in lower correlation values between the two data sources. Despite these discrepancies, over the years different data were used in a variety of studies to describe the daily cycle of convection and convection-related variables in the Tropical Pacific Ocean. Overall, results outlined by several researchers are similar despite the different sources of data.

### 1.3.2 Near-surface air temperature

The diurnal cycle of the near-surface air temperature over the ocean is affected by several factors, such as incoming solar radiation, heat exchange between air and water, occurrence and strength of rainfalls and wind. Above all, the solar radiation is the major driver affecting the behaviour of several physical parameters on a daily scale. Indeed, a large fraction of the globally averaged solar energy variance is concentrated in the daily frequency band, especially at the tropics (Bergman and Salby, 1996). Along the equator, the annual evolution of solar radiation is characterised by the absence of a noticeable seasonal cycle and by the steady sunrise and sunset local times throughout the year, i.e. at 06 and 18 local time. Moreover, equatorial regions receive the highest amount of sun solar radiation over the whole year (Barry and Chorley, 2009; Ahrens, 2012). Ahrens (2012) provided a simple description of the air temperature cycle above land areas as a function of the incoming solar radiation. As the sun rises in the morning, sunlight heats the Earth's surface. Consequently, the ground starts to warm the air above through conduction. As the air temperature warms, convection starts and redistributes the heat in the lower atmosphere. The Sun continues to rise in the sky and reaches the maximum elevation at noon. After noon, as the Sun elevation decreases, the incoming radiation becomes less intense, although it still exceeds the outgoing heat energy from the surface. The outgoing longwave radiation resulting from the cooling of the ground equals the incoming shortwave radiation at, approximately, 15 local time. At this point, the air temperature starts decreasing. Therefore, there is a lag between the time of maximum solar heating and the time of maximum air temperature above the surface. Figure 1.4 describes the diurnal cycles of the incoming radiation, outgoing radiation and near-surface air temperature in on-land locations.

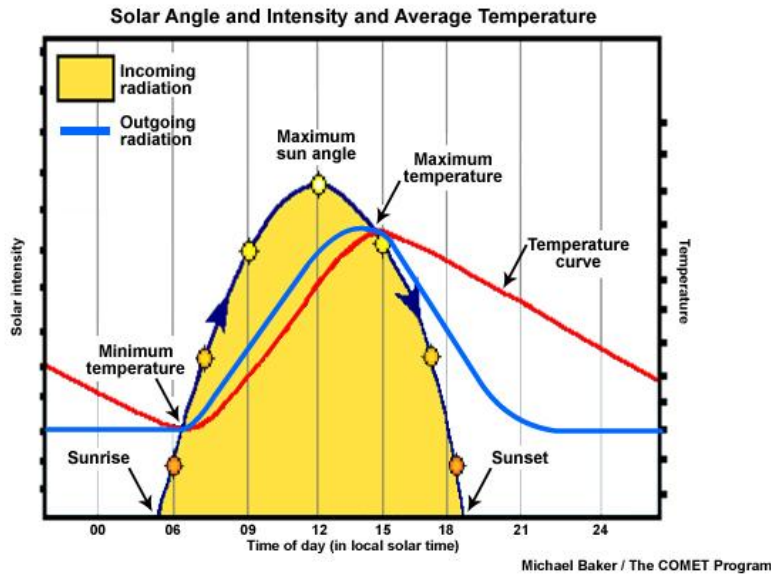
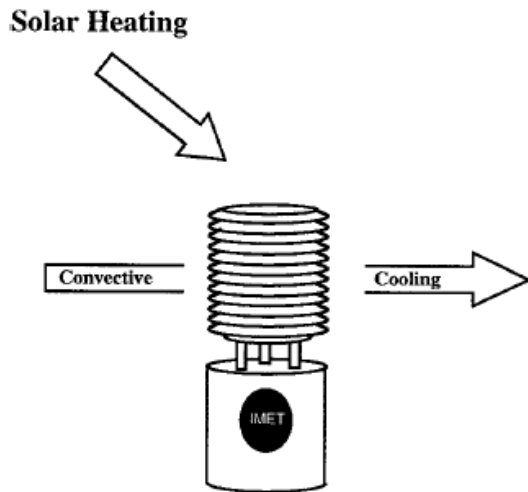


Figure 1.4: Schematic representation of the typical diurnal cycle of surface temperature, incoming solar radiation and outgoing thermal radiation. Source: GOES-R (2017).

Scientific literature lacks studies concerning the diurnal near-surface air temperature cycle over the oceans. The oceanic near-surface air temperature may have a different diurnal cycle compared to the one described previously. Indeed, the presence of water, which is a weak heat conductor and changes temperature slowly, influences differently the air temperature due to its thermal inertia. The presence of clouds as well as precipitation events exert a strong influence on the diurnal temperature cycle. Clouds reflect the incoming solar radiation and prevent the solar energy to reach the surface. Moreover, clouds contain water particles that absorb the Earth's infrared radiation and radiate it to the ground (Ahrens, 2012). Thus, the presence of clouds limits both the warming and cooling of the Earth's surface, lowering the daily range of air temperature variations. In addition, precipitation phenomena lower the ambient temperature near the surface (Ahrens, 2012). As further explained in sub-section 1.3.5, also the winds can modify the near-surface air temperature daily cycle.

### 1.3.3 The radiative heating error

This study examines near-surface atmospheric and oceanographic data acquired by the TAO array. The TAO buoys are equipped with a naturally ventilated radiation shield protecting the air temperature sensor. The shield is illustrated in Figure 1.5, along with the major heating and cooling processes.



*Figure 1.5: The major heating and cooling processes affecting a naturally ventilated radiation shield.*

*Source: Anderson and Baumgartner (1998).*

The naturally ventilated radiation shield is composed of 10 to 12 plates, placed one above the other. The height of the shield is 20.3 cm, whereas its diameter is 11.9 cm (Campbell Scientific, 2018). The shield protects the sensor from solar heating and precipitation. The particular shape of this shield allows the air to pass through the openings between the plates. A convective cooling process is triggered resulting in a heat loss, which should equal the solar heating. Anderson and Baumgartner (1998) found that air temperature measurements obtained through this naturally ventilated shield are affected by an error. This error is associated to the heating of the air temperature sensor shield because of solar heating and lack of air refreshing within the shield. Despite these authors examined buoy data coming from TOGA COARE and observational projects in the Arab Sea, they speculated that even the TAO data may be affected by the same error as the TAO buoys mount the same naturally ventilated shield. Anderson and Baumgartner revealed the existence of the error by comparing the air temperature measurements coming from two different sources. The first source was the air temperature sensor installed within a naturally ventilated radiation shield, as the one reported in Figure 1.5. The second source was a sensor measuring the temperature of the air aspirated by a pump working only in day-light hours. The two sensors were equipped on three different moored buoys during the early 1990s, two located in the Arab Sea and one in the Tropical Western Pacific (TOGA COARE). The authors analysed more than five months of data collected in the Western Pacific and approximately one year of data collected in the Arab Sea. Figure 1.6 shows the different air temperature mean daily cycles computed using observations from the two sources. The “aspirated” temperature refers to the aspirated air temperature, whereas the “standalone” temperature identifies the temperature measured by naturally ventilated sensors.

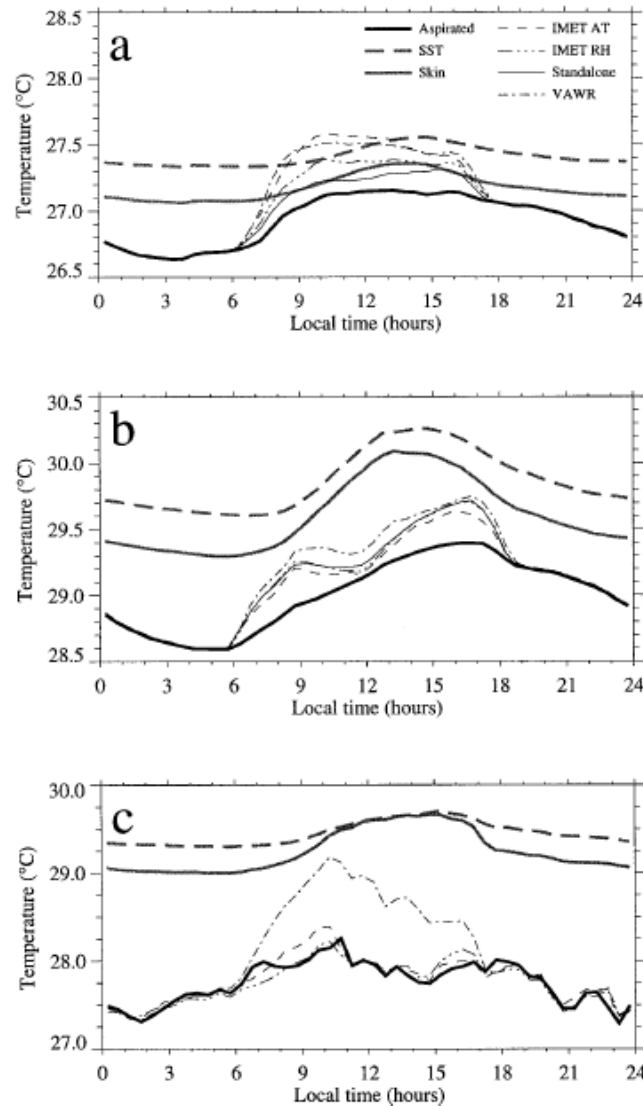


Figure 1.6: Mean diurnal cycles in air temperature and sea surface temperature retrieved from data acquired in the Arab Sea (a-b) and in the Western Pacific (c).

“Standalone” air temperature indicates the temperature measured by naturally ventilated sensors.

“Aspirated” air temperature indicates the temperature measured by aspirated sensors.

Source: Anderson and Baumgartner (1998).

The air temperature measured by naturally ventilated sensors is constantly higher than the aspirated temperature throughout the day. During night, the pump has been turned off. Accordingly, the two sensors reported the same temperature values approximately between 18 and 06 local time. The authors recognised that the shape of the mean diurnal cycle is significantly altered by the presence of a radiative heating error. During daytime hours, the aspirated temperatures show only one peak occurring between 12-15 local time. Instead, naturally ventilated sensors report two peaks occurring around mid-morning and mid-afternoon, respectively. Because of shield geometry, naturally ventilated shields experience maximum heating with a Sun elevation between  $40^\circ$  and  $70^\circ$  (Anderson and Baumgartner, 1998). The elevated difference between the aspirated and standalone air temperatures is absent in the Western Pacific buoy. Anderson and Baumgartner pointed out the dependence of the radiative heating error on meteorological conditions. Greater errors occur with higher solar radiation and low wind speed. In fact, solar insolation heats directly the shield, thus warming the air inside the chamber. On the other hand, increasing wind horizontal velocities enhance convective cooling, hence lowering the error. Anderson and Baumgartner estimated different error thresholds

according to the wind conditions. Errors of  $\pm 1$  °C are associated to winds stronger than 5 m/s,  $\pm 2$  °C to winds of 2-5 m/s and  $\pm 3$  °C to winds between 0-2 m/s. Eventually, the authors argued that their findings may reveal the presence of an error in the TAO air temperature observations as well.

### 1.3.4 Barometric Pressure

The diurnal variation of the barometric pressure variation on a daily temporal resolution is often referred to as the “Atmospheric Tide” (Chapman and Lindzen, 1970; Haurwitz and Cowley, 1973; Pugh, 1987). These authors, both through theoretical studies and observational works, claimed the existence of a semidiurnal cycle (12 hours period) in the surface air pressure. This cycle is characterised by two maxima and two minima occurring approximately at the same local time each day, depending on the location (LeBlancq, 2011). The causes of this variation are not fully understood (LeBlancq, 2011), but, as suggested by Pugh (1987), the solar radiation shall be a dominant component. In the upper atmosphere, diurnal pressure waves are risen by the diurnal heating cycle. However, the semidiurnal harmonic prevails because of the dynamic structure of the atmosphere (Pugh, 1987). The absorption of UV light by ozone in the upper atmosphere and water vapour in the lower atmosphere causes the photodissociation of these compounds, therefore heating the nearby air (Cooper, 1982; Ahrens, 2012). The consecutive warming and cooling of the air creates density oscillations, called also “Thermal Tides” (Ahrens, 2012). At the tropics, where the incoming solar radiation is greatest, the diurnal pressure variation is most noticeable, reaching  $\sim 3$  mb. The variation has a regular sinusoidal pattern characterised by two maxima at approximately 10 and 22 local time and two minima at approximately 4 and 16 local time (Le Blancq, 2011; Ahrens, 2012).

### 1.3.5 Wind

All observational studies concerning near-surface wind velocity and direction over the Tropical Pacific used data coming from the same data array of this thesis work, i.e. the TAO array. In this sub-section, the term “zonal” refers to winds blowing from east to west, or vice versa. Similarly, the term “meridional” identifies winds blowing from north to south, or vice versa. Through the analysis of hourly wind data acquired by 14 moorings near the equator during summer 1992, Deser et al. (1994) found evidences of semidiurnal and diurnal cycles. The phase of the semidiurnal component is homogeneous across the domain, characterised by westerly winds peaking at 03 and 15 local time and reaching maximum values varying by a few tenths of m/s. Instead, the diurnal cycle is dominated by the daily march of the meridional wind component, with a variation range of  $\sim 0.6$ - $0.8$  m/s. The flow is generally southward across the equator at night, relative to the daily mean. Deser and Smith (1997) utilised data coming from 60 TAO buoys acquired during a 3 years period to document the large-scale pattern of daily variations in the low-level atmospheric circulation. Deser and Smith (1997) confirmed the previous finding of Deser et al. (1994). The semidiurnal cycle in wind velocity accounts for much of the mean daily variance of the zonal wind component, while the diurnal cycle explains much of the mean daily variance of the meridional wind component. Again, the characteristics of the zonal wind variation are practically uniform across the basin. Its amplitude and phase are  $0.15 \pm 0.04$  m/s and 03:10 (and 15:10)  $\pm$  00:30 local time. The wind diurnal variation in the equatorial zone exhibits a maximum at 07 local time, with a general pattern of southerly flow. Deser and Smith (1997) found an interesting variation in the diurnal meridional winds from the east to the west Pacific. Specifically, the

diurnal cycle at the equator is larger in the Eastern Pacific and negligible in the Western Pacific. Ueyama and Deser (2008) based their study on data coming from 51 TAO buoys over a 12 years period. These authors confirmed the previous findings described above and added few considerations: the meridional wind variability is mainly diurnal, with maximum southerly wind anomalies around 07 local time at 5°N and around 19 local time at 5°S over the Western Pacific. Instead, the equatorial Eastern Pacific shows a southerly wind anomaly maximum at noon. Moreover, these authors found that during the cold season the diurnal mean wind variation is larger than in the warm season. Overall, the listed studies detected approximately the same behaviour in the Tropical Pacific. Equatorial winds present a semidiurnal component majorly characterised by air currents flowing westward and peaking around 03 and 15 local time. The amplitude of this component is small, reaching only 0.1/0.2 m/s. The semidiurnal zonal cycle is considered to be consistent with the diurnal pressure wave propagating westward (following the Sun's path). In addition, equatorial winds show a diurnal component defined by a southerly flow maximum at 07 local time. However, Ueyama and Deser (2008) indicated a different pattern in the equatorial eastern Pacific composed by a maximum at noon. Moreover, previous works suggested the greater importance of the diurnal cycle compared to the semidiurnal cycle, sometimes even negligible as in the case of the Western Tropical Pacific.

### 1.3.6 Sea Surface Temperature (SST)

The daily cycle of the sea surface temperature has been studied since high temporal resolution (*in situ* measurements) became available in the last century (Kawai and Wanda, 2007). Moreover, the development of remote sensing systems has permitted the acquisition of data with large spatial coverage and high temporal frequencies (usually four daily measurements). The SST diurnal cycle has an almost sinusoidal shape. Temperature peaks in the early afternoon, around 15-16 local time, while the minimum occurs between 06 and 08 local time. The phase of the cycle is approximately the same throughout all the considered studies reviewed by Kawai and Wanda (2007). Both in the tropical regions (Fairall et al., 1996; Webster et al., 1996; Soloviev and Lukas, 1997; Tanahashi et al., 2003; Clayson and Weitlich, 2007) and at higher latitudes (Stommel et al., 1969; Halpern and Reed, 1976; Deschamps and Frouin, 1984; Price et al., 1986), it has been noted that the daily temperature range of the ocean surface (hereafter referred also as daily  $\Delta$ SST or amplitude) is principally dependent on two factors: insolation and wind. The absorption of solar radiation by the near-surface ocean layer causes diurnal warming of the SSTs. More specifically, 60% of the incident solar radiation is absorbed in the first meter of the ocean (Soloviev and Lukas, 2006), which trigger the temperature's rise. The SST warming is hampered by mechanical as well as thermal wind forcing. Winds enhance mechanical mixing of surface waters and the latent heat exchange between sea and air. High wind speeds keep the upper part of ocean well mixed, while low wind speeds permit a strong stratification, hence leaving the warmest layers confined near the surface (Gentemann et al., 2003; Kawai and Wanda, 2007). Moreover, high wind velocities enhance the latent heat exchange between air and water, causing the oceanic water to lose heat. The SST is cooled also by precipitation (Wester et al. 1996; Tanahashi et al., 2003), with the strongest cooling occurring during night-time (Webster et al., 1996). Overall, previous studies pointed to the occurrence of high SST diurnal warming under high levels of incoming solar radiation and low wind velocities. The largest SST diurnal warming measured at the tropics reaches maximum values of up to 3°C (Gentemann et al., 2003; Kawai and Wanda, 2007). Tanahashi et al. (2003) suggested that the greatest SST diurnal warming occurs in tropical coastal areas due to the larger heat radiation caused by the surrounding land. Focusing specifically to the Tropical Pacific region, several studies noted few new characteristics. Webster et al. (1996) found the largest amplitudes of the SST diurnal cycle in regions with the greatest insolation. On the other hand, wind speeds greater than 10 m/s can effectively suppress the SST daily

variation, regardless of insolation and precipitation regimes. As a result, the amplitude of the SST diurnal variations increases with the formation of a fresh and stable layer at the surface, which favours surface heating. Gentemann et al. (2003) highlighted the higher susceptibility of the SST to the diurnal warming in the Western Pacific. Clayson and Weitlich (2007) analysed the difference between the daytime SST peak value and night-time SST minimum over the global tropics using satellite (ISCCP and SMI/I) and *in situ* (TAO/TRITON and PIRATA) measurements. They found that wind speed variations explain better the SST's diurnal variation rather than changes in the solar radiation because the solar radiation peak does not vary greatly at the tropics. By considering all the available data, Clayson and Weitlich (2007) found average wind speeds of about 3-4 m/s in areas of  $\Delta$ SST measuring 0.7 °C. Wind velocities greater than 8 m/s are associated to a  $\Delta$ SST smaller than 0.2 °C. Deser and Smith (1998) and Clayson and Weitlich (2005, 2007) revealed that the diurnal SST amplitude presents a local maximum over the cold surface waters in the Eastern equatorial Pacific. Furthermore, they found that the largest amplitudes occur between boreal winter and spring. Cronin and Kessler (2002) and Kawai and Kawamura (2005) studied the influence of ENSO events on the diurnal SST variation. They found that the different surface conditions existing during an ENSO event could change the spatial and temporal variations of the diurnal SST warming. The impact of daily  $\Delta$ SST on the atmosphere is not yet fully understood (Kawai and Wanda, 2007). Different researchers suggested that a large diurnal SST variation must be coupled to the presence of weak winds, which in turn suppresses the turbulent heat transfer between water and air (Kawai and Wanda, 2007). This may result in a condition of suppressed convection.

### 1.3.7 Convection and precipitation

The diurnal cycle of convection in the Tropical Pacific Ocean has been studied by several authors during the latter 50 years. Earlier studies were based on ship observations and precipitation data from *in situ* stations, whereas recent studies used remote sensing data and rain gauges deployed on moored buoys. Works using inferred cloud properties through remote sensing data to investigate convection are based on measurements of different variables, including cloud top radiating temperature, cloud coverage and microwave radiation temperature of water droplets. The general results of these studies are mostly in agreement with each other, despite the different types of measurement and spatio-temporal resolutions of the data. Overall, researchers indicate the presence of one clear peak in the tropical convective activity over oceanic regions in the early morning, before dawn. Here, previous observational studies are described. Gray and Jacobson (1977) analysed hourly precipitation data acquired by few stations located on small and large islands over the Western and Central Pacific. They found an early morning maximum around 03-06 local time and an evening minimum between 18-23 local time. The differences between maxima and minima are more prominent on small islands than on larger islands. Small islands more likely reproduce the true conditions over the open ocean than large islands. Furthermore, Gray and Jacobson (1977) distinguished precipitation data into different rainfall categories. They found that, while light rain does not show a variation during the day, heavy rain dominates in the morning. Therefore, deep convective activity seems to peak in the morning. Kraus (1963) and Trent and Gathman (1972) found similar evidences. Moreover, Ruprecht and Gray (1976) studied tropical cloud clusters over the Western Pacific Ocean. They reported that rainfall amounts from cloud clusters are twice as much in the morning (07-12 local time) as in the evening (19-24 local time). Augustine (1984) used satellite infrared images of five locations along the equatorial Pacific Ocean (180°W, 165°W, 150°W, 135°W and 120°W). In contrast with previous findings, he discovered a primary maximum in the mid-afternoon and a secondary maximum near dawn at four locations (180°W, 165°W, 135°W and 120°W). However, the author examined only data retrieved on August 1979. Thus, results concerns a limited

period that is possibly not representative of longer-term behaviours. In agreement with Augustine, Albright et al. (1985) examined the diurnal variation in deep convection and precipitation in the Central Tropical Pacific during a limited period (January and February 1979). They used infrared satellite of  $1.5^{\circ} \times 1.5^{\circ}$  spatial resolution to assess the spatial coverage of clouds' tops colder than certain thresholds ( $-36^{\circ}\text{C}$ ,  $-55^{\circ}\text{C}$ ) as indicators of deep convective activity. These authors found different diurnal behaviours in the fractional coverage of cold clouds top characterising several sub-regions. The western side of the SPCZ region shows a maximum coverage in the evening. Besides, the eastern part of the SPCZ shows an afternoon peak. Cloud cover in the ITCZ region peaks near sunrise, while in the region south of the ITCZ, approximately along the equator, an early morning peak is identified. In addition, Albright et al. (1985) studied the atmospheric levels reached by clouds founding a common characteristic among the different sub-regions. Deep convective clouds with tops reaching a corresponding height of 100-250 mb exhibit a peak around sunrise. Hence, all these evidences pointed to a pronounced diurnal cycle in deep atmospheric convection over the Tropical Pacific Ocean. Meisner and Arkin (1987) investigated the spatial patterns of the annual variation of the diurnal cycle in cold cloudiness fractional coverage over a three year period (December 1981 – November 1984). Infrared satellite data were used to estimate the clouds' top temperature. They found different results compared to previous studies, suggesting a convection's tendency to exhibit more maxima in the 12-24 local time than in the 00-12 local time period. Janowiak et al. (1994) examined the diurnal fluctuations in the frequency of occurrence of cold clouds in the tropical regions through satellite infrared and microwave data. Infrared data were categorised into three groups, i.e. clouds' top colder than  $-38^{\circ}\text{C}$ ,  $-48^{\circ}\text{C}$  and  $-58^{\circ}\text{C}$ . In addition, they analysed precipitation data coming from ship and buoy observations. Satellite data revealed a diurnal cycle peaking during morning. In particular, tops colder than  $-38^{\circ}\text{C}$  have a maximum near local noon, between 06-09 local time for tops colder than  $-48^{\circ}\text{C}$  and generally earlier than 06 local time for tops colder than  $-58^{\circ}\text{C}$ . Over the Pacific Ocean, these authors distinguished a daily peak in convection at about 06 local time, with a minimum around 18 local time. *In situ* observations seem to confirm these findings. Ship records suggest a diurnal rainfall preference for the 06-09 local time interval. Buoy data were used to distinguish between heavy, medium and light rainfalls. The three categories occur most frequently near 03 local time with a probability of occurrence much higher than any period except around 06 and 21 local time. Heavy rainfall events are relatively less frequent but have a disproportional contribution to the total rainfall over oceanic regions. Finally, Janowiak et al. (1994) compared rainfall categories and satellite data. They highlighted the correspondence between the occurrence of heavy rainfall events and deep convection. Yang and Slingo (2001) confirmed that deep oceanic convection typically peaks in the early morning. Moreover, they suggest that the strong diurnal cycle on land may spread to the surrounding ocean, therefore modifying the diurnal convection processes over the ocean. Serra and McPhaden (2004) examined the diurnal rainfall variability over the Tropical Pacific Ocean. They used rain gauge observations obtained by moored buoys (TAO/TRITON array). Then, data were distinguished based on accumulation, intensity and frequency of rainfalls. Each parameter shows a diurnal cycle with a maximum in between 04 and 08 local time and a minimum around 18 local time. Furthermore, data also suggest the presence of a semidiurnal cycle peaking near sunrise and afternoon/early evening. The diurnal and semidiurnal harmonics explain much of the data variability. Furthermore, these cycles vary significantly with region and season. Serra and McPhaden (2004) concluded that the rainfall maximum occurring during afternoon and late evening identifies the manifestation of small and unorganised systems. On the other hand, the early morning peak marks the occurrence of deep and organised convective systems. Bowman et al. (2005) performed an examination of the diurnal cycle in tropical precipitation considering both satellite (TRMM) and in situ (TAO array) data. They individuated a diurnal harmonic indicating the occurrence of maximum rainfall between 03 and 06 local time. The amplitude of this harmonic is greater in areas of large mean rain rates, namely the Western Pacific and north of the equator near the ITCZ. Kikuchi and Wang (2008) used two kinds of satellite (TRMM) datasets to analyse the diurnal precipitation regimes in the tropics. They distinguished three different regimes: coastal, continental and oceanic. In oceanic regions, the diurnal precipitation cycle shows a moderate amplitude and an early morning peak between 06 and 09 local time.

In general, literature presents a high number of observational studies concerning the diurnal cycle of tropical rainfall and convective activity. Researchers distinguished a clear morning maximum in convection over the Tropical Pacific Ocean. Most of the times, this maximum is related to the occurrence of deep convection leading to the formation of high altitude clouds and resulting in heavy rainfall events. Light and medium rainfalls are not bound to a particular period of the day, but tends to occur mostly in the early evening, around 18 local time. In addition, previous studies reported the higher variability of *in situ* data, i.e. ships and buoys' observations, than remote sensing data.

Still, a convincing explanation to the diurnal behaviour of convection lacks. During the years, different mechanisms have been proposed based on the retrieved evidences. Kraus (1963) argued that radiative cooling at the clouds top during night triggers a destabilisation process ending in rainfall events. On the other hand, solar heating stabilises clouds top during the day. Randall et al. (1991) reinforces the hypothesis of Kraus utilising a global climate model. They found that the stabilization of the atmosphere through the absorption of solar radiation by clouds is a dominant factor for the convective diurnal cycle. During the day, solar radiation warms the higher levels of clouds, enhancing stability and restricting convective activity. During the night, cloud tops are destabilised due to radiative cooling. Chen and Houze (1997) theorised a complex mechanism involving surface-cloud-radiation interactions. These authors highlighted the air temperature and the SST as important surface thermal variables affecting the convection mechanism. These variables reach their daily maxima in the afternoon, and then the system starts cooling. This cooling is intended to favour the beginning of convective processes, which grow throughout the rest of the day and the following morning. Chen and Houze (1997) considered also the life cycle of cloud systems as an important factor affecting the diurnal variability of convection. Since deep convective phenomena tend to decrease the moist-static energy and lead to the formation of a cloud canopy preventing the solar radiation to reach the surface, surface conditions at the end of the convective process do not facilitate again widespread convective processes. Hence, it is claimed that convection will occur in nearby regions unaffected by previous convective events.

## 1.4 General aim and objectives of the thesis work

As presented in Section 1.3, several observational studies regarding the analysis of daily surface and atmospheric cycles in the Tropical Pacific Ocean are available in the scientific literature. Above all, sea surface temperature and convection are the most studied variables, whereas satellite observations are the most used source of data. Nonetheless, the deployment of the next generation ATLAS buoys during early 1990s and the development of the TAO array has led to the acquisition of point data characterised by a high temporal resolution. Buoys, deployed in several tropical locations, have constantly monitored the evolution of surface oceanic and atmospheric conditions throughout the day over the last 20 years. Therefore, this kind of array constitutes an extraordinary opportunity to investigate the daily cycles of different atmospheric and oceanographic variables.

This study aims to assess the daily cycles of different physical parameters over the Tropical Pacific Ocean, taking advantage of the unique opportunity given by the availability of the TAO array.

The first objective of this work is the characterisation of the diurnal behaviour of several physical parameters, i.e. solar radiation, wind speed, air temperature, sea surface temperature, relative and specific humidity, sea level pressure, wind direction and precipitation. Three buoys have been selected to describe the daily cycles in the Eastern, Western and Central Equatorial Pacific Ocean. Their locations are, respectively: 0°N 95°W, 0°N 140°W, 0°N 165°E. The second objective of this work is the examination of daily cycle variations under different background local meteorological conditions, i.e. during sunny, cloudy, windy and calm days. Above all, this differentiation is used to evaluate the presence and magnitude of a radiative heating error in the air temperature measurements. Second, this study inspects the dependency of daily cycles on “background” large-scale climatic conditions. To this purpose, measurements retrieved under “warm” and “cold” ENSO phases are compared to highlight any influence of this climatic mode on the diurnal cycles. Another objective consists in the characterisation of the variation of daily cycles on the long-term, highlighting the variability of the cycles under different parameters regimes. The fourth objective of this work is to examine the relations existing between the different physical parameters on a daily time scale. The findings of this thesis work are compared with the existing results provided by the scientific literature.

## 2. Data, methods and software description

This chapter is dedicated to the description of the methodology adopted in this thesis work. Specifically, section 2.1 describes the characteristics of the TAO array as well as the specific data used in this thesis. Section 2.2 illustrates the methods utilised in the data elaboration to accomplish the objectives listed in section 1.4. Finally, section 2.2 delineates the software utilised for the data analysis and the creation of the graphics.

### 2.1 Data

This thesis uses atmospheric and oceanographic measurements acquired by moored buoys deployed in the Tropical Pacific Ocean. These *in situ* observations constitute the Tropical Atmosphere Ocean (TAO) dataset. The buoys are managed by the Pacific Marine Environmental Laboratory (PMEL), which is part of the National Oceanic and Atmospheric Administration (NOAA) agency of the United States of America. Data are publicly available and can be retrieved from the PMEL web page, at: <https://www.pmel.noaa.gov/tao/drupal/disdel/>.

This section describes different aspects of the dataset utilised in this study. First, a general overview of the TAO project and its development over the years is reported, starting from early 1980s to the present (sub-section 2.1.1). Then, the structure of the moorings, buoys' sensors and data management are illustrated (sub-section 2.1.2). Finally, the specific data used in this study are delineated by focusing on buoys' location and operating periods (sub-section 2.1.3).

#### 2.1.1 The evolution of the TAO project

The TAO project was designed in response to growing needs of monitoring, understanding and predicting the El Niño events and related phenomena during the 1980s. The lack of a quick detection of the 1982-83 El Niño, the strongest climatic event in the Tropical Pacific in over a hundred years, motivated the demand for an *in situ* observing system capable of sending high-quality data in real time (McPhaden et al., 1998). Ship-based observations of the ocean surface were available at that time but they covered only a small portion of the total Tropical Pacific area (Hayes et al., 1991). Overall, ship measurements were not able to describe different regions of the ocean continuously in time. Between 1985 and 1994, PMEL deployed an array of approximately 70 buoys in the Tropical Pacific Ocean between 8°N and 8°S, 95°W and 137°E to systematically monitoring ENSO and to provide a better interpretation of ENSO-related phenomena (McPhaden, 1995). The array was named Tropical Atmosphere Ocean (TAO) array. According to McPhaden et al. (1998), the major advantage of the TAO array is its ability to acquire data at high frequency (from hourly to 2-minutes) for several key parameters such as winds and ocean and atmospheric temperatures. In January 2000, the array was renamed TAO/TRITON array in recognition of the contribution of the Triangle Trans-Ocean Buoy Network (TRITON) moorings to the observations of the western side of the Tropical Pacific Ocean. TRITON moorings are still managed by the Japan Agency for Marine-Earth Science and Technology (JAMSTEC). The success of this major effort prompted the deployment of similar moored buoy

arrays in other ocean basins during the years: the Prediction and Research Moored Array in the Atlantic (PIRATA) and the Research Moored Array for African-Asian-Australian Monsoon Analysis and Prediction (RAMA). These arrays constitute the Global Tropical Moored Buoy Array (GT MBA) (PMEL, 2017). Figure 2.1 illustrates the buoys composing the GT MBA and their characteristics.

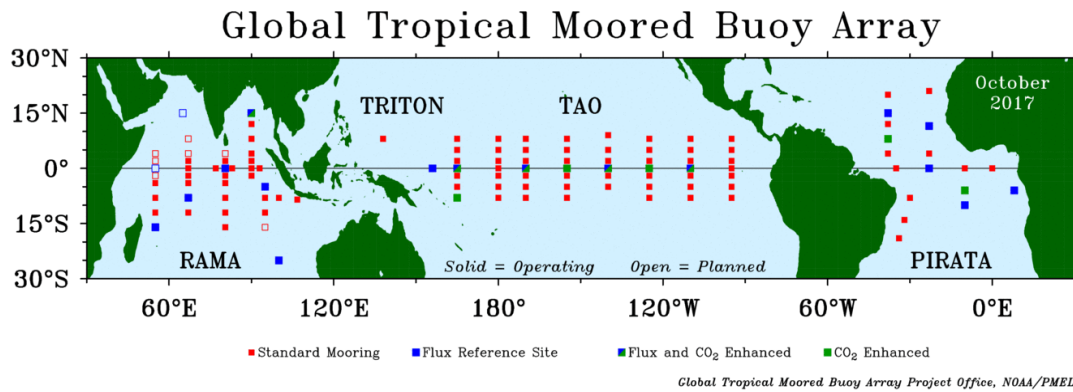


Figure 2.1: The Global Tropical Moored Buoy Array. This study uses data coming from the TAO array in the Pacific Ocean. Source: PMEL (2017).

The GT MBA contributes to the advancement of the Global Ocean Observing System (GOOS), the Global Climate Observing System (GCOS), and the Global Earth Observing System of Systems (GEOSS) (PMEL, 2017).

### 2.1.2 Moorings' specifications

The TAO array is currently composed by the Next Generation ATLAS (Autonomous Temperature Line Acquisition System) moorings. Next Generation systems replaced the standard ATLAS moorings, deployed between 1984 and mid-90s. The transition to Next Generation systems began in May 1996 and ended in November 2001 (PMEL, 2017). The standard ATLAS moorings were designed and tested by PMEL in NOAA laboratories in the early 80s (NDBC, 2016b). These buoys measured surface winds, air temperature, relative humidity, sea surface temperature and subsurface temperatures at different depths. Daily mean data were telemetered to shore in real time via NOAA's polar-orbiting satellites and Service Argos. Hourly data were recorded internally and available after mooring recovery (NDBC, 2016b). In the mid-90s, the Next Generation ATLAS moorings were designed to improve several characteristics of the array. The efforts were made to enhance data quality, add new sensors, increase temporal resolution of internally recorded data, improve systems' lifetime, simplify fabrication procedures and reduce costs (NDBC, 2016b). Next Generation ATLAS moorings use as many components and procedures of the older systems as possible. New sensors were added for measuring rainfall, down-going shortwave and longwave radiation, barometric pressure, salinity and currents. Moreover, most measurements began to be acquired at a sampling rate of 10 minutes, except for precipitation (1 minute), longwave and shortwave radiation (2 minutes) and barometric pressure (1 hour). Precipitation measurements are filtered with a 16-point Hanning filter to produce smoothed 10-minutes data (Serra et al., 2001). These high-resolution data are recorder internally and available after recovery of the mooring (NDBC, 2016b). Daily and lower frequency data are telemetered

through satellites to PMEL laboratories. Figure 2.2 illustrates a model of the Next Generation ATLAS mooring.

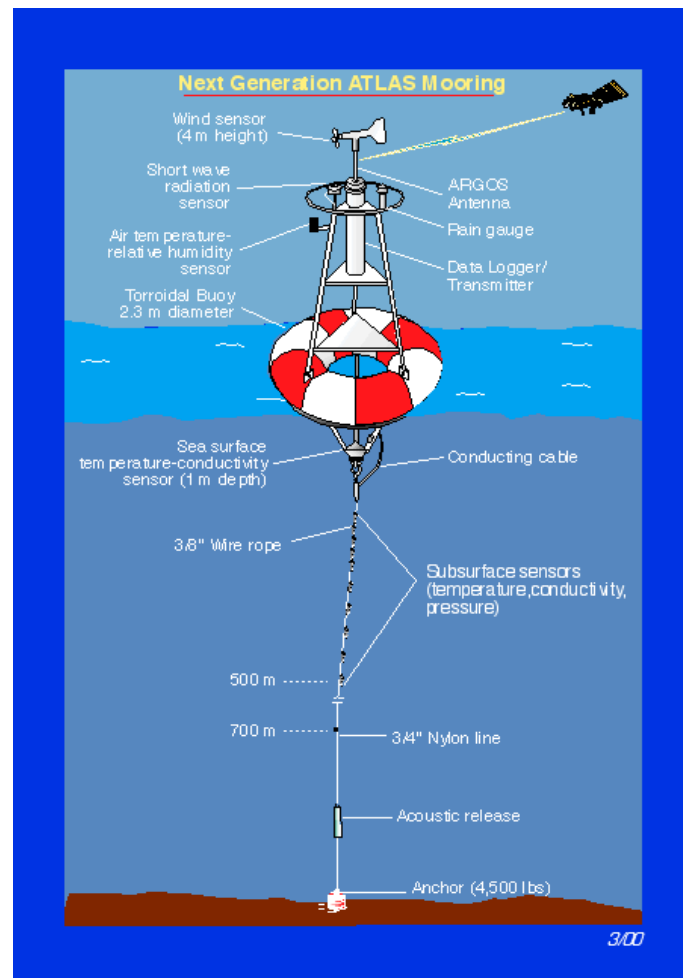


Figure 2.2: A model of the Next Generation ATLAS Mooring. Source: NDBC (2016b).

The Next Generation ATLAS buoy has a toroidal shape of a 2.3 m diameter. It is made of fiberglass-over-foam, with an aluminium tower and a stainless-steel bridle. It weighs approximately 660 kg and has an overall height of 4.9 m. The buoy is anchored at the sea bottom through a non-rotating wire rope in the upper 700 m to guard from fish bite damage and the remainder by a nylon line with an anchor at the end. Moorings' locations have depths ranging from 1500 to 6000 m (PMEL, 2017). The height of the sensors above the sea level are listed in the Table 2.1.

Table 2.1: Height above the sea level of Next Generation ATLAS mooring sensors.

Sensor	Wind	Shortwave radiation	Precipitation	Air Temperature	Relative Humidity	Barometric Pressure	Sea Surface Temperature
Height (m)	4	3.5	3.5	3	3	3	-1

The negative height value for the sea surface temperature indicates that the sensor is located at 1 meter depth. For a complete description of the sensors, including sensors specifications, the reader is referred to Appendix A of this thesis. Figure 2.3 schematises the processes of moorings' maintenance and data dissemination.

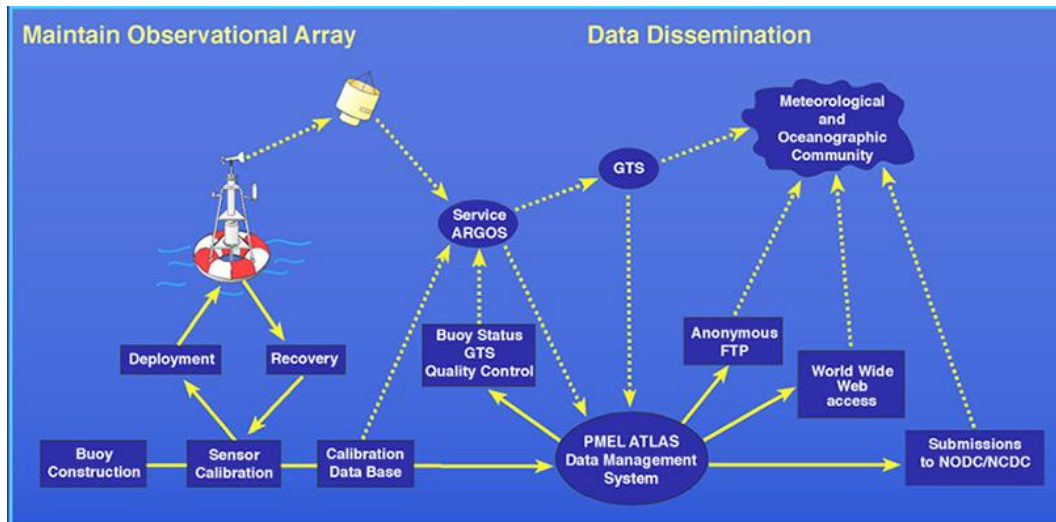


Figure 2.3: TAO data management description. Source: NDBC (2016a).

In brief, daily TAO measurements are telemetered in near-real-time via Service Argos through NOAA polar-orbiting satellite. High frequency TAO measurements (10 or 2-minutes) are made available after moorings' recovery. The data are then processed by the TAO Project at PMEL, when calibration coefficients and quality controls are performed. Finally, data are distributed to the general public and to the international scientific community. Sensors are calibrated before moorings' deployment and after moorings' recovery (NDBC, 2016a).

### 2.1.3 Data used in this study

This study uses data from selected TAO moorings positioned along the equator representative of different key regions of the Tropical Pacific Ocean: the Western Pacific Warm Pool in the westernmost part, the Central Pacific, and the Cold Tongue in the Eastern Pacific. Representative buoys are selected based on the amount of data available at the highest possible time resolution. Therefore, the buoys considered in this study are those located at 0°N 95°W, 0°N 140°W and 0°N 165°E (see Figure 2.4). The three buoys are denominated with their location throughout the remainder of the text. The choice of the equator as latitudinal reference for all the studied buoys was motivated by the desire of minimising potential biases in the monitored parameters linked to the annual seasonal cycle, i.e. the asymmetric alternation of a warm and cold season. Another important reason is the following: at the equatorial latitude the daylight period is constant throughout the year. It lasts twelve hours, starting at 06 and ending at 18 local time. Figure 2.4 illustrates the whole TAO array and the buoys selected in this study.

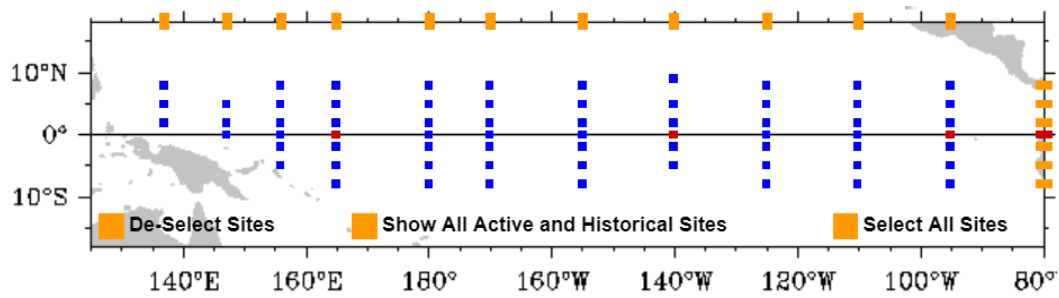


Figure 2.4: Location of the TAO buoys composing the TAO array (blue dots). The red dots represent the location of the buoys used in this study (i.e. at 0°N 95°W, 0°N 140°W and 0°N 165°E).

Source: NOAA/PMEL

The physical parameters considered in this study and their associated maximum monitoring frequency are reported in the Table 2.2.

Table 2.2: Variables used in this study and maximum available time resolution.

Variable	Time Resolution
Air Temperature	10 minutes
Sea Surface Temperature	10 minutes
Wind (speed and direction)	10 minutes
Relative Humidity	10 minutes
Precipitation	10 minutes
Sea Level Pressure	Hourly
Downgoing Shortwave Radiation	2 minutes

This study uses all the available data measured at the time resolution reported in Table 2.2, but, as discussed in section 2.2 (Methods), the sea level pressure and shortwave radiation data are pre-processed to allow the analyses to be conducted on a 10-minute time resolution. Ten-minute and 2-minute data have been acquired since the end of 1990s, while hourly sea level pressure data are available since the year 2000. The data periods, total number of recorded days and percent of data coverage for the three reference buoys are shown in the Tables 2.3, 2.4 and 2.5.

Table 2.3: Data availability for the different variable measured by 0°N 95°W.

Variable	Start date and time (UTC format)	End date and time (UTC format)	Total number of recorded days (approximated)	Percent data coverage
Air Temperature	1998-11-07 00:00:00	2009-10-08 09:10:00	2480	0.62
Sea Surface Temperature	1998-11-06 00:00:00	2017-11-16 02:50:00	2597	0.57
Wind (speed and direction)	1998-11-07 00:00:00	2009-10-05 18:50:00	1852	0.46
Relative Humidity	1998-11-07 00:00:00	2017-06-28 17:10:00	2502	0.37
Precipitation	1998-11-07 00:00:00	2009-10-05 18:40:00	2184	0.55
Downgoing Shortwave Radiation	1998-11-07 00:00:00	2003-08-23 02:14:00	1175	0.81
Sea Level Pressure	2000-04-27 00:00:00	2003-11-02 15:00:00	948	0.74

Table 2.4: Data availability for the different variable measured by 0°N 140°W.

Variable	Start date and time (UTC format)	End date and time (UTC format)	Total number of recorded days (approximated)	Percent data coverage
Air Temperature	1998-05-11 00:00:00	2013-06-23 21:20:00	5090	0.92
Sea Surface Temperature	1998-05-10 00:00:00	2013-07-12 00:20:00	5173	0.93
Wind (speed and direction)	1998-05-11 00:00:00	2013-06-11 10:20:00	5109	0.93
Relative Humidity	1998-05-11 00:00:00	2017-09-18 04:10:00	6014	0.85
Precipitation	1998-05-11 00:00:00	2017-10-18 21:40:00	5063	0.71
Downgoing Shortwave Radiation	1998-05-11 00:00:00	2013-06-24 21:24:00	3808	0.83
Sea Level Pressure	2006-09-15 00:00:00	2013-06-23 20:00:00	2127	0.86

*Table 2.5: Data availability for the different variable measured by 0°N 165°E.*

<b>Variable</b>	<b>Start date and time (UTC format)</b>	<b>End date and time (UTC format)</b>	<b>Total number of recorded days (approximated)</b>	<b>Percent data coverage</b>
Air Temperature	1998-01-08 00:00:00	2013-01-15 14:00:00	3719	0.68
Sea Surface Temperature	1998-07-11 00:00:00	2011-02-28 11:00:00	3676	0.80
Wind (speed and direction)	1998-01-08 00:00:00	2013-01-15 14:00:00	3684	0.67
Relative Humidity	1998-01-08 00:00:00	2017-10-18 13:50:00	4391	0.61
Precipitation	1998-01-08 00:00:00	2012-12-27 13:40:00	3481	0.64
Downgoing Shortwave Radiation	1998-01-08 00:00:00	2013-01-15 14:08:00	3128	0.68
Sea Level Pressure	2006-07-12 00:00:00	2013-01-15 11:00:00	1816	0.76

Tables report that records present different gaps from buoy to buoy. Therefore, this study uses different periods according to the type of the analysis. The characterisation of the daily cycles is based on all the available data for each variable and each buoy; instead, the assessment of relations between parameters, where homogeneous sampling is necessary, bases on overlapping recorded periods of the different parameters for each buoy.

## 2.2 Methods

This section describes the data analysis methods used to pre-process the data (sub-section 2.2.1), determine the daily cycles (sub-section 2.2.2), cluster the data based on climatological (sub-section 2.2.3) and meteorological (sub-section 2.2.4) conditions, determine the diurnal cycle variation over the long period (sub-section 2.2.5), data smoothing (sub-section 2.2.6) and assess the relations between the variables on a diurnal time scale (sub-section 2.2.7).

### 2.2.1 Data pre-processing

This sub-section is divided into different parts: homogenization of time series' frequency, precipitation data correction and treatment, wind direction data transformation and transition from "UTC" time to local time.

The main analysis is conducted on time series with sampling rate of 10-minute. Downgoing shortwave radiation data are available at a higher frequency (2-minutes, see Table 2.2), hence, they shall be rescaled. Ten-minute time series are obtained by selecting those measurements acquired during minutes 00, 10, 20, 30, 40 and 50 of each hour, corresponding to the sampling time for the reference 10-minute data. Sea level pressure data are available at a lower frequency (hourly, see Table 2.2) and they shall be rescaled as well. The original data are available for every 00 minutes of each hour. The other required values at minutes 10, 20, 30, 40, 50 are created by linear interpolation between each couple of originally available values for consecutive hours.

Precipitation data are acquired using self-siphoning rain gauges fabricated by R. M. Young Co. Serra et al. (2001) discussed the different sources of potential errors affecting precipitation measurements. In particular, large errors surrounds a "siphon event". A siphon event occurs when the rain gauge reaches its maximum capacity of 0.5 l and water is expelled through a siphon tube. Siphoning occurs over a 30 seconds period and it is recognised by a sharp decrease in measured volume. Post-deployment data processing removes the obviously erroneous data and averages the acquired 1-minute data. However, siphon events are characterised by errors averaging 1.8 mm/hr for the 10-minutes data whereas typical errors unrelated to siphon events averages 0.4 mm/hr. Therefore, siphon events remain affected by large errors despite post-processing. Evaporation leads to errors in the order of 0.2 mm/day. Sensor drift and sea spray produce negligible errors. The expected greatest source of error is undercatchment due to wind. Serra et al. (2001) analysed different possible correction schemes for rain gauge data, eventually recommending the estimate of the actual rain rates as in Koschmieder (1934). Koschmieder examined the percent rain undercatchment  $c$  at a given wind speed  $w$ . These quantities are related by the following empirical equation:

$$c(w) = -0.0141w^3 + 0.4409w^2 + 0.9927w + 0.1010$$

In this study, precipitation data are corrected to account for wind undercatchment using wind speed data acquired by the same buoy. The correction is performed only in those periods characterised by wind speed data availability. Wind undercatchment correction is not performed in periods characterised by missing wind speed values. Once the percent rain undercatchment  $c$  at time  $t$  is estimated, the correct precipitation intensity estimate  $P$  at time  $t$  is calculated as in the following equation:

$$P_t = r_t + [(c_t/100) * r_t]$$

In this equation,  $r$  represents the uncorrected rain intensity at time  $t$ .

Precipitation data are treated with another pre-processing step as follows. Rain gauges devices installed on ATLAS buoys register rain rates occurring during the day, independently from the presence or absence of rainfalls. As a result, a large part of precipitation data are composed by near-zero measures representing dry conditions. Therefore, data are handled to identify rainfall events and exclude noisy data by excluding from the analysis precipitation rates smaller than 0.5 mm/hr, as implemented by Serra and McPhaden (2004). Subsequently, 10-minutes data are grouped together according to the associated hour. Furthermore, rainfall events are divided into three magnitude categories: light (0.5-3 mm/hr), medium (3-10 mm/hr) and heavy (>10 mm/hr) events. Finally, extreme rainfalls are examined by selecting only those values greater than the 98<sup>th</sup> percentile of the distribution of the rain rates values associated to rainfall events for each different buoy. The percentiles values are 17.34 mm/hr for 0°N 95°W, 13.26 mm/hr for 0°N 140°W and 43.98 mm/hr for 0° 165°E.

Wind direction data measuring the wind-blowing angle spans in the interval 0-360°. This range can potentially induce a bias in the calculation of the mean values, which, as introduced in sub-section 2.2.2, consequently affects the determination of the diurnal cycle. Indeed, the angles at the extremes of the 0°-360° interval are assumed to indicate opposite directions, whereas this is not true. For example, the simple average between two values such as 350° and 10° is 180°, when, intuitively, the “real” average angle is 0° (or 360°). Hence, wind direction data are transformed accounting for the specific data distribution for each buoy to allow a more correct computation of the mean. The distribution of the wind direction data is examined and the frequencies of each measurements in the interval 0°-360° are calculated. The angle with the highest frequency is flagged. Then, a new angle is computed by subtracting 180 to the flagged angle. Finally, the observations measuring less than the resulting angle are added to 360. The “transformed” wind direction data do not range anymore in the 0-360° interval, but assume larger values i.e. approximately from 100° to 500°. However, all the new intervals measure 360°. This procedure pre-processes the wind direction data to allow a more accurate estimation of the wind direction diurnal cycle.

Raw data report observations along with date and time in the “UTC” format. Therefore, the “UTC” time is transformed into local time to allow the main analyses to be conducted. Shortwave radiation values are used as local time estimator for all the other variables. Specifically, the mean shortwave radiation diurnal cycle is centred at 12 local time and the time value correspondent to midnight is flagged. Therefore, the other time series are shifted accordingly to the flagged time value.

## 2.2.2 Diurnal cycle determination

The different variables (except precipitation) are firstly examined through a spectral analysis. This assessment aims to determine the presence of a diurnal periodicity in the analysed time series. The spectral analysis computes the spectral density to determine the most relevant frequencies composing a time series. The spectral density is smoothed with a Daniell running filter with a interval of 21 values. The results of the spectral analysis are reported in one periodogram for each variable, which illustrates the smoothed spectral densities of the data retrieved by the three selected buoys. The periodograms presented in chapter 3 incorporate a vertical black dashed line indicating the frequency corresponding to a daily periodicity. This vertical line is depicted to facilitate the identification of a diurnal periodicity in the time series. The spectral

analysis is conducted on periods spanning approximately half a year, which must exclude missing data. The choice of this length is motivated by the presence of frequent missing observations in the raw data, which reduces the maximum length of consecutive observed measurements. The starting and ending dates of each period as well as the total number of measurements composing the periods are reported in each sub-section of chapter 3. Since three smoothed spectral densities are illustrated in the same figure, the length of the periods must be equal.

The determination of the diurnal cycle is conducted considering both absolute data and relative anomalies. The anomaly is defined as the deviation in a quantity from its expected value (Wilks, 2011). In simple terms, it is equivalent to the difference between a measurement and the mean over a time interval. In this study, the term *daily anomaly* refers to the difference between the measurements taken in a day and the mean of all those measurements. Anomalies are computed over the 24-hours period in order to remove the effect of climatic variations with periods greater than 24 hours on the mean state of the system. These variations include seasonalities, interannual variations (e.g. linked to ENSO) and decadal and interdecadal trends. Therefore, resulting anomalies highlight the observed diurnal cycles without the influence of non-stationarities arising from periodicities and trends. Anomalies are computed for all the variables except for shortwave radiation and precipitation data.

Diurnal cycles are assessed through the determination of the anomaly and absolute mean values for each time interval, i.e. every ten minutes. In addition, the 5<sup>th</sup> and the 95<sup>th</sup> percentiles of values' distribution at each time interval are calculated to observe the robustness of the mean.

The diurnal cycle of precipitation is examined by considering the number of observations of rainfall events during each hour of the day. The amounts of rainfall events lying in the same hour are summed together, regardless the minute of the hour. Moreover, precipitation data are further analysed to examine the frequency of rainfall events over the 24-hours period. The frequency is computed by dividing the number of observations of rainfall events for a given hour over the total number of precipitation observations collected for that hour. The graphics presented in the Data Elaboration (chapter 3) report the occurrences and frequencies of the total rainfall events as well as each rainfall category i.e. light, medium and heavy rainfalls.

### 2.2.3 Distinction according to the “background” climatic conditions

As part of the main analysis, data are clustered to distinguish between days observed during El Niño and La Niña events (also called “warm” and “cold” phases of ENSO). This differentiation is based on the values assumed by the monthly Southern Oscillation Index (SOI). Specifically, days observed in months with SOI values greater than 1.5 are grouped in the *cold phase class*. Days observed in months with SOI value less than -1.3 are clustered in the *warm phase class*. The particular threshold values are chosen to allow the selection of at least one month of data, depending on the available data of each analysed variable. The SOI time series is retrieved from the web page of NOAA, at <https://www.ncdc.noaa.gov/teleconnections/enso/indicators/soi/>. Figure 2.6 shows the evolution of the monthly SOI index in time, over the latter 20 years. The horizontal lines represent threshold values used to differentiate the observed months between the cold and warm class.

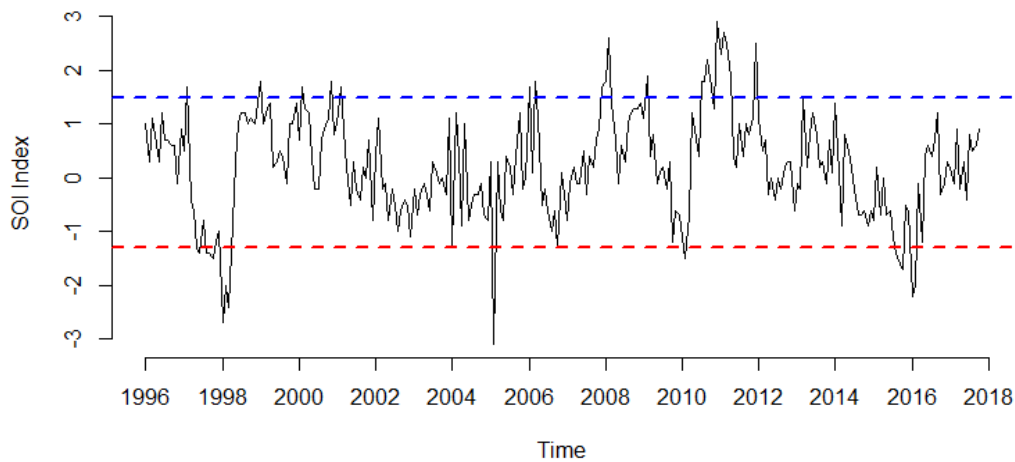


Figure 2.6: Monthly Southern Oscillation Index (SOI) calculated by NOAA in the period between 1996 and 2018. The blue line identifies the threshold for the cold phase class while the red line indicates the threshold for the warm phase class.

Strong El Niño events occurred during 1997-1998 and 2015-2017. Strong La Niña events occurred during 1998-1999, 1999-2000, 2007-2008, 2010-2011. The differentiation distinguishes also days observed during moderate events such as 2005 and 2009-2010 for El Niño and 2011-2012 for La Niña. The selected months are listed in Table 2.8 and 2.9.

Table 2.8: List of months selected in the warm phase class.

Warm ENSO phase	
Year	Month(s)
2005	February;
2010	February;
2015	August; September; October
2016	January; February

Table 2.9: List of months selected in the cold phase class.

Cold ENSO phase	
Year	Month(s)
1999	January
2000	February; November
2001	February
2006	January; March
2007	December
2008	January; February
2009	February
2010	July; August; September; October; December
2011	January; February; March; April; December

The assessment of the diurnal cycle under different “background” climatic conditions is performed on all the variables except the shortwave radiation.

## 2.2.4 Assessment of the diurnal cycle according to different meteorological and climatological conditions

As part of the main analysis, data are clustered together to distinguish between the different insolation conditions of each single day. Hence, a classification method able to distinguish between sunny and cloudy days is produced. The classification is based on the downgoing shortwave radiation measurements acquired during the 24-hours period of the day. All the shortwave radiation measurements acquired in the selected time interval are added together to produce one single value per day. It is assumed that the highest values represent sunny days characterised by a strong insolation, while the lowest values identify days with little insolation that reaches the surface due to clouds reflection. Four insolation categories are created, which are based on the distribution of shortwave radiation sums. *Sunny days* present radiation sum values above the 80<sup>th</sup> percentile of the sums’ distribution, whereas *cloudy days* present radiation sum values below the 20<sup>th</sup> percentile of the same distribution. Two intermediate classes (namely *moderate-cloudy* and *moderate-sunny days*) are defined in between the two end classes, as reported in Table 2.6.

Table 2.6: Classes names and boundaries percentiles for the distinction based on different insolation regimes.

<b>Classes names</b>	<b>Boundaries</b>	
<i>Cloudy-days</i>	0 <sup>th</sup> percentile	20 <sup>th</sup> percentile
<i>Moderate cloudy-days</i>	20 <sup>th</sup> percentile	50 <sup>th</sup> percentile
<i>Moderate sunny-days</i>	50 <sup>th</sup> percentile	80 <sup>th</sup> percentile
<i>Sunny-days</i>	80 <sup>th</sup> percentile	100 <sup>th</sup> percentile

The *Cloudy-days* and *Sunny-days* classes are used to analyse the behaviour of the variables under conditions of strong and poor insolation. Instead, all classes are used to assess the radiative heating error in the air temperature data, specifically to distinguish any relation between the magnitude of the error and the amount of insolation.

As part of the main analysis, data are clustered to distinguish between the different wind regimes, i.e. weak, moderate and strong, of each single day. Hence, a classification method able to distinguish between windy and calm days is produced. The classification is based on the wind velocity measurements acquired during the 24 hours period of the day. Three wind classes are created and each day is labelled according to its wind speed values measured in the specific time interval. A day is assigned to a wind class if it has at least the 85% of the wind speed observations lying in between the specific wind class’ boundaries. Table 2.7 reports the name of the wind classes and the defined boundaries.

Table 2.7: Class names and boundaries percentiles for the distinction of days based on different wind regimes.

Wind classes names	Wind velocity intervals
<i>Wind class 1</i>	0-3 m/s
<i>Wind class 2</i>	3-6 m/s
<i>Wind class 3</i>	>6 m/s

*Wind class 1* and *wind class 2* are used to examine the behaviour of the different variables under conditions of weak and strong winds, respectively. Instead, all the wind classes are used in the analysis of the air temperature data to distinguish any relation between the magnitude of the radiative heating error and the wind speed conditions. All the wind classes are used also in the assessment of the mean diurnal cycle of wind speed under different wind regimes.

## 2.2.5 Assessment of the diurnal cycle variation over the long period

Anomaly data are examined to determine the variation of the diurnal cycle over the long period. Hourly time series are used to accomplish this task. Daily anomalies are computed from the raw 10-minutes data. Then, anomalies are averaged considering six 10-minutes values centred at each hour of the day to produce hourly anomalies. Hourly anomalies are smoothed with a linear filter (see sub-section 2.2.6) to produce smoothed hourly anomalies. The 24 resulting time series are plotted together in time with different colours according to the period of the day. A second plot representing the smoothed absolute values of each time series is produced. The diurnal cycle variation over the long period is examined through the comparison between the two plots. Specifically, the behaviour of the smoothed hourly anomalies are analysed considering the different regimes of the specific physical parameter. The sea level pressure parameter is examined with a different method. Instead of the hourly smoothed values, only the daily maximum and minimum values are considered. The data smoothing technique is described in Sub-Section 2.2.6.

## 2.2.6 Data smoothing

All the analysed variables are displayed in a time-series graphic at the beginning of each section of chapter 3. In addition to the raw data, smoothing lines are superimposed to the time series. Smoothing values are computed using a linear moving average filter with bandwidth equal to the number of observation taken in 20 days.

The assessment of the diurnal cycle variation over the long period is performed through the representation of 24 smoothed time series. These time series are smoothed utilising a linear moving average filter with bandwidth equal to 21, i.e. considering 21 consecutive values. Thus, each value of the smoothing lines represents the average computed over 21 days.

## 2.2.7 Assessment of the relationships between physical parameters on a diurnal scale

The assessment of the relationships between the different physical parameters on a diurnal scale is implemented through the application of the cross-correlation function. The cross-correlation analysis is performed on diurnal anomaly values of each variable except the shortwave radiation, i.e. the raw data are used. The cross correlation analysis examines the strength of the linear relation between two variables as the first variable is lagged in time. The maximum lags considered in this analysis are  $\pm 72$ , since the number of 10-minutes observations retrieved in one day is 144. Only those pairs of variables exhibiting a maximum correlation higher than 0.4, thus suggesting the existence of a significant linear relation, are reported in section 2.9.

## 2.3 Description of the utilised software

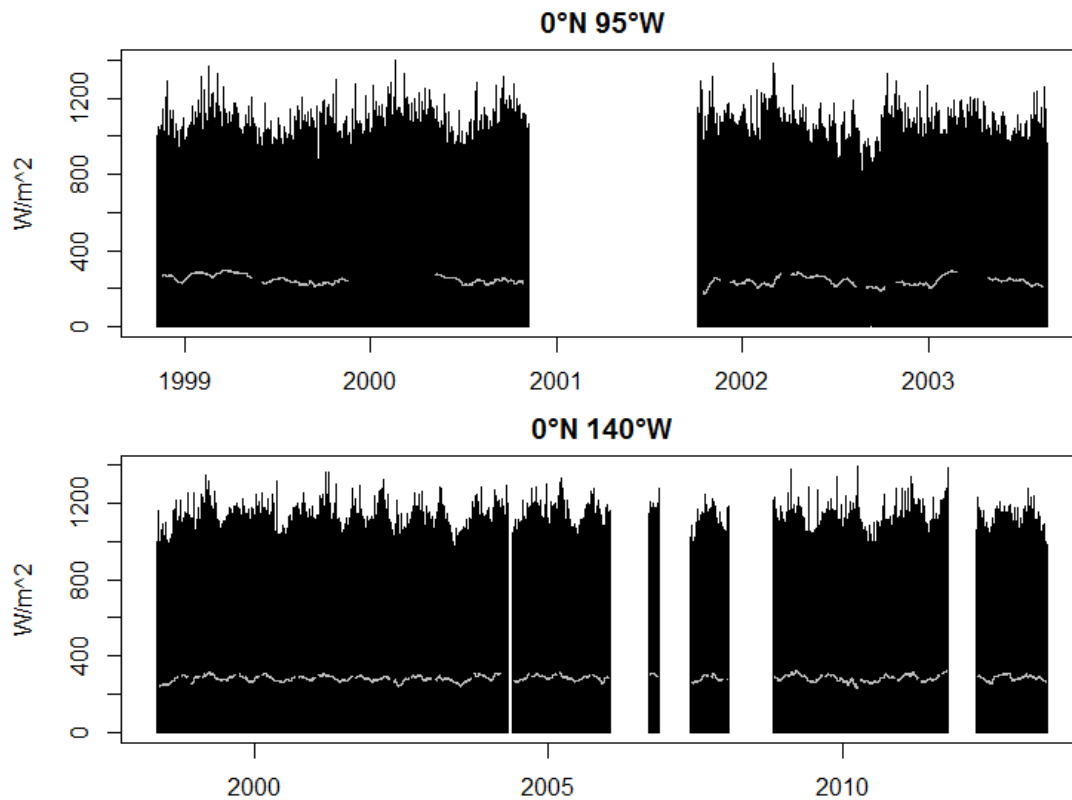
The software used for all data analyses is R. R is an open source software used for statistical elaborations and graphics' creation. R is constantly updated and anyone can participate to improve its features. Specifically, libraries of functions are created by users to perform specific tasks, e.g. performing special statistical analysis, creating complex graphics or handling different data types. This thesis work has been performed with the help of two libraries: "RNetCDF" and "ncdf.tools" for handling NetCDF data. The R code written to elaborate the data (as reported in section 2.2) and to produce different graphics (presented in chapter 3) is reported in Appendix B. The R software and supporting information are available at [www.r-project.org](http://www.r-project.org).

### 3. Data elaboration

This chapter presents and comments the elaboration performed on the data, as described in section 2.2. Sections 3.1 to 3.7 are dedicated to the analysis of the following variables, individually: downgoing shortwave radiation (section 3.1), wind velocity (section 3.2), air temperature (section 3.3), sea surface temperature (section 3.4), relative humidity (section 3.5), sea level pressure (section 3.6), wind direction (section 3.7) and precipitation (section 3.8). Each section presents the diurnal cycles analysis for each parameter. Moreover, sections 3.2 to 3.8 present variables' behaviour according to the different meteorological and "background" climatic conditions. Section 3.9 focuses on the detection of possible relationships between the different variables. In this chapter, figures illustrating the daily cycles of the different variables reports the local time in hours. The buoys considered in this study are those located at 0°N 95°W, 0°N 140°W and 0°N 165°E (see Figure 2.4). The three buoys are denominated with their geographic locations.

#### 3.1 Downgoing Shortwave Radiation

Figure 3.1 illustrates the time series of downgoing shortwave radiation acquired by the three buoys. The grey lines represent the corresponding smoothed values.



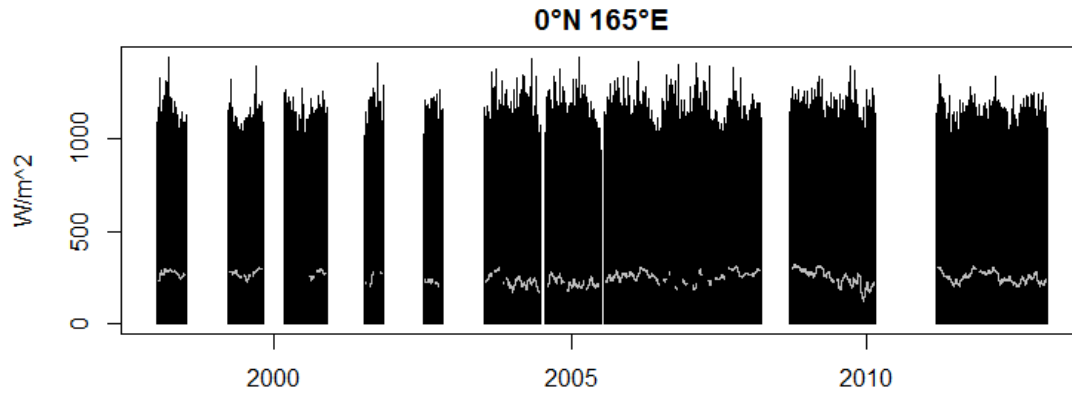


Figure 3.1: Shortwave radiation time series retrieved by buoys 0°N 95°W, 0°N 140°W and 0°N 165°E. The grey lines represent smoothed values.

Periods of missing data are present in all the buoys, ranging from a few months to approximately one year. The time series retrieved at 0°N 95°W contains 4 years of data, a period considerably shorter compared to the one associated to the other two time series, which spans over almost 10 years. In all series, maximum values range between 1000 and 1200  $W/m^2$ , sometimes even reaching 1300  $W/m^2$ . As indicated by the grey lines, the variation on a multiannual time scale is rather small. Smoothed values of 0°N 140°W fluctuate with a period of less than one year. Yet, this fluctuation is not detected in the evolutions of the other two smoothing lines.

The assessment of the diurnal cycle of all the analysed variables follows the methods described in section 2.2.2. A spectral analysis is performed on the raw data to detect the most important periodicities. Then, the observed daily anomalies are displayed together with the mean and the 5<sup>th</sup> and 95<sup>th</sup> percentiles calculated at each time step.

Table 3.1 reports the periods and the total number of measurements utilised in the spectral analysis.

Table 3.1: Periods and total number of measurements utilised in the spectral analysis.

	Period start	Period end	Total number of measurements
0°N 95°W	1998-11-07 00:40:00	1999-05-06 15:00:00	26007
0°N 140°W	2001-09-11 01:40:00	2002-03-10 16:00:00	26007
0°N 165°E	2000-02-29 00:10:00	2000-08-27 14:30:00	26007

Figure 3.2 illustrates the smoothed periodogram of the shortwave radiation time series.

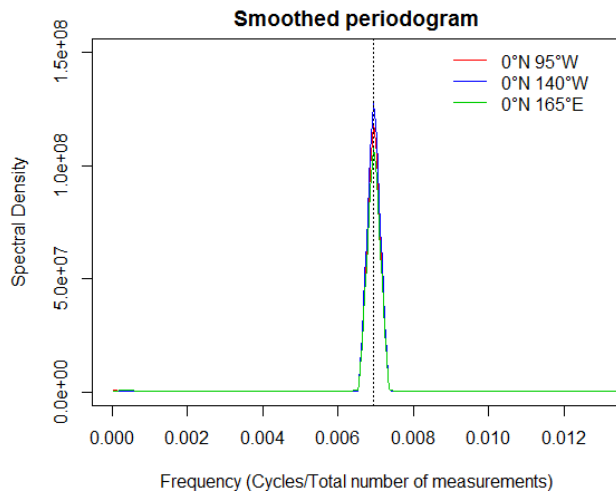


Figure 3.2: Smoothed periodogram of shortwave radiation measurements for each buoy. The vertical black dashed line identifies the daily frequency.

All the three buoys exhibit the presence of a dominant diurnal periodicity in the shortwave radiation measurements.

Figure 3.3 presents the shortwave radiation daily cycles retrieved by the three buoys.

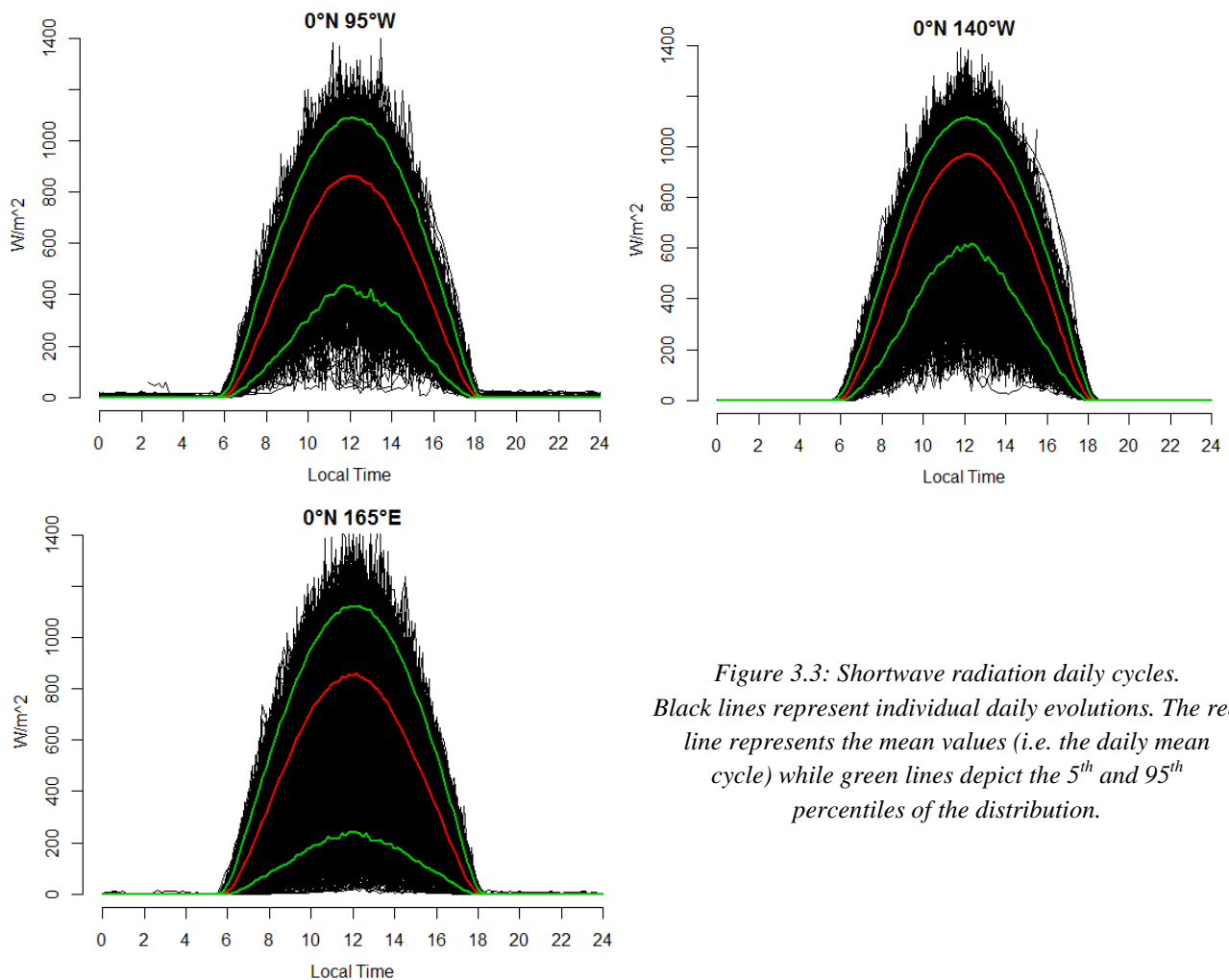


Figure 3.3: Shortwave radiation daily cycles. Black lines represent individual daily evolutions. The red line represents the mean values (i.e. the daily mean cycle) while green lines depict the 5<sup>th</sup> and 95<sup>th</sup> percentiles of the distribution.

The shortwave radiation diurnal cycle features an individual daily peak few minutes after noon. The incoming solar radiation starts to increase some minutes before 06 and reaches the maximum around 12. Then, radiation decreases and reaches zero few minutes after 18. During night-time, i.e. from 18 to 06, radiation remains stable to zero although sometimes values increase up to a few tens of  $W/m^2$ , as can be seen in  $0^\circ N$   $95^\circ W$  and  $0^\circ N$   $165^\circ E$ . The mean daily maximum value of  $0^\circ N$   $95^\circ W$  mean radiation is quantified to  $863 W/m^2$ , whereas the maximum values of the 5<sup>th</sup> and 95<sup>th</sup> percentiles reach, respectively, at  $436 W/m^2$  and  $1088 W/m^2$ . The daily mean maximum radiation value of  $0^\circ N$   $140^\circ W$  rises up to  $972 W/m^2$ , whereas the 5<sup>th</sup> and 95<sup>th</sup> percentiles reach, respectively,  $618 W/m^2$  and  $1117 W/m^2$ . The mean maximum radiation value of  $0^\circ N$   $165^\circ E$  measures  $858 W/m^2$ , whereas the 5<sup>th</sup> and 95<sup>th</sup> percentiles reach  $241 W/m^2$  and  $1125 W/m^2$ . Thus, the data point out that solar radiation reaches on average the highest value at  $0^\circ N$   $140^\circ W$ . The 95<sup>th</sup> percentile values vary slightly across the buoys, whereas the 5<sup>th</sup> percentile values are notably different. Overall, Figure 3.3 shows that  $0^\circ N$   $165^\circ W$  experiences the greatest variability, as confirmed by the range of the two percentiles. In addition, during daylight hours, some days feature downgoing shortwave radiation values close to zero for  $0^\circ N$   $165^\circ W$  and close to  $100 W/m^2$  for the other two buoys.

Shortwave radiation is used to distinguish between different meteorological conditions (see section 2.2.4). To this purpose, days are selected according to the sum of their shortwave radiation values calculated over the whole day. Figure 3.4 shows the distribution of the sums associated to the shortwave radiation values. The 20<sup>th</sup> and 80<sup>th</sup> percentiles, used as thresholds for distinguishing *cloudy* and *sunny* days, are highlighted by the horizontal blue dashed lines.

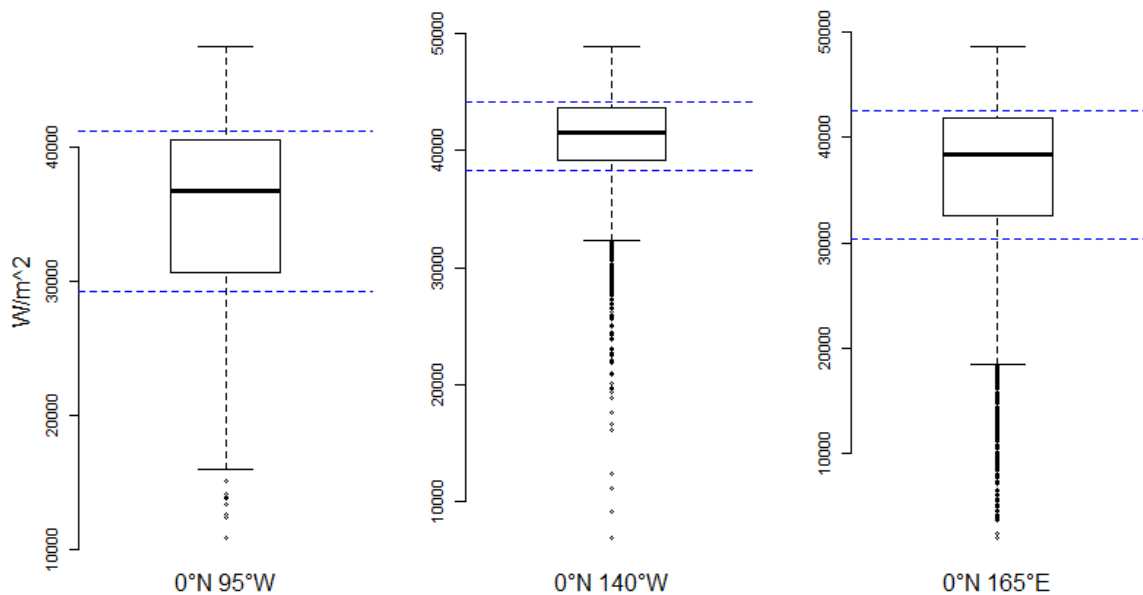


Figure 3.4: Distribution of the cumulative sums of the shortwave radiation values measured over the whole day for the three buoys.

The 20<sup>th</sup> and 80<sup>th</sup> percentiles of  $0^\circ N$   $95^\circ W$  measure approximately  $29000$  and  $41000 W/m^2$ , respectively. The two percentiles calculated for  $0^\circ N$   $140^\circ W$  measure approximately  $38500$  and  $44000 W/m^2$ . The percentiles computed for  $0^\circ N$   $165^\circ W$  amount to approximately  $30500$  and  $42500 W/m^2$  for, respectively, the 20<sup>th</sup> and 80<sup>th</sup> percentiles.

The differentiation based on shortwave radiation sum values is performed on radiation data to distinguish the different solar radiation diurnal cycles under the four insolation conditions mentioned in sub-section 2.2.4,

i.e. cloudy, moderate-cloudy, moderate-sunny and sunny. The number of selected days for each class is displayed in Table 3.2.

Table 3.2: Number of days selected for each insolation class based on the total amount of solar radiation received by the surface of the ocean over the day.

	0°N 95°W	0°N 140°W	0°N 165°E
<i>Cloudy days</i>	267	905	733
<i>Moderate-cloudy days</i>	401	1360	1100
<i>Moderate-sunny days</i>	400	1359	1099
<i>Sunny days</i>	268	907	734

Figures 3.5, 3.6 and 3.7 display the downgoing shortwave radiation daily cycles according to the four insolation classes for the three buoys.

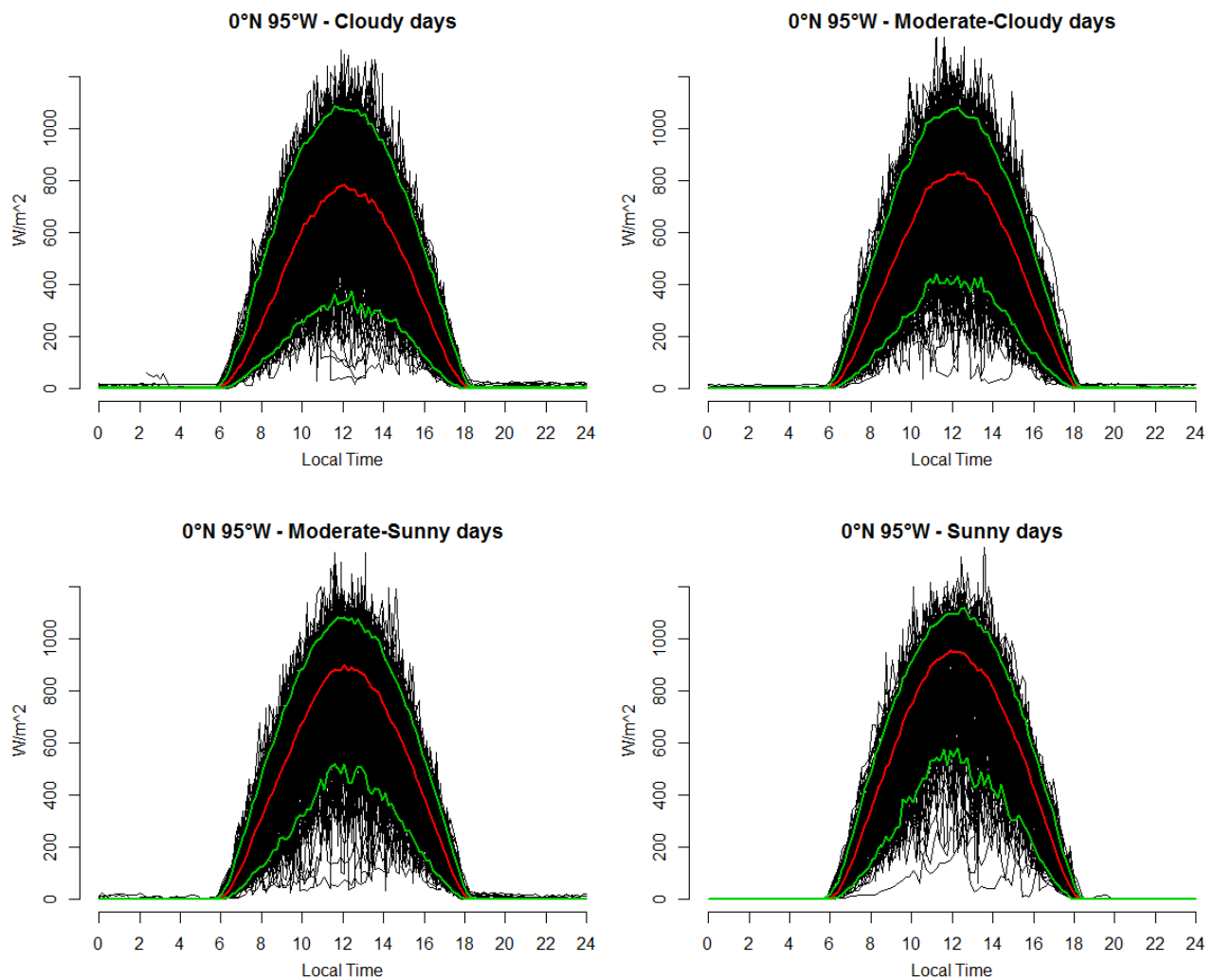


Figure 3.5: Shortwave radiation daily cycles divided according to the insolation classes for buoy 0°N 95°W. Black lines represent individual daily evolutions. The red line represents the mean values (i.e. the daily mean cycle) while green lines depict the 5<sup>th</sup> and 95<sup>th</sup> percentiles of the distribution.

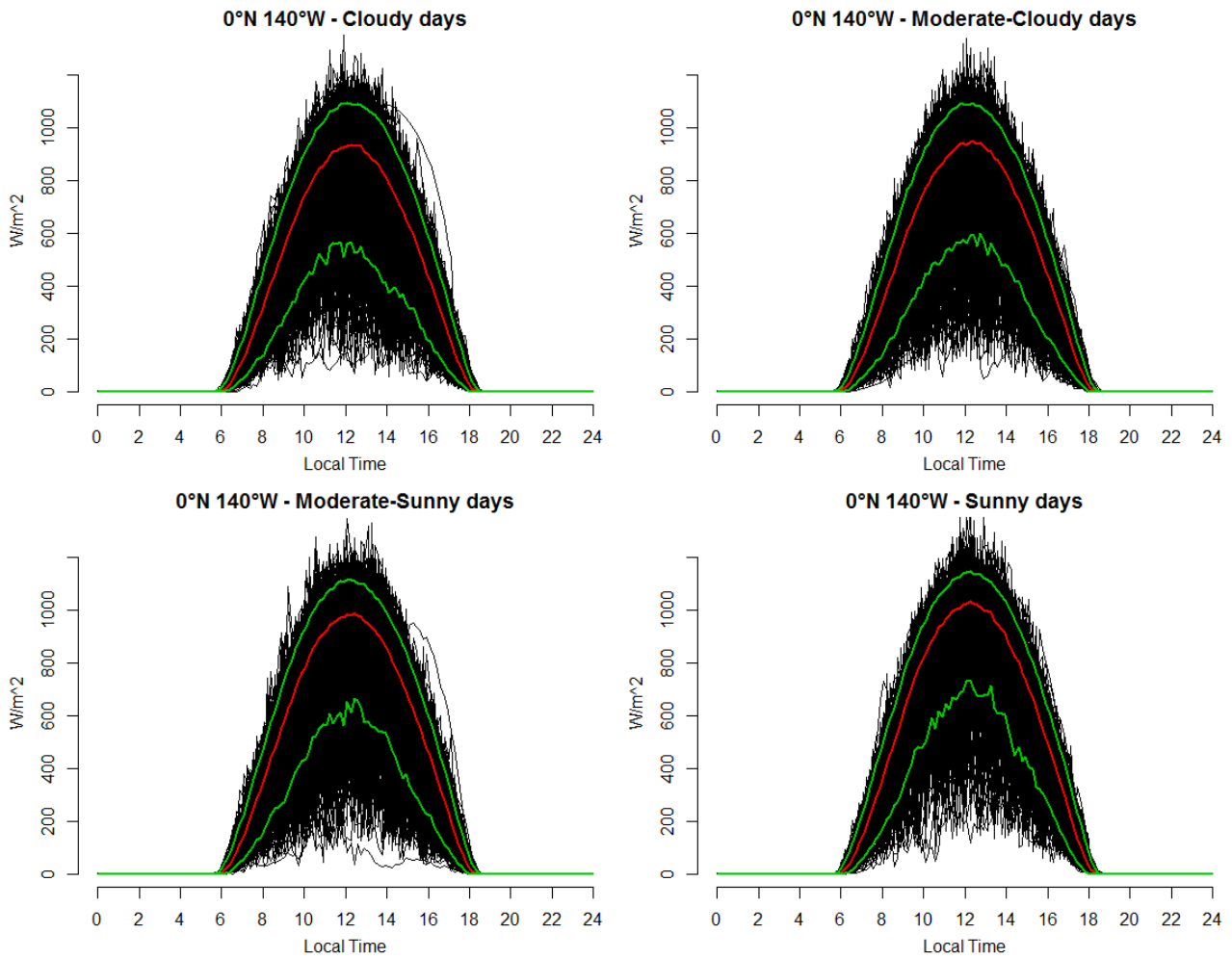
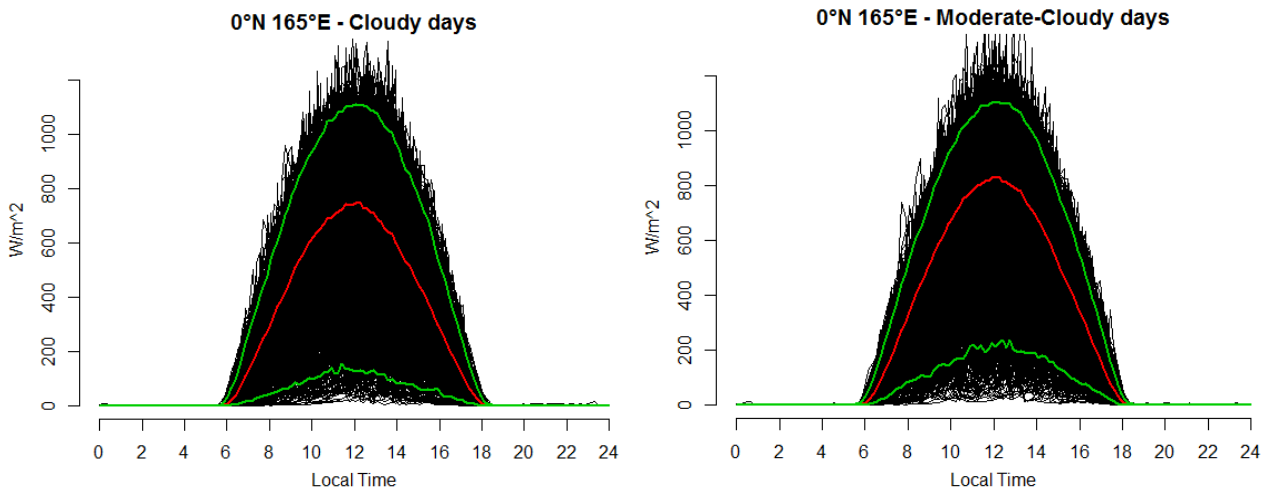


Figure 3.6: Shortwave radiation daily cycles divided according to the insolation classes for buoy 0°N 140°W. Black lines represent individual daily evolutions. The red line represents the mean values (i.e. the daily mean cycle) while green lines depict the 5<sup>th</sup> and 95<sup>th</sup> percentiles of the distribution.



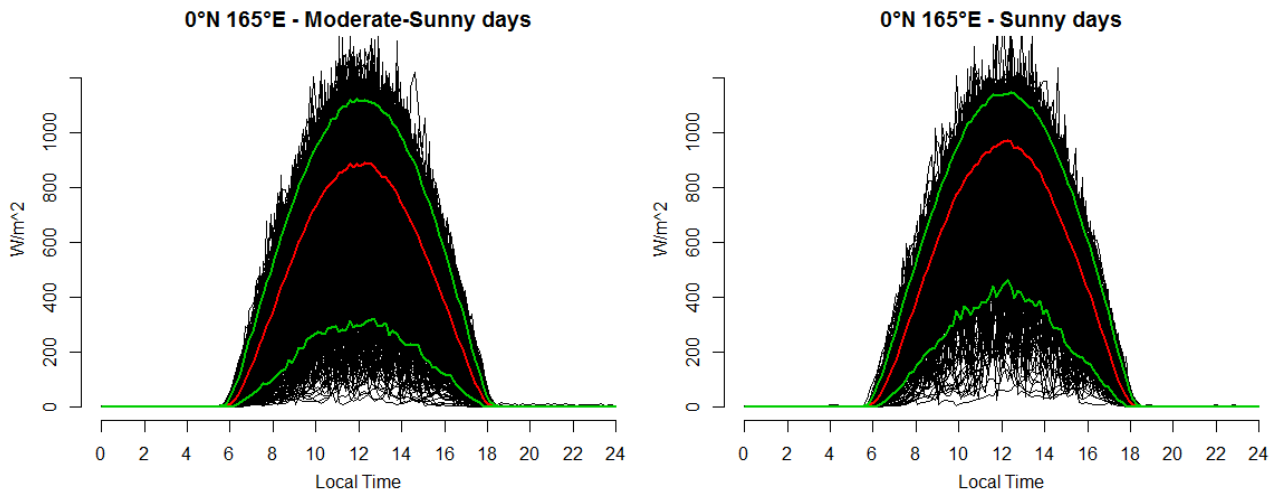


Figure 3.7: Shortwave radiation daily cycles divided according to the insolation classes for buoy 0°N 165°E. Black lines represent individual daily evolutions. The red line represents the mean values (i.e. the daily mean cycle) while green lines depict the 5<sup>th</sup> and 95<sup>th</sup> percentiles of the distribution.

The three buoys share a common behaviour. The mean daily maximum of the shortwave radiation mean value grows from *cloudy* to *sunny days*. However, differences emerge beyond this common general behaviour. *Cloudy days* feature a lower peak value in 0°N 95°W and 0°N 165°E, respectively of 785  $W/m^2$  and 748  $W/m^2$ , compared to 0°N 140°W, showing a mean peak value reaching 935  $W/m^2$ . During *sunny days*, the mean daily maximum of the three buoys amounts to 954, 1032 and 972  $W/m^2$ , respectively. The diurnal evolutions of the 5<sup>th</sup> and 95<sup>th</sup> percentiles are similar between sunny and cloudy conditions, considering all the buoys. Figure 3.7 confirms the higher variation of the solar radiation diurnal cycle for 0°N 165°E, as previously observed.

## 3.2 Wind Velocity

Figure 3.8 illustrates the wind velocity time series acquired by the three selected buoys. Green lines represent the smoothed values.

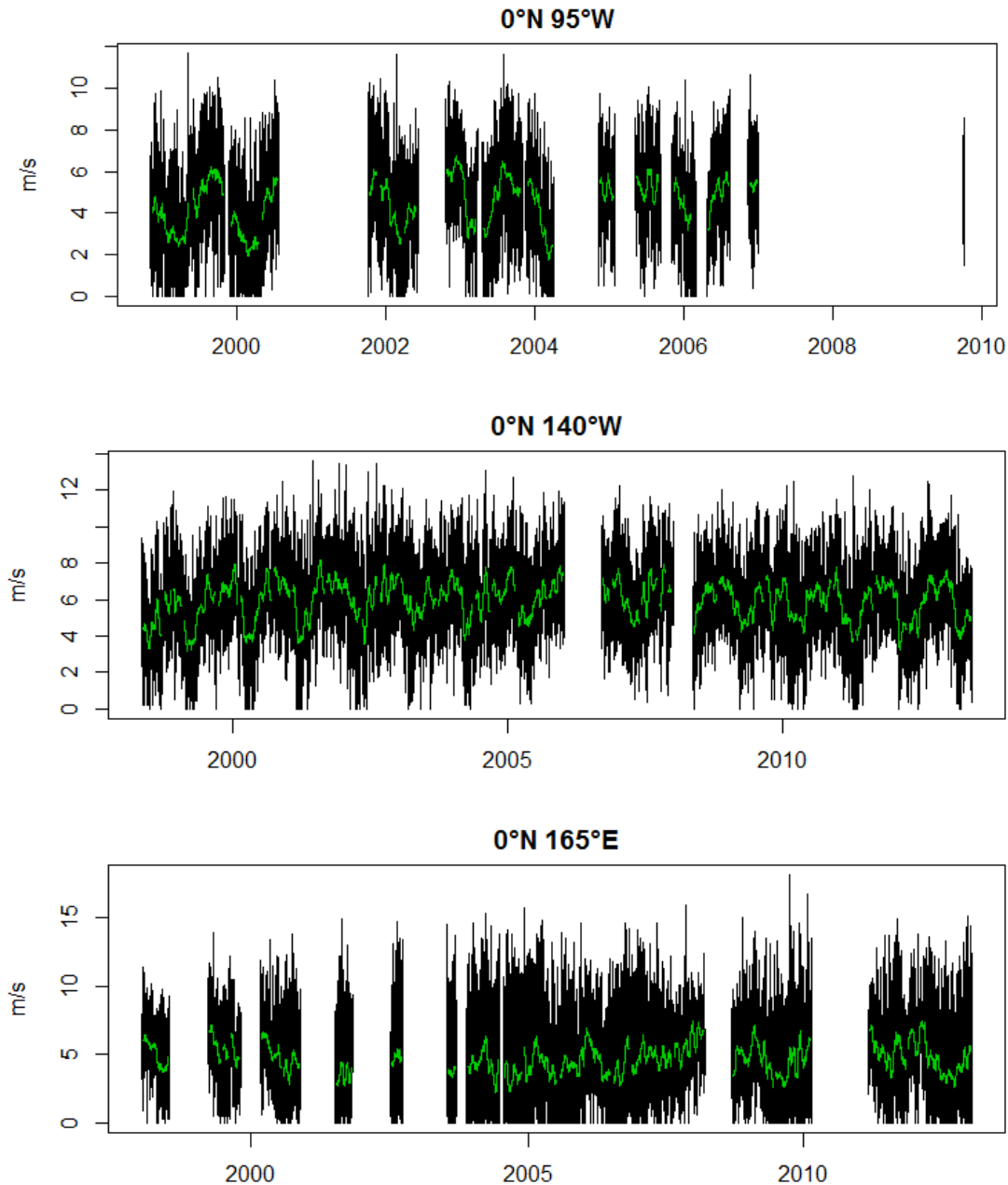


Figure 3.8: Wind velocity time series retrieved by buoys  $0^{\circ}\text{N } 95^{\circ}\text{W}$ ,  $0^{\circ}\text{N } 140^{\circ}\text{W}$  and  $0^{\circ}\text{N } 165^{\circ}\text{E}$ . The green lines represent smoothed values.

Wind velocity displays a different behaviour among the three buoys. At  $0^{\circ}\text{N } 95^{\circ}\text{W}$ , velocity varies between 0 and 11 m/s. Data reveal the presence of an annual seasonal cycle although its characterisation is prevented by the presence of large periods affected by missing values. The smoothed values range between 2 and 6 m/s. Wind velocity at  $0^{\circ}\text{N } 140^{\circ}\text{W}$  shows the presence of an annual seasonal cycle characterised by maximum values in the boreal spring and minimum values in boreal summer. The seasonal variation remains

rather constant throughout the analysed period. The raw wind speed values span from 0 to more than 12 m/s, while smoothed values range from 3.5 to 8 m/s. The lowest raw wind speed values are enclosed nearby seasonal minima, while the highest values are found throughout the entire time series. 0°N 165°W displays a highly variable wind velocity during the recorded period. This buoy is characterised by the highest number of low wind observations amongst the three considered moorings even though sometimes wind blows at 15 m/s. Smoothed values ranges around 5 m/s and indicate the presence of a weak annual seasonal cycle. Indeed, the highest wind velocities are found generally between boreal winter and spring. Overall, even if not defined accurately, the wind speed annual cycle seems to be consistent among the different buoys, featuring a small period dominated by high velocities almost at the beginning of the year, while the lowest velocities are found in boreal summer and fall.

The assessment of the diurnal cycle is performed according to the methods described in Section 2.2.2. A spectral analysis is performed on the raw data to detect the most important periodicities. Then, the observed daily anomalies are displayed together with the mean and the 5<sup>th</sup> and 95<sup>th</sup> percentiles calculated at each time step.

Table 3.3 reports the periods and total number of measurements utilised in the spectral analysis.

Table 3.3: Periods and total number of measurements utilised in the spectral analysis.

	Period start	Period end	Total number of measurements
<b>0°N 95°W</b>	2001-11-26 21:40:00	2002-06-09 15:00:00	28023
<b>0°N 140°W</b>	2001-11-26 21:40:00	2002-03-24 15:20:00	28023
<b>0°N 165°E</b>	2000-03-01 01:00:00	2000-09-11 15:20:00	28023

Figure 3.9 illustrates the smoothed periodogram of the wind velocity time series.

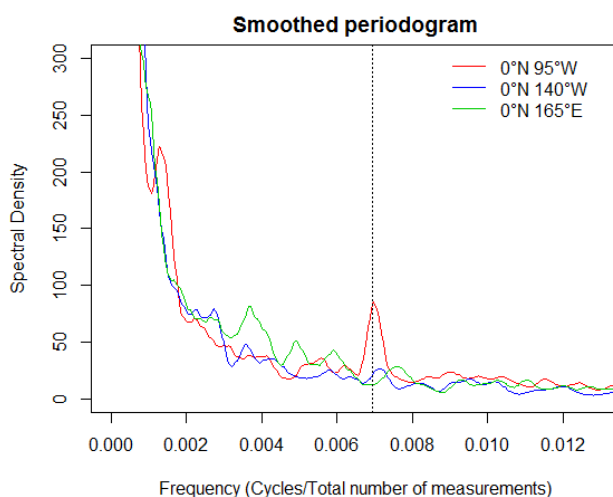


Figure 3.9: Smoothed periodogram of wind velocity measurements for each buoy. The vertical black dashed line identifies the daily frequency.

0°N 95°W shows a peak in the spectral density around the daily frequency, thus suggesting the presence of a diurnal periodicity. Yet, 0°N 140°W and 0°N 165°E are not characterised by a clear diurnal periodicity. Figure 3.10 reports the diurnal cycles of wind velocity for the three buoys.

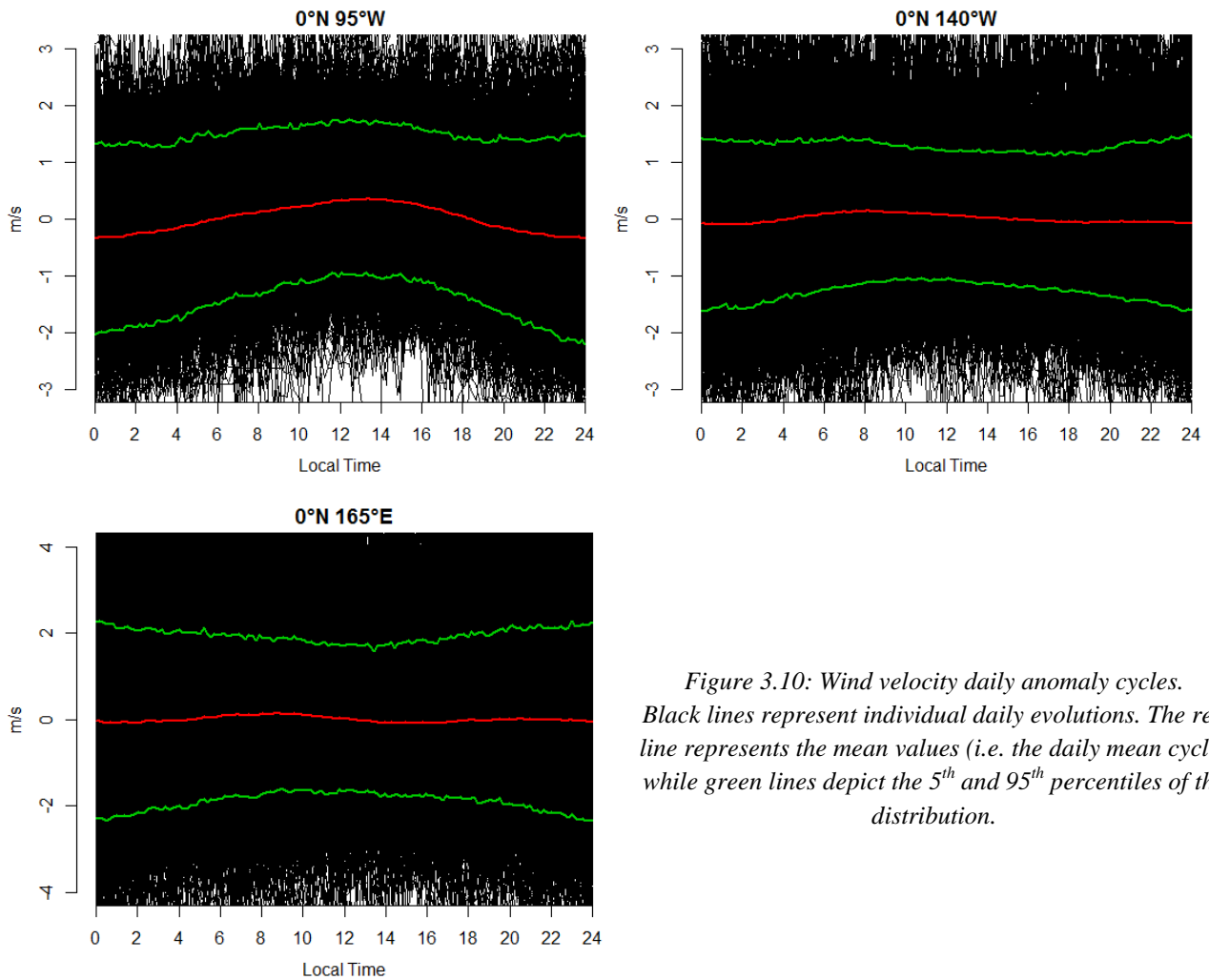


Figure 3.10: Wind velocity daily anomaly cycles. Black lines represent individual daily evolutions. The red line represents the mean values (i.e. the daily mean cycle) while green lines depict the 5<sup>th</sup> and 95<sup>th</sup> percentiles of the distribution.

The averaged daily cycle of wind velocity is almost flat in all the three buoys, exhibiting a mean diurnal amplitude ranging less than 1 m/s. 0°N 95°W displays a mean diurnal cycle characterised by an amplitude ranging between -0.3 and +0.3 m/s. The other two buoys feature lower amplitudes, ranging between -0.1 and +0.1 m/s for 0°N 140°W and -0.1 and +0.1 m/s for 0°N 165°E. For the three buoys, the evolutions of daily percentiles maintain the shape of the mean cycles. 0°N 165°E percentiles differ up to 2 m/s in respect to the mean, while the other two buoys measures less than 1.5 m/s. The mean wind velocity anomaly peaks around 13:30 for 0°N 95°W. The minimum is located some minutes before midnight. For 0°N 140°W and 0°N 165°E, the average daily maximum is located between 08 and 09, whereas two minima occur at 01 and 16.

Wind velocity is further analysed according to wind conditions of the day. Data from each buoy are divided in three wind classes as describe in subsection 2.2.3. The differentiation is based on the wind speed values characterising each day. A day pertains to a certain class if it has at least 85% of the observations lying in that wind class interval. Table 3.4 reports the number of days lying in each wind class for every buoy.

Table 3.4: Number days pertaining to each wind class, for every buoy.

	0°N 95°W	0°N 140°W	0°N 165°E
<b>Wind Class 1 (&lt;3 m/s)</b>	98	16	123
<b>Wind Class 2 (3-6 m/s)</b>	232	744	308
<b>Wind Class 3 (&gt;6 m/s)</b>	89	1344	286

0°N 95°W shows a predominance for diurnal wind velocities in between 3-6 m/s. Instead, 0°N 140°W is dominated by days with overall strong winds. In 0°N 165°E, wind classes have more than a hundred days each and *wind class 2* is the most represented class.

Figure 3.11 displays the mean daily cycles calculated for the different wind regimes. Here, the diurnal cycles are computed from absolute data and not from anomalies. The mean diurnal cycles observed during different wind regimes are displayed together for each single buoy to allow a more direct comparison.

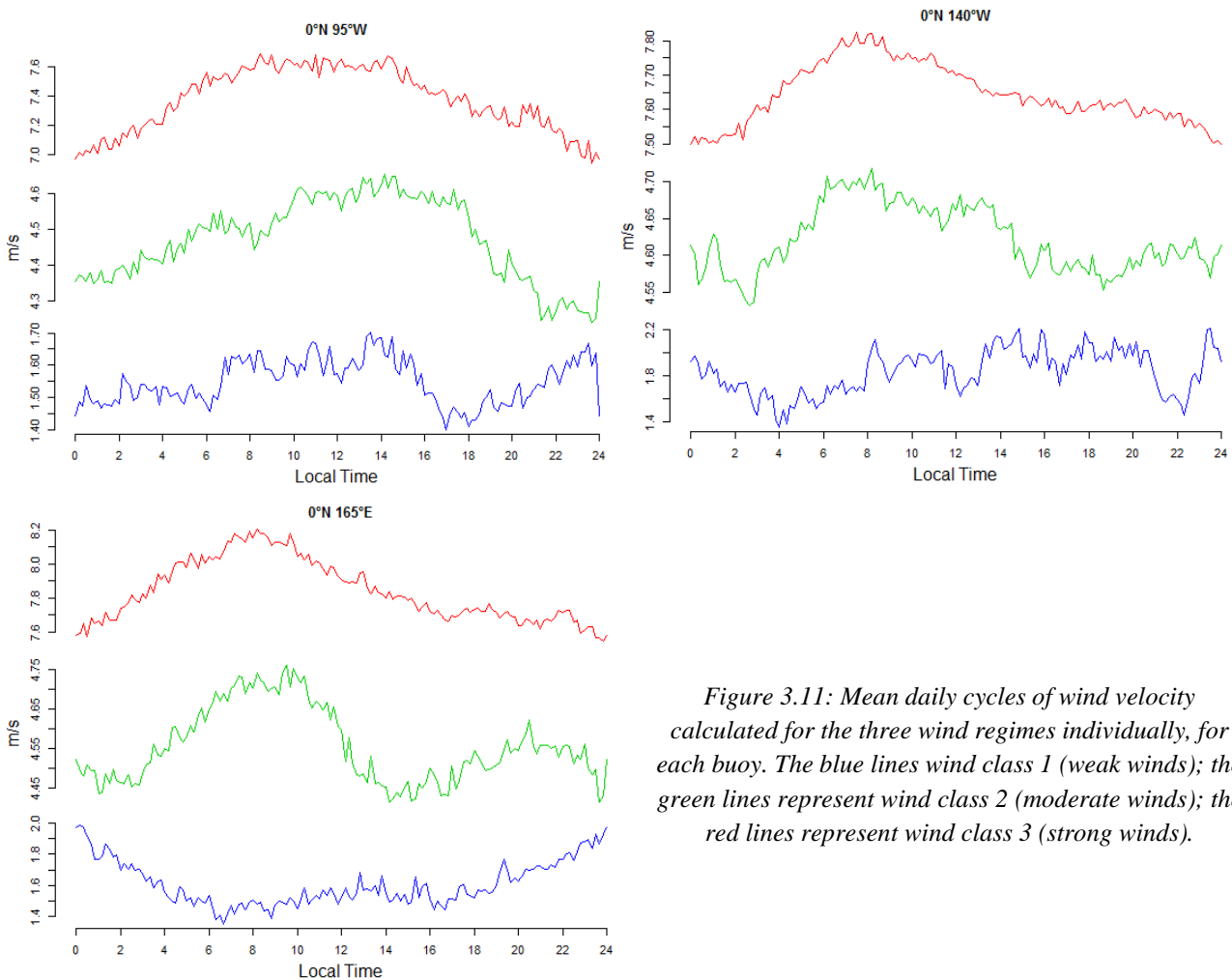


Figure 3.11: Mean daily cycles of wind velocity calculated for the three wind regimes individually, for each buoy. The blue lines wind class 1 (weak winds); the green lines represent wind class 2 (moderate winds); the red lines represent wind class 3 (strong winds).

The mean diurnal cycles obtained for the different wind regimes vary within a range of a few decimals, as previously noticed. The diurnal cycle of days characterised by low winds does not show the same behaviour among the three buoys. 0°N 95°W has high mean values in between 07 and 15, with a maximum near 14, and during the last few hours of the day. On the other hand, the lowest values are located near 17 and

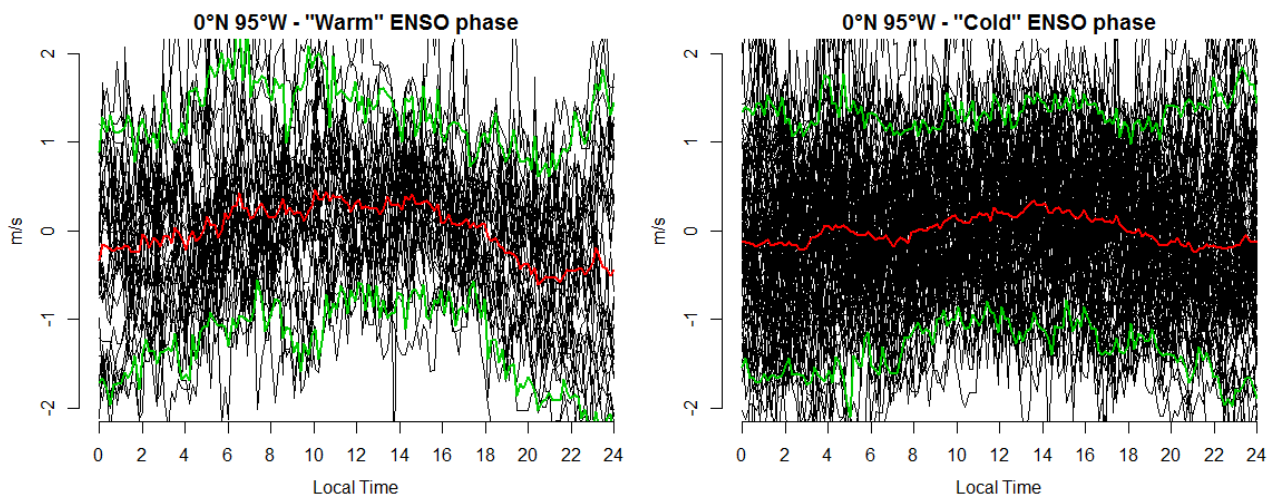
midnight. 0°N 140°W exhibits a higher probability to find high values during the second part of the day, where different peaks are present, than during the first part of the day. Minima occur near 04 and 22. 0°N 165°E reports lower mean values during daylight hours and higher values close to midnight. However, this mean cycle is calculated using only 16 days, i.e. only 16 measurements at each time step, and, therefore, it should be considered cautiously. The mean cycles feature an amplitude of 0.3 m/s for 0°N 95°W, 0.6 m/s for 0°N 165°E and 0.8 for 0°N 140°W. *Wind class 2* features a clear daily peak during morning for 0°N 140°W and 0°N 165°E, respectively around 07-08 and 10. In contrast, 0°N 95°W reports a maximum peak in the early afternoon, near 14. Minima occur between 22 and 24 for 0°N 95°W, near 03 and 19 for 0°N 140°W and around 15 and midnight for 0°N 165°E. The mean cycles observed under moderate winds feature an amplitude of 0.15 m/s for 0°N 140°W and 0.3 m/s for 0°N 95°W and 0°N 165°E. Regarding *Wind class 3*, 0°N 140°E and 0°N 165°E have a distinguishable daily peak during morning hours in between 07 and 09, while 0°N 95°W features higher values from 08 to 14. Minimum values are located nearby midnight for all the buoys. The amplitude of the cycles observed under strong winds measures 0.3 m/s for 0°N 140°W and 0.6 m/s for 0°N 95°W and 0°N 165°E.

Wind velocity data are examined according to the background climatic conditions, as explained in subsection 2.2.3. Table 3.5 reports the number of days lying in each phase of ENSO for each of the three buoys.

Table 3.5: Number of wind speed recorded days during the two ENSO phases for each buoy.

	0°N 95°W	0°N 140°W	0°N 165°E
<b>Cold ENSO phase</b>	91	495	292
<b>Warm ENSO phase</b>	30	117	224

Figure 3.12 shows the wind speed diurnal cycles under the “warm” and “cold” phases of ENSO.



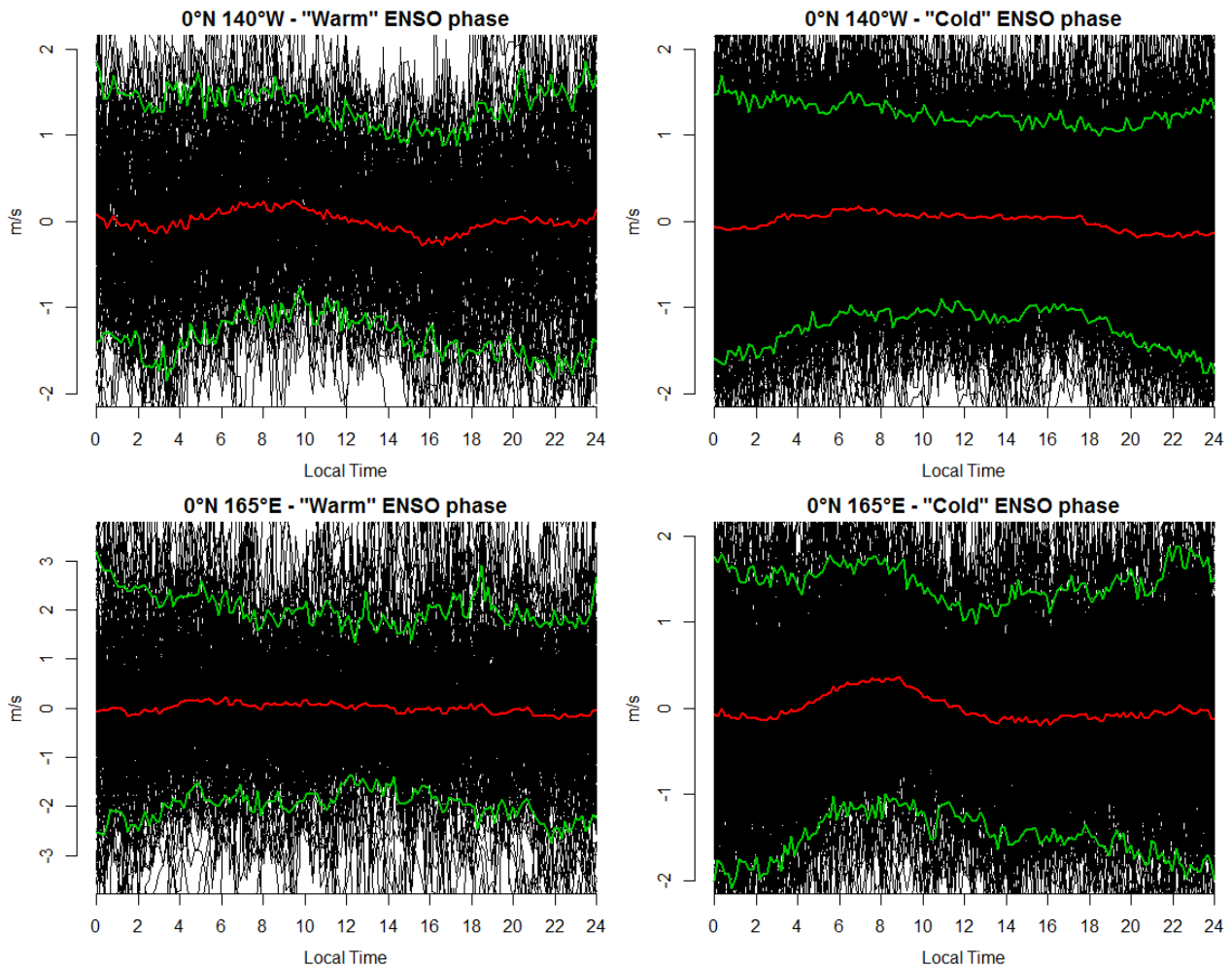


Figure 3.12: Daily cycles of wind velocity calculated for different wind classes during “warm” and “cold” ENSO phases.

Black lines represent individual daily evolutions. The red line represents the mean values (i.e. the daily mean cycle) while green lines depict the 5<sup>th</sup> and 95<sup>th</sup> percentiles of the distribution.

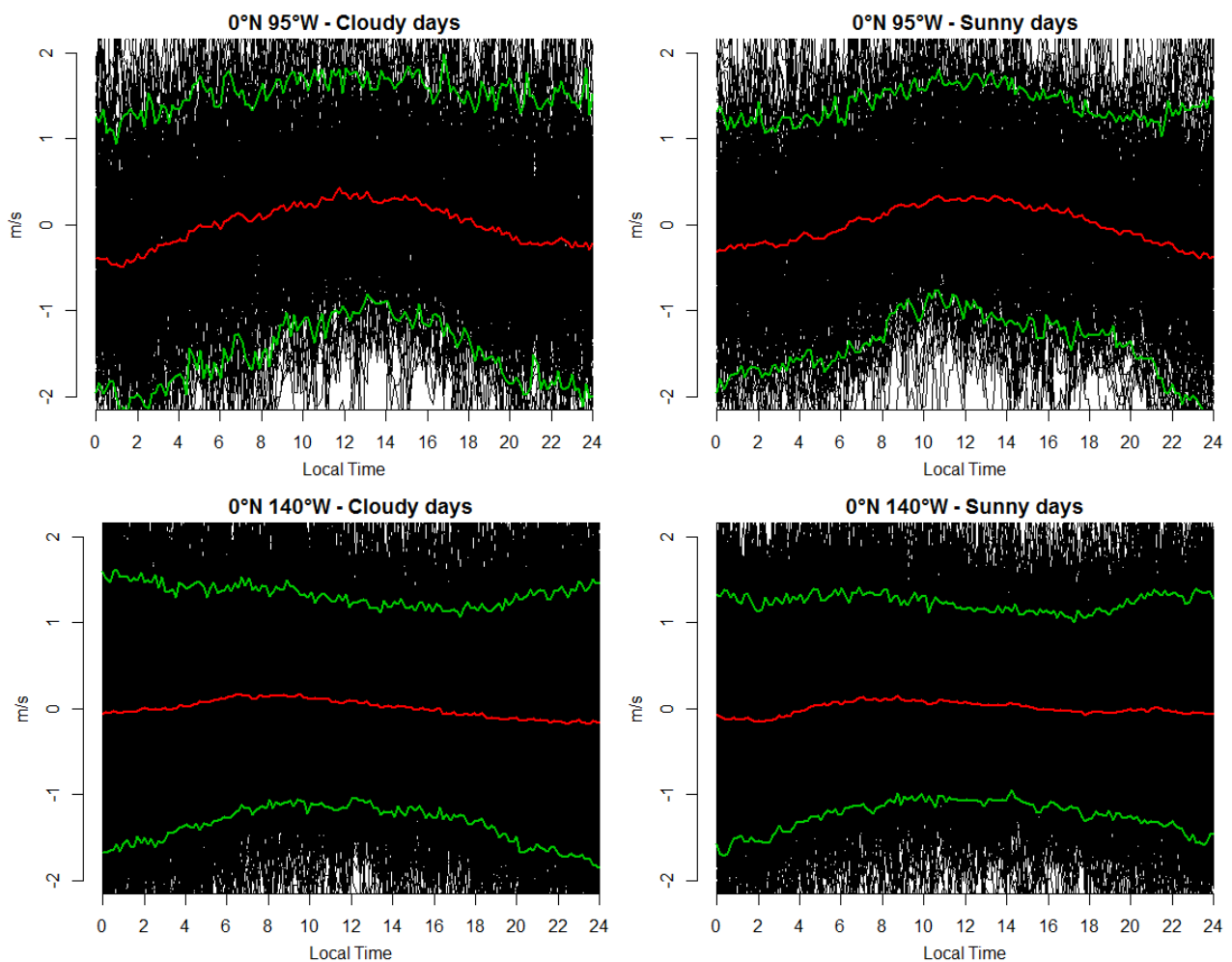
The diurnal cycles of wind velocity observed during both ENSO phases show a similar timing of minimum and maximum values compared to those reported in Figure 3.10. 0°N 95°W displays similar diurnal cycles between the two ENSO phases. During El Niño events, the wind speed typically drops from the maximum value occurring around 15 to the minimum value near 20. The amplitude of the cycles is small under both cold and warm ENSO phases, measuring 0.7 and 1 m/s, respectively. As regards 0°N 140°W, the amplitude of the mean diurnal cycle under the warm ENSO phase is higher than under the cold phase, measuring respectively 0.3 and 0.5 m/s, while timing and shape are similar. The cold phase displays higher values during daylight hours than during night-time hours. On the contrary, the warm phase presents a peak around 08 and a minimum around 16. After reaching its minimum, the mean wind velocity tends to reach the daily mean value and remains stable until 04. Regarding 0°N 165°E, the mean daily cycle under cold phases has a distinct peak during the early morning, around 08. In this case, the mean wind velocity anomaly grows from -0.1 to 0.3 m/s and then descends again to the daily mean, remaining approximately stable from 12 to 03. On the other hand, the mean diurnal cycle under the warm phase has an amplitude of 0.4 m/s. Maxima values are encountered after 06, while minima values occur around 22. Daytime hours appear to be characterised by higher values compared to night-time hours.

The diurnal cycle of the wind speed is examined according to the local insolation conditions, as described in sub-section 2.2.4. Two classes are considered: *cloudy* and *sunny* days. Table 3.6 presents the number of days selected in the *cloudy* and *sunny* days classes.

Table 3.6: Number of wind speed recorded days lying in the Cloudy and Sunny days classes.

	0°N 95°W	0°N 140°W	0°N 165°E
<i>Cloudy Days</i>	271	905	725
<i>Sunny Days</i>	272	907	694

Figure 3.13 illustrates the diurnal cycles of the wind speed anomaly for the three buoys calculated for the different meteorological conditions.



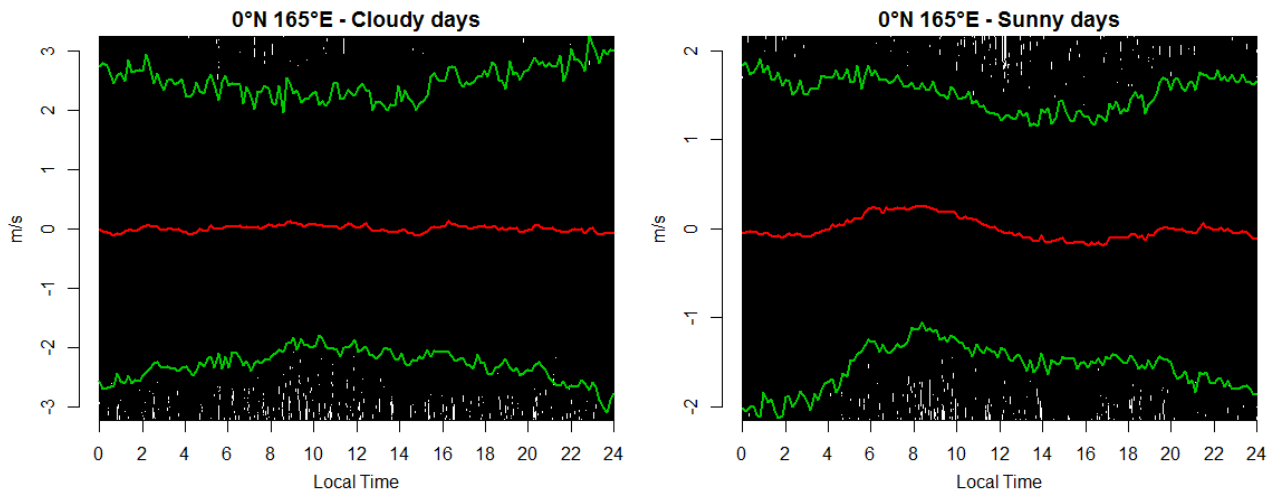
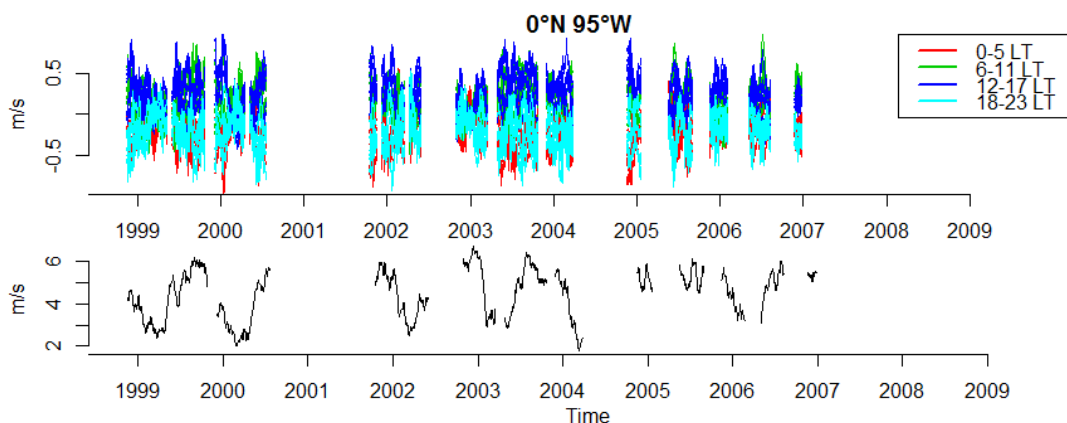
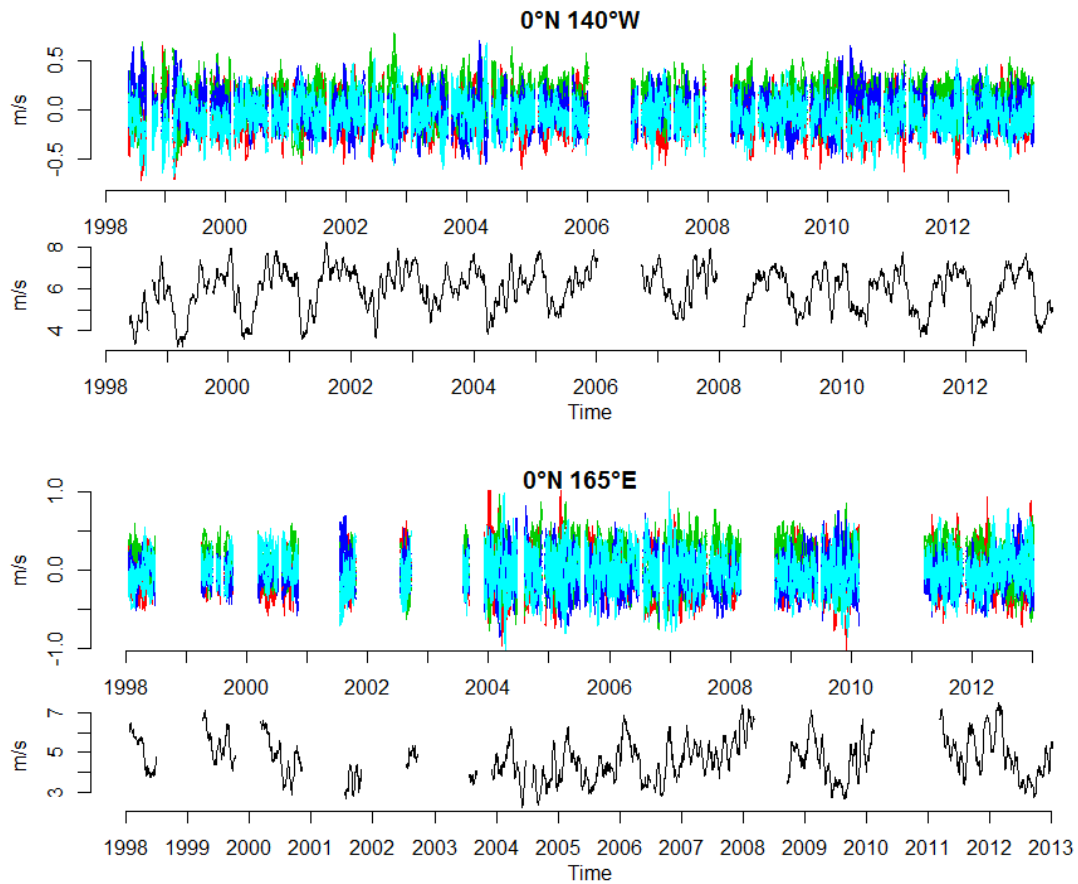


Figure 3.13: Daily cycles of wind velocity calculated for “cloudy” and “sunny” days for each buoy. Black lines represent individual daily evolutions. The red line represents the mean values (i.e. the daily mean cycle) while green lines depict the 5<sup>th</sup> and 95<sup>th</sup> percentiles of the distribution.

Mean anomalies of *cloudy* and *sunny* days share similar characteristics with the mean anomaly cycles analysed previously. 0°N 95°W exhibits a very similar diurnal anomaly cycle in both conditions peaking around 13, while minima values occur during night, near midnight. The amplitude of the mean daily anomaly measures 0.9 m/s for *cloudy days* and 0.7 m/s for *sunny days*. Percentiles follow the variation of the mean along the day. 0°N 140°W displays similar mean anomaly cycles for *cloudy* and *sunny* days. Values peak in the morning around 08 and then decrease until night, where minima are found around midnight. The amplitude of the cycles measures approximately 0.3 m/s. 0°N 165°E presents different mean anomaly cycles for the two classes. *Cloudy days* display a flat cycle lacking of maxima and minima peaks. On the other hand, *sunny days* have a maximum peak during morning between 07 and 09 reaching almost 0.2 m/s. Minima values occur near 16 and reach -0.2 m/s. After this period, the mean anomaly increases and remains steady until 05. Overall, the variation of the anomaly values during the day are still very high in both conditions for all the buoys.

The assessment of the diurnal cycle variation is conducted as delineated in sub-section 2.2.5. Figure 3.14 shows the coupled evolution of the wind speed smoothed hourly anomaly time series along with the wind speed smoothed time series. Each graph is distinguished into two parts: the upper part reports the hourly anomaly time series depicted with 4 different colors according to the period of the day. The legend reports the time periods and the associated colors. The lower part displays the wind velocity conditions averaged over a period of 21 days.





*Figure 3.14: Variations of the diurnal cycle of wind speed over the long period.*

*For each buoy, the upper panel reports the hourly wind speed anomaly time series, while the lower panel shows the wind speed absolute smoothed values.*

*Red lines correspond to hours between 00 and 05. Green lines correspond to hours between 06 and 11. Blue lines correspond to hours between 12 and 17. Light blue lines correspond to hours between 18 and 23.*

The lowest values of 0°N 95°W are constantly those retrieved during night-time hours while the highest values are those retrieved during daytime hours. This feature is consistent with the characteristics observed in the analysis of the diurnal cycle. 0°N 140°W does not display a clear distinction between day and night hours even though the highest hourly anomalies are often associated with the 06-11 time period. On the other hand, the lowest values are reached in measurements belonging to the other three time-periods. 0°N 165°E shows common features in respect to 0°N 140°W. The four time-periods appear to be unrelated to both high or low wind speed anomalies. Again, values related to the 06-11 time-period are often the highest of the period. Overall, wind speed hourly values do not show particular features related to the parameter's regime for the three different buoys.

### 3.3 Near-surface air Temperature

Figure 3.15 illustrates the different air temperature time series acquired by the three selected buoys and the associated smoothing lines.

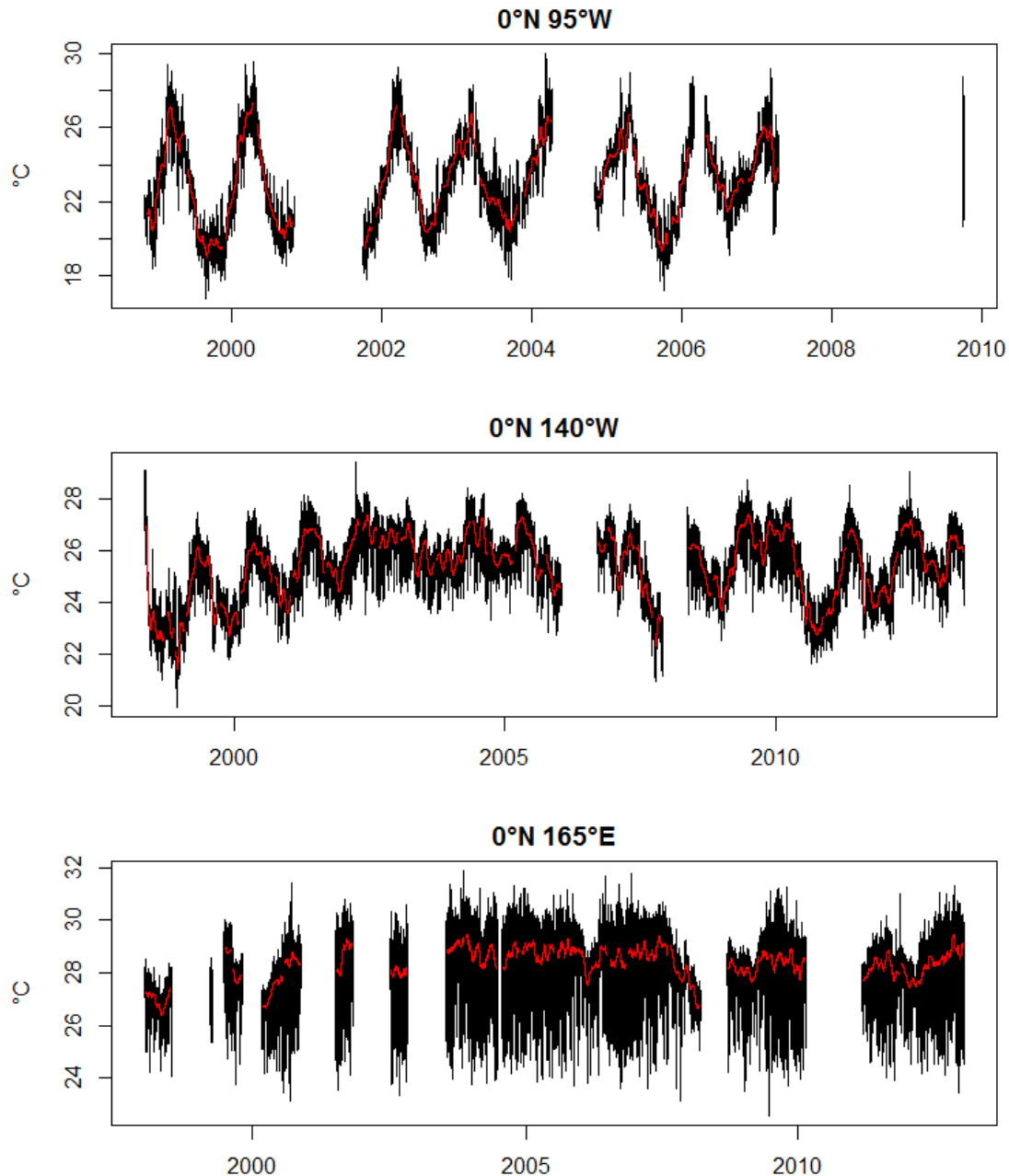


Figure 3.15: Near-surface air temperature time series retrieved by buoys  $0^{\circ}\text{N } 95^{\circ}\text{W}$ ,  $0^{\circ}\text{N } 140^{\circ}\text{W}$  and  $0^{\circ}\text{N } 165^{\circ}\text{E}$ . The red lines represent smoothed values.

The air temperature shows different behaviours among the three selected buoys. The air temperature varies between 18 and 30 °C in  $0^{\circ}\text{N } 95^{\circ}\text{W}$ . Moreover, it displays a clear annual seasonal variation. The annual maximum occurs in the early boreal spring, while minima are found in the late boreal fall. Over the years, the yearly average temperature remains steady.  $0^{\circ}\text{N } 140^{\circ}\text{W}$  displays a seasonal cycle throughout the

recorded periods. Air temperature varies between ~ 20 and 28 °C; however, the amplitude of the seasonal cycle is smaller than this range, amounting to approximately 3°C. Between 1998 and 2003, the yearly average temperature shows a linear increase. After 2003, the mean temperature remains constant. Air temperature in 0°N 165°W shows maximum values near 32 °C and minimum values near 23°C. In this location, the presence of a seasonal cycle is not apparent and the high frequency variation is greater than in the other two locations. As in 0°N 140°W, an increasing trend in the average temperature in the earliest portion of the record is clearly apparent, despite the numerous missing data.

The assessment of the diurnal cycle is performed according to the methods described in section 2.2.2. A spectral analysis is performed on the raw data to detect the most important periodicities. Then, the observed daily anomalies are displayed together with the mean and the 5<sup>th</sup> and 95<sup>th</sup> percentiles calculated at each time step.

Table 3.7 reports periods and total number of measurements utilised in the spectral analysis.

Table 3.7: Periods and total number of measurements utilised in the spectral analysis.

	Period start	Period end	Total number of measurements
<b>0°N 95°W</b>	2004-11-06 07:50:00	2005-06-06 01:20:00	30510
<b>0°N 140°W</b>	2008-05-10 05:20:00	2008-12-08 02:20:00	30510
<b>0°N 165°E</b>	2006-07-12 02:20:00	2007-02-08 19:50:00	30510

Figure 3.16 shows the smoothed periodogram of the three air temperature time series.

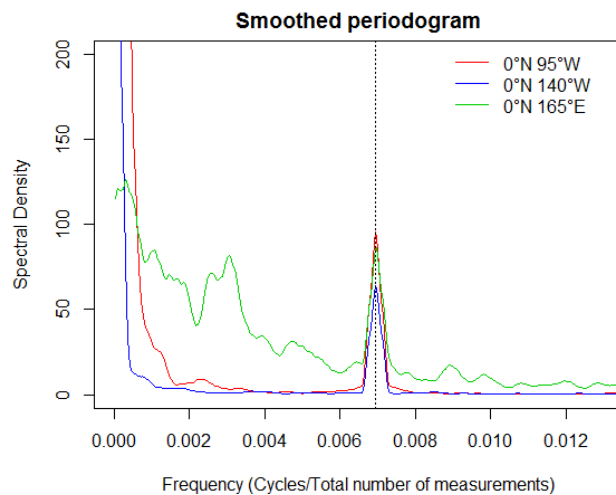


Figure 3.16: Smoothed periodogram of air temperature measurements for each buoy. The vertical black dashed line identifies the daily frequency.

The smoothed periodogram shows that all the time series contain a strong signal, corresponding to the diurnal periodicity.

Figure 3.17 illustrates the air temperature diurnal cycles retrieved by the three buoys.

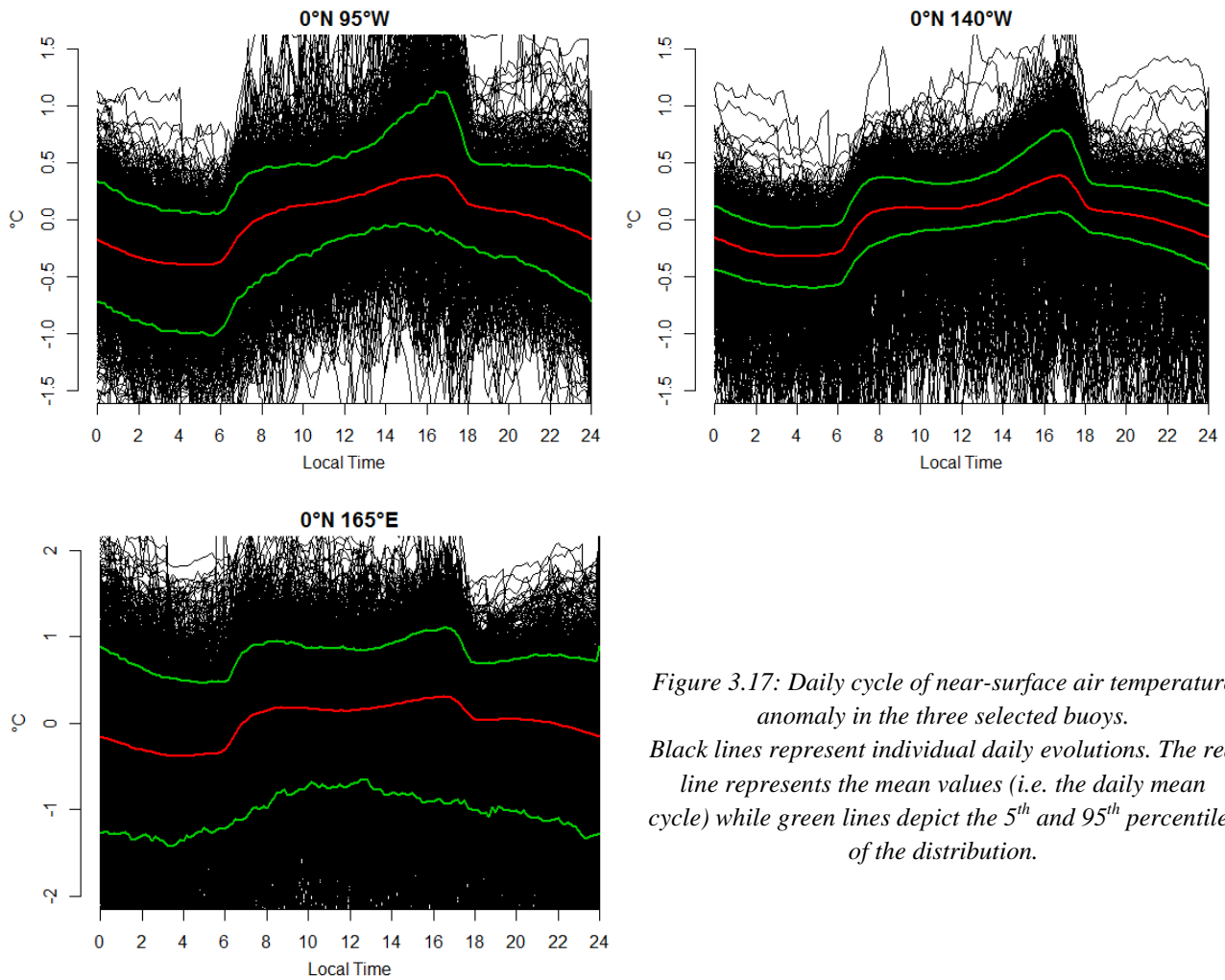


Figure 3.17: Daily cycle of near-surface air temperature anomaly in the three selected buoys. Black lines represent individual daily evolutions. The red line represents the mean values (i.e. the daily mean cycle) while green lines depict the 5<sup>th</sup> and 95<sup>th</sup> percentiles of the distribution.

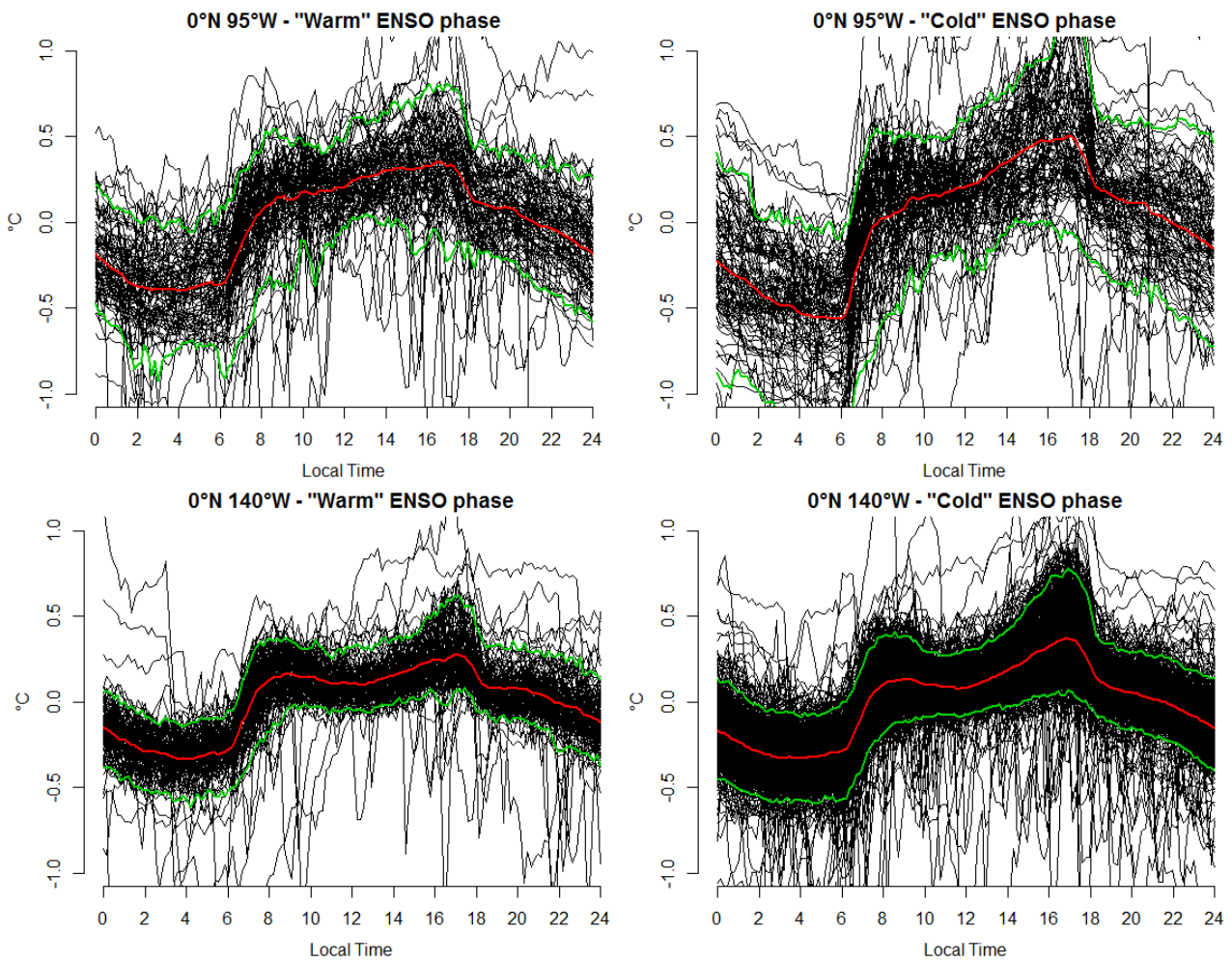
Figure 3.17 shows that the three buoys are characterised by a very similar mean anomaly daily cycle. The cycles includes two peaks, occurring at mid-morning and mid-afternoon. After sunrise, i.e. after 06, the air temperature increases sharply reaching a peak few minutes before 08. During this time interval, temperature increases by 0.40 °C. Then, the air temperature remains approximately constant until 12, except for 0°N 95°W. Observations retrieved from this buoy indicate that temperature continues to rise gently of 0.12 °C after 08. After 12, temperature starts again to increase sharply until 17 when it reaches its daily maximum. During this time interval, the measured values increase between 0.15 and 0.30 °C. The maximum diurnal air temperature measures 0.40 °C for buoys 0°N 95°W and 0°N 140°W, and 0.30 °C for buoy 0°N 165°E. Then, temperature drops sharply until 18, reaching approximately the same values registered around mid-day. After sunset, the air temperature decreases gently throughout the evening and night until 03. During the night, the average temperature drops of 0.5 °C for 0°N 95°W, 0.4 °C for 0°N 140°W, and 0.37 °C for 0°N 165°E. Finally, the temperature stabilises before 04 and remains constant until dawn. The diurnal mean temperature anomaly ranges between 0.39 °C and -0.4 °C for 0°N 95°W, 0.38 °C and -0.33 °C for 0°N 140°W, 0.31 °C and -0.38 °C for 0°N 165°E. The variability of the 95<sup>th</sup> percentiles resembles the mean diurnal evolution. On the contrary, the 5<sup>th</sup> percentiles have a different shape compared to the mean anomalies, except for 0°N 140°W. The difference between mean anomalies and the two considered percentiles is highest during the mid-afternoon peak and lower during the rest of day.

The diurnal cycle of air temperature data is further analysed by differentiating between measurements retrieved under both “warm” and “cold” phases of ENSO, as described in sub-section 2.2.3. Table 3.7 summarises the number of recorded days for each ENSO phase.

Table 3.7: Number of days used to derive the daily cycle of near-surface air during the warm and cold ENSO phase for every buoy.

	0°N 95°W	0°N 140°W	0°N 165°E
Cold ENSO phase	96	465	292
Warm ENSO phase	87	117	224

Figure 3.18 shows the air temperature daily anomaly cycles retrieved during El Niño and La Niña periods.



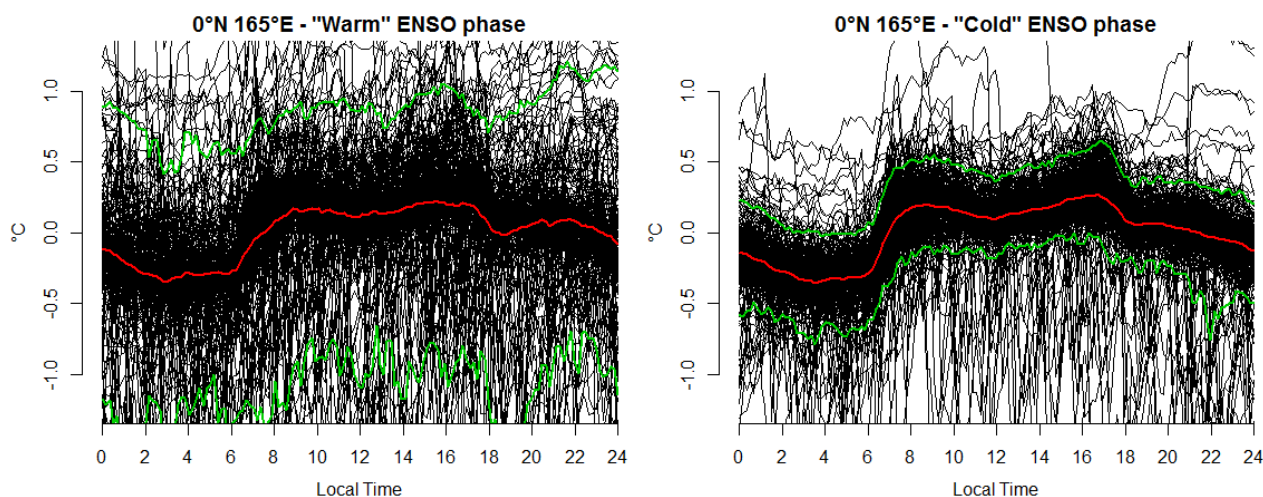


Figure 3.18: Daily cycle of near-surface air temperature anomaly in the three selected buoys retrieved during both the cold and warm ENSO phases.

Black lines represent individual daily evolutions. The red line represents the mean values (i.e. the daily mean cycle) while green lines depict the 5<sup>th</sup> and 95<sup>th</sup> percentiles of the distribution.

Warm and cold ENSO phases of 0°N 95°W share a similar mean diurnal cycle shape. The mid-morning and mid-afternoon peaks are still distinguishable. The main difference between the two phases mostly consists in the amplitudes of the observed cycles, which measure 1.07 °C for the cold phase and 0.75 °C for the warm phase. A similar behaviour is observed for 0°N 140°W, whose main difference regards the amplitude of the observed diurnal cycles, which reaches 0.7 °C during the cold phase and 0.61 °C during the warm phase. In contrast, 0°N 165°E features very similar mean diurnal cycles as well as similar mean amplitudes under the two ENSO conditions, featuring 0.62 °C for the cold phase and 0.57 °C for the warm phase.

The diurnal cycle of near-surface air temperature is further analysed by examining measurements retrieved under different insolation and wind conditions. Table 3.9 summarizes the number of days lying in the different meteorological classes.

Table 3.9: Number of days lying in the wind and insolation classes for the different buoys.

	0°N 95°W	0°N 140°W	0°N 165°E
<i>Cloudy days</i>	271	908	742
<i>Moderate-Cloudy days</i>	408	1364	1114
<i>Moderate-sunny days</i>	407	1363	1113
<i>Sunny days</i>	272	910	743
<i>Wind class 1</i>	143	32	219
<i>Wind class 2</i>	414	1064	524
<i>Wind class 3</i>	132	1598	360

Figure 3.19 represents the air temperature daily cycles according to the four insolation classes for buoy 0°N 95°W.

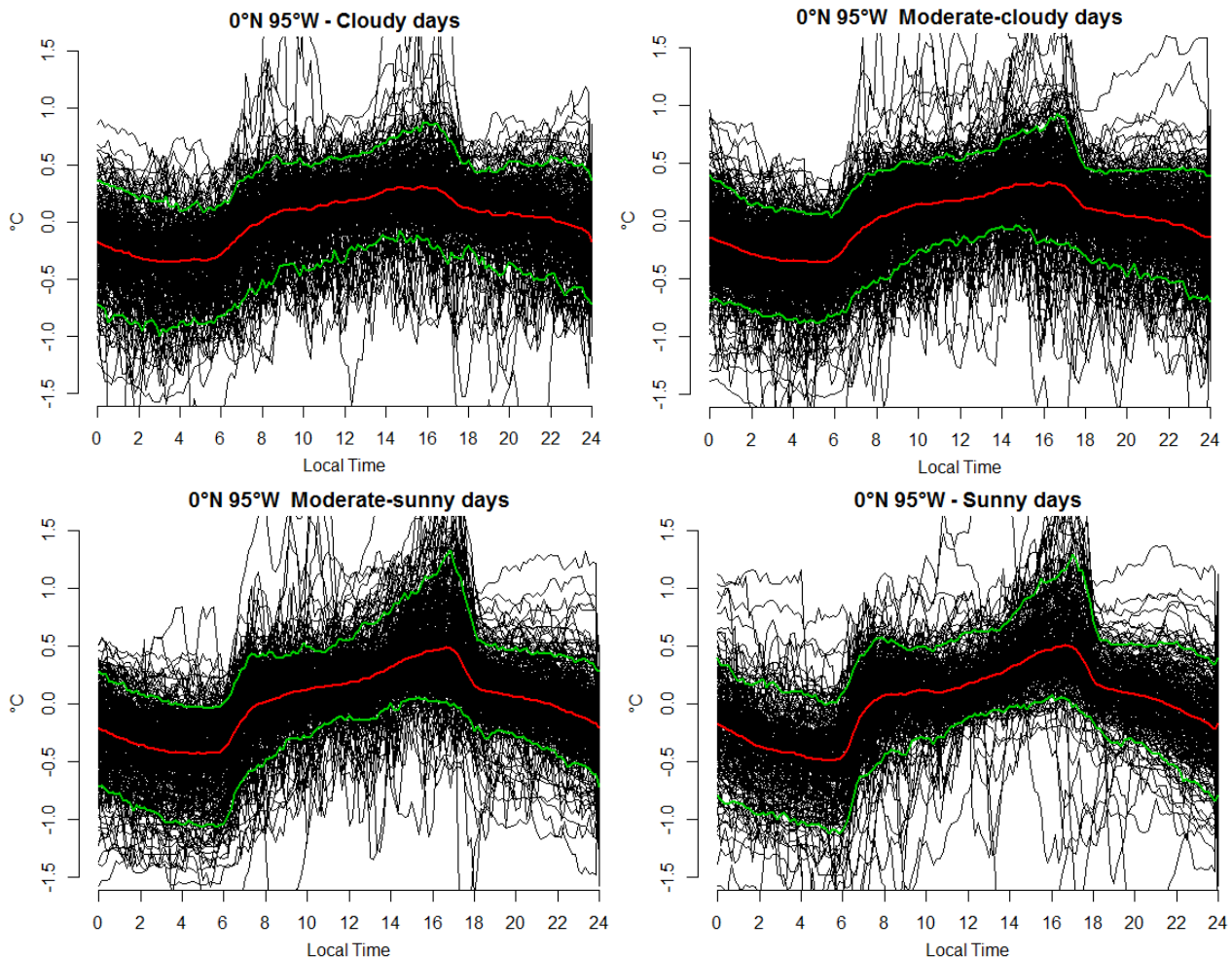


Figure 3.19: Daily cycle of near-surface air temperature anomaly for buoy 0°N 95°W according to the four solar radiation classes.

Black lines represent individual daily evolutions. The red line represents the mean values (i.e. the daily mean cycle) while green lines depict the 5<sup>th</sup> and 95<sup>th</sup> percentiles of the distribution.

The air temperature cycle changes with the insolation conditions. The mean cycle under cloudy days is characterised by the presence of just one peak, occurring in the mid-afternoon. Temperature starts to increase after sunrise and reaches the maximum anomaly value of 0.32 °C near 16. Temperature decreases suddenly between 17 and 18; then it decreases more gently. Finally, approximately between 03 and 06, the air temperature remains almost stable. The mean diurnal temperature variation is about 0.66 °C. As insolation increases, the two-peaks shape becomes more and more prominent. Sunny days are characterised by two marked peaks occurring before 08 and around 17, respectively. After 18, the air temperature decreases until sunrise. The amplitude of the mean diurnal cycle during sunny days grows to 1°C.

Figure 3.20 illustrates the air temperature daily cycles observed during the four insolation conditions for buoy 0°N 140°W.

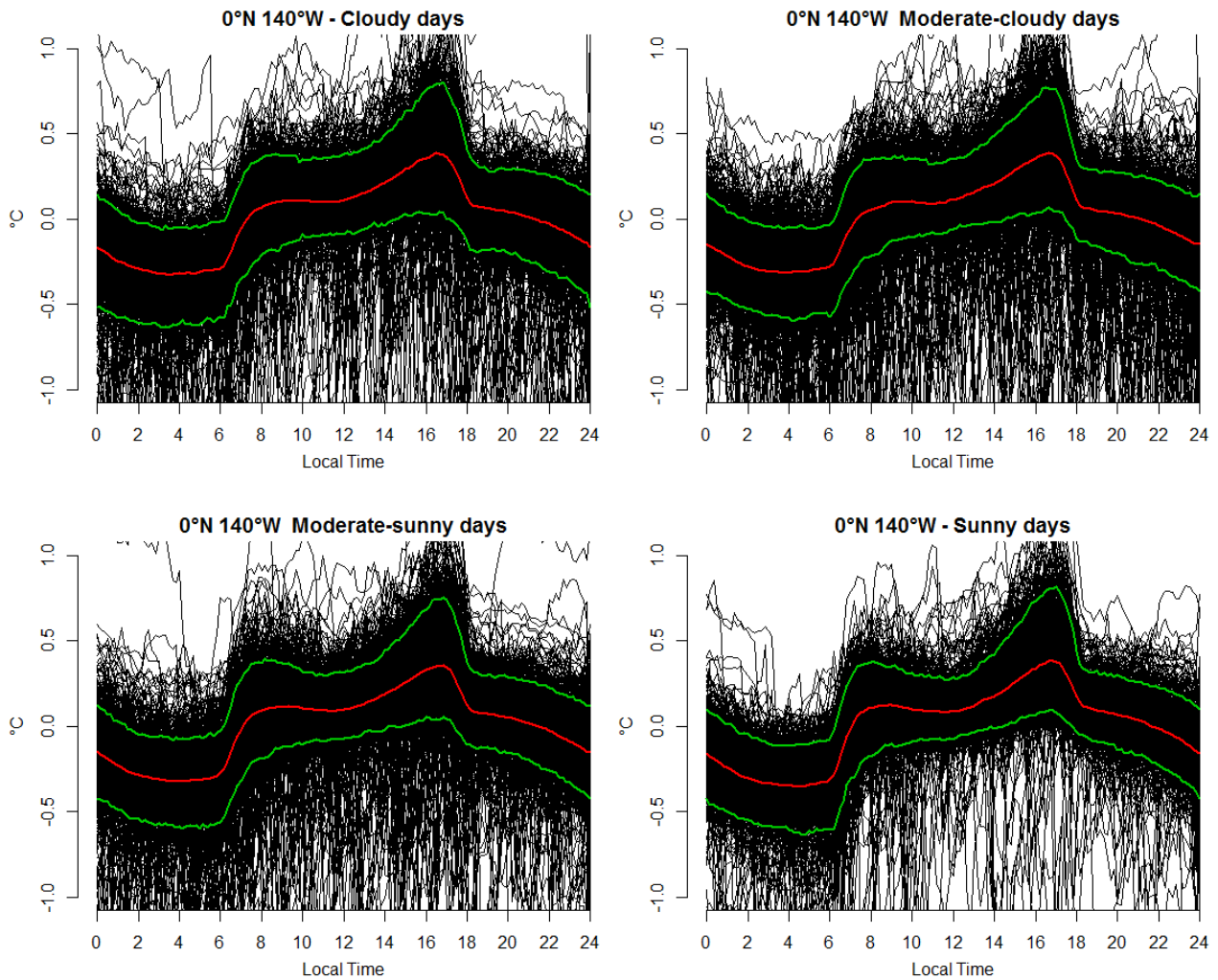


Figure 3.20: Daily cycle of near-surface air temperature anomaly for buoy 0°N 140°W according to the four solar radiation classes.

Black lines represent individual daily evolutions. The red line represents the mean values (i.e. the daily mean cycle) while green lines depict the 5<sup>th</sup> and 95<sup>th</sup> percentiles of the distribution.

Figure 3.20 reveals the clear presence of a double peak in this buoy under all insolation conditions. The amplitude of the mean diurnal cycle remains approximately steady as insolation increases, spanning from 0.71 °C for *cloudy days* to 0.74 °C for *sunny days*. The temperature in the pre-dawn hours, i.e. from 03 to 06, remains approximately stable in all the analysed conditions for 0°N 140°W.

Figure 3.21 illustrates the air temperature daily cycles according to the four insolation classes for buoy 0°N 165°E.

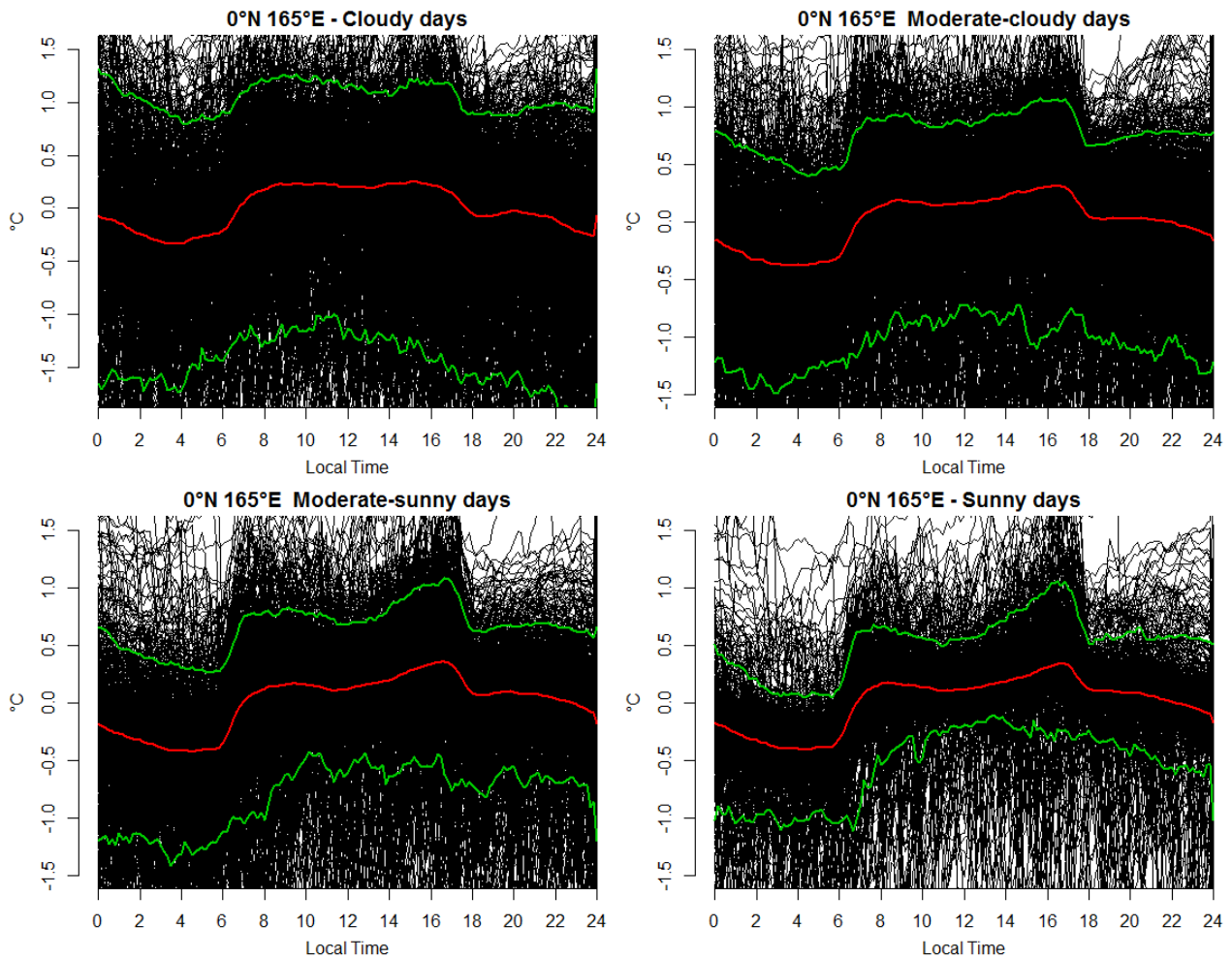


Figure 3.21: Daily cycle of near-surface air temperature anomaly for buoy 0°N 165°E according to the four solar radiation classes.

Black lines represent individual daily evolutions. The red line represents the mean values (i.e. the daily mean cycle) while green lines depict the 5<sup>th</sup> and 95<sup>th</sup> percentiles of the distribution.

According to the figure, the gaps between percentiles and mean values diminishes as the insolation increases. Thus, as insolation increases, the variability of the individual daily evolutions diminishes. The amplitude of the mean diurnal cycles expands as the solar radiation increases, which largely results from the amplification of the mid-afternoon peak. *Cloudy days* feature an almost constant temperature between 08 and 17. Instead, as insolation increases, the mean diurnal cycle features a more prominent mid-afternoon peak. The amplitudes of the diurnal cycles, ordered from *cloudy* to *sunny days*, measure 0.59 °C, 0.69 °C, 0.78 °C and 0.74 °C. 0°N 165°E features a clearly increasing temperature in the pre-dawn hours in *cloudy* and *moderate-cloudy days*, whereas temperature remains stable in the remaining two classes.

Overall, the differentiation based on insolation conditions reveals common characteristics in the air temperature diurnal cycle among the three buoys. First, the height of the mid-morning and mid-afternoon peak is considerably reduced during *cloudy days*. Furthermore, the two peaks grow as the insolation increases. The amplitude of the diurnal air temperature is markedly lowered under cloudy conditions, while it grows as the insolation increases. Finally, as recognised before in Figure 3.17, the air temperature is stable in the early morning, i.e. from 03 to 06, and sometimes even increases.

Figure 3.22 shows the air temperature daily cycles according to the three wind classes for buoy 0°N 95°W.

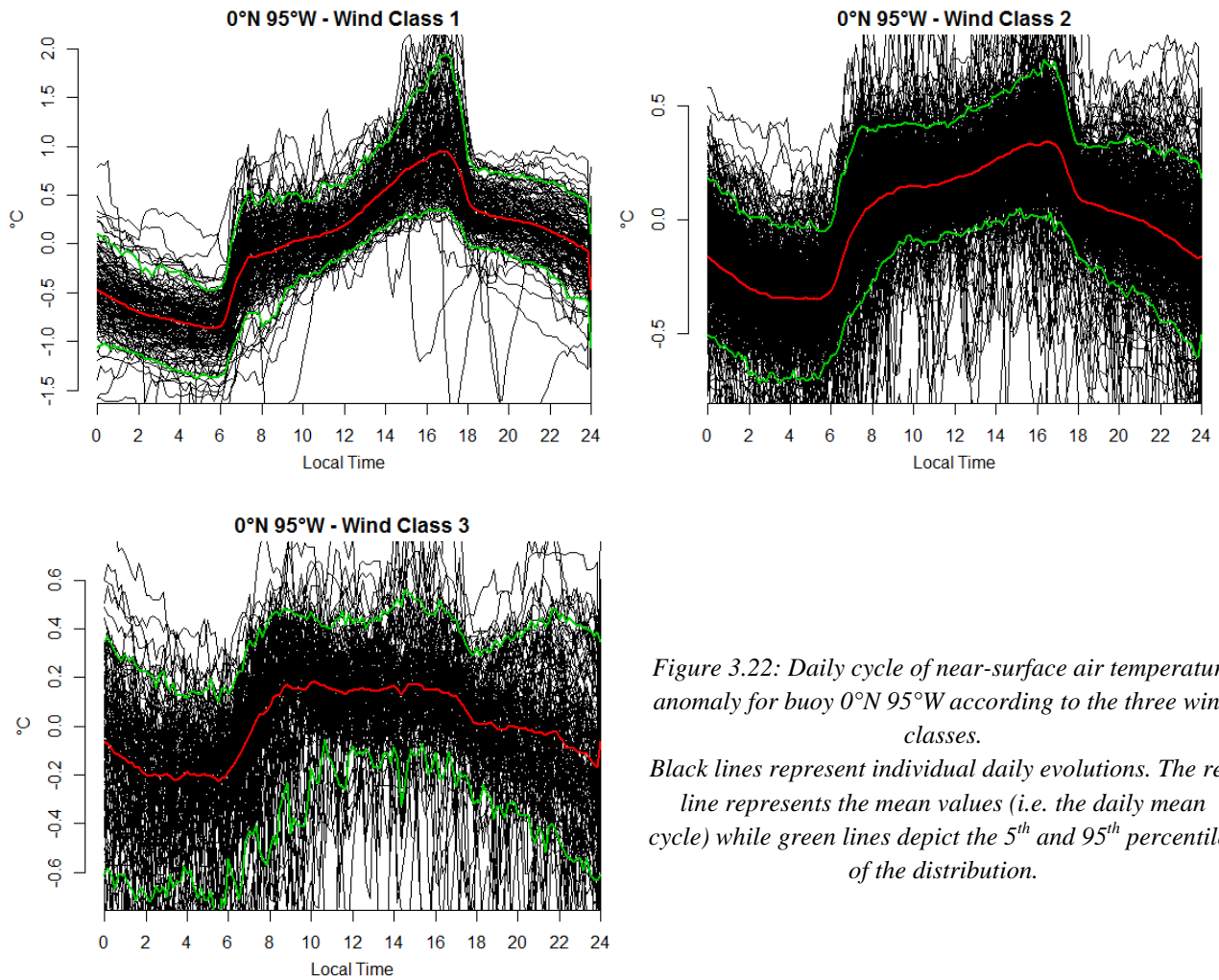


Figure 3.22: Daily cycle of near-surface air temperature anomaly for buoy 0°N 95°W according to the three wind classes. Black lines represent individual daily evolutions. The red line represents the mean values (i.e. the daily mean cycle) while green lines depict the 5<sup>th</sup> and 95<sup>th</sup> percentiles of the distribution.

The air temperature diurnal cycles retrieved by 0°N 95°W present the two-peaks shape already observed, but they are noticeably affected by the local wind conditions. The amplitude of the cycle diminishes as the wind velocity increases i.e. from *wind class 1* to *wind class 3*. Amplitudes measure 1.81 °C for low winds, 0.69 °C for moderate winds, and 0.41 °C for strong winds. The height of the peaks, especially the mid-afternoon one, is considerably reduced as wind velocities increase. Under strong winds, the mid-afternoon peak is even lower than the mid-morning peak, causing the temperature to be approximately stable between 09 and 17. Figure 3.23 represents the air temperature daily cycles observed under the three wind conditions for buoy 0°N 140°W.

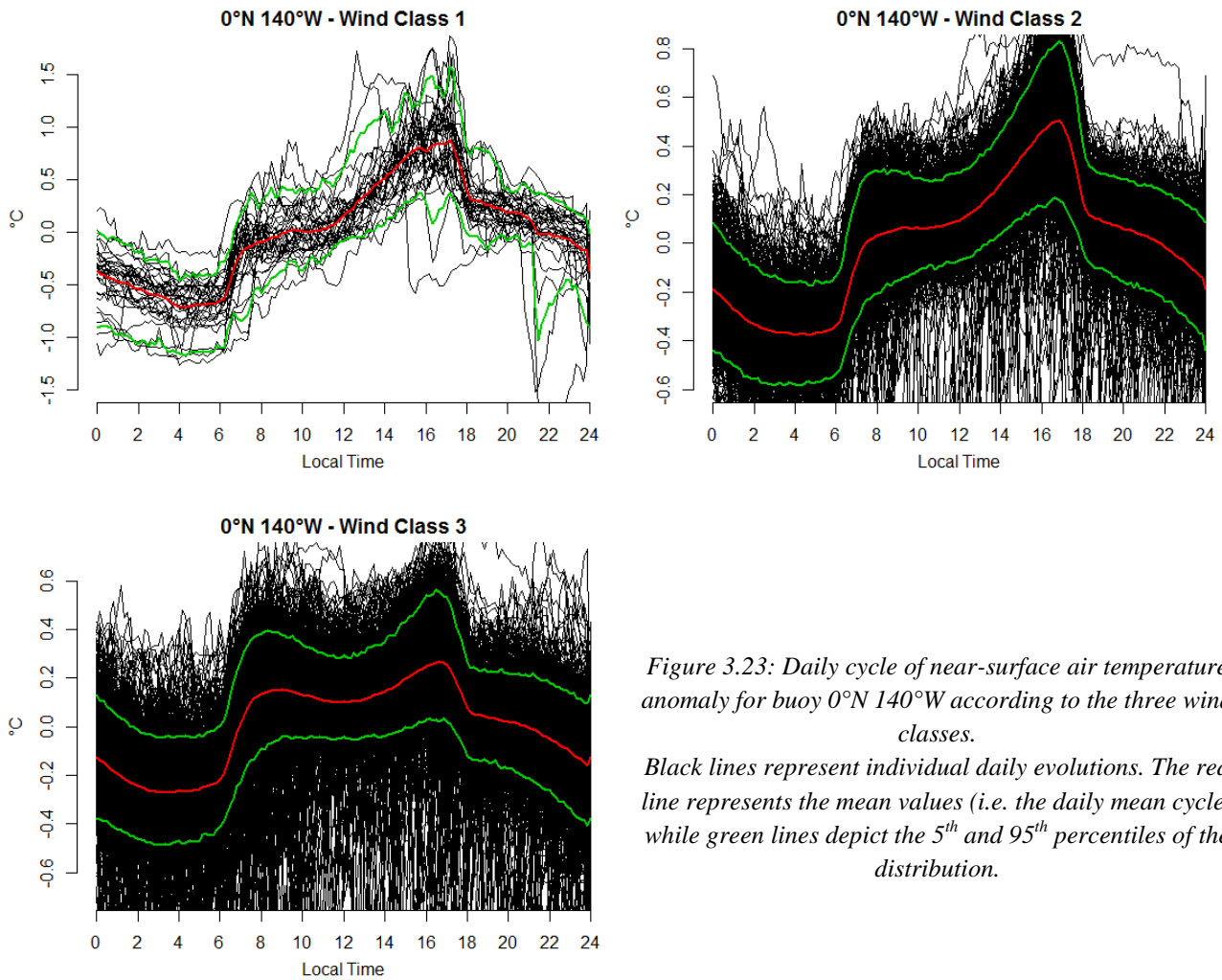


Figure 3.23: Daily cycle of near-surface air temperature anomaly for buoy 0°N 140°W according to the three wind classes.

Black lines represent individual daily evolutions. The red line represents the mean values (i.e. the daily mean cycle) while green lines depict the 5<sup>th</sup> and 95<sup>th</sup> percentiles of the distribution.

The amplitudes of the mean anomaly cycles are 1.59 °C for weak winds, 0.88 °C for moderate winds, and 0.54 °C for strong winds. Hence, as the wind velocity increases, the diurnal near-surface air temperature range decreases. The two peaks are present in all wind classes although the air temperature exhibit a different behaviour in between these two peaks. *Wind class 1* seems to feature a gentle, approximately constant mean temperature increment. However, the limited number of days lying in *wind class 1* does not allow conclusive statements. *Wind class 2* is characterised by stable temperature between 08 and 12; afterwards, it begins to increase. *Wind class 3* features even a decreasing temperature from 08 to 12, followed by growing values.

Figure 3.24 shows the air temperature daily cycles belonging to the three wind classes for buoy 0°N 165°E.

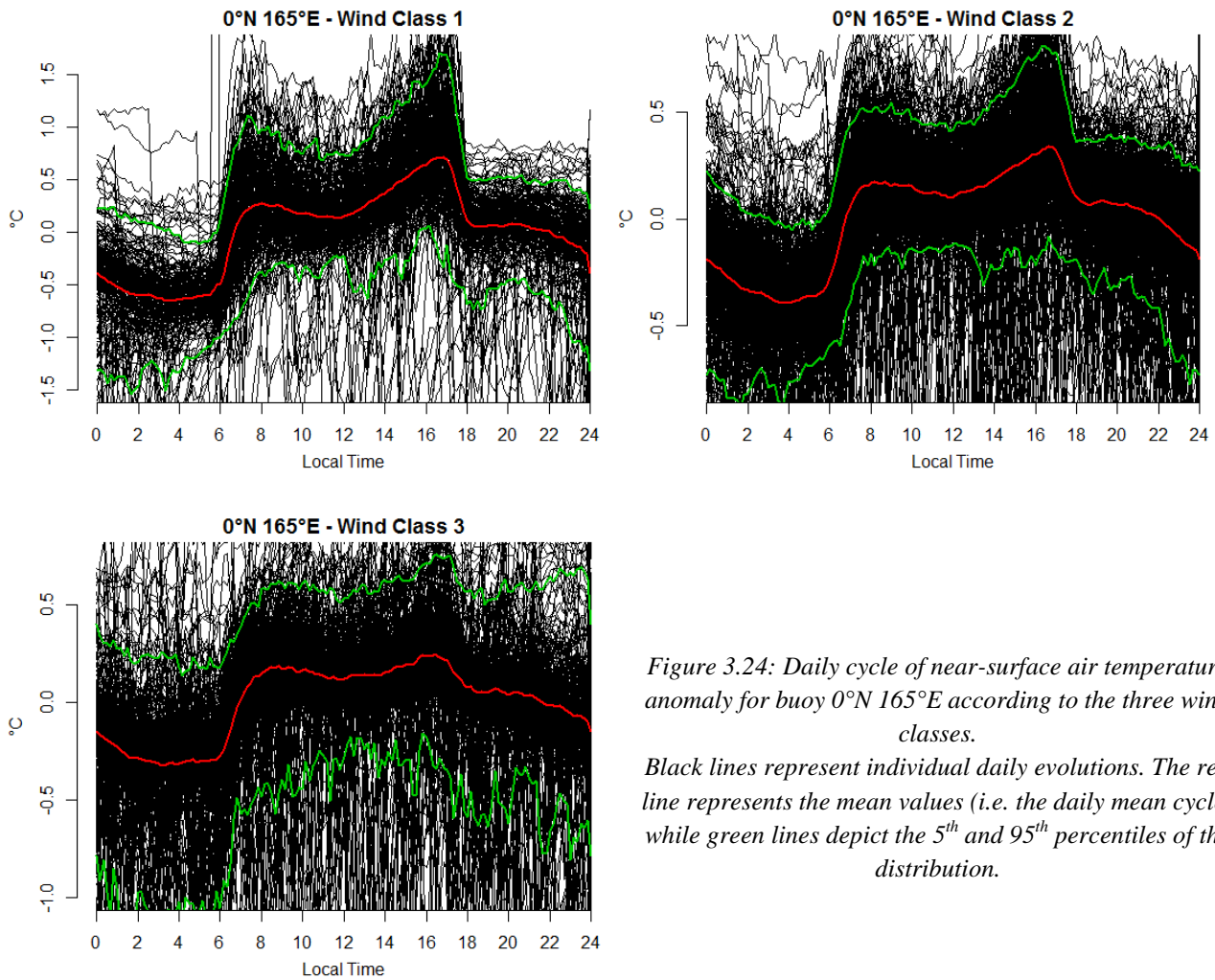
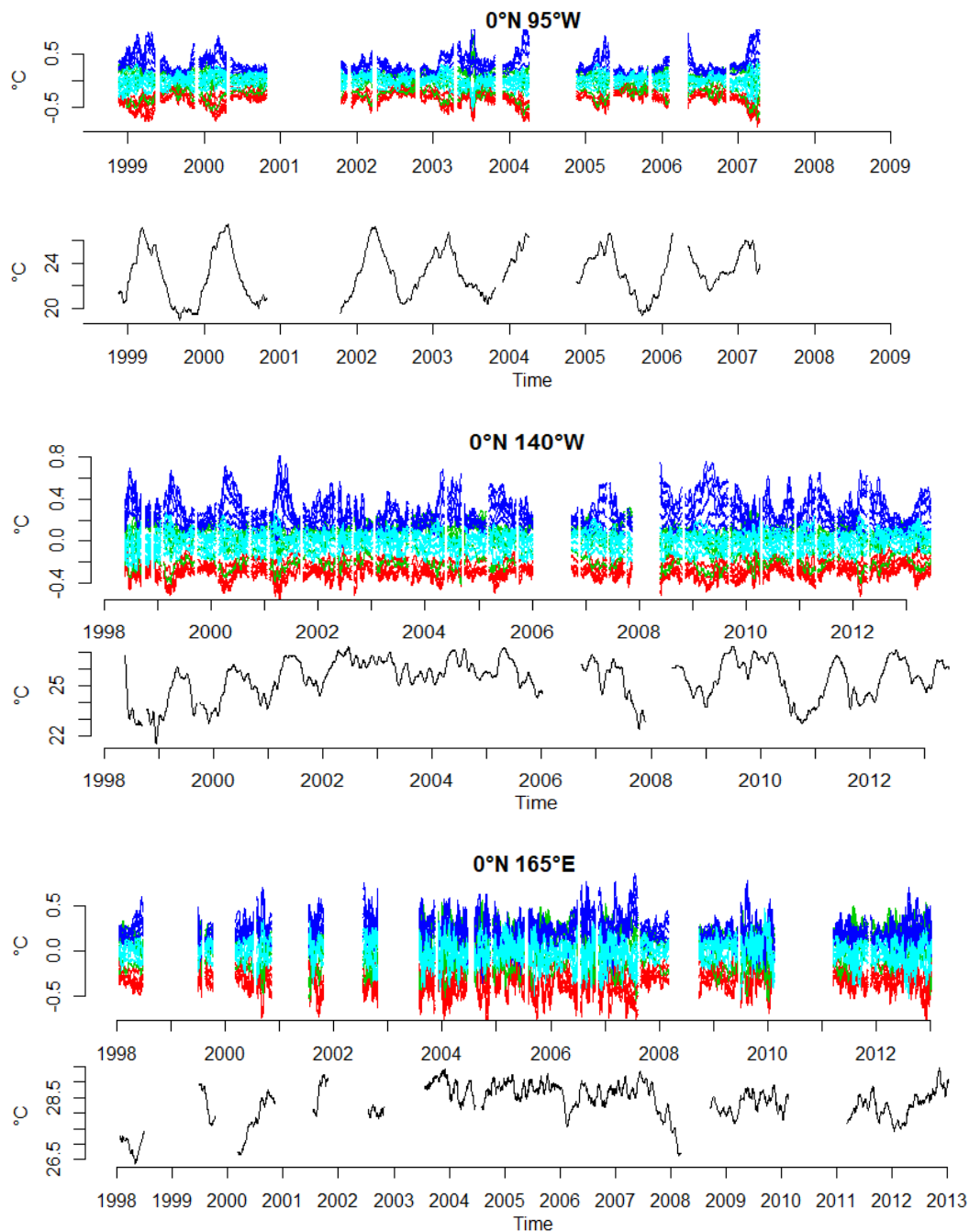


Figure 3.24: Daily cycle of near-surface air temperature anomaly for buoy 0°N 165°E according to the three wind classes. Black lines represent individual daily evolutions. The red line represents the mean values (i.e. the daily mean cycle) while green lines depict the 5<sup>th</sup> and 95<sup>th</sup> percentiles of the distribution.

The mean near-surface air temperature cycles at 0°N 165°E show the presence of the two peaks under all wind conditions. In between the two spikes, the mean temperature remains stable in *wind class 1*, while it slightly decreases for *wind class 2* and *3*. The amplitudes of the mean cycles are 1.37 °C for *wind class 1*, 0.73 °C for *wind class 2* and 0.57 °C for *wind class 3*. Hence, as the wind velocity increases, the amplitude of the mean diurnal cycle decreases.

The differentiation based on wind classes shows two major features common to the three buoys. First, the amplitude of the mean diurnal cycle is largely reduced as wind velocity increases. Second, even under strong wind conditions, the mean diurnal cycles display a mid-morning and a mid-afternoon peak. As recognised previously, the air temperature is almost constant in the pre-dawn hour, from approximately 03 to 06, under almost all the considered wind conditions and buoys.

The evolution of the diurnal cycle of the near-surface air temperature over the long period is assessed in Figure 3.25. This figure shows the evolution of the air temperature smoothed hourly anomalies in comparison with the air temperature smoothed time series.



*Figure 3.25: Variations of the diurnal cycle of near-surface air temperature over the long period. For each buoy, the upper panel reports the hourly near-surface air temperature anomaly time series, while the lower panel shows the near-surface air temperature absolute smoothed values. Red lines correspond to hours between 00 and 05. Green lines correspond to hours between 06 and 11. Blue lines correspond to hours between 12 and 17. Light blue lines correspond to hours between 18 and 23.*

Figure 3.25 displays the variation of the diurnal cycle in time throughout the entire periods of record. Similarly in all the buoys, hourly averages between 6 and 11 exhibit the lowest values, while hourly averages between 12 and 17 constitute the highest values throughout the whole time series. Anomalies lying between 18 and 23 are close to zero. Particularly in the case of buoys 0°N 95°W and 0°N 140°W, a comparison between hourly anomaly averages and absolute smoothed values reveals an interesting feature. The diurnal temperature range increases regularly under regimes of warmer temperatures. Instead, 0°N 165°E does not display a similar pattern.

### 3.4 Sea Surface Temperature

Figure 3.26 illustrates the sea surface temperature (SST) time series acquired by the three selected buoys and the associated smoothing lines.

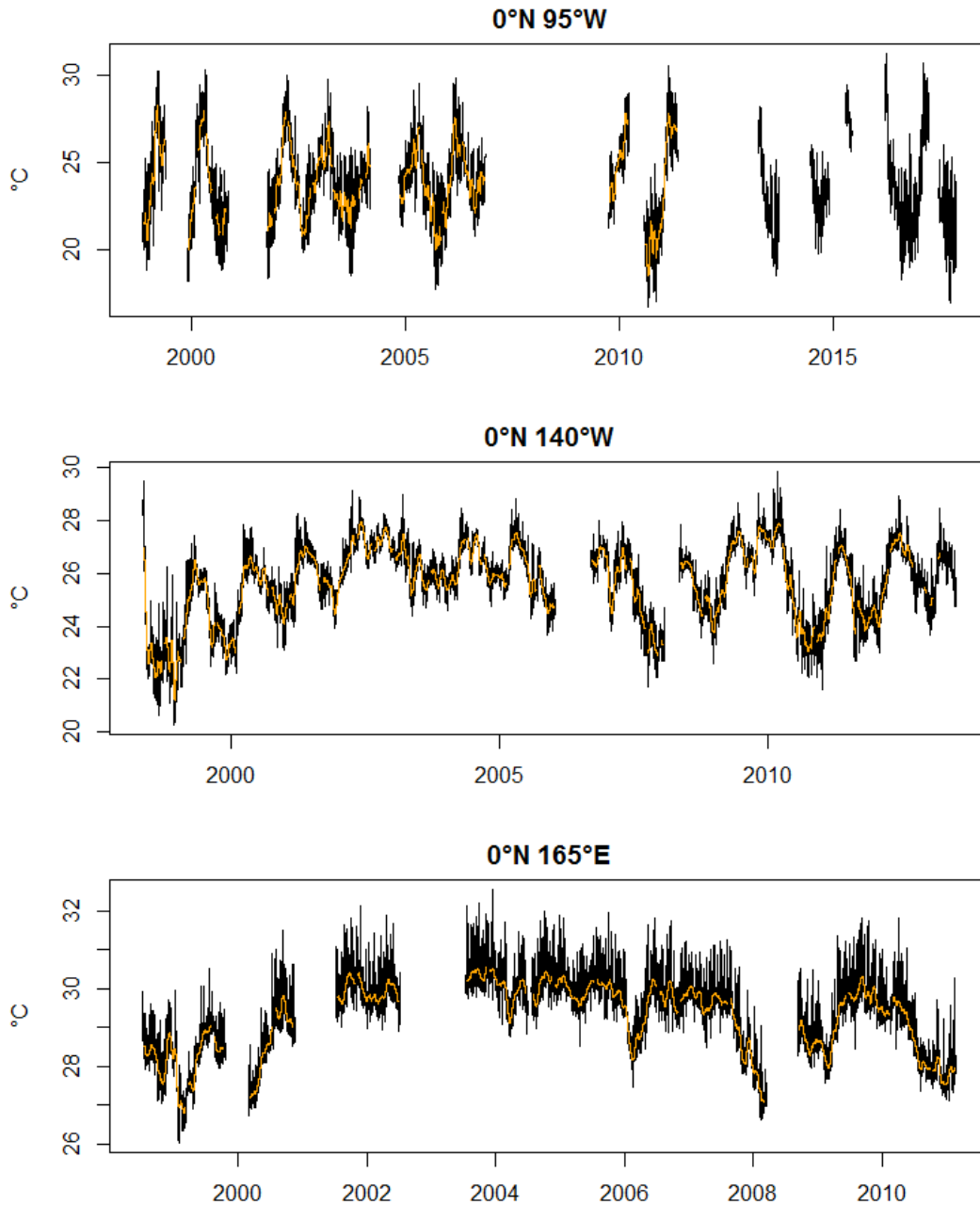


Figure 3.26: Sea surface temperature time series retrieved by buoys 0°N 95°W, 0°N 140°W and 0°N 165°E. The orange lines represent smoothed values.

The SST evolution over the entire period shares several common aspects with the near-surface air temperature evolution. 0°N 95°W features a strong yearly seasonal cycle characterised by an amplitude of approximately 10 °C. The time series seems to be stable over the years as it does not show presence of a distinguishable trend. 0°N 140°W displays a yearly seasonal cycle with an amplitude of approximately 4-5

°C. The yearly averaged SST increases from the beginning of the record until 2002, then it stabilises. In between 2007 and 2011, the amplitude of the seasonal cycle increases. Unlike the other two buoys, 0°N 165°E does not show a strong annual cycle. The time series features an increasing trend in late 1990s and early 2000s and a decreasing trend from 2005 to 2010. 0°N 165°E features higher high-frequency variability compared to the other buoys.

The spectral analysis introduces the assessment of the diurnal cycle.

Table 3.10 reports the periods and total number of measurements utilised in the spectral analysis.

Table 3.10: Period and total number of measurements utilised in the spectral analysis.

	Period start	Period end	Number of total measurements
<b>0°N 95°W</b>	2004-11-05 07:10:00	2005-05-09 15:40:00	26692
<b>0°N 140°W</b>	2008-05-10 05:20:00	2008-11-11 13:50:00	26692
<b>0°N 165°E</b>	2008-09-10 00:10:00	2009-03-14 08:40:00	26692

Figure 3.27 illustrates the periodogram of the SST time series.

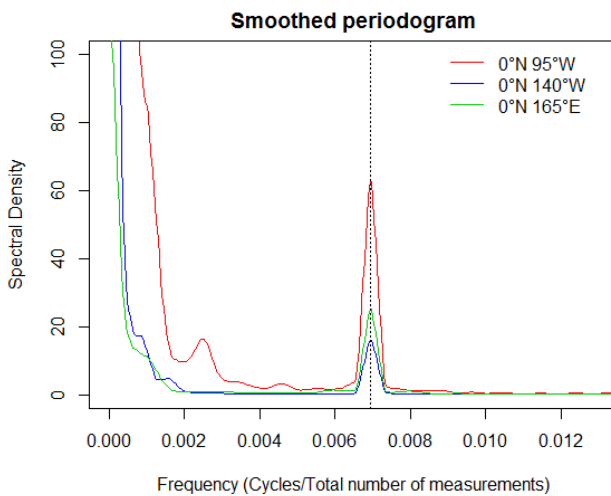


Figure 3.27: Smoothed periodogram of sea surface temperature measurements for each buoy. The vertical black dashed line identifies the daily frequency.

The smoothed periodogram reveals the presence of a diurnal periodicity within each time series. Moreover, a small peak can be distinguished on the right side of Figure 3.26 indicating a periodicity of half a day. Figure 3.28 illustrates the diurnal cycles of SST retrieved by the three buoys.

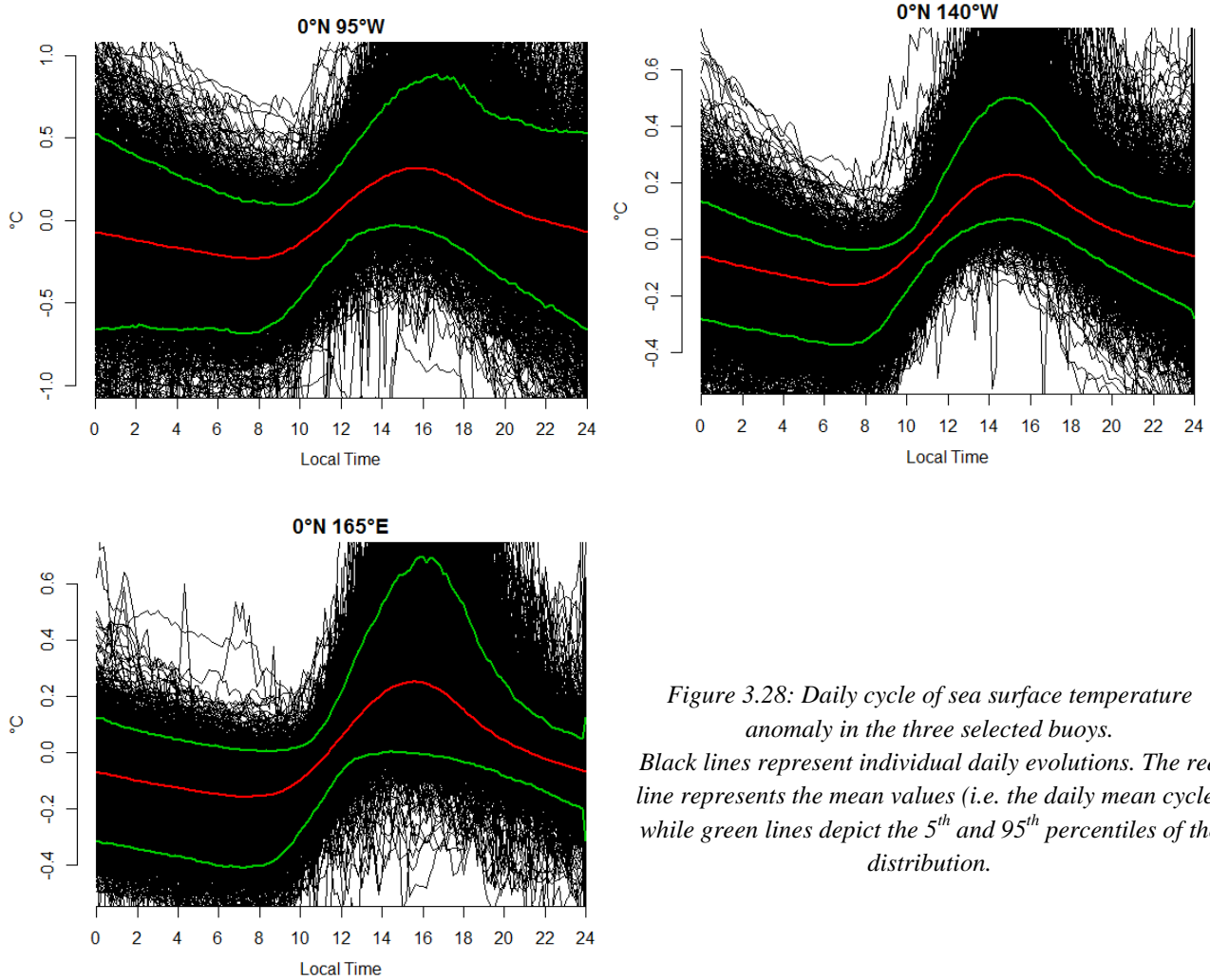


Figure 3.28: Daily cycle of sea surface temperature anomaly in the three selected buoys. Black lines represent individual daily evolutions. The red line represents the mean values (i.e. the daily mean cycle) while green lines depict the 5<sup>th</sup> and 95<sup>th</sup> percentiles of the distribution.

The diurnal cycle of SST is similar among the three buoys. The minima values of the mean daily cycle are located few minutes after 07, while the maximum values occur between 15 and 16. The amplitudes of the mean cycles are 0.55 °C for 0°N 95°W, 0.39 °C for 0°N 140°W and 0.41 °C for 0°N 165°E. The diurnal  $\Delta$ SST is similar amongst the different buoys. The 95<sup>th</sup> percentile indicates that measurements observed nearby the diurnal spike are skewed toward positive values in all the buoys.

The SST diurnal cycle is assessed during the occurrence of El Niño and La Niña events.

Table 3.11 reports the number of days in which the sea surface temperature was recorded during the warm and cold phases of ENSO.

Table 3.11: Number of sea surface temperature recorded days during the two ENSO phase for every buoy.

	0°N 95°W	0°N 140°W	0°N 165°E
<b>Cold ENSO phase</b>	96	465	292
<b>Warm ENSO phase</b>	89	117	224

Figure 3.29 illustrates the diurnal cycles retrieved during the warm and cold phases for all the buoys.

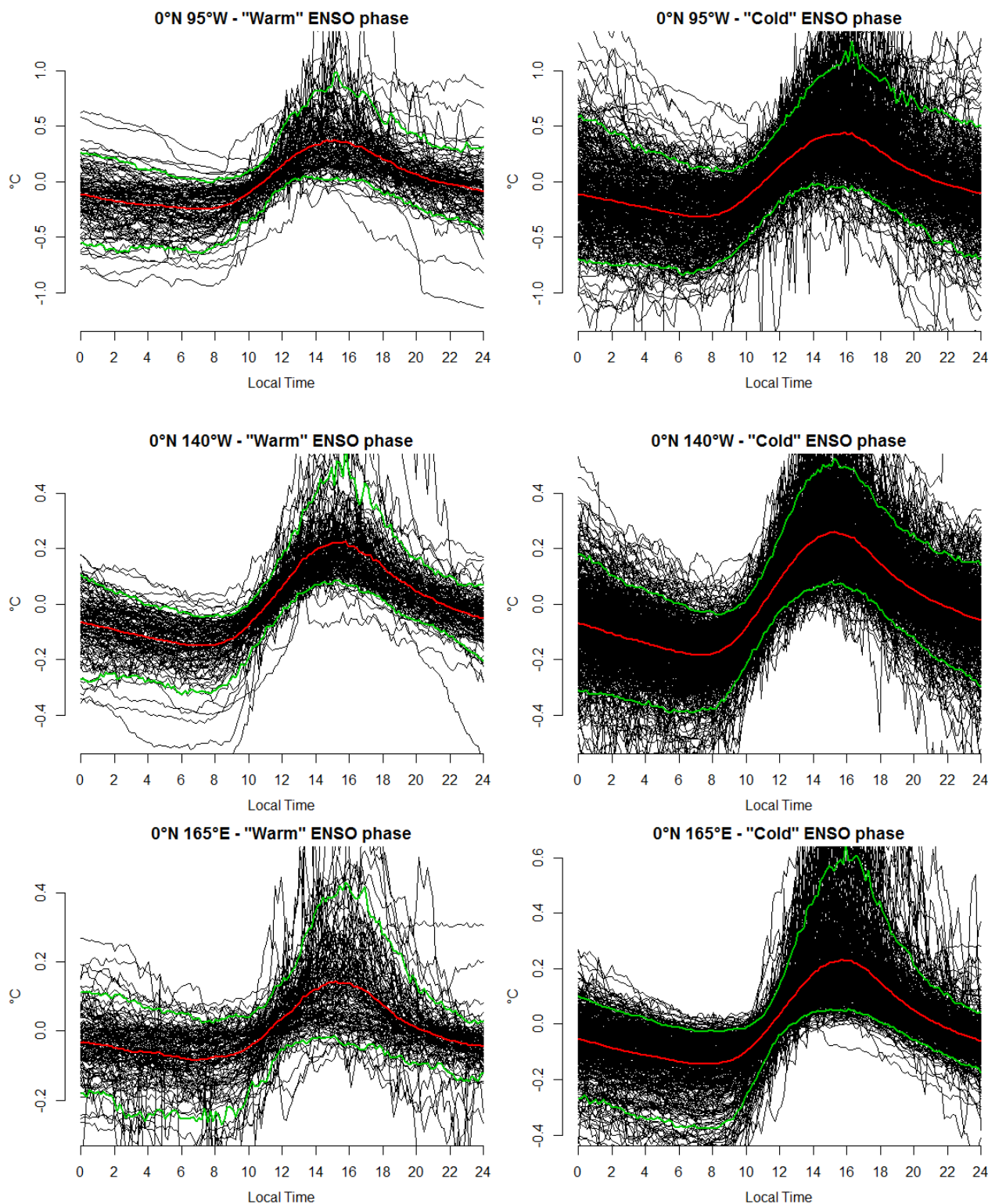


Figure 3.29: Daily cycle of sea surface temperature anomaly in the three selected buoys retrieved during both the cold and warm ENSO phases.

Black lines represent individual daily evolutions. The red line represents the mean values (i.e. the daily mean cycle) while green lines depict the 5<sup>th</sup> and 95<sup>th</sup> percentiles of the distribution.

The shape of the diurnal cycles observed during El Niño and La Niña’s conditions are not notably different from the diurnal cycles observed over the entire periods of study and reported in Figure 3.27. The mean

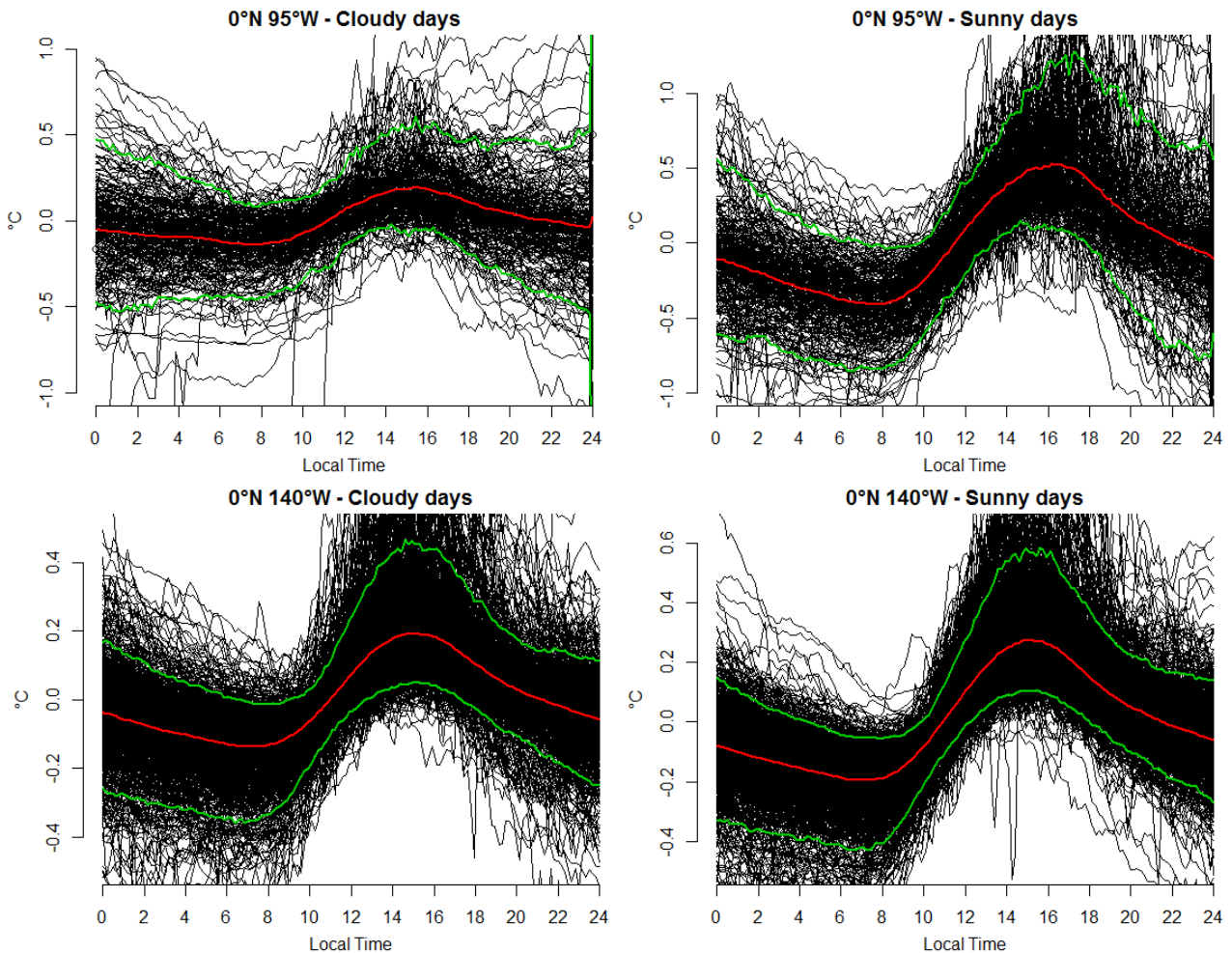
diurnal cycles observed at 0°N 95°W are characterised by an amplitude of 0.62 °C during the warm phase and 0.75 °C during the cold phase. 0°N 140°W features a diurnal amplitude of 0.38 °C during the warm phase and 0.44 °C during the cold phase. The diurnal  $\Delta$ SST observed at 0°N 165°E are 0.23 °C and 0.38 °C for the warm and cold phases, respectively. Percentiles appear to follow the mean diurnal evolution and vary similarly among the different buoys. Overall, La Niña conditions are associated to larger  $\Delta$ SSTs.

Table 3.12 reports the number of days lying in the different wind and insolation classes.

Table 3.12: Number of days lying in the wind and insolation classes according to the different buoys.

	0°N 95°W	0°N 140°W	0°N 165°E
<i>Cloudy days</i>	271	908	569
<i>Sunny days</i>	272	910	570
<i>Wind class 1</i>	128	31	176
<i>Wind class 3</i>	105	1607	244

Figure 3.30 illustrates the SST diurnal cycle under different insolation conditions.



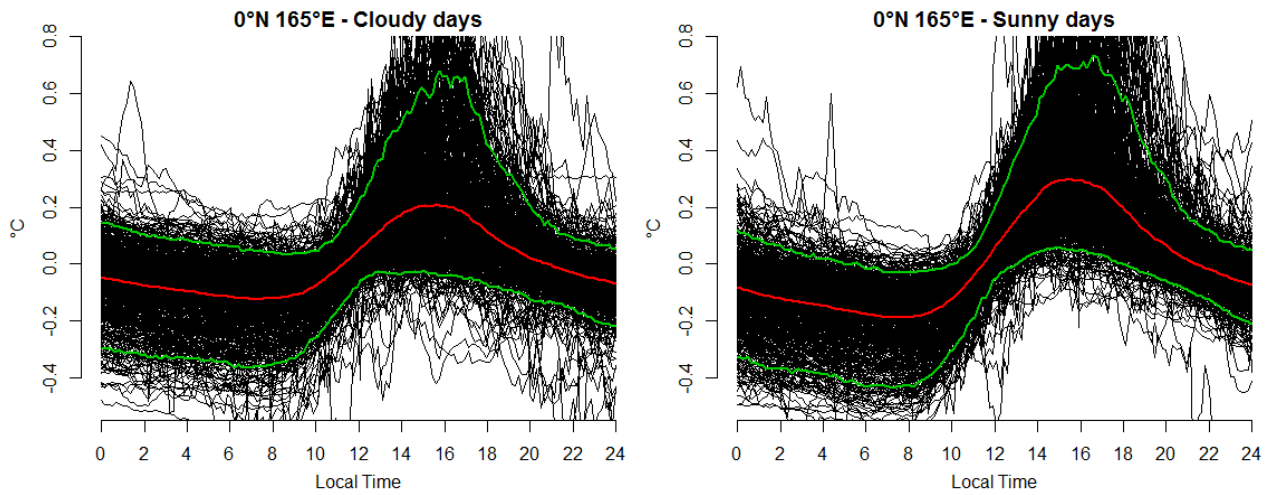
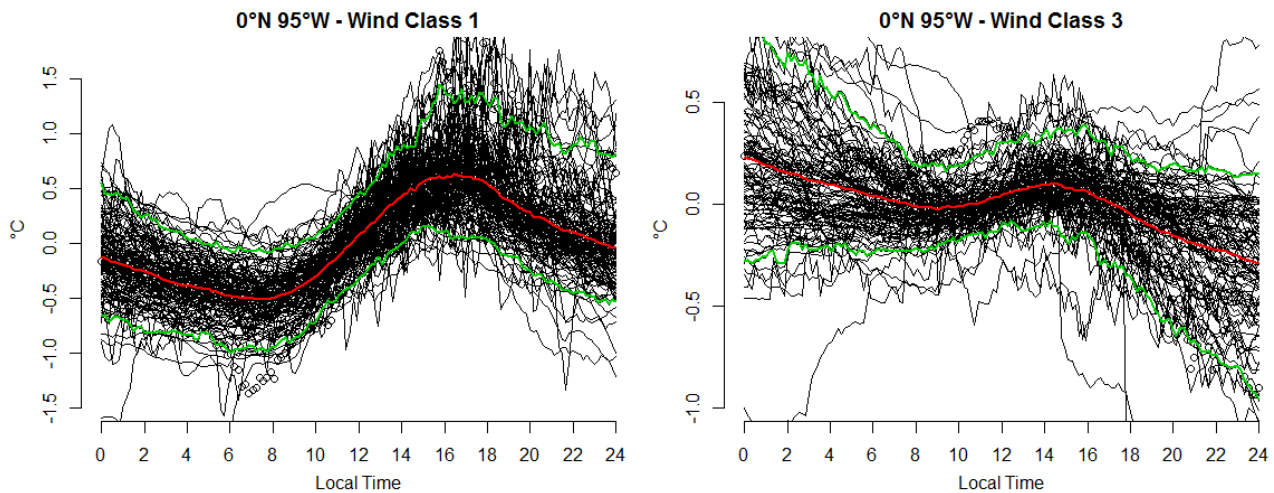


Figure 3.30: Daily cycle of sea surface temperature anomaly observed during cloudy and sunny days in the three buoys.

Black lines represent individual daily evolutions. The red line represents the mean values (i.e. the daily mean cycle) while green lines depict the 5th and 95th percentiles of the distribution.

Meteorological conditions do not significantly affect shape and timing of the SST diurnal cycles. Nevertheless, the diurnal cycle amplitude is lower during *cloudy days* than during *sunny days*. *Cloudy days* feature an amplitude of 0.33 °C for 0°N 95°W, 0.33 °C for 0°N 140°W and 0.34 °C for 0°N 165°E. *Sunny days* are associated to amplitudes of 0.94 °C for 0°N 95°W, 0.47 °C for 0°N 140°W and 0.49 °C for 0°N 165°E.

Figure 3.31 illustrates the SST daily cycles under conditions of weak and strong winds.



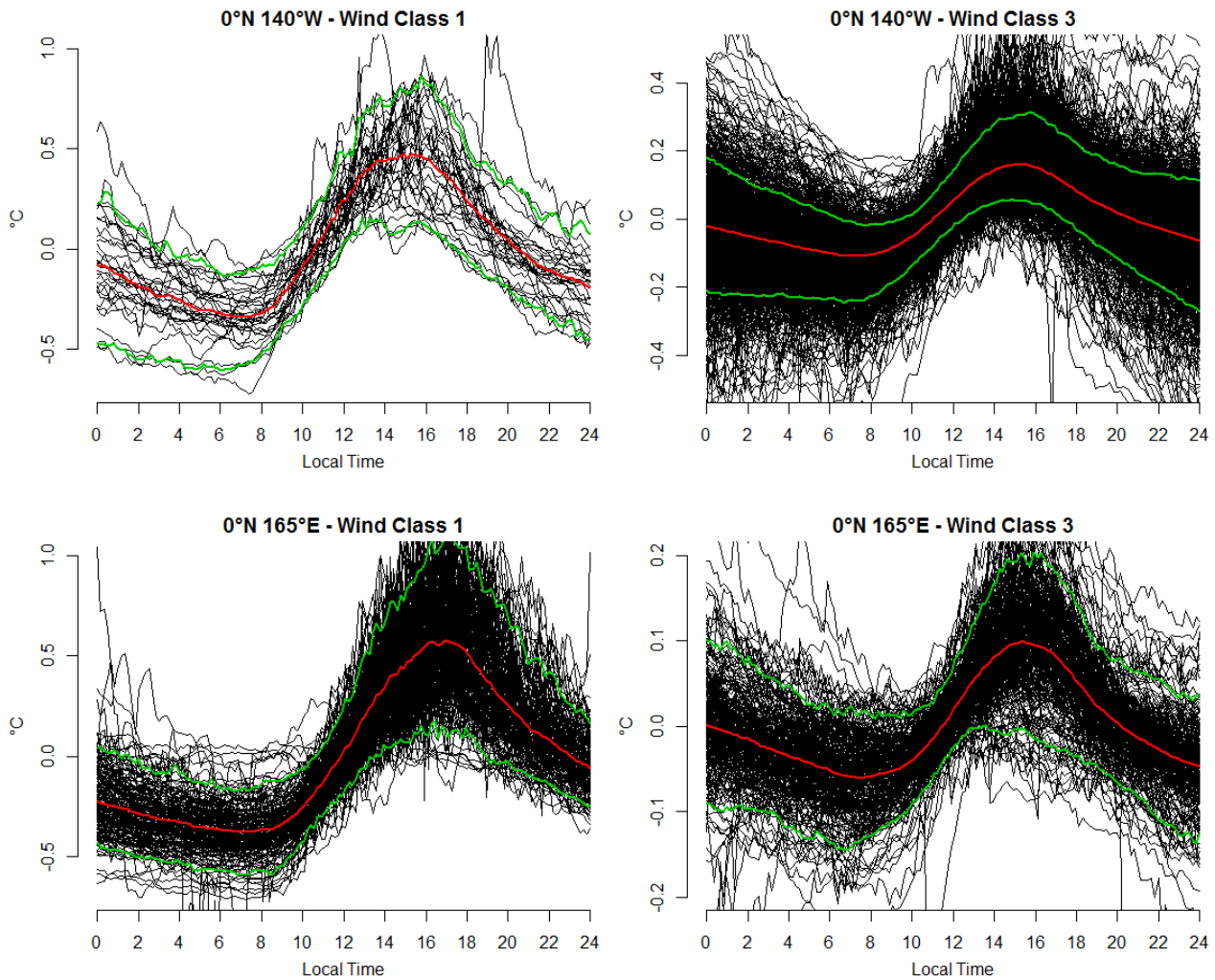


Figure 3.31: Daily cycle of sea surface temperature anomaly according to different wind conditions (weak and strong winds) for the three buoys.

Black lines represent individual daily evolutions. The red line represents the mean values (i.e. the daily mean cycle) while green lines depict the 5th and 95th percentiles of the distribution.

The average shape of the diurnal cycle does not change during days characterised by the presence of strong and weak winds. Nonetheless, larger wind velocities diminishes the diurnal  $\Delta$ SST. Indeed, *Wind class 3* is linked to amplitudes measuring 0.52 °C for 0°N 95°W, 0.27 °C for 0°N 140°W and 0.16 °C for 0°N 165°E. Instead, *wind class 1* features amplitudes of 1.14 °C for 0°N 95°W, 0.81 °C for 0°N 140°W and 0.95 °C for 0°N 165°E. Percentiles behave similarly in the two different classes. Strong winds limit the difference between the mean and both percentiles while weak winds feature larger differences. Days recorded during strong wind conditions by buoy 0°N 95°W show a particular behaviour. The SST mean diurnal cycle attains the maximum anomaly value at midnight and ends with the minimum value. This observation is consistent with a constantly decreasing SST during the selected days.

Figure 3.30 displays the hourly smoothed SST anomalies and the smoothed absolute SST values for the three buoys.

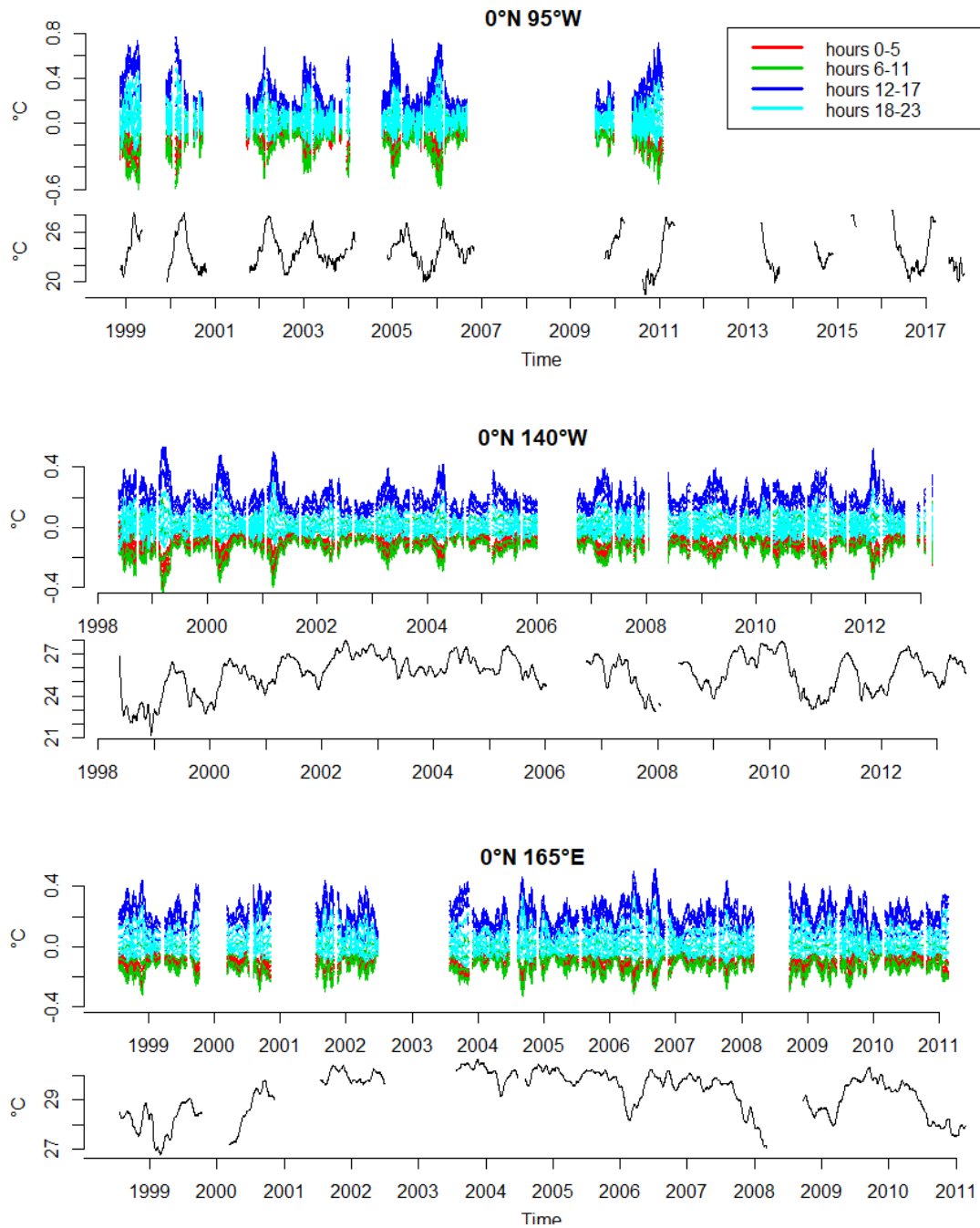


Figure 3.30: Variations of the diurnal cycle of sea surface temperature over the long period.

For each buoy, the upper panel reports the hourly sea surface temperature anomaly time series, while the lower panel shows the sea surface temperature absolute smoothed values.

Red lines correspond to hours between 00 and 05. Green lines correspond to hours between 06 and 11. Blue lines correspond to hours between 12 and 17. Light blue lines correspond to hours between 18 and 23.

The hourly SST time series show a similar behaviour compared to the near-surface air temperature. The diurnal  $\Delta$ SST exhibits a periodic increase in phase with the occurrence of warmer SSTs. This behaviour can be observed also for  $0^{\circ}\text{N } 165^{\circ}\text{E}$  though it does not occur in each warm SST regime. The time period between 12 and 17 appears to be the warmest in each analysed buoy. The lowest SSTs are constantly the those observed between 00 and 11, with a preference for the 6-11 period. Hours between 18 and 23 exhibit anomalies near zero.

### 3.5 Relative Humidity

Figure 3.33 illustrates the different relative humidity time series acquired by the three selected buoys and the associated smoothing lines.

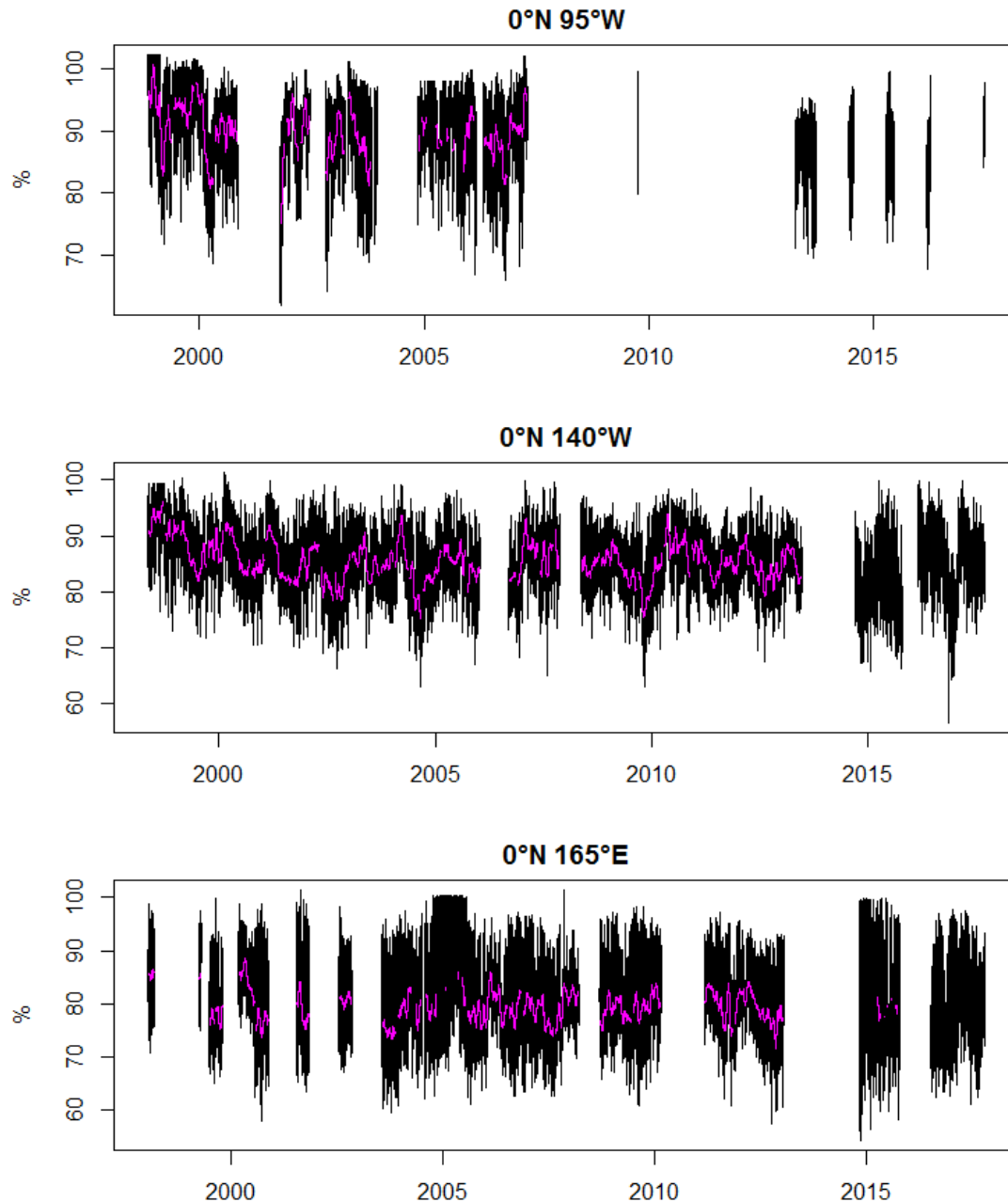


Figure 3.33: Relative humidity time series retrieved by buoys 0°N 95°W, 0°N 140°W and 0°N 165°E. The violet lines represent smoothed values.

0°N 95°W exhibits the presence of long periods of missing data. The time series is characterised by a high variability, with minimum values reaching almost 60% and maximum values outranging 100%. The associated smoothing line oscillates between 80% and 100%; moreover, it does not reveal the presence of a clear periodic oscillation. 0°N 140°W displays longer recorded time periods. Time series values range between 65% and 100%, while smoothed values oscillate between 75% and 95%. The examined time period

shows the occurrence of more humid conditions at the beginning of the record. Then, the yearly averaged humidity decreases until 2002. From 2003, averaged values become more stable throughout the years even though a clear yearly periodicity is not present. 0°N 140°W exhibits the presence of an annual cycle. 0°N 165°E shows the greatest high frequency variation in local humidity conditions among the three buoys. Measures range from less than 60% to 100% while averaged values fluctuate around 80%. Moreover, data do not exhibit the presence of a strong yearly seasonal cycle.

The diurnal cycle of relative humidity is firstly assessed through a spectral analysis. Then, the daily anomalies are displayed to allow the characterisation of the diurnal cycle.

Table 3.13 reports the periods and total number of measurements utilised in the spectral analysis.

Table 3.13: Periods and total number of measurements utilised in the spectral analysis.

	Period start	Period end	Number of total measurements
0°N 95°W	2006-04-23 02:30:00	2006-10-23 02:20:00	26352
0°N 140°W	2008-05-10 12:30:00	2008-11-09 05:10:00	26352
0°N 165°E	2006-07-12 02:30:00	2007-01-11 02:20:00	26352

Figure 3.34 illustrates the smoothed periodogram of the analysed time series.

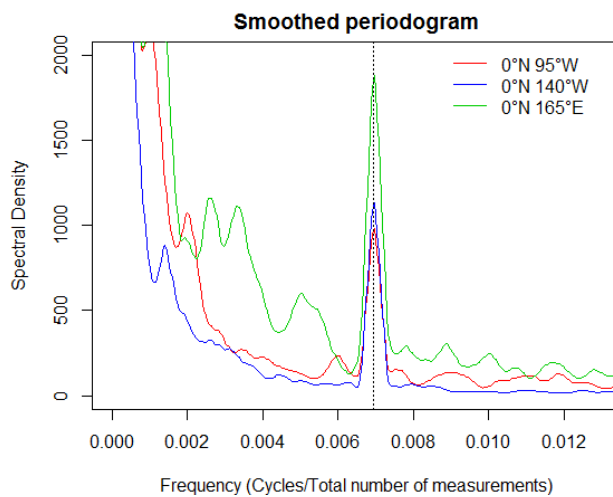
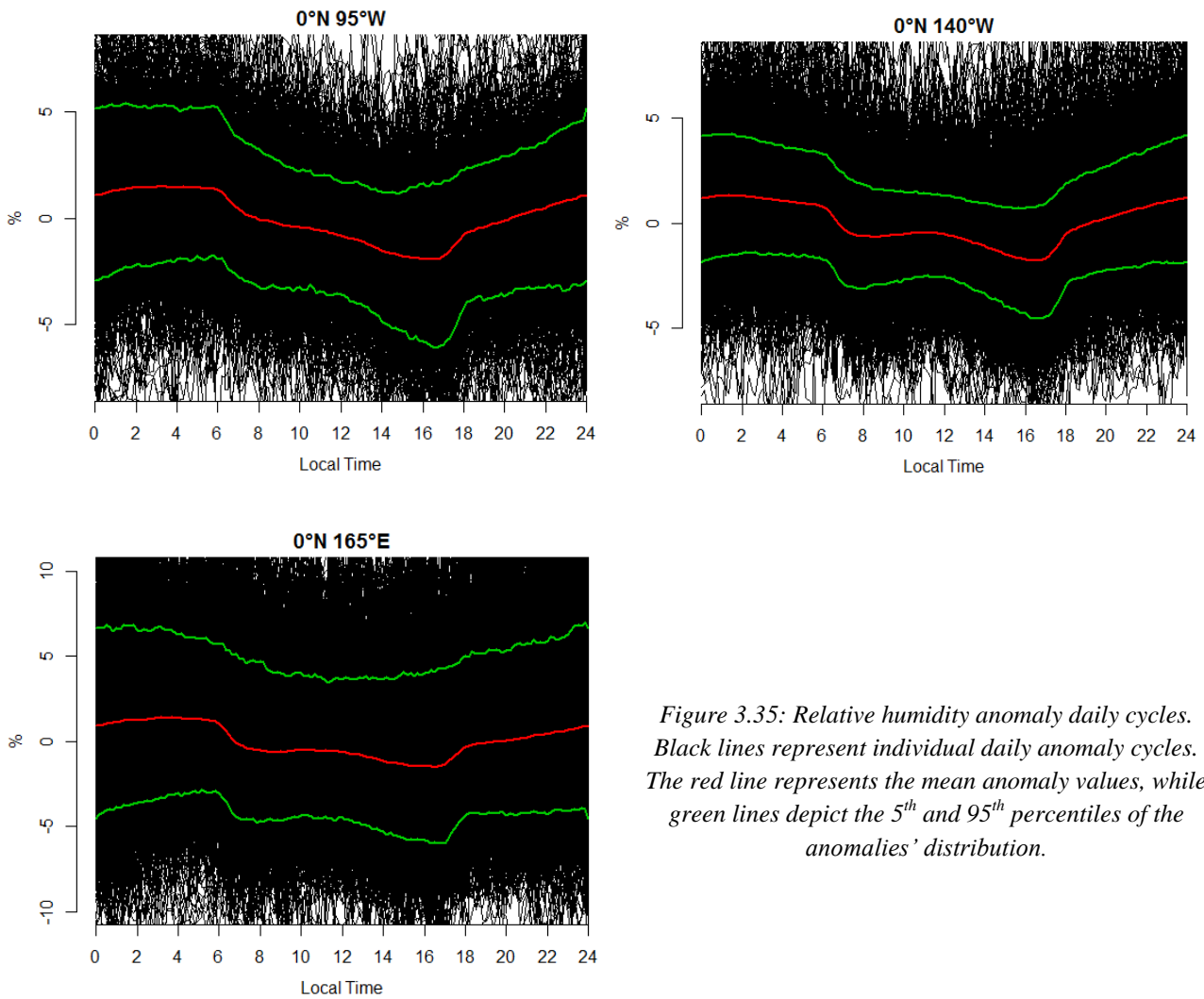


Figure 3.34: Smoothed periodogram of relative humidity measurements for each buoy. The vertical black dashed line identifies the daily frequency.

Each one of the three buoys exhibits a clear peak in power spectrum indicating the presence of daily periodicity within the data.

Figure 3.35 illustrates the relative humidity diurnal cycle for the three buoys.



*Figure 3.35: Relative humidity anomaly daily cycles. Black lines represent individual daily anomaly cycles. The red line represents the mean anomaly values, while green lines depict the 5<sup>th</sup> and 95<sup>th</sup> percentiles of the anomalies' distribution.*

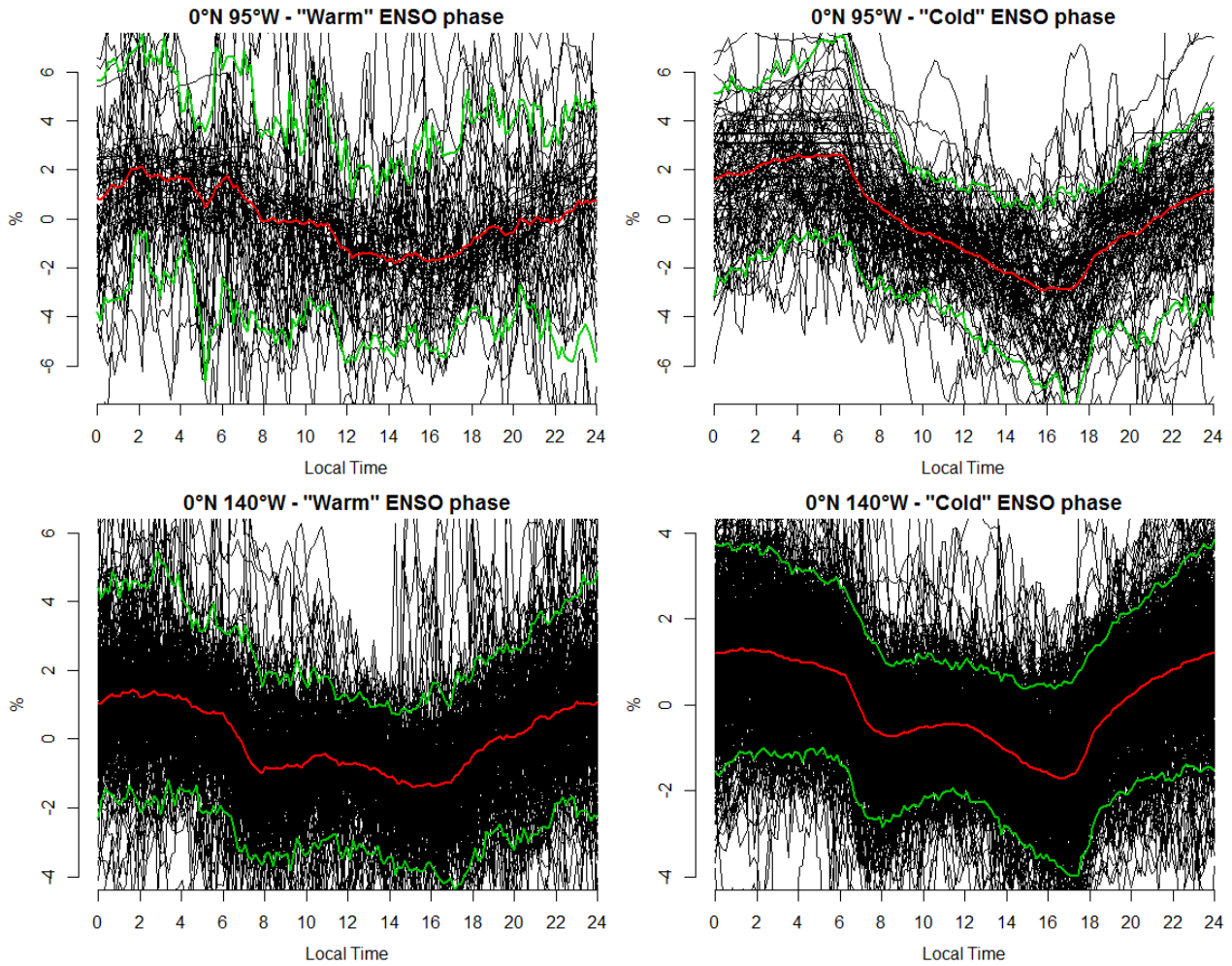
The shape and timing of the three mean diurnal cycles is consistent among the three buoys. Humidity remains approximately stable during night and maxima values occur between 03 and 04. After sunrise, humidity decreases rapidly until before 08 when it starts to decrease more gently and reaches minimum values around 16-17. Between 17 and 18, humidity increases sharply. Finally, after sunset, humidity increases slowly until midnight. Between 00 and 06, the relative humidity remains approximately constant in 0°N 95°W and 0°N 165°E, whereas it slightly decreases in 0°N 140°W. The amplitudes of the three mean diurnal cycles are 3.4 % for 0°N 95°W, 3.1 % for 0°N 140°W and 2.9 % for 0°N 165°E. Percentiles display a general consistence with the mean values. The difference between percentiles and mean values is the greatest for 0°N 165°E and the lowest for 0°N 140°W.

The diurnal cycle of relative humidity is examined under the occurrence of the warm and cold ENSO phases. Table 3.14 reports the number of recorded days observed during the El Niño and La Niña events.

Table 3.14: Number of relative humidity recorded days observed during the cold and warm phases of ENSO.

	0°N 95°W	0°N 140°W	0°N 165°E
Cold ENSO phase	96	495	292
Warm ENSO phase	27	137	183

Figure 3.36 illustrates the different diurnal cycles according to the warm and cold phases of ENSO.



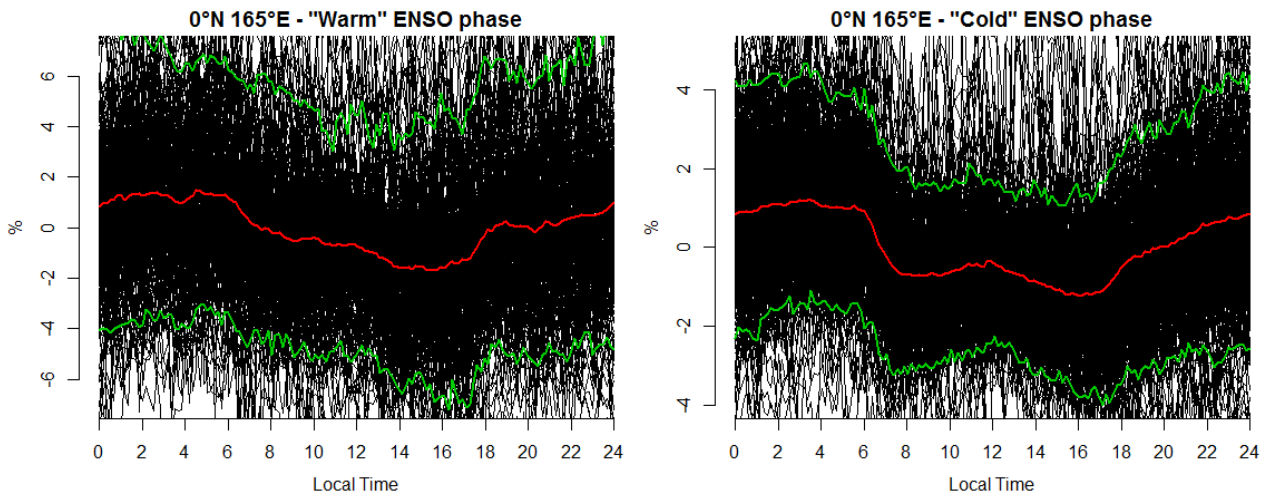


Figure 3.36: Relative humidity anomaly daily cycles for the three buoys retrieved during warm and cold phases of ENSO.

Black lines represent individual daily evolutions. The red line represents the mean values (i.e. the daily mean cycle) while green lines depict the 5th and 95th percentiles of the distribution.

Figure 3.36 indicates that ENSO's warm and cold phases maintain mostly unaltered the shape of the mean diurnal cycle.  $0^{\circ}\text{N } 95^{\circ}\text{W}$  features a diurnal humidity amplitude of 4.8 % during El Niño and 5.5 % during La Niña. The amplitudes of the diurnal cycles observed by  $0^{\circ}\text{N } 140^{\circ}\text{W}$  measure 3.1 % for the warm phase and 3 % for the cold phase. The diurnal cycles at  $0^{\circ}\text{N } 165^{\circ}\text{W}$  have an amplitude of 3.3 % during El Niño and 2.4 % during La Niña. Overall, the relative humidity cycle is similar amongst the two phases.

Table 3.15 presents the number of days selected according to the differentiation based on wind speed and insolation.

Table 3.15: Number of days lying in wind and insolation classes according to the different buoys.

	<b><math>0^{\circ}\text{N } 95^{\circ}\text{W}</math></b>	<b><math>0^{\circ}\text{N } 140^{\circ}\text{W}</math></b>	<b><math>0^{\circ}\text{N } 165^{\circ}\text{E}</math></b>
<i>Cloudy days</i>	271	908	742
<i>Sunny days</i>	272	910	743
<i>Wind class 1</i>	122	32	216
<i>Wind class 3</i>	126	1598	360

Figure 3.37 illustrates the relative humidity diurnal cycles under different insolation conditions (cloudy and sunny) for all the buoys.

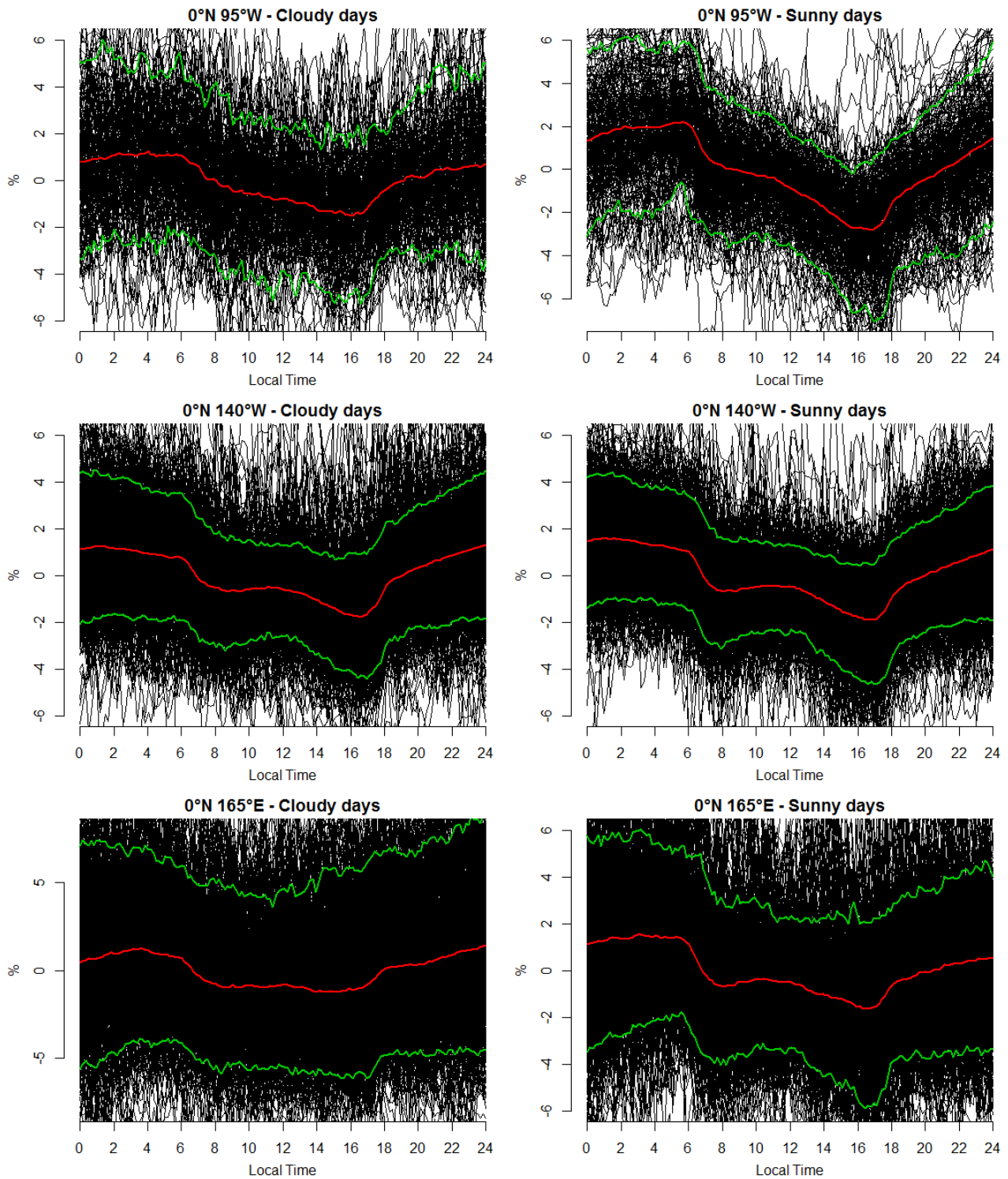


Figure 3.37: Daily cycle of relative humidity anomaly observed during cloudy and sunny days in the three buoys. Black lines represent individual daily evolutions. The red line represents the mean values (i.e. the daily mean cycle) while green lines depict the 5th and 95th percentiles of the distribution.

The relative humidity mean diurnal cycle is not significantly different during *sunny* and *cloudy* days. *Sunny days* show the presence of a prominent double minima period around 06-08 and 16-18. Instead, *cloudy days* feature more limited minimum peaks in the mid-morning and mid-afternoon. The amplitude of the mean cycle under *sunny days* measures 5 % for 0°N 95°W, 3.5 % for 0°N 140°W and 3.2 % for 0°N 165°E. Instead, *cloudy days* exhibit an amplitude of 2.7 % for 0°N 95°W, 3.1 % for 0°N 140°W and 2.7 % for 0°N

165°E. The diurnal evolution of the percentiles indicate the lowest variance for 0°N 140°W and the highest one for 0°N 165°E.

Figure 3.38 illustrates the relative humidity diurnal cycles according to different wind conditions for each buoy.

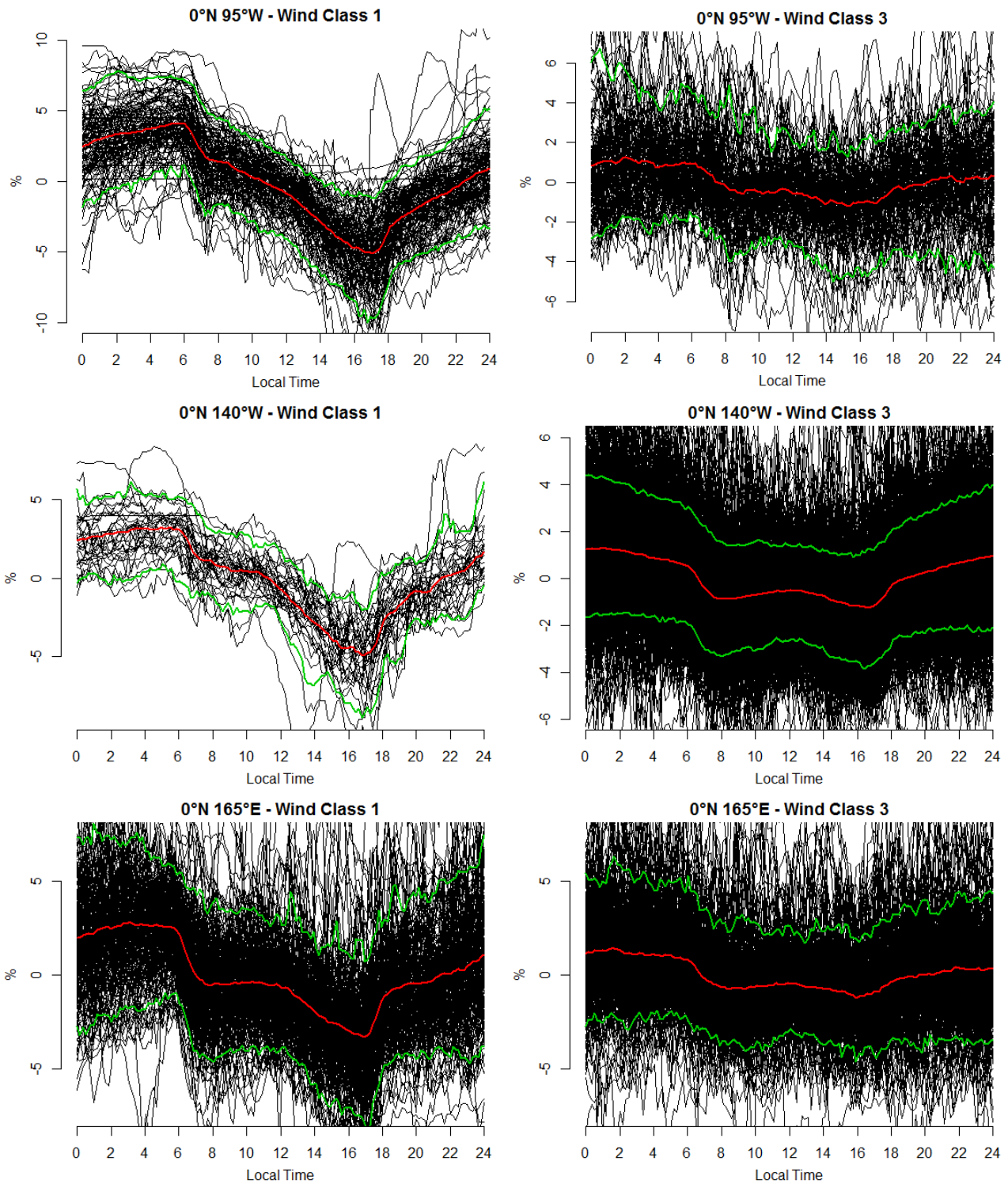


Figure 3.38: Daily cycle of relative humidity anomaly according to different wind conditions (weak and strong winds) for the three buoys.

Black lines represent individual daily evolutions. The red line represents the mean values (i.e. the daily mean cycle) while green lines depict the 5th and 95th percentiles of the distribution.

Wind conditions influence the amplitude of the mean diurnal cycles. Under conditions of weak winds, the range of the mean diurnal cycles is 9.2 % for 0°N 95°W, 8.2 % for 0°N 140°W and 6.1 % for 0°N 165°E. Instead, the occurrence of strong winds are associated to lower amplitudes: 2.5 % for 0°N 95°W, 2.5 % for 0°N 140°W and 2.6 % for 0°N 165°E. Moreover, weak winds feature lower values during the mid-afternoon minimum period than strong winds.

The assessment of the diurnal cycle variation is conducted as delineated in sub-section 2.2.5. Figure 3.39 shows the coupled evolution of the relative humidity smoothed hourly anomalies along with the relative humidity smoothed time series.

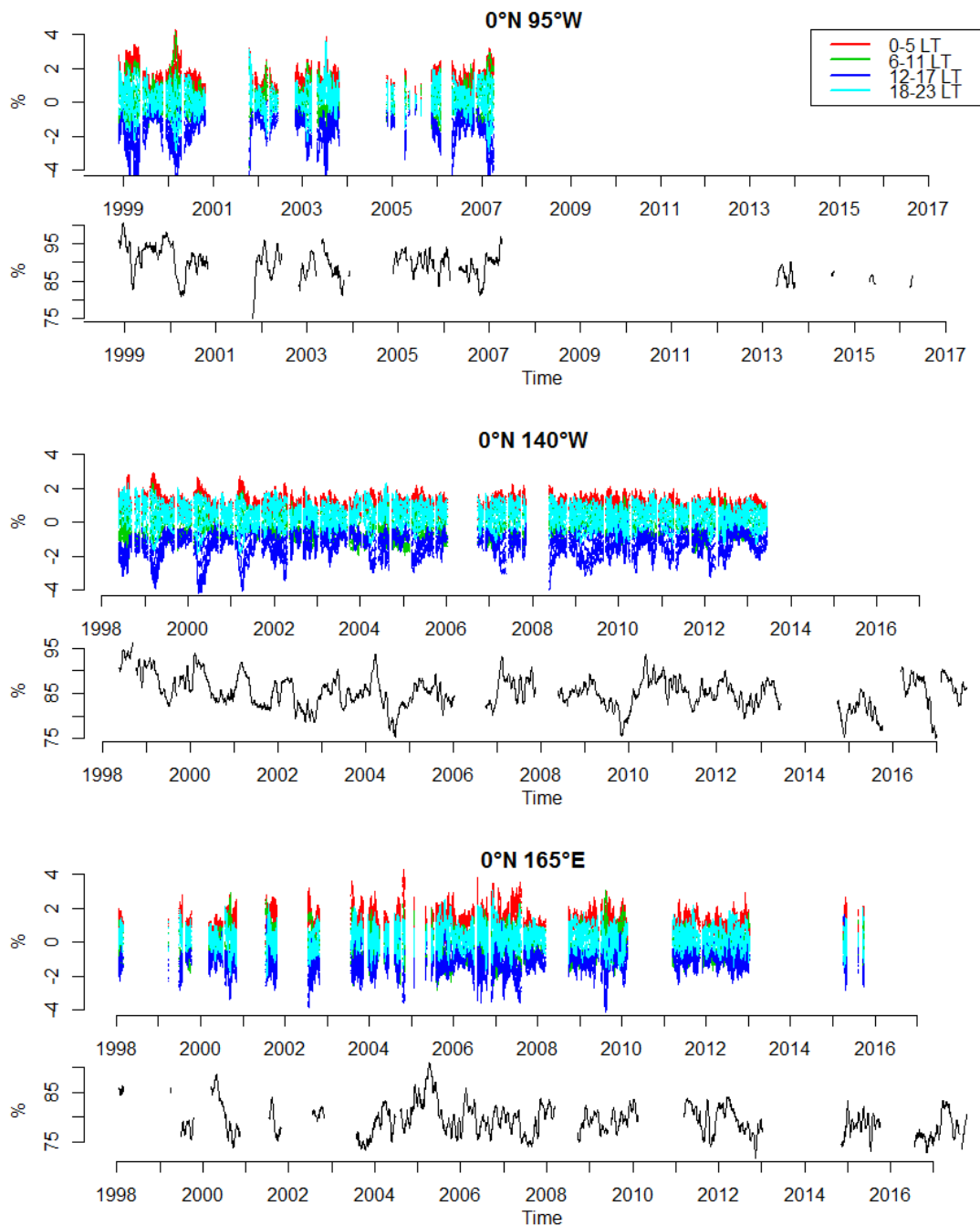


Figure 3.39: Variations of the diurnal cycle of relative humidity over the long period.

For each buoy, the upper panel reports the hourly relative humidity anomaly time series, while the lower panel shows the relative humidity absolute smoothed values.

Red lines correspond to hours between 00 and 05. Green lines correspond to hours between 06 and 11. Blue lines correspond to hours between 12 and 17. Light blue lines correspond to hours between 18 and 23.

The hourly time series show the same behaviour for all the buoys. Hours between 00 and 05 exhibit the highest values of the day. On the other hand, the lowest values are regularly present in the 12-17 period. Intermediate values ranging around zero are constantly found between 18 and 23. 0°N 95°W features the highest mean diurnal variation with averaged values ranging between -4 % and 4 %. The other two buoys display a more limited variation. A noteworthy characteristic is the higher variation assumed by hourly smoothed values during regimes of high relative humidity. This aspect is present in 0°N 95°W, while 0°N 140°W shows this behaviour only at the beginning of the time series. Differently, 0°N 165°E does not clearly exhibit the same tendency. Periods of high variation of the hourly anomaly are characterised by another peculiarity present in all buoys: maxima and minima anomalies reach asymmetric values indicating a tendency for deeper negative values. For instance, 0°N 95°W displays periods of large variation featuring maxima anomalies reaching +4 %, while negative anomalies outbound -4 %. Accordingly, periods of high variation at 0°N 140°W are characterised by maxima anomalies between +2 and +3 %, while negative anomalies reach -4 %. A similar behaviour can be detected also for 0°N 165°E.

### 3.6 Sea Level Pressure

Figure 3.36 illustrates the different sea level pressure (SLP) time series acquired by the three selected buoys.

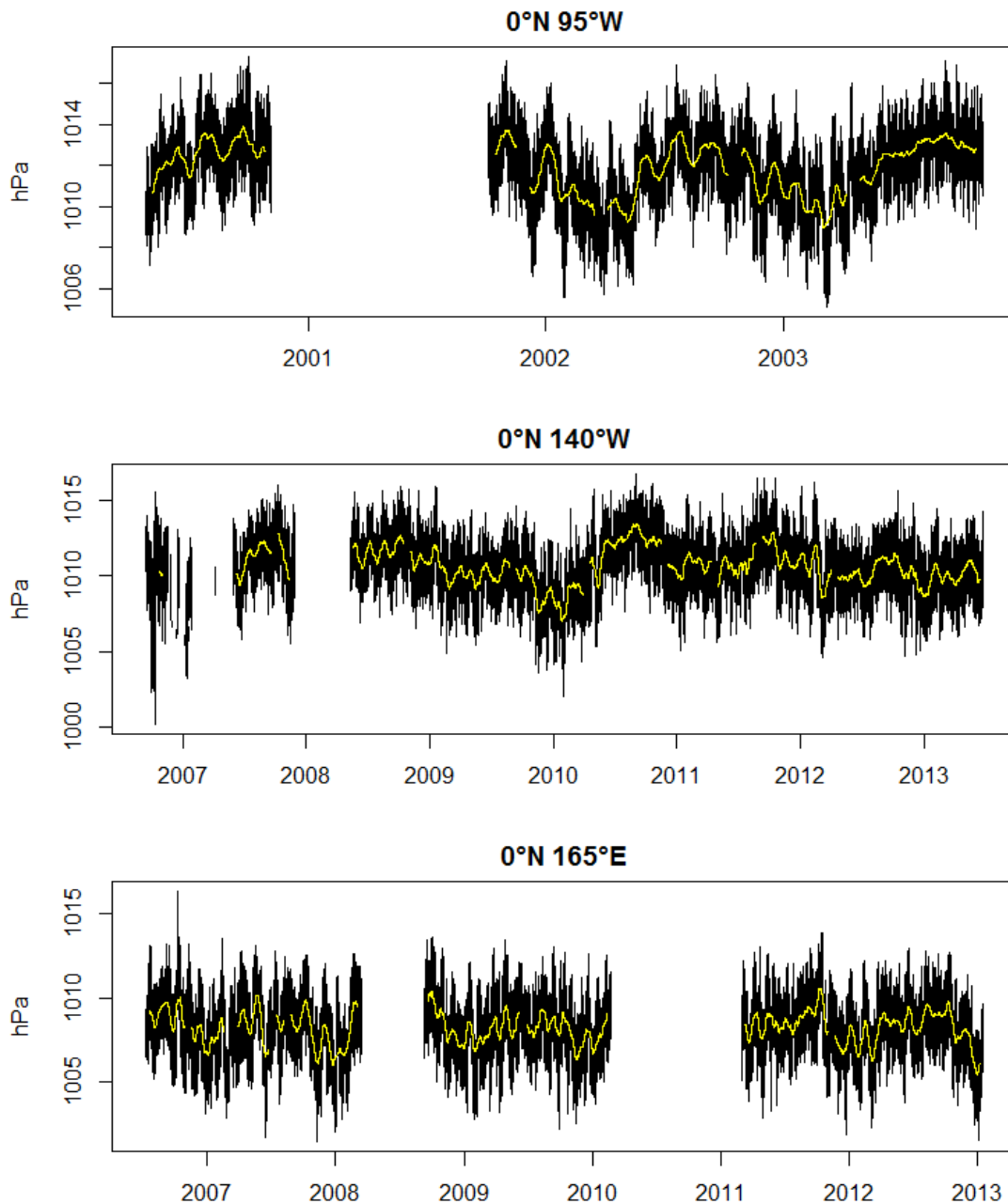


Figure 3.36: Sea level pressure time series retrieved by buoys  $0^{\circ}\text{N } 95^{\circ}\text{W}$ ,  $0^{\circ}\text{N } 140^{\circ}\text{W}$  and  $0^{\circ}\text{N } 165^{\circ}\text{E}$ . The yellow lines represent smoothed values.

$0^{\circ}\text{N } 95^{\circ}\text{W}$  is characterised by a yearly seasonal cycle composed by maxima values encountered in late boreal summer and minima values occurring in boreal spring. The seasonal cycle variation measures approximately 4 hPa. Sea level pressure values span around the smoothing line within the  $\pm 1.5$  hPa interval.  $0^{\circ}\text{N } 140^{\circ}\text{W}$  features a yearly seasonal cycle characterised by a similar timing and amplitude of  $0^{\circ}\text{N } 95^{\circ}\text{W}$ . Instead,  $0^{\circ}\text{N } 165^{\circ}\text{E}$  does not exhibit the presence of a strong yearly periodicity. The three smoothing lines highlight the

presence of a monthly cycle in the sea level pressure time series. Figure 3.36 shows a progressive westward shift of the SLP time series toward lower values. Indeed, smoothed values at 0°N 95°W varies between 1010 and 1014 hPa, around 1010 hPa for 0°N 140°W and between 1006 and 1010 hPa for 0°N 165°E.

The assessment of the SLP diurnal cycle considers the spectral analysis and the characterisation of the diurnal evolutions. Table 3.16 reports the periods and total number of measurements utilised in the spectral analysis.

Table 3.16: Periods and total number of measurements utilised in the spectral analysis.

	Period start	Period end	Total number of measurements
<b>0°N 95°W</b>	2002-10-18 18:00:00	2003-10-18 16:00:00	26197
<b>0°N 140°W</b>	2008-05-10 04:30:00	2008-11-08 04:00:00	26197
<b>0°N 165°E</b>	2011-02-28 21:00:00	2011-08-29 23:00:00	26197

Figure 3.37 illustrates the smoothed periodograms computed for the three time series.

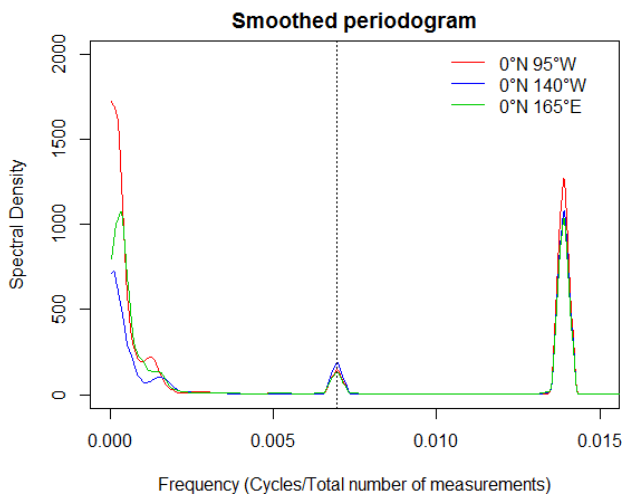


Figure 3.38: Smoothed periodogram of sea level pressure measurements for each buoy. The vertical black dashed line identifies the daily frequency.

The SLP smoothed periodograms reveal the presence of two peaks indicating the existence of a diurnal as well as semidiurnal periodicity. However, the semidiurnal component is more prominent compared to the diurnal component.

Figure 3.38 displays the SLP diurnal cycle.

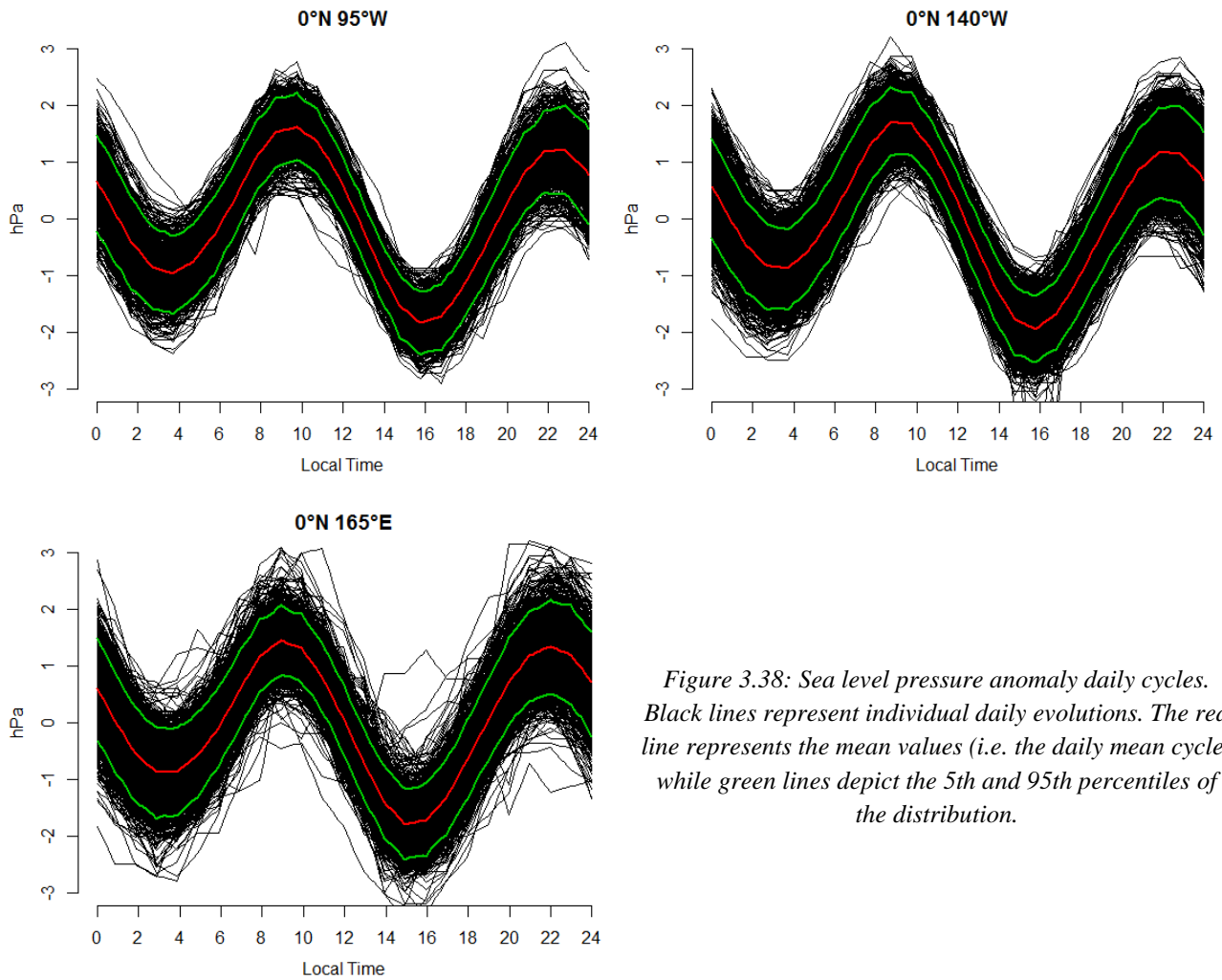


Figure 3.38: Sea level pressure anomaly daily cycles. Black lines represent individual daily evolutions. The red line represents the mean values (i.e. the daily mean cycle) while green lines depict the 5th and 95th percentiles of the distribution.

The SLP diurnal cycle is almost identical among the different buoy. The diurnal cycle resembles a sinusoidal evolution featuring two maxima and two minima. 0°N 95°W, 0°N 140°W and 0°N 165°E exhibit a primary peak around 09-10. The secondary maximum occurs nearby 21-22. The two minima periods occur at 03-04 and 15-16. The variability of the individual SLP daily anomalies is extremely low, which indicates the occurrence of almost the same cycle almost every day of the record. The differences between the primary maximum and minimum points are 3.5 hPa for 0°N 95°W, 3.6 hPa for 0°N 140°W and 3.2 hPa for 0°N 165°E. The difference between the two diurnal maxima and minima measures 0.4 and 0.9 hPa for 0°N 95°W, 0.5 and 1.1 hPa for 0°N 140°W and 0.1 and 0.9 hPa for 0°N 165°E. One notable aspect is the similar height of the two maxima peaks in 0°N 165°E. Overall, data point to the occurrence of the same diurnal cycle throughout the whole study periods.

The SLP diurnal cycle is observed during the occurrence of El Niño and La Niña events. Table 3.17 reports the number of recorded days retrieved during the warm and cold ENSO phases.

Table 3.17: Number of days retrieved during the warm and cold phases of ENSO

	0°N 95°W	0°N 140°W	0°N 165°E
<b>Cold ENSO phase</b>	4	362	211
<b>Warm ENSO phase</b>	0	48	52

Figure 3.39 illustrates the SLP diurnal cycles retrieved during the warm and cold phases of ENSO.

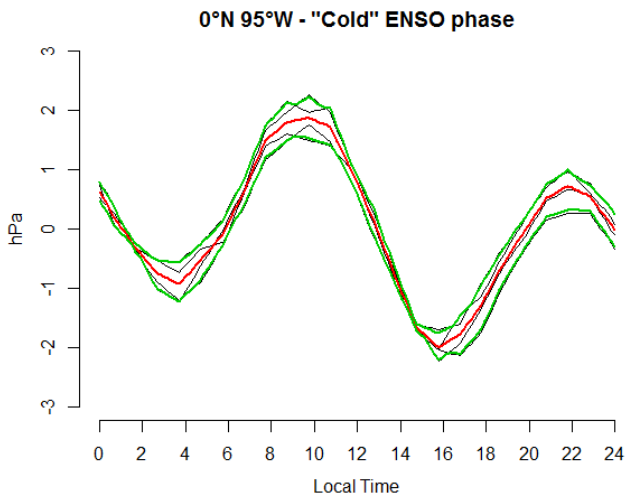
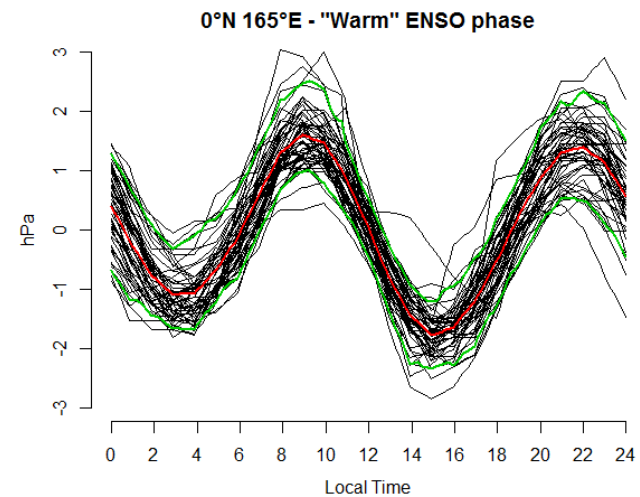
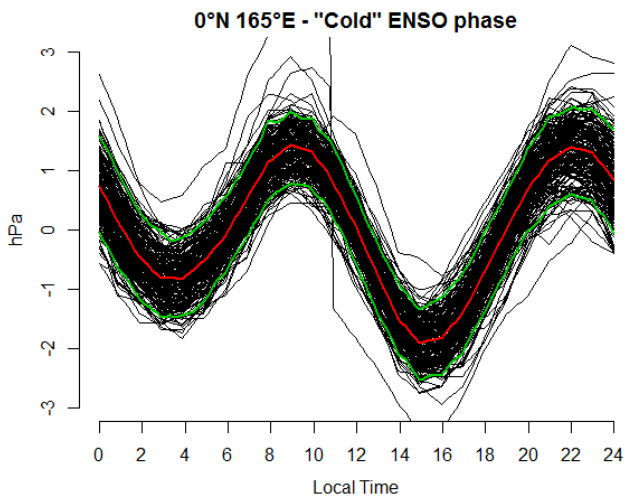
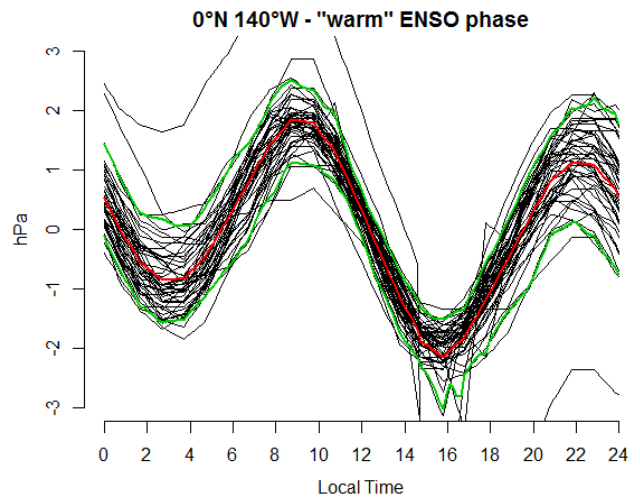
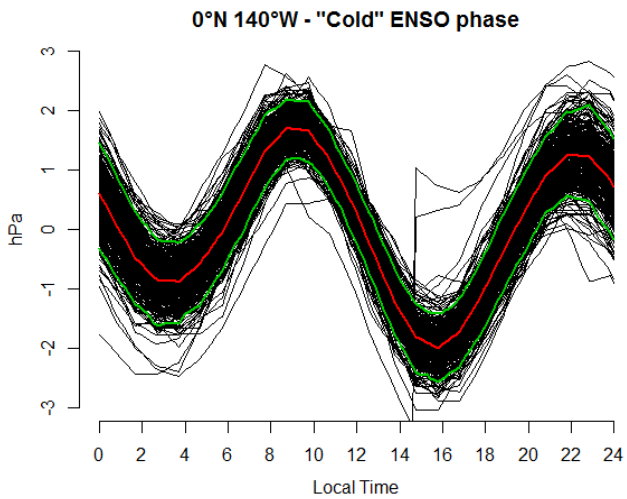


Figure 3.39: Sea level pressure anomaly daily cycles for the three buoys retrieved during warm and cold phases of ENSO.

Black lines represent individual daily evolutions. The red line represents the mean values (i.e. the daily mean cycle) while green lines depict the 5th and 95th percentiles of the distribution.



0°N 95°W features only 4 recorded days during the cold ENSO phase and zero during the warm phase. Therefore, results will not be commented since they are not representative. 0°N 140°W and 0°N 165°E features an almost equal diurnal cycle during both conditions. The diurnal cycles are characterised by two maxima and minima occurring with the same timing as identified previously. During El Niño days, the

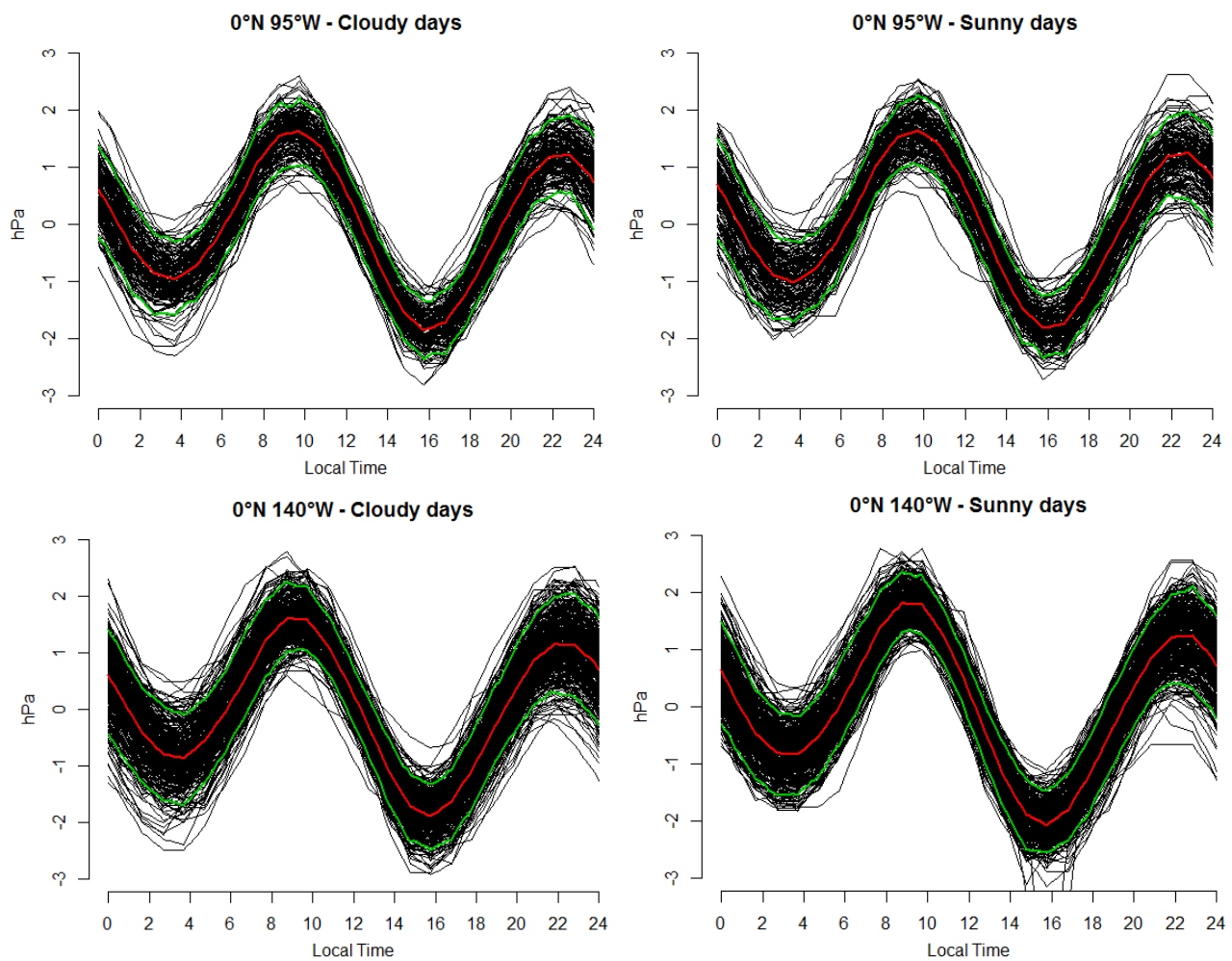
difference between the primary maximum and minimum measures 4 hPa for 0°N 140°W and 3.4 hPa for 0°N 165°E. During La Niña days, the difference measures 3.7 hPa for 0°N 140°W and 3.3 hPa for 0°N 165°E.

The SLP diurnal cycle under different local meteorological conditions is assessed. Table 3.18 reports the number of days divided according to the different meteorological conditions for the three buoys.

Table 3.18: Number of days lying in wind and insolation classes according to the different buoys.

	0°N 95°W	0°N 140°W	0°N 165°E
<i>Cloudy days</i>	170	363	362
<i>Sunny days</i>	170	363	363
<i>Wind class 1</i>	25	11	93
<i>Wind class 3</i>	54	649	235

Figure 3.40 displays the SLP diurnal cycles retrieved during *cloudy* and *sunny* days for each buoy.



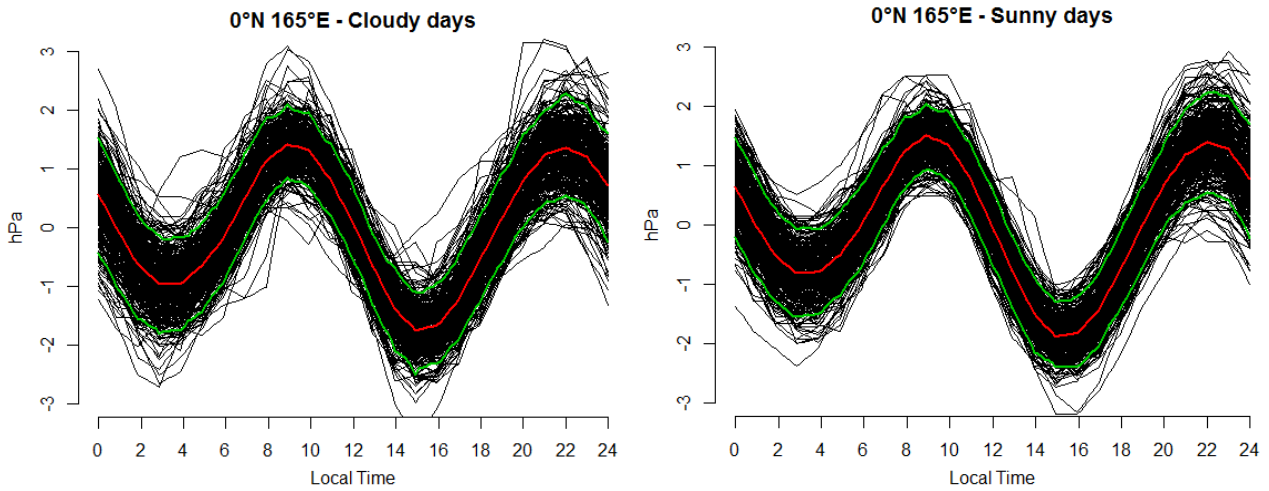
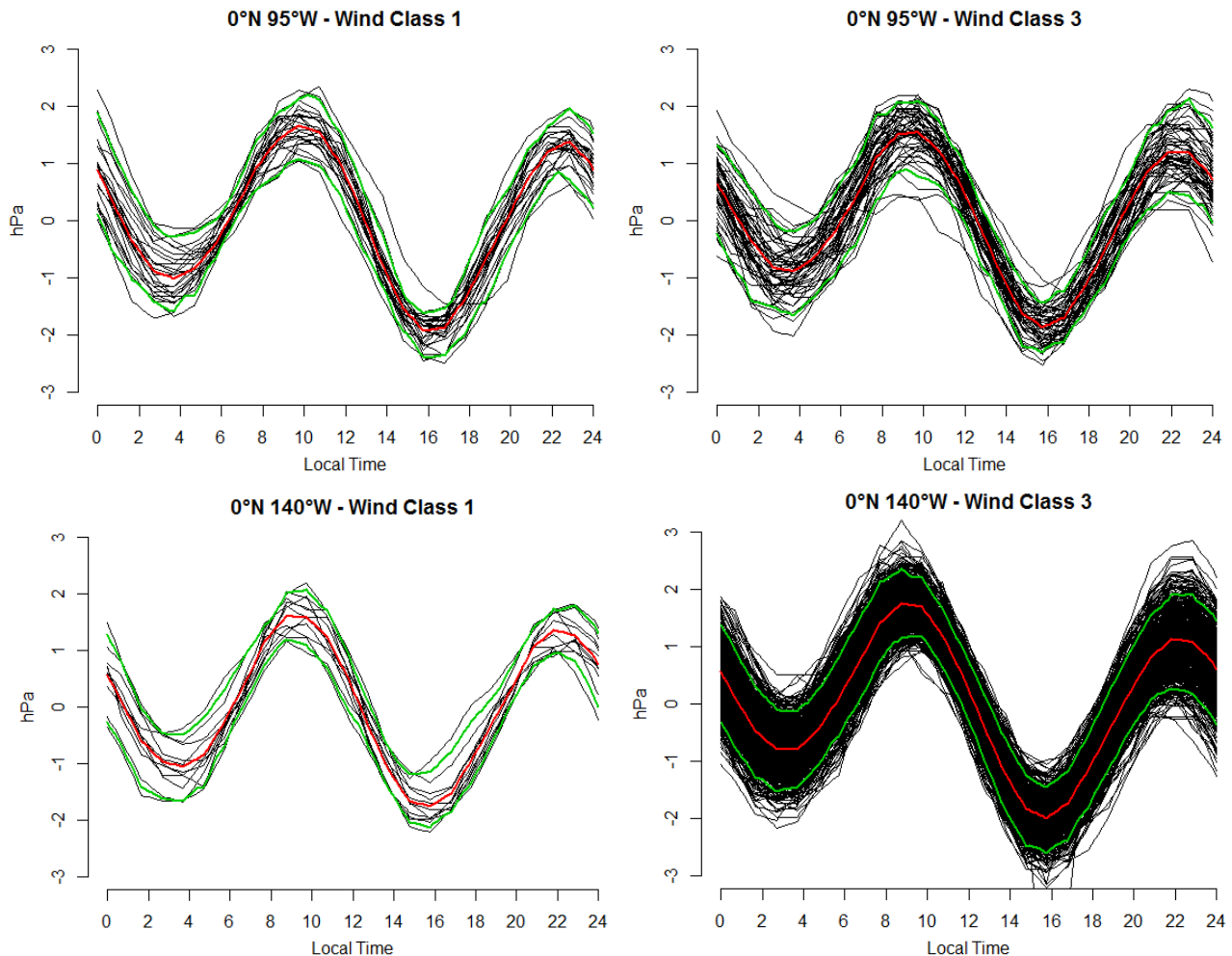


Figure 3.40: Daily cycle of sea level pressure anomaly observed during cloudy and sunny days in the three buoys. Black lines represent individual daily evolutions. The red line represents the mean values (i.e. the daily mean cycle) while green lines depict the 5th and 95th percentiles of the distribution.

The SLP diurnal cycle seems to be unaffected by the different meteorological conditions. During *cloudy days*, the difference between the primary maximum and minimum measures 3.49 hPa for 0°N 95°W, 3.50 hPa for 0°N 140°W and 3.17 hPa for 0°N 165°E. Under *sunny* conditions, the difference between the primary maximum and minimum measures 3.46 for 0°N 95°W, 3.88 for 0°N 140°W and 3.40 for 0°N 165°E. Figure 3.41 represents the different diurnal cycles occurring during weak and strong winds conditions.



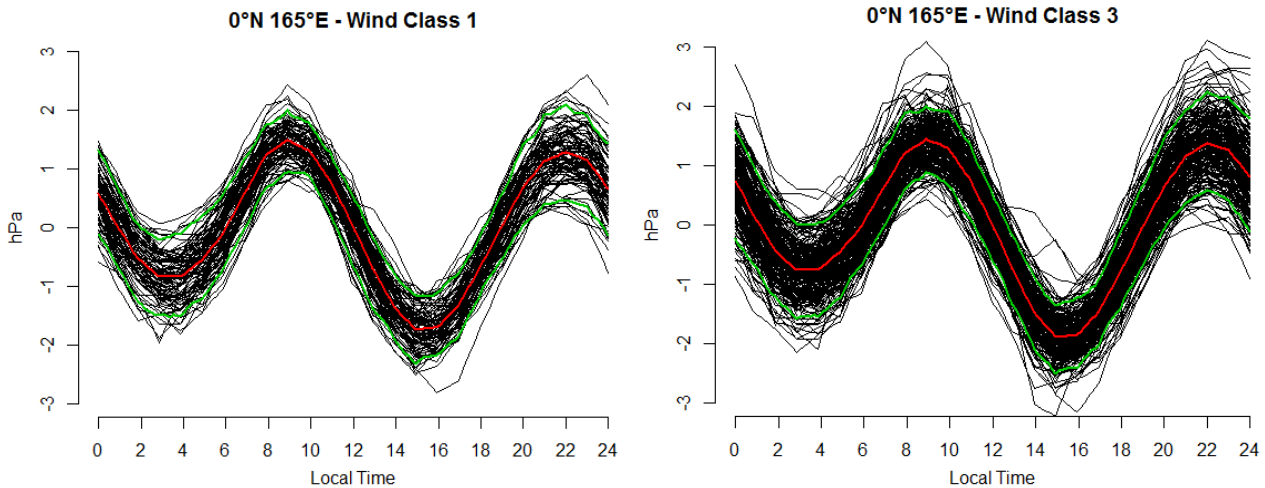
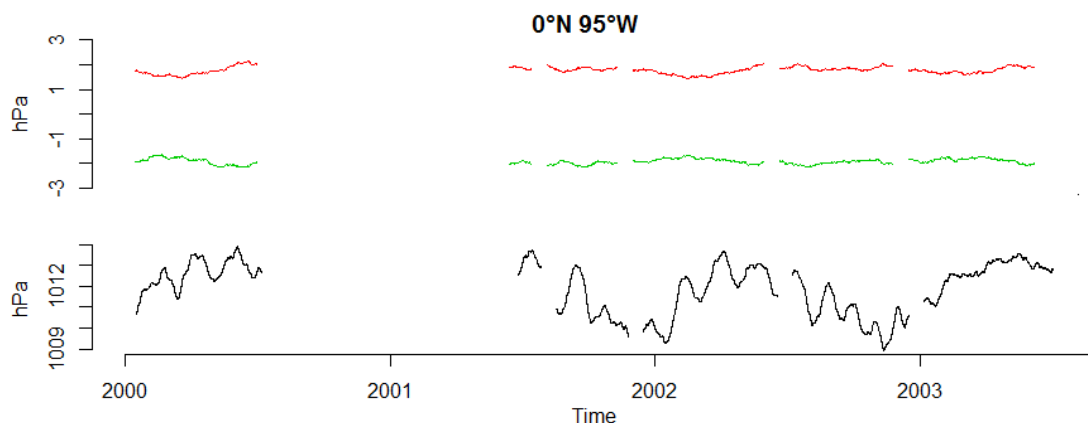


Figure 3.41: Daily cycle of sea level pressure anomaly according to different wind conditions (weak and strong winds) for the three buoys.

Black lines represent individual daily evolutions. The red line represents the mean values (i.e. the daily mean cycle) while green lines depict the 5th and 95th percentiles of the distribution.

The diurnal cycles represented in Figure 3.39 are similar to the ones illustrated in Figure 3.37. Overall, the different wind conditions appear to not affect the SLP diurnal cycle. Days observed in *wind class 1* feature a difference between the primary maximum and minimum measuring 3.58 hPa for 0°N 95°W, 3.35 hPa for 0°N 140°W and 3.23 hPa for 0°N 165°E. Days observed during the occurrence of strong winds have a difference between the primary maximum and minimum measuring 3.41 hPa for 0°N 95°W, 3.76 hPa for 0°N 140°W and 3.33 hPa for 0°N 165°E.

The assessment of the SLP diurnal cycle variation over the long term is performed by considering the average evolution of the daily maximum and minimum. Figure 3.42 shows the evolutions of the SLP daily maximum (red line) and minimum (green line) in time. The lower part of the each graph displays the smoothed original time series.



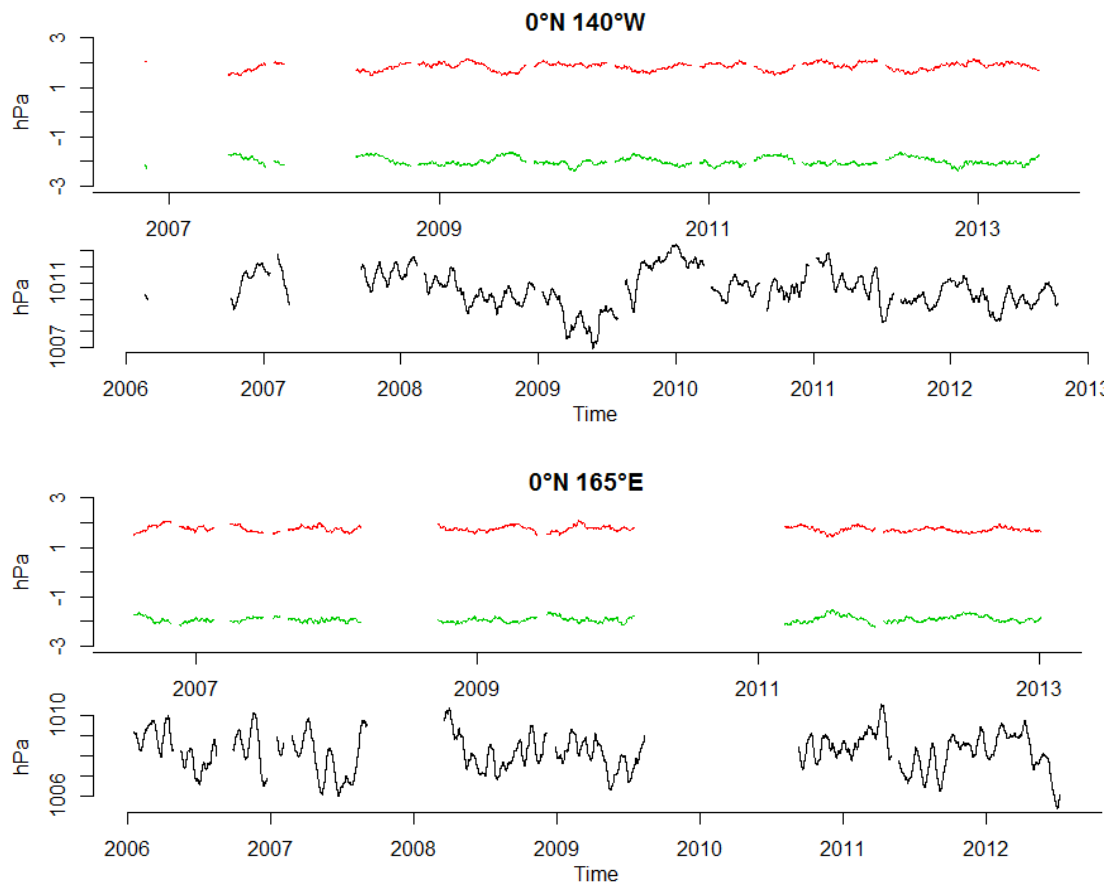


Figure 3.42: Variations of the diurnal cycle of sea level pressure over the long period. For each buoy, the upper panel reports sea level pressure maximum (red line) and minimum (green line) anomaly time series for all the buoys, while the lower panel shows the absolute smoothed values.

The evolutions of the daily maximum and minimum anomalies are almost constant over the entire recorded periods. Hence, the diurnal SLP range is constant in time. The daily SLP maxima and minima do not show any particular relations with the SLP regime.

### 3.7 Wind Direction

Figure 3.43 illustrates the wind direction time series, transformed as explained in Sub-Section 2.2.1.

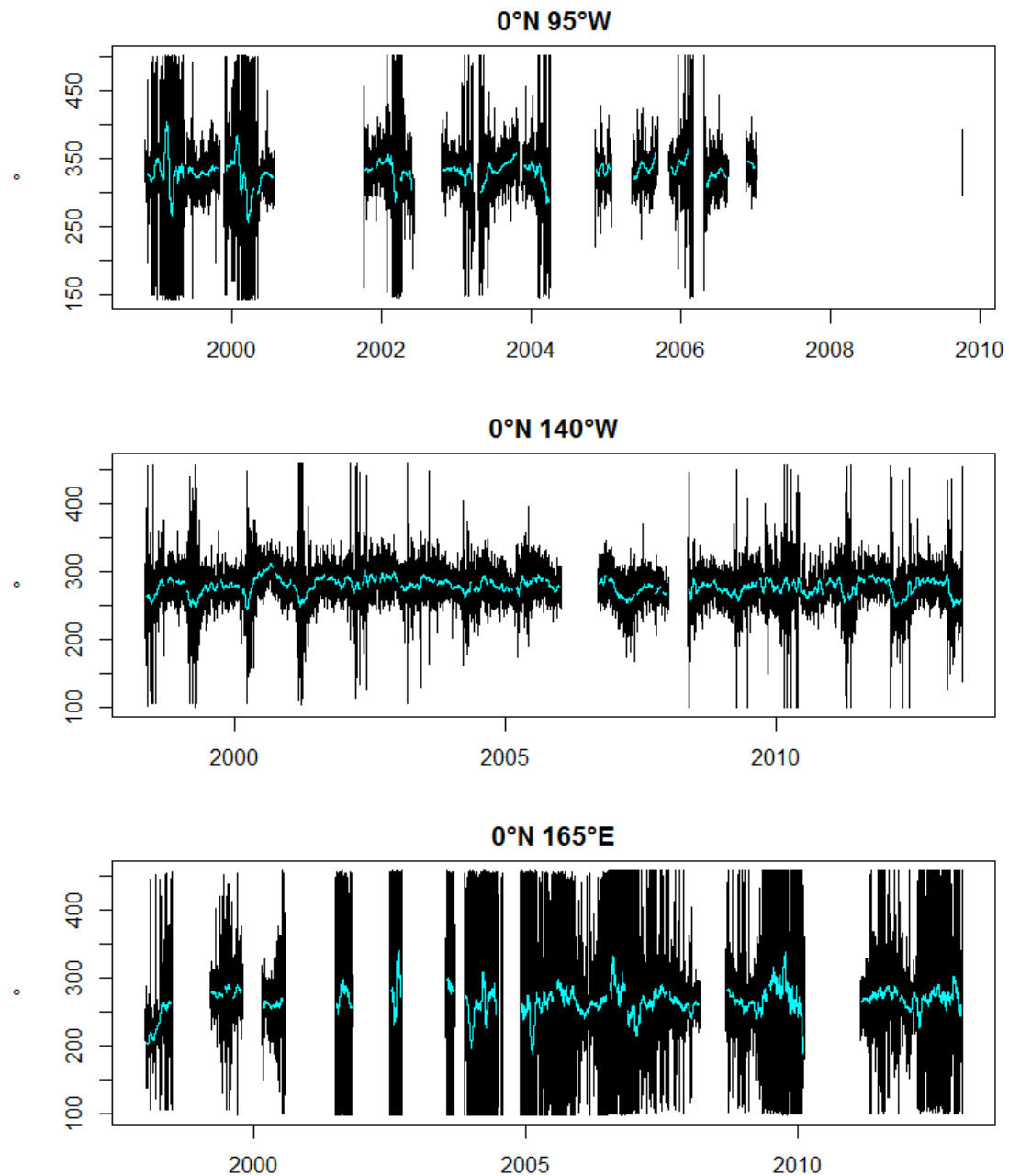


Figure 3.43: Wind direction time series retrieved by buoys  $0^{\circ}\text{N } 95^{\circ}\text{W}$ ,  $0^{\circ}\text{N } 140^{\circ}\text{W}$  and  $0^{\circ}\text{N } 165^{\circ}\text{E}$ . The light blue lines represents smoothed values.

Winds at  $0^{\circ}\text{N } 95^{\circ}\text{W}$  are mainly directed north-westward. Occasionally, the averaged values drops to  $150\text{--}200^{\circ}$ , indicating a temporary wind direction toward south and south-east. This change in wind direction regime seems to occur during boreal winter, after the beginning of the year. However, recorded periods feature a very high variability.  $0^{\circ}\text{N } 140^{\circ}\text{W}$  is characterised by the presence of winds constantly directed north-westward. Averaged values range from  $250^{\circ}$  to  $300^{\circ}$  and the variation is contained during almost the

whole time period. As previously noted for 0°N 95°W, the averaged wind direction changes periodically during boreal winter to lower values indicating a westward flow. During the occurrence of these events, the variation in wind direction values increases. 0°N 165°E features the highest wind direction variation. The whole period is not characterised by constant smoothed values, which varies between 270° and 100°. However, smoothed values show a preference for angles near 250° i.e. almost westward.

The wind direction data are examined to detect the presence of a diurnal signal and determine the wind direction diurnal cycle. Table 3.19 reports the periods and number of days utilised in the frequency analysis.

Table 3.19: Periods and total number of measurements utilised in the frequency analysis.

	Period start	Period end	Number of days
<b>0°N 95°W</b>	2002-10-18 20:30:00	2003-03-26 09:00:00	22828
<b>0°N 140°W</b>	2008-05-10 12:10:00	2008-10-16 00:40:00	22828
<b>0°N 165°E</b>	2011-03-01 03:00:00	2011-08-06 15:30:00	22828

Figure 3.44 illustrates the smoothed periodograms of the analysed time series.

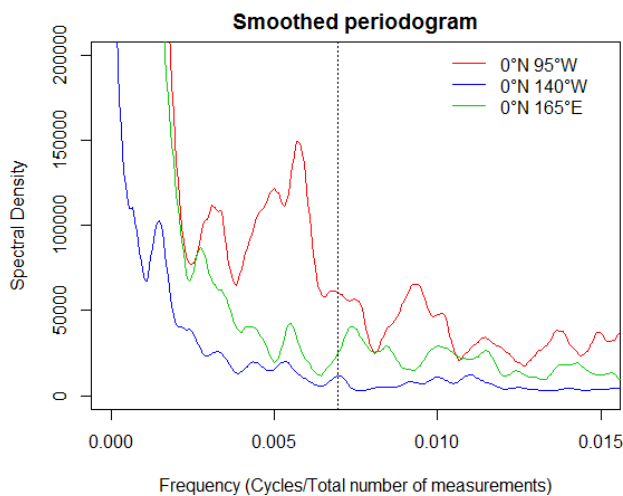


Figure 3.44: Smoothed periodogram of wind direction measurements for each buoy. The vertical black dashed line identifies the daily frequency.

The smoothed periodogram reveals the absence of a clear diurnal periodicity in each of the three wind direction time series.

Figure 3.45 illustrates the wind direction diurnal cycles for the three different buoys. The daily cycles are computed utilising the wind direction data transformed as described in sub-section 2.2.1.

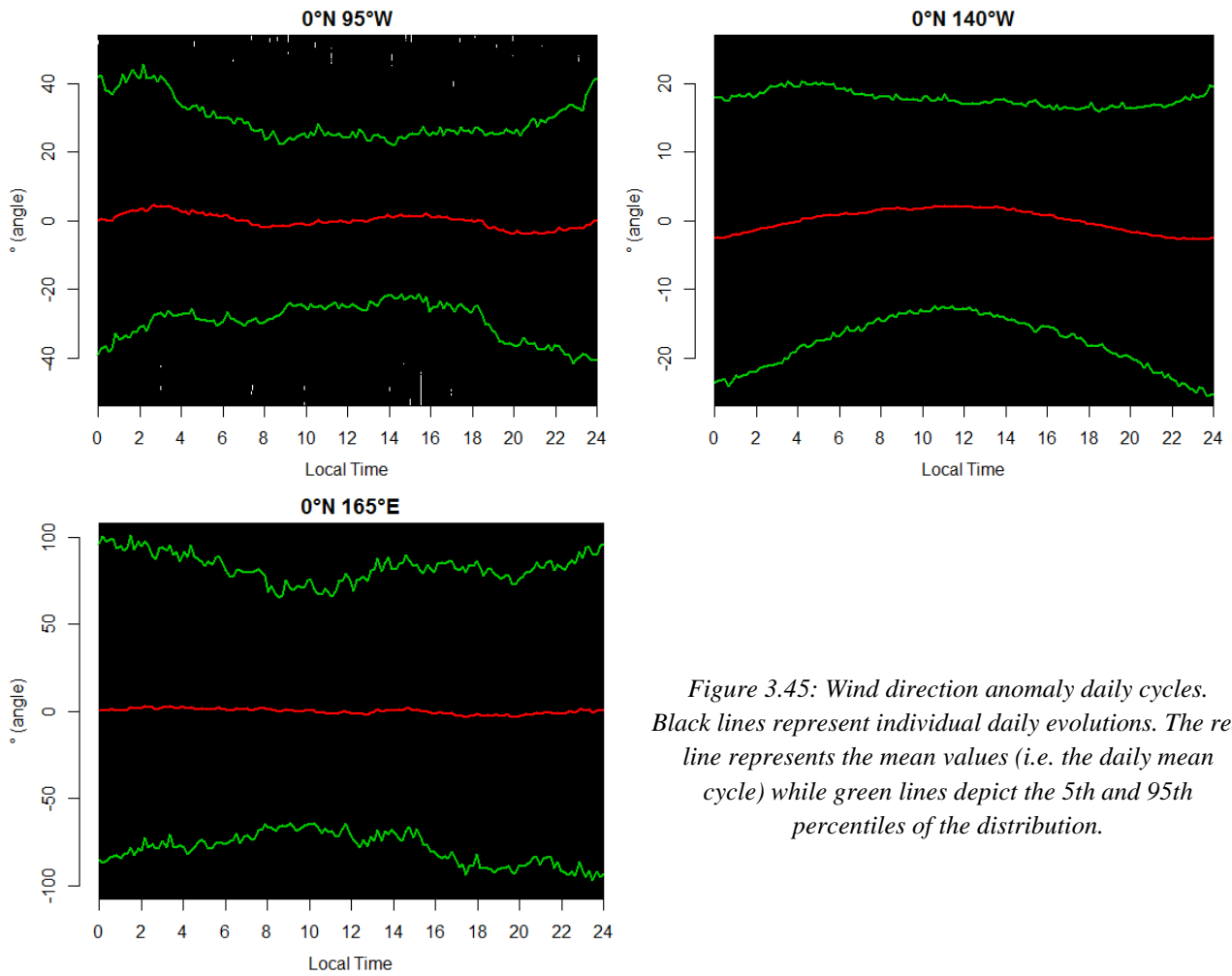


Figure 3.45: Wind direction anomaly daily cycles. Black lines represent individual daily evolutions. The red line represents the mean values (i.e. the daily mean cycle) while green lines depict the 5th and 95th percentiles of the distribution.

The wind direction anomaly cycles are characterised by a very high variability. The shape of the mean diurnal cycles are not clearly distinguishable. Thus, the mean diurnal anomaly variation is evaluated through Figures 3.46 and 3.47, reporting the mean diurnal cycles and the density of the different directions observed by the different buoys.

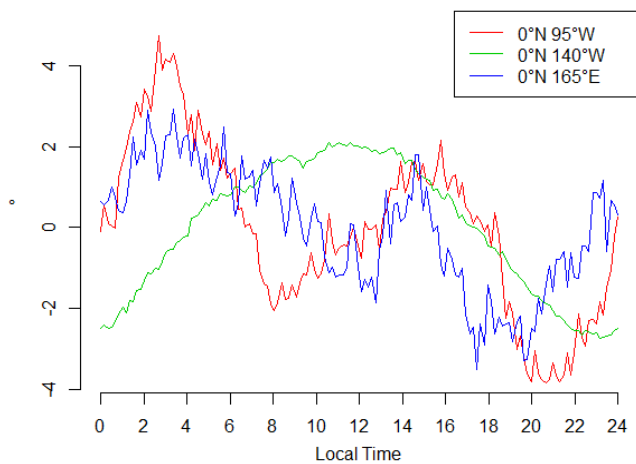


Figure 3.46: Mean diurnal cycles of wind direction for all the buoys.

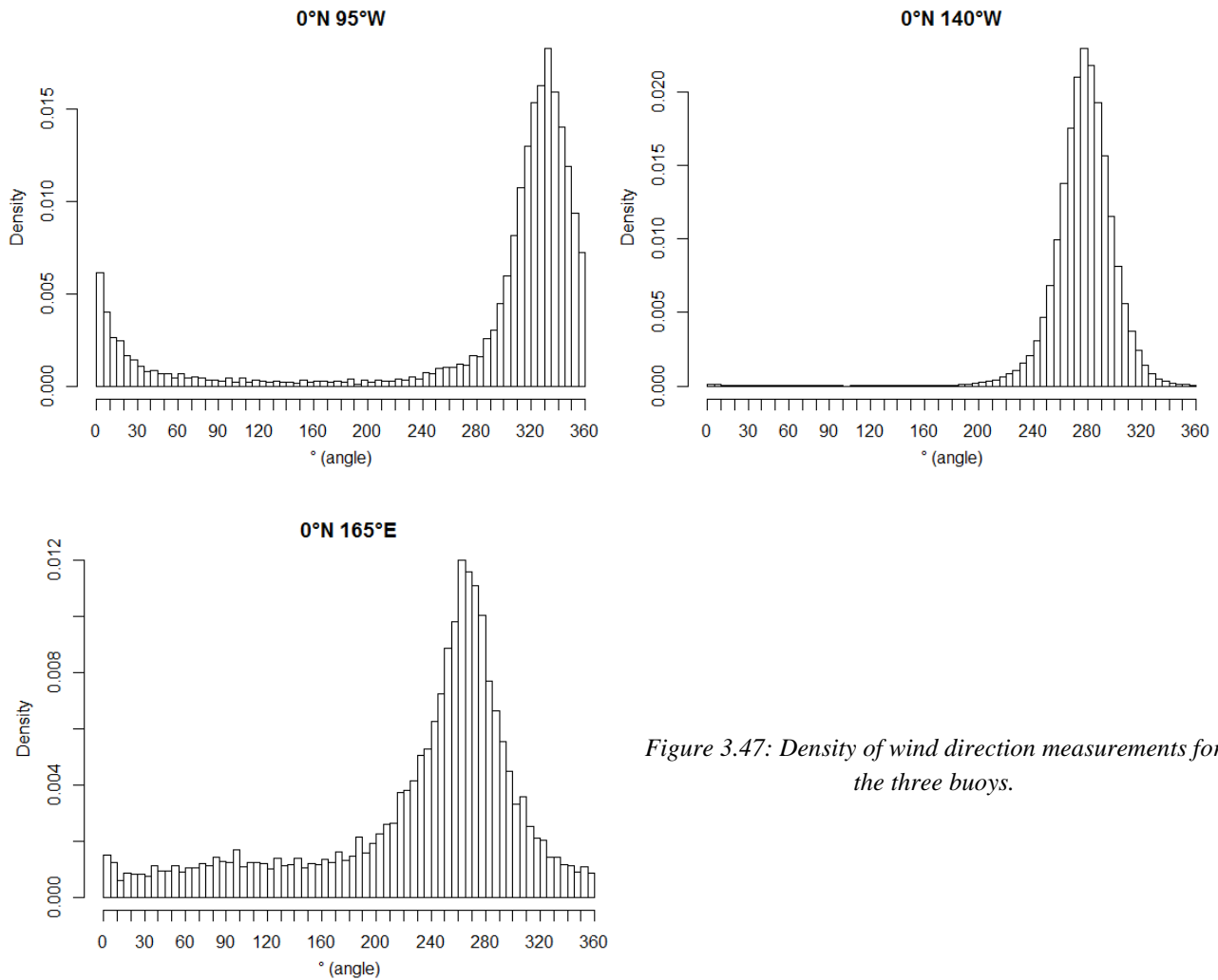


Figure 3.47: Density of wind direction measurements for the three buoys.

Wind direction measurements displayed in Figure 3.47 reveal that each buoy is characterised by the predominance of a clear wind direction. In particular, the wind blows more frequently toward north in 0°N 95°W and westward in 0°N 140°W and 0°N 165°E. The wind direction shifts from north to west as we move westward along the equator. As represented in Figure 3.46, the mean diurnal cycle shape of 0°N 95°W is characterised by two peaks encountered near 09 and 20, while minima values are found between 02 and 04. The mean diurnal cycle of 0°N 140°W features a peak at 09 and another at 22. 0°N 165°E presents one peak before noon. The amplitudes of the wind direction mean diurnal cycles measure 20° for 0°N 95°W, 5° for 0°N 140°W and 8° for 0°N 165°E. Overall, data indicate that wind does not considerably change its direction in the three analysed buoys.

The wind direction diurnal cycle is assessed during the occurrence of El Niño and La Niña events. Table 3.20 reports the number of recorded days observed during the warm and cold phases of ENSO.

Table 3.20: Number of wind direction recorded days observed during the cold and warm phases of ENSO.

	0°N 95°W	0°N 140°W	0°N 165°E
<b>Cold ENSO phase</b>	91	524	274
<b>Warm ENSO phase</b>	31	118	224

Figure 3.48 illustrates the wind direction diurnal cycles retrieved during the two phases of ENSO.

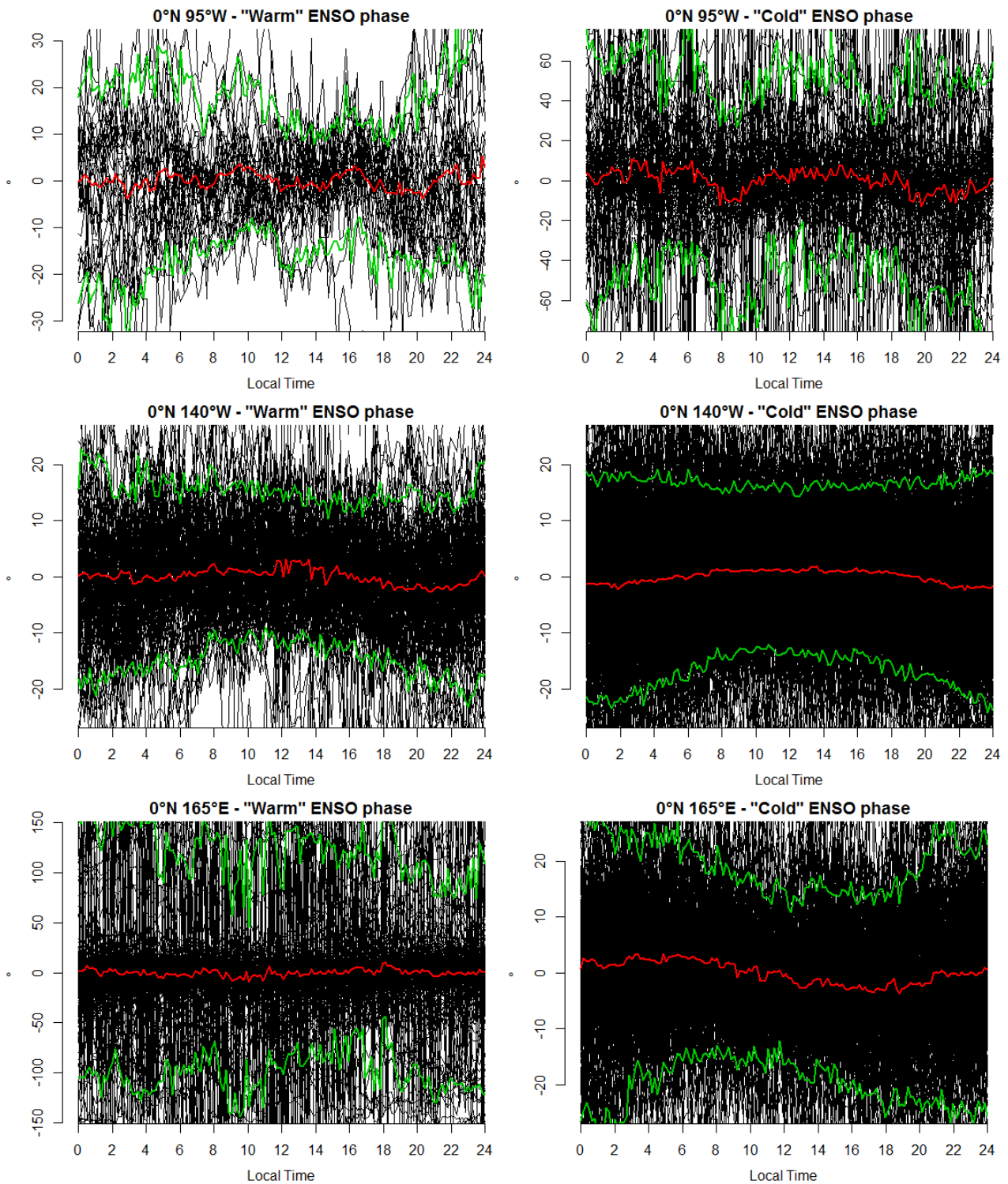


Figure 3.48: Wind direction anomaly daily cycles for the three buoys retrieved during warm and cold phases of ENSO. Black lines represent individual daily anomaly cycles. The red line represents the mean anomaly values, while green lines depict the 5<sup>th</sup> and 95<sup>th</sup> percentiles of the anomalies' distribution.

Wind direction measurements present a high degree of variability. El Niño conditions are linked to a steady diurnal cycle and the absence of a notable amplitude. Instead, La Niña conditions feature similar mean

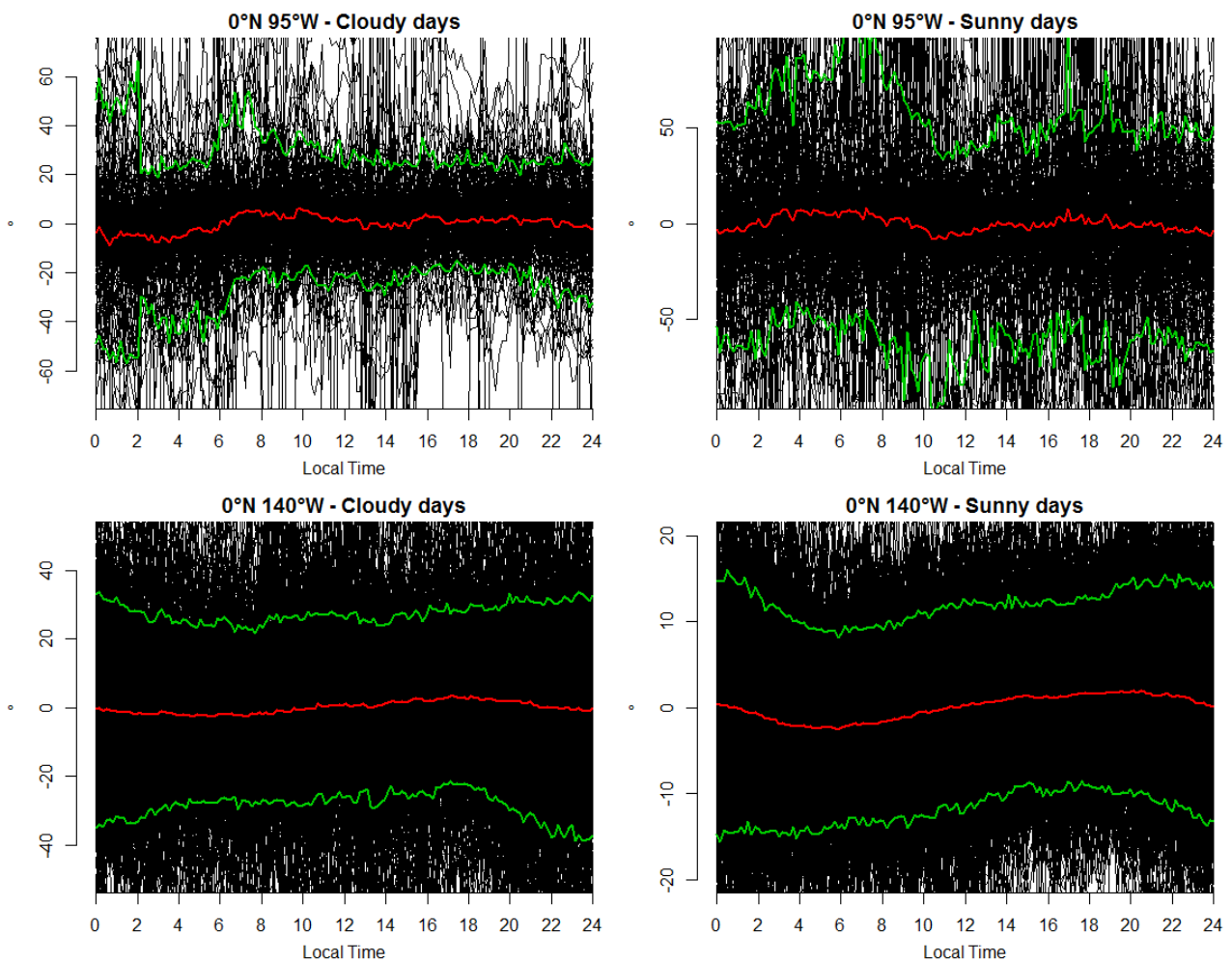
diurnal cycles compared to the ones computed using the entire datasets. However, all the graphs point to the occurrence of an almost steady diurnal cycle for each buoy in each period.

Table 3.21 summarises the number of days divided according to the distinction based on meteorological conditions.

Table 3.21: Number of days lying in each class for all the buoys.

	0°N 95°W	0°N 140°W	0°N 165°E
<i>Cloudy days</i>	275	1018	734
<i>Sunny days</i>	276	1019	734
<i>Wind class 1</i>	143	36	190
<i>Wind class 3</i>	133	1610	388

Figure 3.49 illustrates the wind direction diurnal cycles under cloudy and sunny conditions.



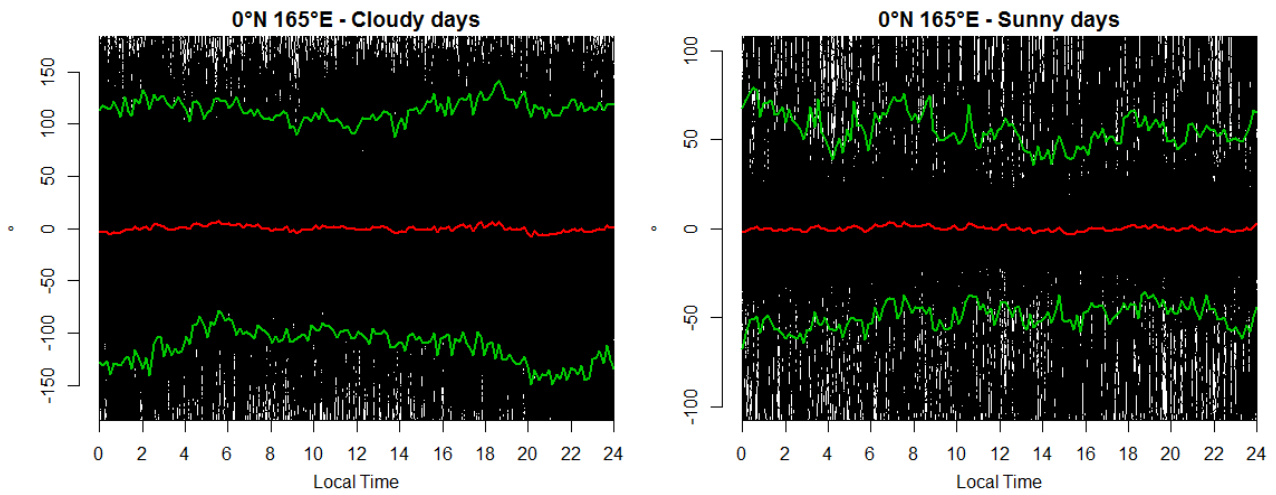
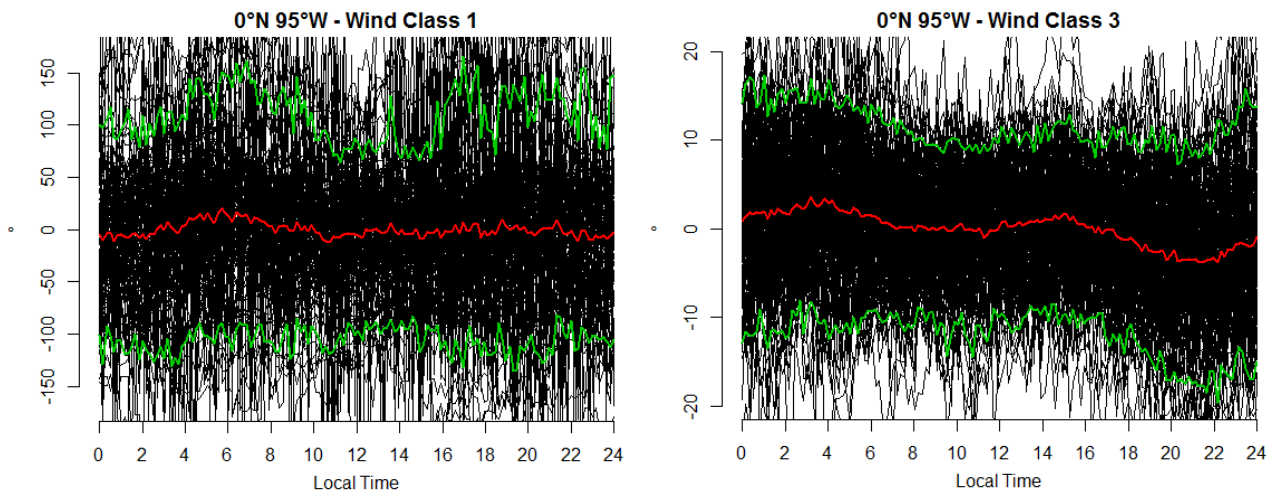


Figure 4.49: Daily cycle of wind direction anomaly observed during cloudy and sunny days in the three buoys. Black lines represent individual daily evolutions. The red line represents the mean values (i.e. the daily mean cycle) while green lines depict the 5th and 95th percentiles of the distribution.

The *sunny* and *cloudy* conditions feature almost equal cycles amongst the different buoys, hence pointing out the lack of a strong influence of different insolation conditions on the wind direction diurnal cycle. Compared to Figure 4.44, the shape and timing of the mean diurnal cycles of the different buoys are not remarkably influenced.

Figure 4.50 shows the wind direction diurnal cycle during strong and weak winds.



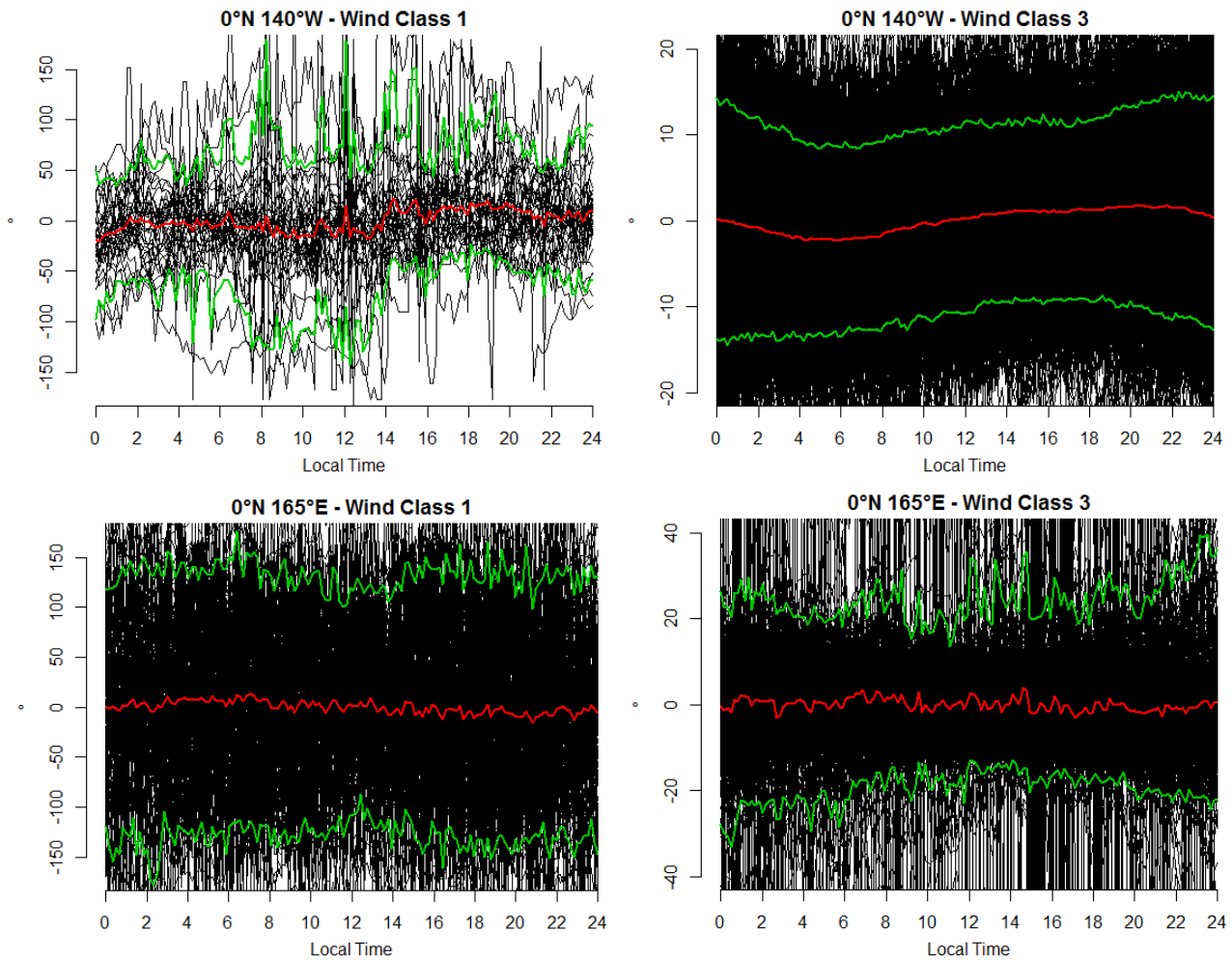
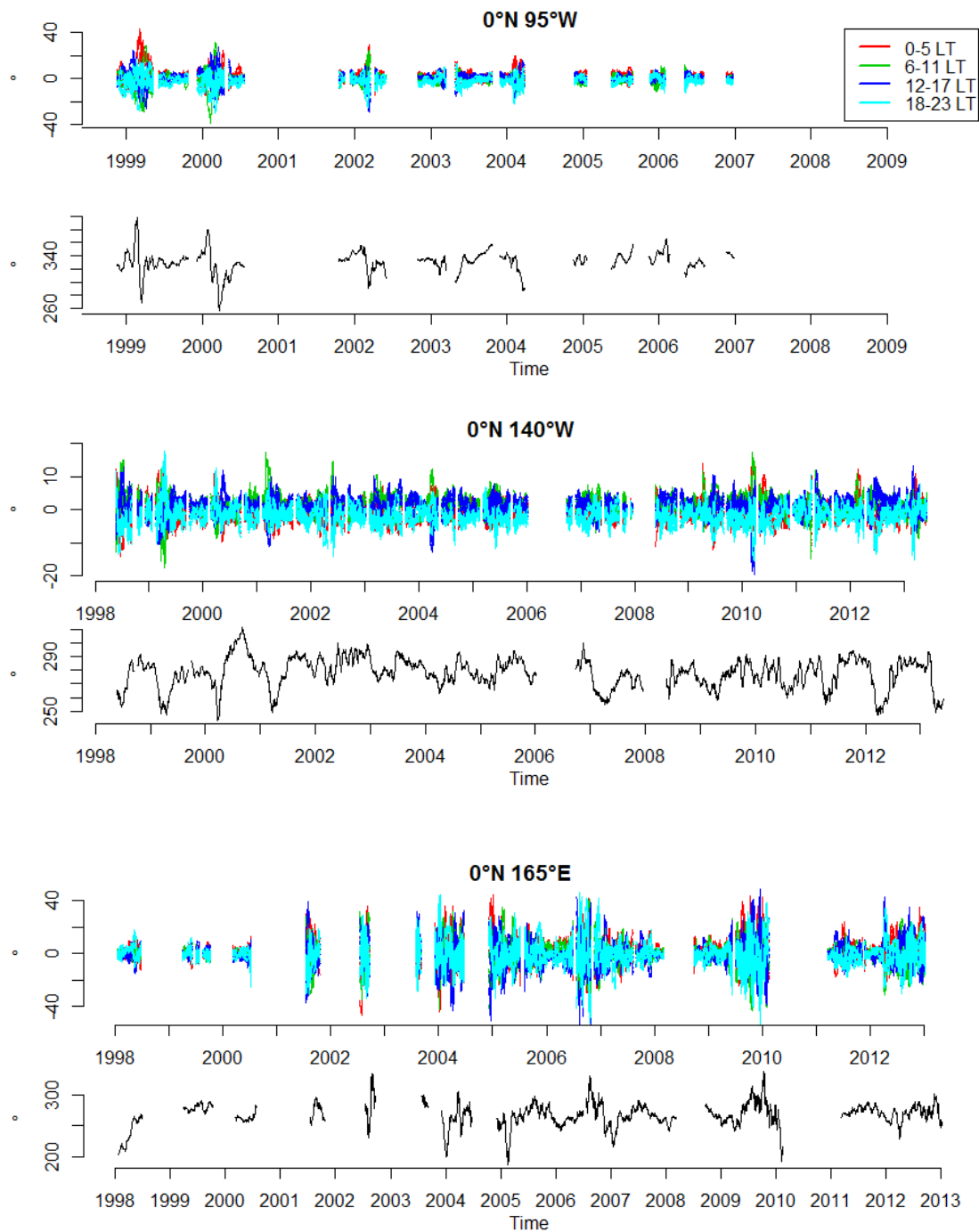


Figure 3.51: Daily cycle of wind direction anomaly according to different wind conditions (weak and strong winds) for the three buoys.

Black lines represent individual daily evolutions. The red line represents the mean values (i.e. the daily mean cycle) while green lines depict the 5<sup>th</sup> and 95<sup>th</sup> percentiles of the distribution.

Strong wind conditions lead to the occurrence of similar diurnal cycles compared to those calculated using the whole time series. Instead, weak wind conditions are linked to the occurrence of a mean diurnal cycle fluctuating around zero i.e. the daily mean. A notable aspect involves the intra-diurnal variation of the anomalies. In fact, the 5<sup>th</sup> and 95<sup>th</sup> percentiles outbound the  $\pm 100^\circ$  interval in *wind class 1* whereas, in *wind class 3*, the differences between the mean and percentiles differ less than  $20^\circ$ . Thus, weak winds feature a more variable direction, while strong winds are linked to much less variable directions.

The assessment of the diurnal cycle variation is conducted as delineated in sub-section 2.2.5. Figure 3.51 shows the evolution of the wind direction smoothed hourly anomalies and relative humidity smoothed time series for each buoy.



*Figure 3.51: Variations of the diurnal cycle of relative humidity over the long period.*

*For each buoy, the upper panel reports the hourly relative humidity anomaly time series, while the lower panel shows the relative humidity absolute smoothed values.*

*Red lines correspond to hours between 00 and 05. Green lines correspond to hours between 06 and 11. Blue lines correspond to hours between 12 and 17. Light blue lines correspond to hours between 18 and 23.*

The hourly time series vary differently among the three buoys. As highlighted previously in Figure 3.42, 0°N 140°W presents the lowest variability. As regards all the buoys, hours between 18 and 5 assume often negative anomalies while hours between 06 and 17 are likely associated with the occurrence of positive anomalies. The hourly time series display some peaks, but they do not appear to match any particular wind direction regime. In addition, smoothed anomalies spread between the  $\pm 20^\circ$  interval.

### 3.8 Precipitation

Figure 3.50 illustrates the different precipitation time series acquired by the three selected buoys.

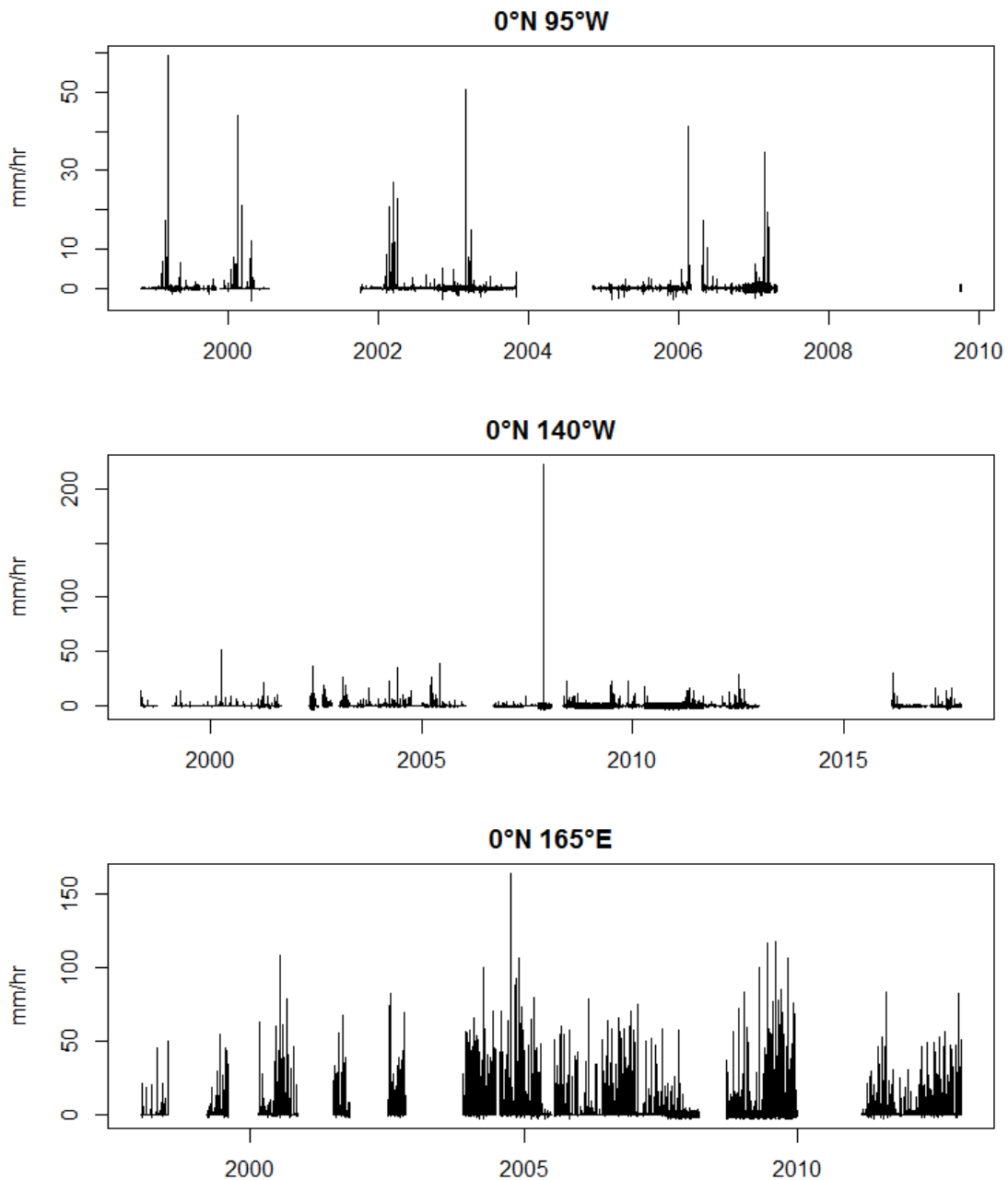


Figure 3.52: Precipitation intensity time series retrieved by buoys 0°N 95°W, 0°N 140°W and 0°N 165°E.

The time series report several rainfall intensity peaks during the recorded periods. 0°N 95°E is characterised by the presence of several measurements exceeding the 1 mm/hr and reaching 30 mm/hr. 0°N 140°W presents a short period of intensive precipitations exceeding the 200 mm/hr in 2007. Nevertheless, this buoy displays several periods characterised by rainfall intensities outbouding the 10 mm/hr. 0°N 165°E shows several measurements beyond the 10 mm/hr threshold. Indeed, almost each recorded period possesses at least

one observation reaching the 50 mm/hr. Overall, the largest presence of high rainfall intensities occurs at 0°N 165°E.

Figure 3.53 reports the rainfall diurnal cycle of the total rainfall events (>0.5 mm/hr) for the three buoys, composed by light events (0.5-3 mm/hr), medium events (3-10 mm/hr) and heavy events (>10 mm/hr).

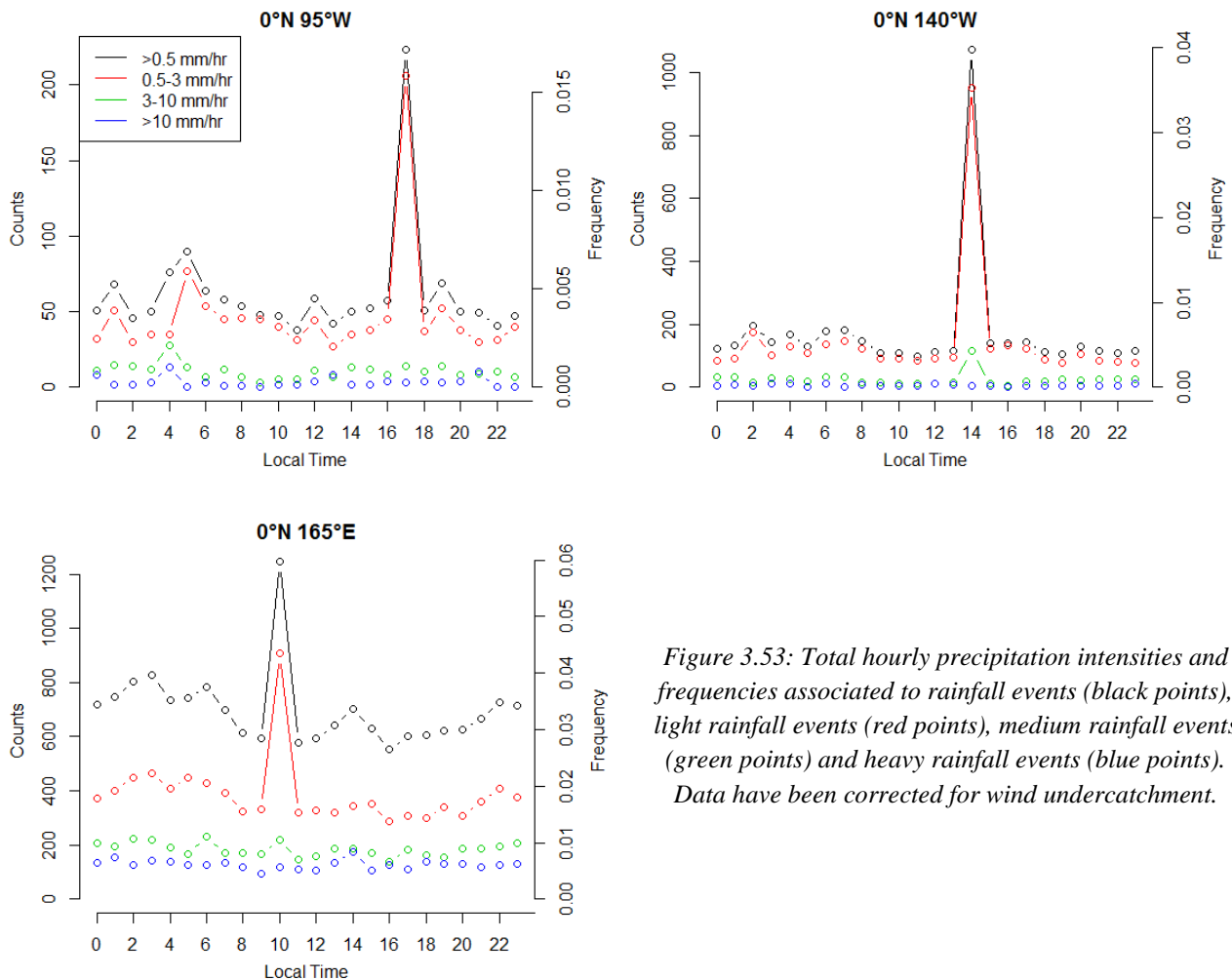


Figure 3.53: Total hourly precipitation intensities and frequencies associated to rainfall events (black points), light rainfall events (red points), medium rainfall events (green points) and heavy rainfall events (blue points). Data have been corrected for wind undercatchment.

The three graphs show the presence of an individual dominant peak in rainfall and light events occurring at different hours. The peak occurs at 17 for 0°N 95°W, at 14 for 0°N 140°W and at 10 for 0°N 165°E. Yet, medium and heavy rainfall intensities do not assume the same behaviour. The presence of an individual dominant peak during a single hour is probably caused by an error in the data sampling. Without considering the contribution of the individual dominant peaks, buoys point to similar results. Rainfalls are principally composed by light events in 0°N 95°W and 0°N 140°W whereas 0°N 165°E display a higher contribution of medium and large rainfalls to the total rainfalls. The occurrence of light events is more likely during the early morning hours for all buoys. However, the number of counts does not vary greatly over the day in all the three buoys. As regards 0°N 140°W and 0°N 165°E, medium and heavy rainfalls remain almost steady over the day and do not show a preference for a particular period. Instead, 0°N 95°W features a peak in the medium and heavy rainfalls in the early-morning at 04.

Figure 3.54 displays the extreme rainfall diurnal cycle for each buoy.

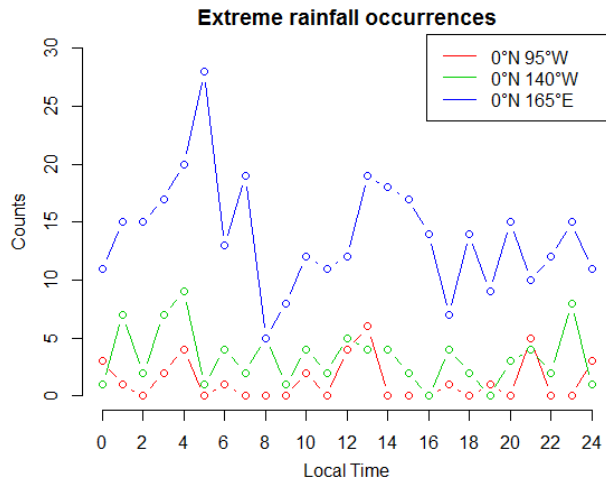


Figure 3.54: Extreme rainfall occurrences for the three different buoys.

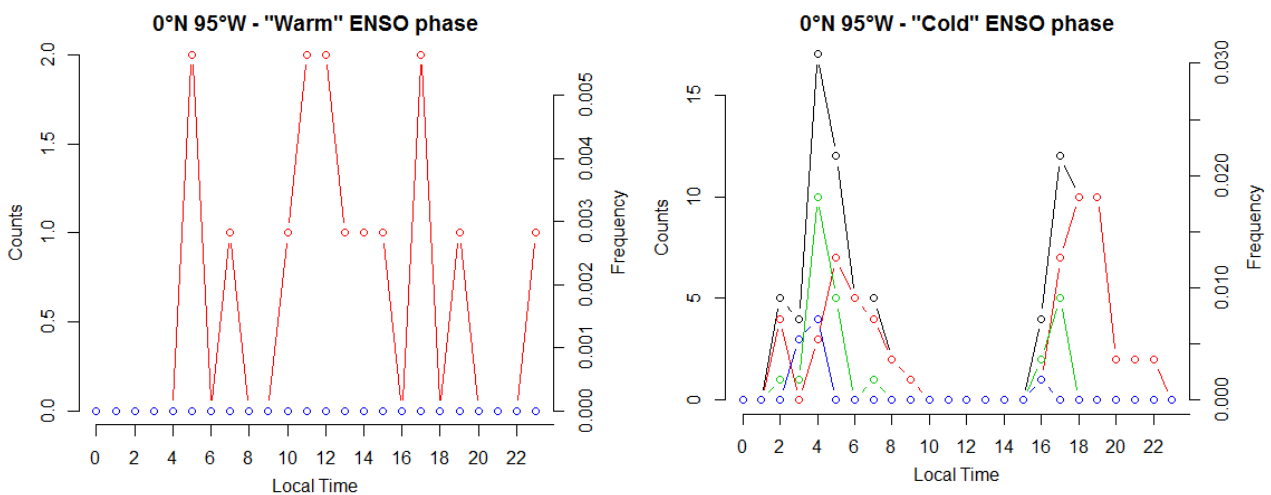
The number of extreme rainfall occurrences at 0°N 95°W spans between 0 and 6. 0°N 95°W displays the greatest counts at 13 even though it does not exhibit a preference for a particular period of the day. 0°N 140°W is characterised by counts ranging from 0 to 10 and averaging 3.5. It shows larger counts during nighttime hours, in particular at 23, 01, 03 and 04. The extreme rainfall occurrences at 0°N 165°E range between 5 and 28 with a mean values of 14. The highest values occur in the early morning between 03-07 and early afternoon between 13-15. The lowest values occur in the morning at 08, 09 and late afternoon-evening at 17, 19, 21 and 24.

Rainfall events are examined during the occurrence of El Niño and La Niña. Table 3.22 reports the number of recorded days observed during the warm and cold ENSO phases.

Table 3.22: Number of wind direction recorded days observed during the cold and warm phases of ENSO.

	0°N 95°W	0°N 140°W	0°N 165°E
<b>Cold ENSO phase</b>	91	486	292
<b>Warm ENSO phase</b>	59	118	202

Figure 3.55 reports the rainfall occurrences recorded during both warm and cold ENSO phases for the three different buoys.



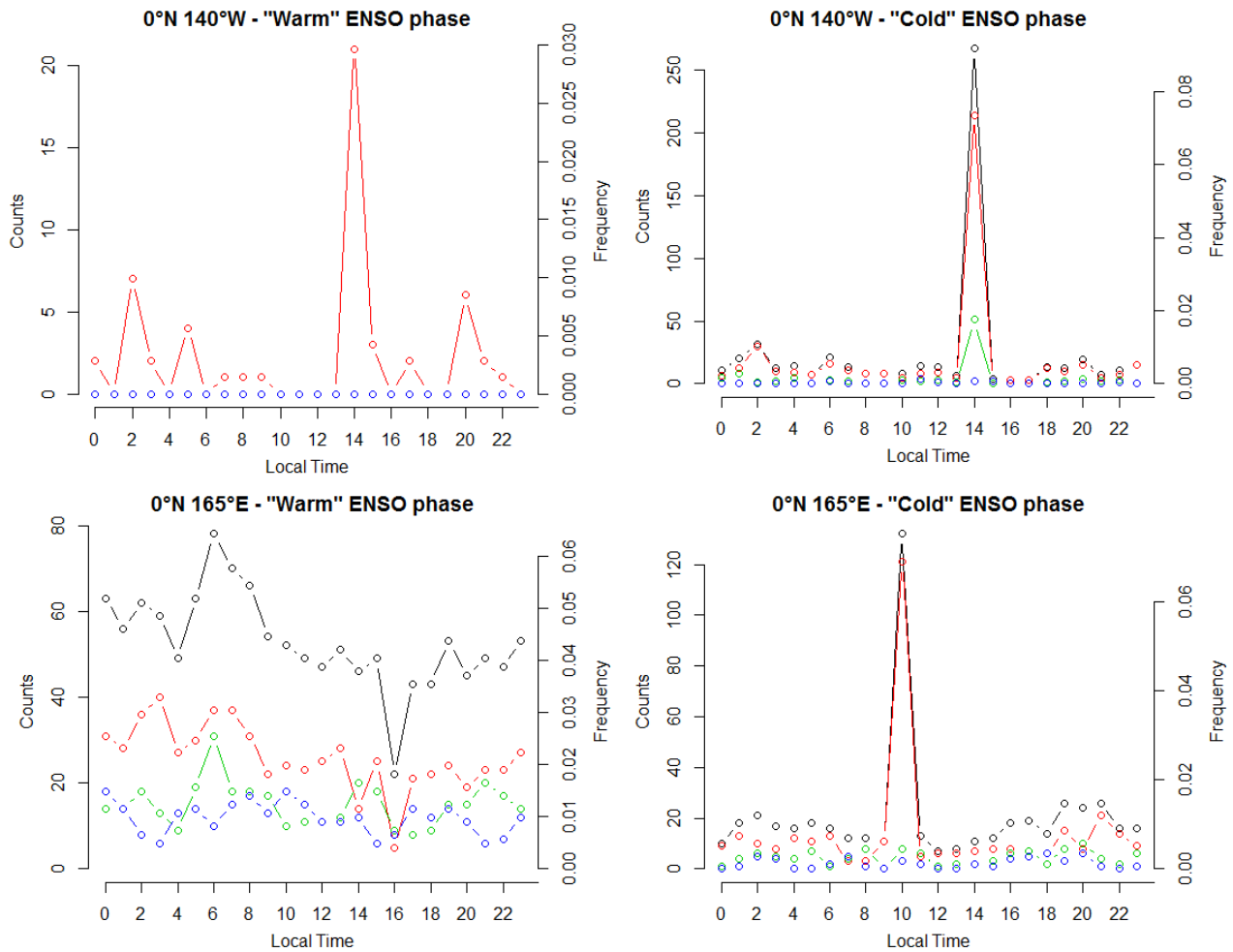


Figure 3.55: Total hourly precipitation intensities and frequencies associated to rainfall events (black points), light rainfall events (red points), medium rainfall events (green points) and heavy rainfall events (blue points). Precipitation measurements have been retrieved during the “warm” and “cold” ENSO phases.

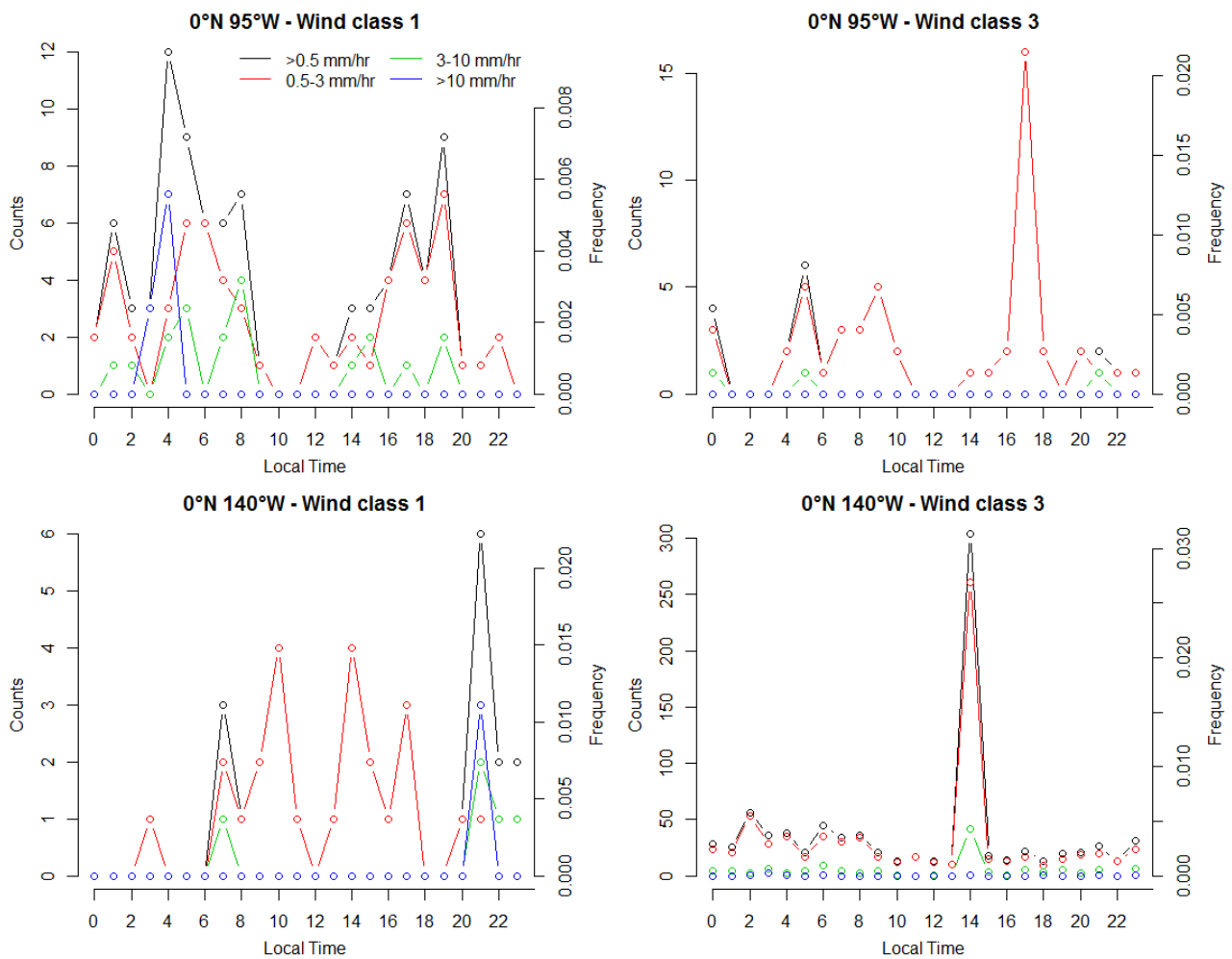
The warm phase of  $0^{\circ}\text{N } 95^{\circ}\text{W}$  and  $0^{\circ}\text{N } 140^{\circ}\text{W}$  is characterised by the presence of few rainfall occurrences. On the other hand, during the cold phase the two buoys report higher occurrences. The cold phase of  $0^{\circ}\text{N } 95^{\circ}\text{W}$  shows the presence of two peaks, one occurring in the early morning hours and the other around sunset. The early morning peak is characterised by higher occurrences for all the rainfall categories compared to the sunset peak.  $0^{\circ}\text{N } 140^{\circ}\text{W}$  displays the presence of a dominant peak at 14, the same previously recognised in Figure 3.53. Without considering this peak, rainfall and light events show a preference for the 00-06 interval during La Niña events.  $0^{\circ}\text{N } 165^{\circ}\text{E}$  exhibits higher occurrences during El Niño periods than during La Niña periods. The warm phase is characterised by a preference for the morning hours by rainfall and light events, especially at 06. On the other hand, medium and heavy events do not show a propensity for any particular time period. The cold phase features a dominant peak at 10, the same previously recognised in Figure 3.52. Without considering this peak, rainfall and light events show a preference for the night-time hours, especially in the 19-22 interval. Medium and heavy rainfall are not linked to a particular time period. The different frequencies reported in Figure 3.55 highlights the different rainfall regimes occurring during the two ENSO phases. Neglecting the individual dominant peaks, the highest frequency of all the rainfall categories is attained by the warm ENSO phase at  $0^{\circ}\text{N } 165^{\circ}\text{W}$ . Overall,  $0^{\circ}\text{N } 95^{\circ}\text{W}$  and  $0^{\circ}\text{N } 140^{\circ}\text{W}$  assume the highest frequencies during La Niña periods. Yet,  $0^{\circ}\text{N } 165^{\circ}\text{W}$  shows the opposite behaviour.

Precipitation data are examined according to the local wind conditions. Table 3.23 reports the number of days divided according to the differentiation based on wind conditions.

Table 3.23: Number of precipitation recorded days lying wind class 1 and 2.

	0°N 95°W	0°N 140°W	0°N 165°E
<i>Wind class 1</i>	121	30	208
<i>Wind class 3</i>	124	1387	372

Figure 3.56 shows the precipitation diurnal cycle during different wind conditions.



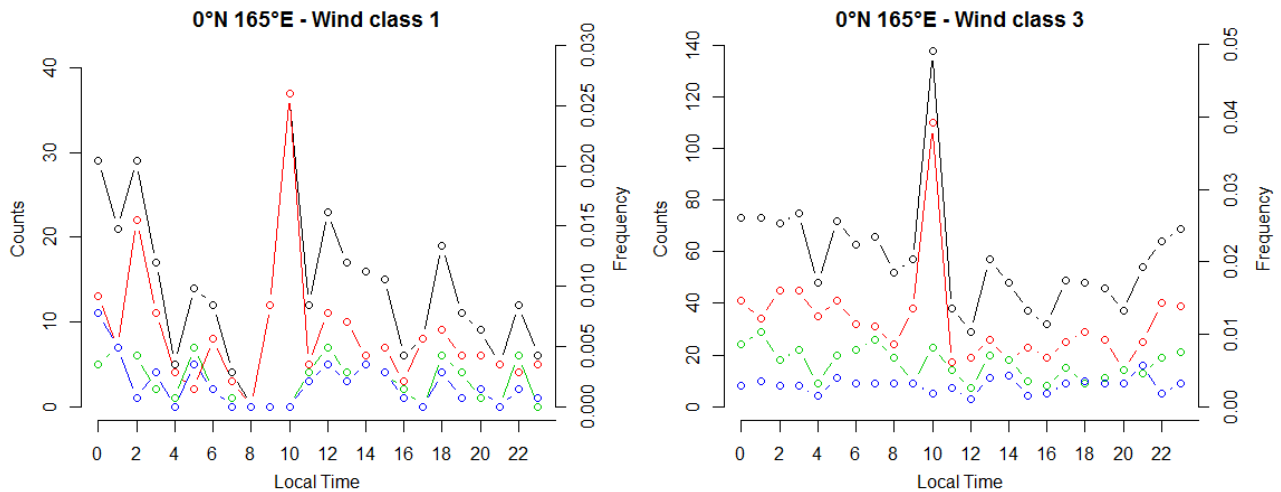
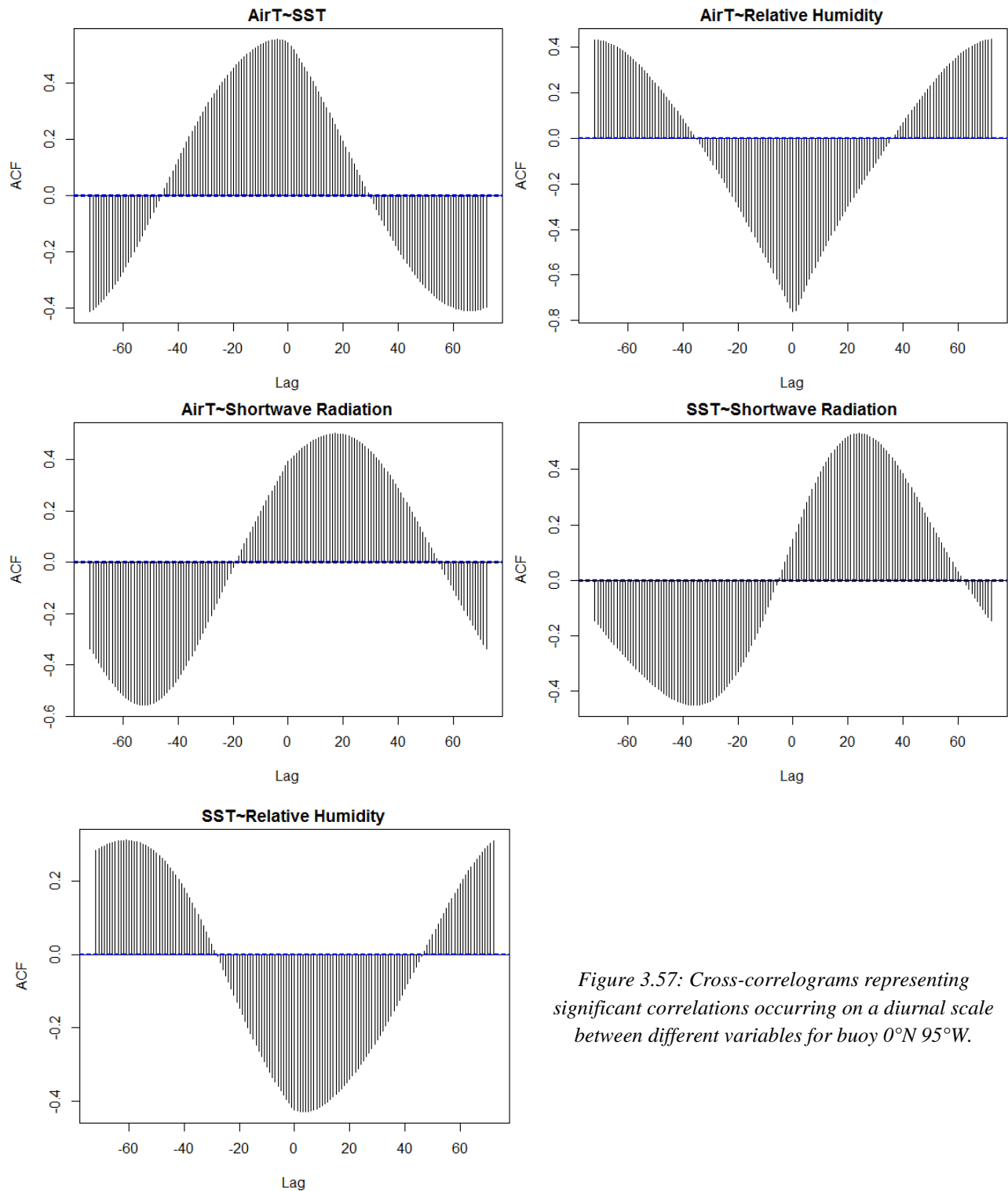


Figure 3.56: Total hourly precipitation intensities and frequencies associated to rainfall events (black points), light rainfall events (red points), medium rainfall events (green points) and heavy rainfall events (blue points). Precipitation measurements have been observed during days classified as calm (wind class 1) and windy (wind class 3).

0°N 95°W displays low rainfall occurrences during the presence of both strong and weak winds. However, without considering the dominant peak, the three rainfall categories occur more often during the morning than during the rest of the day. 0°N 140°W does not exhibit a preference for a particular period of the day during weak winds, even though the early morning period from 00 to 06 is characterised by the almost total absence of rainfall events. As regards strong winds, a dominant peak is present at 14, similar to the one recognised previously. However, without considering this peak, rainfall and light events show a preference for the early morning hours. Medium and heavy events do not exhibit a clear preference for any period of the day. 0°N 165°W shows the presence of the dominant peak at 10, as previously recognised, under both wind conditions. The total rainfalls and light events show a similar behaviour under both conditions. They exhibit higher values during night with maxima at 22 and 02, and minima between the 06-08 interval. During strong wind conditions, the occurrences of all rainfall categories is generally lower from 08 to 20. Considering all the buoys, *wind class 1* is characterised by a preference for night-time hours for medium rainfall and a preference for afternoon hours for heavy rainfall. Instead, *wind class 3* shows a preference for night-time hours (from 22 to 06) for both medium and heavy rainfalls.

### 3.9 Relations between variables

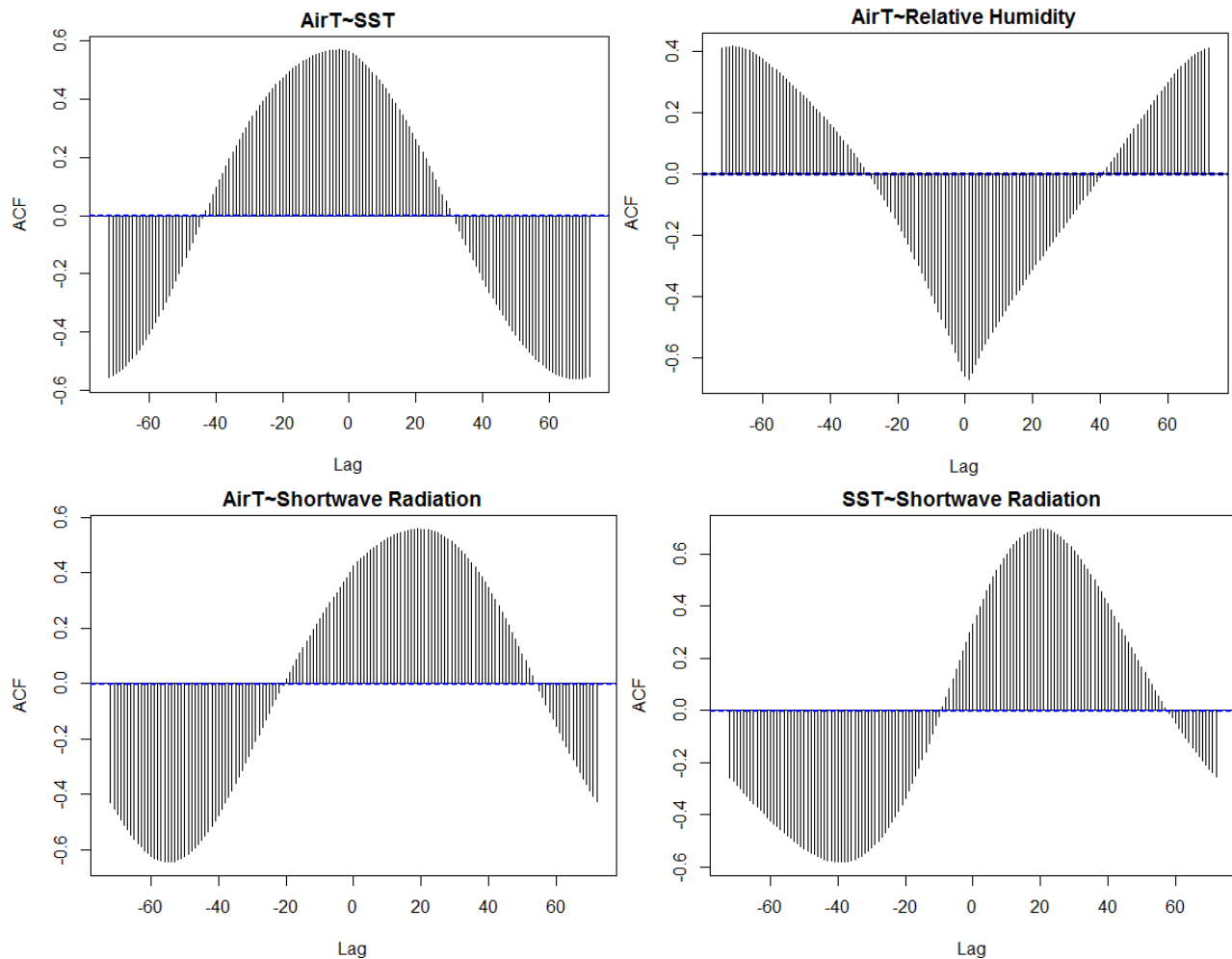
The relations between variables are assessed through the cross-correlation analysis. Figure 3.57 illustrates the cross-correlograms computed among the variables retrieved by 0°N 95°W. The first variable is the series lagged in time. Only cross-correlograms with the maximum correlation coefficient reaching at least  $\pm 0.4$  are considered.



*Figure 3.57: Cross-correlograms representing significant correlations occurring on a diurnal scale between different variables for buoy 0°N 95°W.*

Figure 3.57 reports the presence of few significant relations amongst the different variables in 0°N 95°W. The cross correlation between the near-surface air temperature and the SST is maximum at lag -4 measuring 0.55. Then, correlation values decrease to approximately -0.4 for increasing and decreasing lags. This value is encountered at lags -72 and +68 indicating the existence of a weak negative relationship between the two variables. The correlation between the near-surface air temperature and the relative humidity reaches a maximum at lag 0 measuring -0.76. Then, the correlation coefficients increases for increasing and decreasing lags, exceeding 0.4 for lags  $\pm 72$ . The cross-correlation function computed between the near-surface air temperature and the shortwave radiation assumes the maximum value at lag +18 measuring 0.5. On the other hand, the minimum value occurs at lag -52 and measures -0.56. The SST exhibits a significant correlation with the shortwave radiation. The maximum correlation coefficient occurs at lag +24 and measures 0.53. The minimum correlation coefficient takes place at lag -35 and measures -0.45.

Figure 3.58 illustrates the cross-correlograms computed between the near-surface air temperature and the other variables for 0°N 140°W.



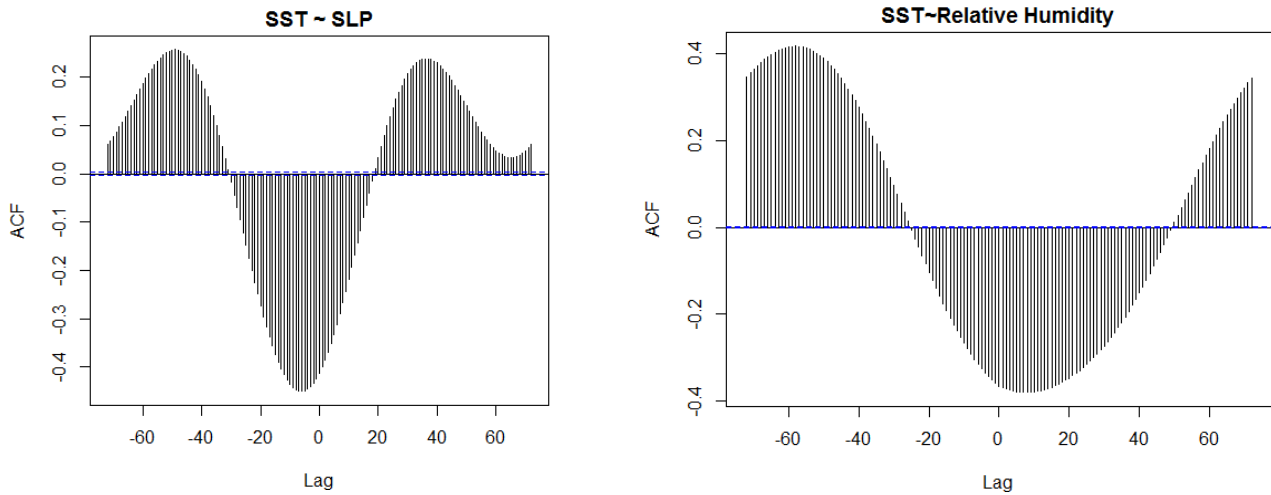


Figure 3.58: Cross-correlograms representing significant correlations between different variables for buoy 0°N 140°W.

0°N 140°W features similar relationships as those recognised in 0°N 95°W. The correlation coefficients between the air temperature and SST is maximum at lag -4 (0.57) and minimum at lag +68 (-0.56). The correlation between the air temperature and relative humidity is the highest at lag +1 (-0.67). Then, correlation increases reaching positive values around 0.4 at the extreme lags  $\pm 72$ . The air temperature shows a moderate positive correlation with the shortwave radiation. The maximum value occurs at lag +19 and measures 0.56 while the minimum value occur at lag -53 measuring -0.64. The correlation between the SST and the shortwave radiation follows a similar behaviour, peaking at lag +20 (0.7) and at lag -38 (-0.58). The SST and SLP show evidences of a negative relation peaking at lag -6 (-0.45). The SST and relative humidity present the maximum correlation value at lag -57 measuring 0.42.

Figure 3.59 illustrates the cross-correlograms computed between the near-surface air temperature and the other variables for 0°N 165°E.

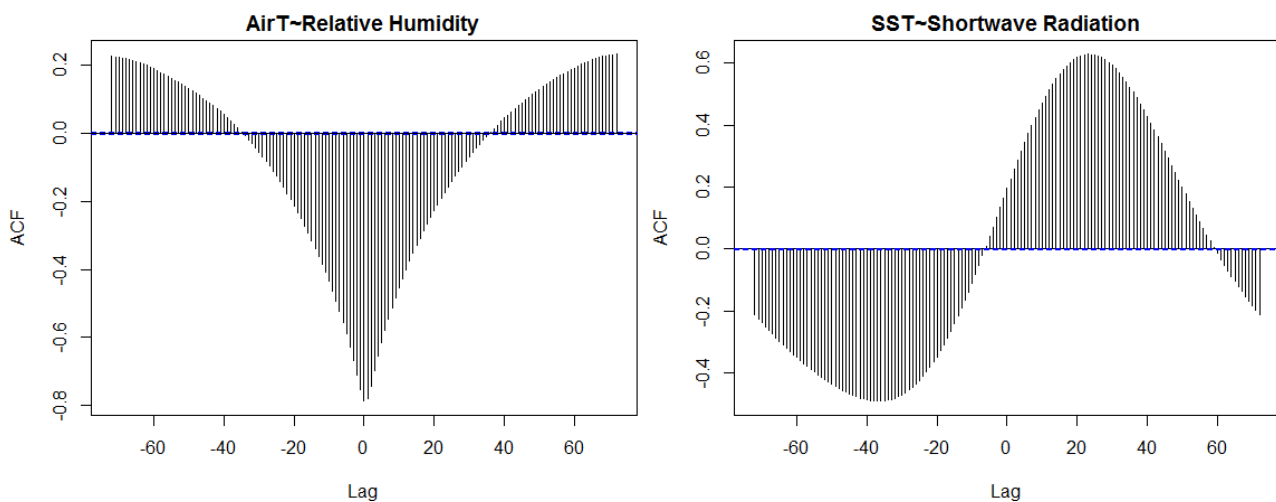


Figure 3.59: Cross-correlograms representing significant correlations between different variables for buoy 0°N 165°E.

0°N 165°E features few significant correlations. The air temperature and the relative humidity show a similar relation as previously recognised for the other buoys. The maximum correlation occurs at lag 0 and measures -0.79. The SST and shortwave radiation exhibit the maximum positive correlation at lag +13 (0.63) and the minimum value at lag -37 (-0.49). A notable aspect is the absence of strong correlations recognised previously in the other buoys between the air temperature and SST and between the air temperature and shortwave radiation.

## 4. Discussion

This chapter discusses the elaboration of the TAO data presented in chapter 3. Section 4.1 focuses on the characterisation of the diurnal cycles of the different parameters in the Eastern, Central and Western Equatorial Pacific. Section 4.2 examines the variation of the diurnal cycle according to large-scale climatic conditions. Section 4.3 analyses the variation of the diurnal cycle under different local meteorological conditions. Section 4.4 assesses the variation of the diurnal cycle over the long period. Section 4.5 targets to define the main relationships existing on a diurnal scale between the different variables. Finally, section 4.6 discusses the possible limitation of this thesis and provides recommendations for future works. The findings of this work are compared with previous results reported in section 1.3.

### 4.1 The diurnal cycles of the different variables observed in the Eastern, Central and Western Equatorial Pacific

The downgoing shortwave radiation presents a single daily peak at all locations. Figure 3.3 shows that the parameter starts to increase some minutes before 06 local time, reaching the peak around 12, and then decreases until a few minutes after 18. During night-time hours, the downgoing shortwave radiation remains close to zero. The Central Equatorial Pacific receives higher amounts of solar radiation compared to the other two regions, as confirmed by the higher maximum reached by the mean cycle compared to those occurring in the Eastern and Western Pacific. In addition, the Central Equatorial Pacific is characterised by the occurrence of homogenous sunny conditions during most of the period of study, as indicated by several evidences. First, the shortwave radiation diurnal values are located closer to the average cycle compared to the other two buoys. The distribution of the shortwave radiation sums of the Central Pacific illustrated in Figure 3.4 presents a smaller variation around the mean compared to the other locations. Moreover, Figure 3.4 displays also the highest values assumed by the shortwave radiation sums compared to the other two locations. Finally, the frequency of rainfall events characterising the Central Pacific is the lowest, as reported in Figure 3.53. On the other hand, data indicate a large variability in the insolation conditions occurring in the Western Equatorial Pacific. Indeed, the low values assumed by the 5<sup>th</sup> percentile in Figure 3.3 indicate the occurrence of many days characterised by a covered sky. The Eastern Pacific features similar conditions to those of the Western Pacific, as indicated by the similar values assumed by the distribution of the shortwave radiation sums and by the mean daily evolutions.

The frequency analysis reported in Figure 3.9 reveals the absence of a wind speed diurnal variation in the Central and Western Pacific, whereas it indicates the presence of a weak wind speed daily cycle in the Eastern Pacific. Generally, the wind shows higher velocities during morning hours around 08, as illustrated in Figure 3.10, although the Eastern Pacific features the maximum in the mean daily cycle around 13 local time. Then, wind speed displays lower velocities during night-time hours, with the minimum value occurring around midnight. The amplitudes of the wind speed diurnal cycles measure 0.6 m/s in the Eastern Pacific and 0.2 m/s in the Central and Western Pacific. The results of the analysis examining the wind speed diurnal cycle broadly agree with previous findings. The low amplitude of the diurnal signals is consistent with the estimates of Deser et al. (1994), Deser and Smith (1997) and Ueyama and Deser (2007). Results confirm another feature reported in the study of Deser and Smith (1997), where a geographic variation of the diurnal amplitude of wind speed over the ocean was identified. In fact, the diurnal amplitude of the wind speed daily

cycle is the largest in the Eastern Pacific and becomes negligible moving toward the Western Pacific. However, these results shall be considered cautiously: the wind speed anomalies undergo diurnal variations much larger than the amplitude of the mean daily cycles.

The mean diurnal cycle of near-surface air temperature displays a double-peak shape in all regions. The two peaks occur in the mid-morning around 07-08 and in the mid-afternoon around 16-17. As illustrated in Figure 3.17, the temperature of the air starts to increase sharply after sunset by almost 0.5 °C. Then, it stabilises in the Central and Western Pacific, while it increases more slowly in the Eastern Pacific. After 12, again the near-surface air temperature begins to increase rapidly and reaches the daily maximum around 17. Afterwards, the air temperature decreases with different rates: firstly, it falls suddenly by almost 0.25 °C until 18 and then it cools more gently until dawn. An interest feature is the constant air temperature during the latter hours of the night, i.e. in between 03 and 06 local time. Therefore, during the pre-dawn hours, the thermal radiative cooling must be balanced by another process that maintains a stationary air temperature. Another interesting element is the evolution of the air temperature mean cycle in the evening hours in the Western Pacific. In fact, Figure 3.17 reports a steady air temperature in between 18 and 21 in this location, while it starts to decrease gently right after 18 in the Eastern and Central Pacific. The observed diurnal cycle of the near-surface air temperature does not agree with the description given by Ahrens (2012) and illustrated in sub-section 1.3.2 indicating a constantly increasing temperature in between sunrise and mid-afternoon and a constantly decreasing temperature from mid-afternoon to dawn. The amplitude of the mean diurnal cycle of air temperature presents a geographical variation, being larger in the East-Pacific and smaller in the West-Pacific. As reported in Figure 3.17, the individual daily evolutions spread differently around the mean daily cycle among the three locations. In particular, the evolution of the percentiles indicates that the Western Pacific features the highest variability, whereas the Central Pacific presents the lowest one.

The diurnal cycles observed in the three locations are characterised by the occurrence of two different peaks during daylight hours in each investigated location. This finding may indicate the influence of convective phenomena on the near-surface air temperature daily cycle. The stable air temperature occurring approximately between 10 and 14 may be caused by the presence of clouds, which prevent the solar radiation to reach the ocean surface and the consequent warming of the near-surface atmospheric layer. Clouds disappear in the early-afternoon and the air temperature returns to warm. However, the analysis of the diurnal cycle of precipitation does not identify a clear mid-morning peak in any of the three rainfall categories. Instead, the observed near-surface air temperature diurnal cycles share similarities with the erroneous air temperature daily cycle examined by Anderson and Baumgartner (1998) and reported in Figure 1.6. Such correspondences are: the shape of the diurnal evolution, characterised by the presence of two peaks, and the timings of these peaks. Hence, data seems to confirm that the TAO measurements of air temperature retrieved by the three buoys (0°N 95°W, 0°N 140°W and 0°N 165°E) are affected by a radiative heating error associated to the naturally ventilated shield covering the sensor. The presence of the same error in the other equatorial buoys of the TAO array is assessed in Figure 4.1. This figure reports the mean diurnal cycle of near-surface air temperature computed using daily anomaly data of all the remaining equatorial buoys of the TAO array (0°N 110°W, 0°N 125°W, 0°N 155°W, 0°N 170°W, 0°N 180°W, 0°N 156°E and 0°N 147°E).

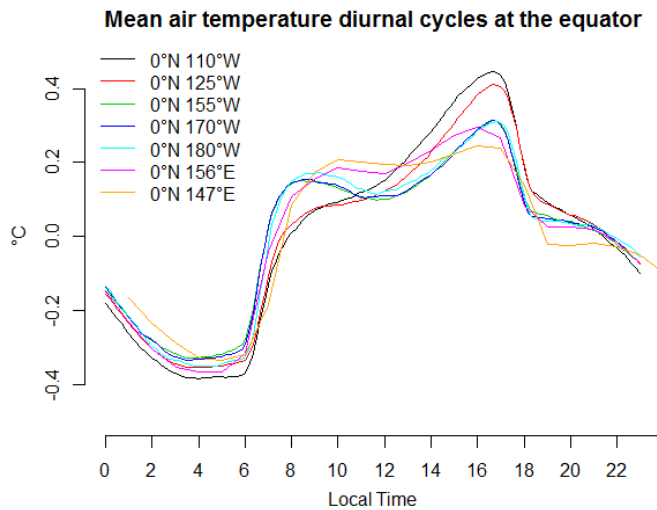


Figure 4.1: Mean near-surface air temperature diurnal cycle observed in the equatorial buoys of the TAO array not used in the main analysis ( $0^{\circ}\text{N } 110^{\circ}\text{W}$ ,  $0^{\circ}\text{N } 125^{\circ}\text{W}$ ,  $0^{\circ}\text{N } 155^{\circ}\text{W}$ ,  $0^{\circ}\text{N } 170^{\circ}\text{W}$ ,  $0^{\circ}\text{N } 180^{\circ}\text{W}$ ,  $0^{\circ}\text{N } 156^{\circ}\text{E}$  and  $0^{\circ}\text{N } 147^{\circ}\text{E}$ ).

The two peaks in the diurnal cycle of air temperature occur at almost the same time in all the equatorial moorings, indicating that they are all affected by the radiative heating error. Nonetheless, the error exhibits an apparent geographical variation. Indeed, the height reached by the mid-morning peak grows westward, being the smallest in buoys deployed in the East-Pacific ( $0^{\circ}\text{N } 110^{\circ}\text{W}$  and  $0^{\circ}\text{N } 125^{\circ}\text{W}$ ) and the largest in the buoys located in the West-Pacific ( $0^{\circ}\text{N } 147^{\circ}\text{E}$  and  $0^{\circ}\text{N } 156^{\circ}\text{E}$ ). On the contrary, the height of the mid-afternoon peak grows eastward, reaching the smallest values in the Western Pacific and the largest ones in the Eastern Pacific.

As explained in sub-section 1.3.3, the magnitude of the error is dependent on the local meteorological conditions, mainly the amount of the solar radiation reaching the surface and wind speed. Sub-section 4.3 discusses the variation of the observed air temperature diurnal cycles under different local meteorological conditions to analyse the variation of the magnitude of the radiative heating error.

The analysis of the SST diurnal cycle shows similar results among the different locations. The SST starts increasing after 08 local time, reaches its maximum near 15-16 and then decreases until the following morning. The SST starts to warm later compared to the near-surface air temperature due the larger thermal capacity of the water compared to the air. The diurnal  $\Delta\text{SST}$ , i.e. the difference between the daily maximum and minimum, is similar in the Central ( $0.39^{\circ}\text{C}$ ) and Western Pacific ( $0.41^{\circ}\text{C}$ ), while it is larger in the Eastern Pacific ( $0.55^{\circ}\text{C}$ ). Thus, the diurnal  $\Delta\text{SST}$  follows a similar geographic variation as the near-surface air temperature, being the largest in the Eastern Pacific and similar in the Central and Western Pacific, as observed also by Deser and Smith (1998) and Clayson and Weitlich (2006).

As indicated by the variation of the percentiles around the mean reported in Figure 3.28, the Central Pacific features a more homogeneous diurnal cycle than the other locations. Overall, the observed SST diurnal cycle is consistent with previous findings described in sub-section 1.3.6.

The SST tends to cool at different rates once the daily peak is reached. In particular, Figure 3.28 reveals that the water temperature declines faster during the last two daylight hours (from 16 to 18 local time) than during night-time hours (after 19 local time). This observation points to the possible presence of an heating process operated by deeper waters. Assuming that sub-surface ocean layers are not significantly influenced by the diurnal solar radiation cycle and their temperature remains stable over the day, upward heat transfer from such layers may limit the cooling of surface waters. However, ignoring circulation factors, the water temperature generally decreases as the depth increases. Hence, the superficial layers of the ocean are usually warmer than deeper layers. Therefore, it is unlikely that the deeper layers warm the superficial layers unless the SST becomes colder than the temperature of the deeper layers. Another possible explanation to this

observation is the occurrence of mechanical mixing processes caused by stronger winds, which mix superficial waters and deeper waters. The process affecting the SST diurnal cooling rate in turns affects the diurnal  $\Delta$ SST by slightly increasing the minimum temperature. Therefore, in addition to the solar radiation and wind speed, other factors may contribute regulating the diurnal SST amplitude. Future studies should investigate the entity of this process and assessing its relation with the diurnal  $\Delta$ SST. In particular, the assessment of the diurnal variation in the temperature of the sub-surface mixed layer shall reveal important information concerning this process.

The relative humidity displays an analogous diurnal cycle among the different locations. As illustrated in Figure 3.35, the cycle is composed by two daily minima located around 07-08 and 16-17 local time. Humidity reaches higher values during night-time hours than during day-light hours. Overall, relative humidity appears to be strictly correlated with the air temperature, as a growing air temperature corresponds to a decreasing relative humidity and vice versa. Indeed, the relative humidity is defined as the ratio of the amount of atmospheric moisture over the amount that would be present if the air were saturated (NOAA, 2009), and the latter factor is dependent on the air temperature. The comparison between the mean diurnal relative humidity and the mean daily near-surface air temperature reveals that the diurnal evolution of the first variable is largely explained by the second one over the entire recorded period. Hence, the presence of other phenomena significantly affecting the relative humidity should be excluded. However, the existence of an error in the near-surface air temperature measurements in turn affects the relative humidity measurements.

The analysis of the SLP diurnal cycle reveals the dominance of a semidiurnal component. Indeed, the diurnal cycle is constituted by two maxima and two minima composing a sinusoidal evolution. Maxima and minima occur every six hours. The diurnal variation of the anomalies strictly follows the mean cycle indicating the occurrence of the same SLP daily evolution over the entire periods of study. The phase of the cycle is consistent among the three locations, with maxima occurring near 10 and 22, and minima around 04 and 16. The observed SLP diurnal cycle reflects previous findings (LeBlancq, 2011; Ahrens, 2012) illustrated in sub-section 1.3.4. Indeed, this observed SLP diurnal oscillation is consistent with the “Atmospheric Tide” theory.

There is no appreciable diurnal signal in wind direction. This is confirmed by the results of the spectral analysis reported in Figure 3.44 and by the daily cycles of wind direction illustrated in Figure 3.45 spanning around zero with small deviations. Therefore, there is a stable wind direction throughout the day. As shown by Figure 3.47, the wind blows predominantly toward north in the Eastern Pacific and toward west in the Central and Western Pacific. These findings do not completely agree with the general trade winds pattern explained in section 1.2, since the Eastern Pacific shows a clear dominance for winds directed northward and not westward.

The diurnal cycle of precipitation is characterised by one dominant peak in light rainfalls at each location. Considering that precipitation in the nearby hours is on average, this dominant peak unlikely represents the occurrence of several precipitation events at the same hour. Instead, this recursive phenomenon is linked with the presence of an error, which could be related to the occurrence of a siphon event (see sub-section 2.2.1). The dominant peaks are encountered at 17 in 0°N 95°W, 14 in 0°N 140°W and 10 in 0°N 165°E. The presence of the same error in the other equatorial TAO moorings not used in the main analysis is assessed here. Figure 4.2 reports the diurnal cycle of rainfall events, i.e. the counts of precipitation intensities exceeding 0.5 mm/hr for each hour, for each of these additional equatorial TAO buoys.

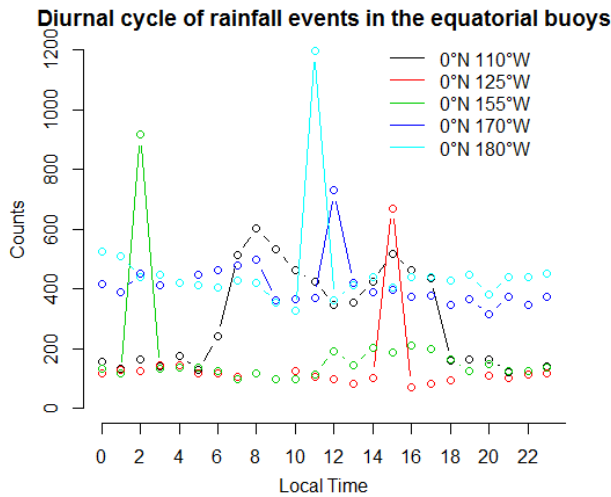


Figure 4.2: Diurnal cycle of rainfall events observed in the additional equatorial buoys of the TAO array ( $0^{\circ}\text{N } 110^{\circ}\text{W}$ ,  $0^{\circ}\text{N } 125^{\circ}\text{W}$ ,  $0^{\circ}\text{N } 155^{\circ}\text{W}$ ,  $0^{\circ}\text{N } 170^{\circ}\text{W}$  and  $0^{\circ}\text{N } 180^{\circ}\text{W}$ )

All the equatorial buoys except  $0^{\circ}\text{N } 110^{\circ}\text{W}$  exhibit extraordinary high occurrences of rainfall events in one specific hour, similarly to the three buoys examined in this study. The dominant peaks occur at different hours of the day i.e. at 15 for  $0^{\circ}\text{N } 125^{\circ}\text{W}$ , 2 for  $0^{\circ}\text{N } 155^{\circ}\text{W}$ , 12 for  $0^{\circ}\text{N } 170^{\circ}\text{W}$  and 11 for  $0^{\circ}\text{N } 180^{\circ}\text{W}$ . Hence, almost all the equatorial buoys are affected by a similar error in the precipitation measurements.

Overall, the dominant peaks are omitted in the assessment of the precipitation diurnal cycle in the Eastern, Central and Western Pacific.

Precipitation data suggest the occurrence of a similar cycle among the three examined locations. Light rainfall events display higher counts values occurring in the morning hours (from 00 to 08 local time) than over the rest of the day. The probability of occurrence of medium and heavy rainfalls seems to remain constant across the 24-hours period. The total counts of rainfall events are largely constituted by light events in the Eastern and Central Pacific. Instead, light events in the Western Pacific compose almost half of the total rainfall events. Overall, the elaboration of the data do not identify a clear early-morning peak in rainfall events as found by several authors and described in sub-section 1.3.7. Indeed, only light events exhibit a little higher probability of occurrence in the early morning.

The three regions of the Pacific Ocean are characterised by different pattern in the extreme rainfall events. Figure 3.53 illustrates that the extreme events in the Eastern Pacific are not clearly associated to a particular period of the day. The extreme rainfall counts in the Central Pacific are almost double during some of the night-time hours, specifically at 23, 01, 03 and 04. The Western Pacific features a clear peak in the early morning hours and the lowest counts in the mid-morning from 08 and 12. Unlike the assessment of the precipitation diurnal cycle, extreme rainfalls in the Central and Western Pacific exhibit a preference for the early-morning.

The rainfall patterns characterising the three locations are further analysed here by estimating the likelihood of rainfall events to occur at each hour of the day (i.e. the return period). Hourly precipitation intensities are computed from 10-minutes data, and only hourly precipitation averages greater than 0.5 mm/hr, corresponding to (at least) six observed 10-minutes rainfall intensities of 0.5 mm/hr in one hour, are considered. Figure 4.3 reports the return period of rainfall events occurring at each hour according to the three examined locations.

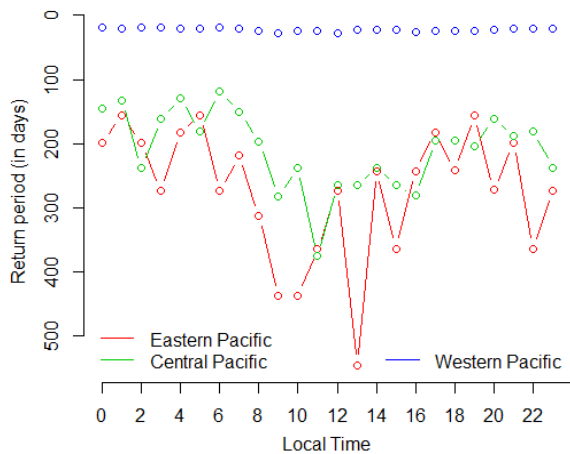


*Figure 4.3: Return period of rainfall events occurring at each hour of the day according to the three examined locations.*

In the Central and Eastern Equatorial Pacific, early morning hours experience a rainfall event approximately every 125-300 days, whereas rainfalls during day-light hours are more sporadic. Late afternoon and evening return periods are similar to early morning ones in the Eastern Pacific, while they are larger in the Central Pacific. Overall, the return periods observed in the Eastern Pacific vary more in the course of the day than the ones observed in the Central Pacific. The Western Equatorial Pacific is characterised by much shorter return periods. In this location, each hour experiences a rainfall event almost every 20 days. Overall, the west Pacific is the region featuring the most “rainy” conditions among the three considered location. The high rainfalls frequencies are probably associated to the SPCZ’s activity, which distinguishes this region. Data related to the Eastern and Central Pacific indicates that the central hours of the day are the driest. Furthermore, as the 10-minutes precipitation intensities are averaged into hourly measurements, the dominant peaks recognised before disappear. Thus, future works examining precipitation data should average 10-minutes data into hourly intensities to obtain accurate results.

## 4.2 The diurnal cycles observed during the “warm” and “cold” phases of ENSO

The analysis of the wind velocity diurnal cycle occurring during ENSO’s warm and cold phases reveals the occurrence of almost the same shape, timing and amplitudes of the cycles observed throughout the entire time series. Hence, this analysis excludes the existence of a systematic and noticeable impact of El Niño and La Niña events on the wind speed diurnal cycle.

The ENSO’s warm and cold phases do not affect the shape of the near-surface air temperature diurnal cycle. The double-peak evolution is present in each buoy. Figure 4.4 reports the amplitudes of the mean air temperature cycle observed over the entire recorded periods, and during the warm and cold ENSO phases.

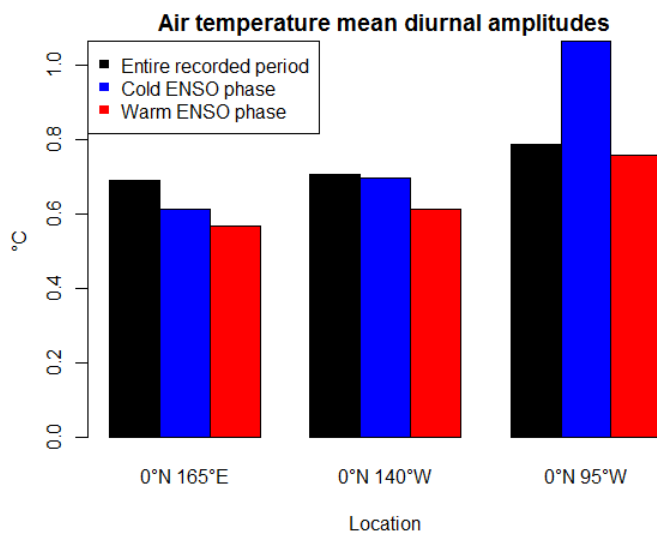


*Figure 4.4: Air temperature mean diurnal amplitudes observed in the three locations over the entire time series, and during both the warm and cold ENSO phases.*

The air temperature measurements retrieved during El Niño and La Niña events show a common tendency among the different buoys. La Niña conditions features higher diurnal amplitudes than during El Niño conditions. The difference between the mean amplitudes observed during the warm and cold phase is largest in the Eastern Pacific and smallest in the Western Pacific. Moreover, the mean diurnal amplitudes observed during La Niña and El Niño periods are generally larger in the Eastern and lower in the Western Pacific, as the corresponding mean amplitudes observed over the entire time series. The highest mean diurnal air temperature amplitude is observed in the Eastern Pacific during the occurrence of La Niña events. However, this observation is not consistent with the general meteorological conditions occurring during the cold ENSO phase. Indeed, the cold ENSO phase is associated with a strengthening of the trade winds over the Eastern Pacific (Barry and Chorley, 2006; Ahrens, 2012). As a result, the presence of strong winds should considerably lower the mean diurnal amplitude of air temperature, as acknowledged in section 4.3.

The shape and timing of the mean diurnal cycle of SST are not altered by the concomitance with an El Niño or La Niña events. However, the SST diurnal amplitude, i.e. the  $\Delta$ SST, is influenced by the background climatic conditions in a similar pattern as the air temperature. Figure 4.5 summarises the mean diurnal  $\Delta$ SSTs observed over the entire recorded periods, and during the warm and cold ENSO phases.

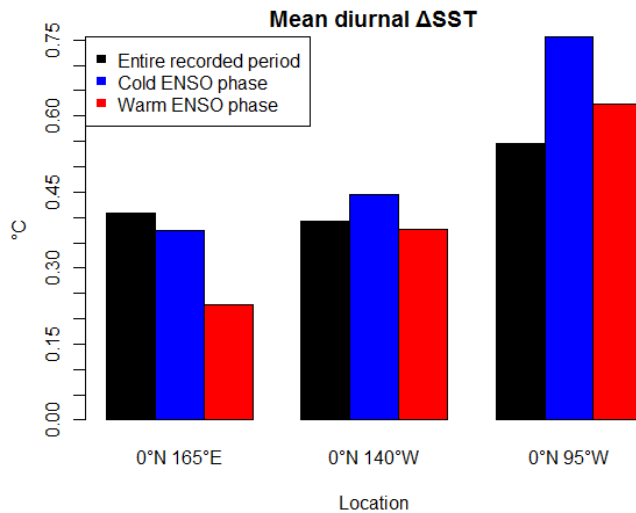


Figure 4.5: SST mean diurnal amplitudes observed in the three locations over the entire time series, and during both the warm and cold ENSO phases.

The amplitudes of the mean SST diurnal cycles are larger during the cold than during the warm ENSO phase. Unlike for the air temperature, the difference between the mean diurnal  $\Delta$ SST observed during El Niño and La Niña is larger in the Western Equatorial Pacific than in the Eastern Pacific. The diurnal  $\Delta$ SST in the Eastern Pacific displays similar characteristics to the air temperature, as recognised above. The stronger winds occurring in this region during La Niña events should result in a lower diurnal  $\Delta$ SST. Yet, the diurnal  $\Delta$ SST during the cold ENSO phase is the largest.

The comparison between the diurnal  $\Delta$ SST retrieved during both ENSO phases and for the full period of analysis (see Figure 4.5) reveals different behaviours among the three locations. In the Eastern Pacific, both ENSO phases feature larger diurnal  $\Delta$ SST than during the whole time series. Instead, the situation is the opposite for the Western Pacific featuring smaller amplitudes during both ENSO phases than when considering the whole dataset. The Central Pacific features similar amplitudes for the “general” and the El Niño diurnal cycles, while La Niña generates a slightly larger amplitude. Overall, Figure 4.5 indicates that both ENSO phases enhance the SST diurnal amplitude in the Eastern Pacific and lower it in the Western Pacific.

The assessment of the relative humidity diurnal cycle observed during the warm and cold phases of ENSO reveals that the diurnal periodicity of this variable is not profoundly affected by the background climatic conditions. As observed before, the diurnal cycle of relative humidity is still largely influenced by the diurnal cycle of near-surface air temperature also under El Niño and La Niña conditions.

The analysis of the SLP diurnal cycle during both ENSO’s phases does not include the Eastern Pacific region due to a lack of measurements during the selected days in this region. However, as regards the other two locations, the SLP diurnal cycle is not considerably altered by the occurrence of El Niño and La Niña events, since the shape, timing and variability of the diurnal cycle are mostly the same as those computed over the full period of analysis.

The wind direction measurements retrieved during both ENSO phases indicate that the wind blows toward the same direction over the entire day, irrespective of the state of ENSO. Presumably, wind direction preserves the same orientation illustrated in Figure 3.47, i.e. toward north in the Eastern Pacific and toward west in the Central and Western Pacific. Hence, the mean diurnal cycle of wind direction is not altered by ENSO. The only notable difference regards the variability of this quantity around the mean diurnal cycle. Figure 4.6 displays the diurnal evolution of the range between the 5<sup>th</sup> and 95<sup>th</sup> percentiles of the distribution of the wind direction anomalies observed at each time interval of the day.

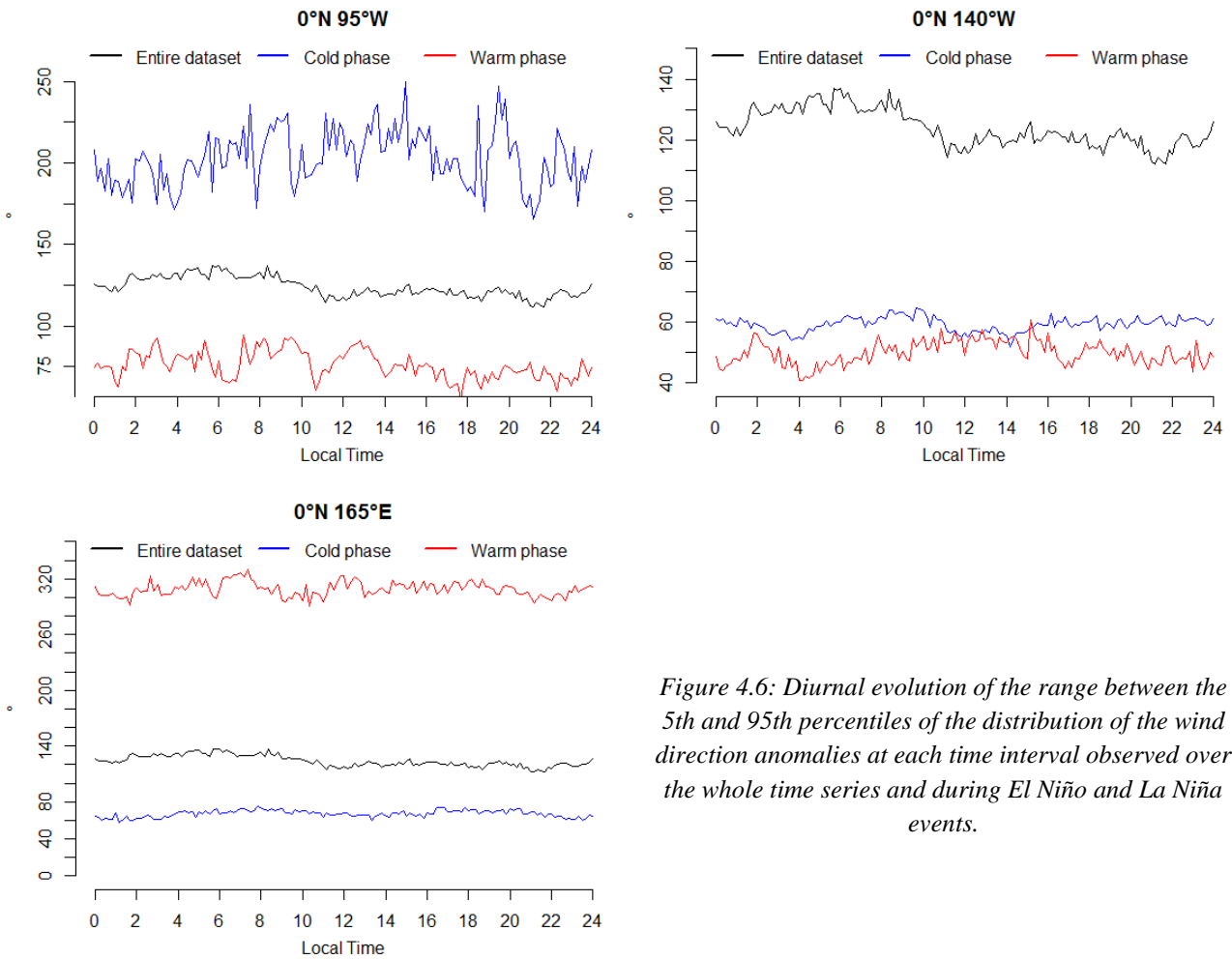


Figure 4.6: Diurnal evolution of the range between the 5th and 95th percentiles of the distribution of the wind direction anomalies at each time interval observed over the whole time series and during El Niño and La Niña events.

La Niña months in the Eastern Pacific and El Niño months in the Western Pacific feature a large variation, even larger than that observed in the diurnal cycle analysis of the whole time series. On the other hand, El Niño events in the Eastern Pacific and La Niña events in the Western Pacific feature a smaller diurnal range measuring in both cases approximately  $70^\circ$ . On the other hand, both ENSO phases reduces consistently the diurnal variability of the wind direction in the Central Pacific, which is consistently smaller than the range observed during the whole dataset.

The results of the analysis of the precipitation diurnal cycles during the warm and cold ENSO phases reveals different characteristics among the different regions. In the Eastern Pacific, more rainfall events occur during La Niña events than during El Niño events. This difference agrees well with the rainfall conditions occurring during the two ENSO phases described in Barry and Chorley (2006) and Ahrens (2012). Indeed, the South-American continent experiences wetter conditions during La Niña events. Over almost 60 days of measurements during El Niño periods, the Eastern Pacific is characterised by rare precipitation events. Instead, over 90 days of measurements during La Niña events, the Eastern Pacific reported the occurrence of several rainfall and light events in the 02-08 and in the 16-20 local time intervals. As regards La Niña events, medium and heavy rainfalls occur more frequently in the early morning between 02 and 08. The Central Equatorial Pacific features a dominant peak at 14 local time both during El Niño and La Niña events. Overall, the Central Equatorial Pacific experiences a lower number of precipitation events during El Niño than during La Niña. During both the warm and cold ENSO phases, precipitation data indicate the occurrence of just light events preferring night-time hours, i.e. from 18 to 06. Overall, the Central Pacific is

characterised by similar rainfalls frequencies for both ENSO phases. This finding does not agree with Barry and Chorley (2006) and Ahrens (2012) reporting the enhancement of convective phenomena in the Central Pacific during the warm ENSO phase, which should result in higher precipitation frequencies during El Niño than during La Niña. In the Western Equatorial Pacific region, El Niño events are characterised by a higher probability of occurrence of light events during 00-08 local time compared to the rest of the day. Instead, medium and heavy rainfalls are not associated to any particular period of the day. During La Niña events, data shows higher occurrences of light events during night-time hours (i.e. from 18 to 06), whereas medium and heavy rainfalls are not bounded to any specific time period.

Overall, the highest rainfall frequencies take place in the Western Pacific during the warm ENSO phase. However, as described by Barry and Chorley (2006) and Ahrens (2012), the Western Pacific features general clear-sky conditions during El Niño periods. Hence, TAO data does not agree with the general ENSO-related meteorological conditions. Overall, the low number of observations recorded during the warm ENSO phase by 0°N 95°W and 0°N 140°W does not allow a robust comparison.

We have seen that El Niño and La Niña events affect differently the mean daily cycles of the analysed variables. Some of them are not much altered by the different background climatic conditions. These variables are the wind speed, relative humidity, sea level pressure and wind direction. The air temperature and the sea surface temperature diurnal cycles, instead, exhibit a markedly altered amplitude, whereas shape and timing remains mostly unchanged. The two variables show a similar amplitude variation according to the type of the event and the geographic location. In particular, the mean amplitudes of the two variables are larger during La Niña events than during El Niño in all locations. Moreover, the difference between the mean amplitudes observed during warm and cold ENSO events is highest in the Eastern Pacific for the air temperature and similar in the Eastern and Western Pacific for the sea surface temperature. The mean diurnal range of the air and sea surface temperature observed during both ENSO phases are larger in the Eastern, almost equal in the Central and lower in the Western Pacific than the mean diurnal ranges observed during the whole time series. As regards precipitation, light rainfall events display a general preference for night-time occurrences, whereas medium and heavy events are rare and not associated to a particular period of the day. Precipitation data shows a common interesting characteristic shared by the different locations: the frequencies of the different rainfall classes are considerably greater than the frequencies computed over the entire precipitation time series. However, often precipitation data do not agree with the description of the general ENSO conditions provided in sub-section 1.2.

### 4.3 The diurnal cycles observed under different local meteorological conditions

This section discusses the results illustrating the analysis of the daily cycles of the different parameters observed during different local meteorological conditions, i.e. sunny and cloudy days, windy and calm days. The analysis of the near-surface air temperature is intended to assess the variation in the magnitude of the radiative heating error.

The differentiation in *sunny*, *moderate-sunny*, *moderate-cloudy* and *cloudy days* is performed considering the sum of the shortwave radiation values observed during the day. Figures 3.4, 3.5, 3.6 and 3.7 are utilised to assess the goodness of this distinction. As reported in Figure 3.4, the distributions of the sums span differently among the three buoys. In fact, the lower sums of the Eastern and Western distributions reach smaller values compared to the lower sums of the Central Pacific. The Central Pacific distribution is more restricted and spans between larger values. Therefore, data indicate that the Central Pacific experiences more homogeneous conditions than the other two regions, which probably resemble a clear-sky mode since the shortwave radiation sums reach high values. Instead, the Eastern and Western Pacific are characterised by lower amounts of incoming solar radiation, which may indicate the occurrence of more frequent covered-sky conditions. The mean diurnal maximum of shortwave radiation increases by approximately  $170 \text{ W/m}^2$  from *cloudy* to *sunny days* in the Eastern Pacific, whereas it grows by  $224 \text{ W/m}^2$  in the Western Pacific. As regards the Central Pacific, the difference in the mean maximum radiation of the two classes is  $97 \text{ W/m}^2$ . Figures 3.5, 3.6, 3.7 illustrate another common aspect: as highlighted by the evolutions of the percentiles, the width of the daily distribution of the shortwave radiation values is larger in *cloudy* than in *sunny days*. Therefore, *cloudy days* experience a highly variable insolation during the 24-hours period, pointing to the probable presence of both clear-sky days and covered-sky days in this class. Probably, covered-sky days occur far more rarely than expected. The frequencies of rainfall events examined in section 4.1 (see Figure 4.3) helps assessing this differentiation. The Eastern and Central Pacific are the regions characterised by the least frequent precipitation events, while the Western Pacific features more rainy conditions. The Central and Western Pacific are respectively, the most dry and wet regions, as indicated by the distribution of the solar radiation sums and the frequency of rainfall events. On the other hand, the Eastern Pacific resembles a more variable pattern. Although the distribution of the solar radiation sums is similar to the one of the Western Pacific, the frequency of the precipitation events approaches the one characterising the Central Pacific. Accordingly, the Eastern Pacific probably experiences frequent cloudy conditions, which do not convert in rainfall events.

The diurnal cycle of wind speed is analysed according to the different wind regimes, i.e. days characterised by strong ( $> 6 \text{ m/s}$ ), moderate (3-6 m/s) and weak ( $< 3 \text{ m/s}$ ) winds. As represented in Figure 3.11, the diurnal variation in strong and moderate winds appears to be similar among the different locations. Instead, weak winds feature more noisy daily cycles. The Eastern Pacific exhibits a peak in strong winds around noon and minima values around midnight. Moderate winds peak in the early afternoon, while the lowest velocities occur during the latter hours of the day. The Central and Western Pacific feature a spike in strong and moderate winds occurring in the morning around 08, while the lowest values are found night-time. The number of days selected according to each wind class reported in Table 3.3 can be used to assess the wind speed daily regime in the different locations. The Central Pacific is dominated by the presence of strong winds, as suggested by the higher number of days lying in *wind class 3* compared to the other classes. The Eastern Pacific shows a preference for moderate wind conditions, while the Western Pacific features more likely strong and moderate wind conditions. The wind speed diurnal amplitudes of strong and moderate winds show a marked geographic variation. In fact, the diurnal amplitude is relatively large in the Eastern

Pacific and smaller in the Central and Eastern Pacific. This finding agrees with the results concerning the diurnal analysis of wind speed and with the findings of Deser and Smith (1997). Moreover, the timing of the wind speed diurnal cycles of strong and moderate winds in the Eastern Pacific are consistent with the timing of the diurnal component detected by Ueyama and Deser (2007).

The wind speed daily cycles are further differentiated according to *sunny* and *cloudy* conditions. The diurnal cycles in the Eastern and Central Pacific do not show a substantial difference between *sunny* and *cloudy days*. Hence, the two different meteorological conditions do not influence on the mean diurnal cycle of wind speed. Instead, the Western Pacific features an almost steady diurnal cycle during *cloudy days*, while *sunny days* resemble the diurnal cycle observed over the entire wind speed time series.

As reported in sub-section 4.1, the analysis of the near-surface air temperature diurnal cycle reveals the presence of the radiative heating error in the TAO buoy measurements. All the four insolation classes and the three wind classes are considered to assess exhaustively the variation of the magnitude variation of the radiative heating error according to the different meteorological conditions.

The analysis of the diurnal cycle associated to the different insolation classes reveals that, as the insolation increases from *cloudy* to *sunny days*, the near-surface air temperature features more and more prominent peaks in the mid-morning and mid-afternoon. Among the different conditions, the *cloudy days* class is the one that features a near-surface air temperature diurnal cycles resembling more similarly the near-surface air temperature daily cycle described in by Ahrens (2012), characterised by a constantly increasing temperature from sunrise to mid-afternoon and a constantly decreasing temperature from mid-afternoon to sunrise (see sub-section 1.3.2). Thus, *cloudy days* incorporate the lowest error among all the considered local conditions. However, considering *cloudy days*, the Central and Western Pacific still display the presence of the double-peak, characterising a sudden increase and decrease in the air temperature nearby the mid-morning and mid-afternoon peaks. Instead, the Eastern Pacific exhibits an increasing near-surface air temperature from sunrise to mid-afternoon. *Sunny days* display the most prominent mid-morning and mid-afternoon peaks in each examined region. The highest amount of incoming solar radiation triggers an air temperature increase of almost 0.5 °C in between 06-08 in each region. The height of the second peak is maximum in the Eastern Pacific and minimum in the Western Pacific. *Moderate-cloudy* and *moderate-sunny* days show intermediate conditions featuring almost the same error's magnitude. The amplitude of the mean diurnal cycles of air temperature observed during different meteorological conditions are compared in Figure 4.7 for each analysed location.

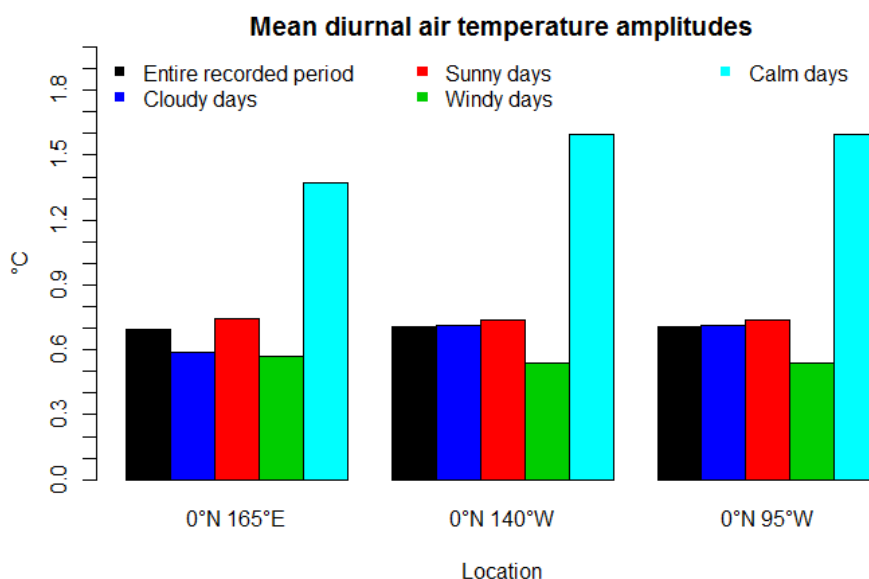


Figure 4.7: Amplitudes of the mean diurnal air temperature cycles observed during different meteorological conditions for each analysed location.

The amplitude of the diurnal near-surface air temperature cycle observed during *sunny days* is larger than the one observed during *cloudy days*. In fact, as the diurnal air temperature range is defined by the difference between the mid-afternoon peak (highest diurnal value) and the pre-dawn temperature minimum (lowest diurnal values), the radiative heating error affects also the diurnal near-surface air temperature range by modifying the height of the mid-afternoon peak. The amplitudes observed during *sunny* and *cloudy days* differ by 0.34 °C in the Eastern Pacific, 0.02 °C in the Central Pacific and 0.16 °C in the Western Pacific. Figures 3.19 and 3.21 indicate the higher diurnal variability assumed by measurements of air temperature during *cloudy days* than during *sunny days* in the Eastern and Western Pacific.

The diurnal cycles of near-surface air temperature observed in the different locations varies similarly among the different wind classes. In particular, as illustrated in Figures 3.22, 3.23 and 3.24, increasing wind speeds progressively lower the height of the air temperature peaks. However, strong winds do not reduce the sudden near-surface air temperature increase between 06 and 08 local time. The rapid air temperature decrease occurring in between 17 and 18 is still present in each wind class. As illustrated in Figure 4.7, the wind velocity impacts largely on the diurnal near-surface air temperature amplitude, featuring the largest amplitude during weak winds and the smallest amplitude during strong winds. In particular, strong winds render the near-surface air temperature approximately stable from 08 to 17 local time in the Eastern and Western Pacific. The mean amplitudes observed during strong and weak winds differ by 1.40 °C in the Eastern Pacific, 1.05 °C in the Central Pacific and 0.80 °C in the Western Pacific. The difference of the near-surface air temperature amplitudes observed between windy and calm days are much larger than the differences observed between sunny and cloudy conditions.

These results are consistent with Anderson and Baumgartner (1998), indicating a large radiative heating error associated to abundant incoming solar radiation and low wind speeds. As described in sub-section 1.3.3, the solar radiation enhances the heating of the naturally ventilated shield, thus warming the air contained in the shield's chamber, whereas greater wind speeds strengthen the convective cooling of the shield and circulate the contained air. However, all the analysed local meteorological conditions appear to feature a mean near-surface air temperature cycle affected by the radiative heating error. The exact quantification of the error is not possible due to the lack of accurate near-surface air temperature measurements. The evaluation of the radiative heating error may be performed using the empirical model formulated by Anderson and Baumgartner (1998) predicting the error in the air temperature measurements of one buoy on the basis of the shortwave radiation and wind speed measurements collected by the same buoy. However, the model requires the estimation of three empirical coefficients, which are linked with the structure of the buoy and its sensors, through the comparison of erroneous and accurate measurements. Therefore, the estimation of the diurnal near-surface air temperature cycle should be performed utilising other sources of data. The radiative heating error is probably affecting also the other moored arrays, i.e. PIRATA and RAMA, since the buoys composing these arrays are equipped with the same naturally ventilated sensor (PMEL, 2017b). The presence of this error should be taken into consideration by the managing agencies such as NOAA and PMEL due to the large use of their data in climate studies. Moreover, moorings' data are used for other purposes such as the effective comparison of in situ surface air temperature with atmospheric model products (Anderson and Baumgartner, 1998).

A near-surface air temperature diurnal evolution not affected by the direct solar radiative heating error is investigated here to determine whether conditions exist for which the error does not influence the observations of the moorings. To this purpose, a procedure is designed to distinguish days receiving the lowest possible amount of solar radiation throughout the day. As an upper bound to this condition, the 20<sup>th</sup> percentile of the distribution of the shortwave radiation measurements observed at each time step is calculated. Then, those days presenting at least 90% of shortwave radiation measurements lower than the 20<sup>th</sup> percentile at each time step are selected. Solar radiation is chosen as the selector variable since, as mentioned above, it is negatively correlated with the intensity of the error, more strongly than the wind speed. This procedure is performed on the three buoys considered in the main analysis. Figure 4.8 displays the near-surface air temperature diurnal cycles observed during the selected days.

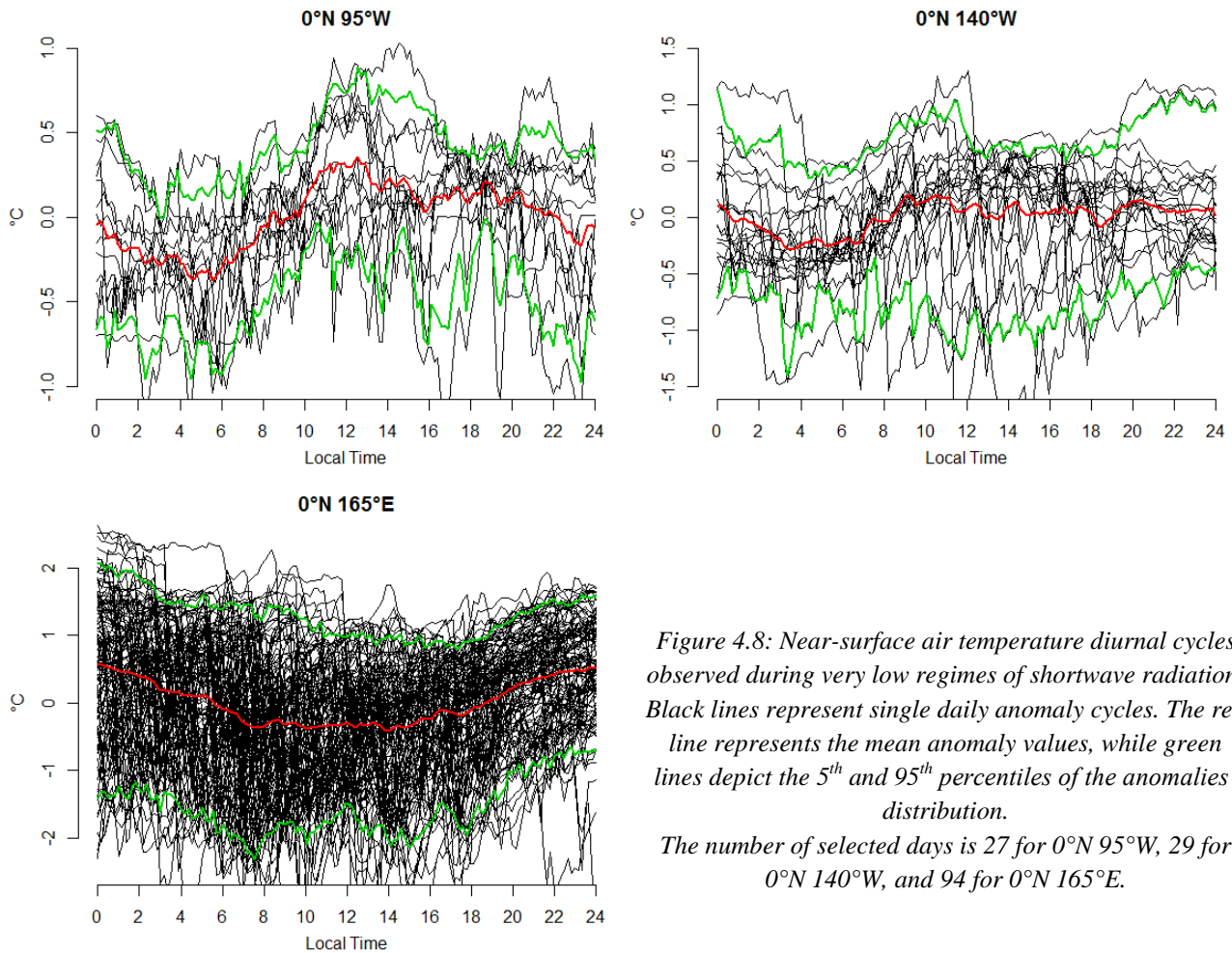


Figure 4.8: Near-surface air temperature diurnal cycles observed during very low regimes of shortwave radiation. Black lines represent single daily anomaly cycles. The red line represents the mean anomaly values, while green lines depict the 5<sup>th</sup> and 95<sup>th</sup> percentiles of the anomalies' distribution.

The number of selected days is 27 for 0°N 95°W, 29 for 0°N 140°W, and 94 for 0°N 165°E.

The diurnal cycle of near-surface air temperature show different behaviours at the three buoys. The Eastern Pacific exhibits a constantly increasing temperature starting from 04 in the morning to around mid-day. Afterwards, temperature decreases until sunrise even though it remains approximately stable between 16 and 19. The Central Pacific features a mean diurnal cycle characterised by increasing temperature between 06 and 10-11, while temperature remains constant until mid-night. Then, from 00 to 04, air temperature decreases. 0°N 165°E shows an unusual air temperature diurnal evolution. Indeed, all the observed diurnal cycles exhibit a decreasing temperature from mid-night to 08 and an increasing temperature from 14 to mid-night. In between 08 and 14, the air temperature is approximately steady. Hence, the air temperature is lower during day-light hours and higher during night-time hours. The three examined mean diurnal cycles do not follow the schematised air temperature cycle described in sub-section 1.3.2 and illustrated in Figure 1.4. This difference points to the occurrence of other phenomena influencing the diurnal evolution of air temperature in the selected days, such as rainfall episodes. Thus, the investigation of an unaffected air temperature cycle should rely on other data sources, such as an automatic air pump as the one utilised by Anderson and Baumgartner (1998).

The analysis of the SST diurnal cycle during different meteorological conditions reveals that the shape of the SST diurnal evolution is not altered. However, the amount of incoming solar radiation and the wind speed regime largely affect the diurnal  $\Delta$ SST. As illustrated in Figures 3.30 and 3.31, results report higher diurnal amplitudes during sunny and calm days than during cloudy and windy days. These findings agree with previous results reported in sub-section 1.3.6 suggesting the existence of the same pattern. Insolation has a great effect on the SST diurnal variation due to the associated warming of the first few meters of the ocean.

This warming enhances water's stratification, allowing the warmest waters to reside nearby the surface. In addition, winds enhance the mechanical mixing of the superficial waters and the latent heat exchange between air and sea, causing the oceanic waters to lose heat. The diurnal  $\Delta$ SST difference between *wind class 1* and *wind class 2* are larger than those calculated between *sunny* and *cloudy days* in each geographic location, indicating that the SST is more susceptible to wind velocity than to insolation. This hypothesis agrees with Clayson and Weitlich (2007) who suggest that, in the tropical areas, the wind daily regime explains better the diurnal  $\Delta$ SST than the solar radiation.

The daily  $\Delta$ SST exhibits some interesting features. During *cloudy days*, the different locations share similar mean diurnal amplitudes, whereas they feature different  $\Delta$ SSTs during *sunny days*. The difference of the mean diurnal amplitude between *sunny* and *cloudy days* is the largest in the Eastern Pacific (0.61 °C) and the lowest in the Central Pacific (0.14 °C). Yet, the mean  $\Delta$ SST difference between windy and calm days is the greatest in the Western Pacific (0.79 °C) and the lowest in the Central Pacific (0.54 °C). Figure 3.31 reports an interesting aspect consisting in a decreasing SST during days of strong winds in the Eastern Equatorial Pacific. Indeed, the diurnal  $\Delta$ SST (0.52 °C) depends entirely on the decreasing diurnal trend rather than the subsequent warming and cooling of the sea surface. Thus, strong winds limit markedly the diurnal  $\Delta$ SST in the Eastern Pacific, enhancing the SST cooling during afternoon and evening. Future studies should further assess this aspect and its functioning. The SST diurnal evolution of those days lying before and after a windy day should be examined to determine whether the occurrence of strong winds may lead to a change in the SST regime. However, previous studies have not recognised the existence of this aspect, suggesting that this observation may be based on misleading data. Indeed, assuming that the selected windy days are contiguous days, the observed decreasing trend may be related to a long-term variation.

The diurnal evolution of relative humidity is not altered profoundly by the occurrence of different meteorological conditions. The daily variation of this variable remains strongly linked with the diurnal variation of the near-surface air temperature even during different meteorological conditions i.e. cloudy, sunny, calm and windy days. Thus, the relative humidity is affected almost only by the same processes influencing the near-surface air temperature.

The analysis of the SLP diurnal cycle observed under different meteorological conditions indicates the insensitivity of the SLP to different shortwave radiation and wind speed regimes in each of the three locations. The daily SLP cycle remains composed by two maxima and two minima points occurring at the same time as recognised in the SLP diurnal cycle analysis (see sub-section 4.1). In addition, the differences between the primary maximum and minimum are analogous to the ones computed over the whole SLP time series.

The diurnal cycles of wind direction observed during the occurrence of different local meteorological conditions lack of a notable diurnal variation, suggesting that the wind direction remains stable throughout the day. The variation of the single diurnal cycles over the day illustrates an interesting characteristic. As reported in Figure 3.50, the range of the percentiles is larger during calm days and smaller during windy days in each of the three different locations. Therefore, the occurrence of weak winds is associated to a highly variable wind direction. Instead, *sunny* and *cloudy days* feature similar wind direction diurnal cycle, thus suggesting the insensitivity of the wind direction to the local insolation conditions in the three locations.

The analysis of the precipitation diurnal cycle during days characterised by the presence of weak and strong winds reveals that, generally, all the rainfall classes display a higher probability of occurrence during night-time hours than during day-light hours in each location. Data exhibit the presence of a dominant peak in each location with similar characteristics as those highlighted in sub-section 4.1. These peak are not considered in this assessment. The Eastern Pacific features a very low number of occurrences of all the rainfall categories during both windy and calm days, and a general preference for the evening. Calm days in the Central Pacific

are characterised by higher occurrences of light and medium events in the evening hours from 17 to 24. Instead, windy days shows greater occurrences of rainfall and light events in the early morning hours from 02 to 06, whereas the occurrences of medium and heavy events are much lower and indicate a general preference for the whole night-time period from 18 to 06. Calm days in the Western Pacific feature the lowest occurrences of light and medium events during the morning from 06 to 11, whereas the highest occurrences occur during the night from 18 to 03. Heavy events show a different pattern, preferring the afternoon and early evening period from 13 to 20. Windy days exhibit higher occurrences of each rainfall category during night-time from 21 to 06, with the highest counts occurring in the early morning around 02. The Western Pacific shows higher occurrences of medium and heavy events than the other two regions of the Pacific Ocean during both calm and windy days. Overall, this analysis reveals that precipitation events observed during wind and calm days occur more likely in night-time period. Calm days show to prefer the evening and the latter part of the day, generally from 18 to 24, whereas windy days exhibits higher precipitation occurrences in the early morning.

The differentiation based on meteorological conditions shows the influence of the solar radiation and wind speed on different parameters. The most affected variables are the near-surface air temperature and the SST. Both the parameters exhibit a lower diurnal amplitude during conditions of strong winds and limited solar radiation. However, the variation of amplitude of the near-surface air temperature cycle is due to the variation of the mid-afternoon peak, which in turn is largely explained by the variation of the radiative heating error under different meteorological conditions. In the Central and Western Pacific, days characterised by the presence of strong winds show a wind velocity peak in the morning around 07-08. Moreover, windy days observed in the same locations are characterised by the presence of a clear early-morning peak in rainfall and light events. Therefore, windy days feature the highest wind velocities after the occurrence of precipitation phenomena in the Central and Western Pacific. The relative humidity, SLP and wind direction do not show evidences for a strong influence of the wind speed and insolation conditions on their diurnal cycles.

## 4.4 The variation of the diurnal cycles over the entire recorded periods

The variation of the diurnal cycles of the different parameters over the long period (i.e. over the entire recorded period of each variable) is examined through the representation of smoothed hourly time series. Moreover, the variation of the daily cycles is assessed against the average evolution of the entire time series for each variable.

The wind velocity, SLP and wind direction do not display the presence of a particular pattern in the evolution of their diurnal cycles. Furthermore, the diurnal cycles of these variables do not exhibit any correlation with their long-term evolutions in the three locations.

The evolutions of the near-surface air temperature and SST smoothed hourly time series are characterised by a periodic increase in the diurnal temperature range. As illustrated in Figures 3.25 and 3.32, this higher diurnal temperature variation develops in phase with the warm periods of the yearly seasonal cycle, occurring in the boreal spring. This aspect is distinctly observed in the Eastern and Central Pacific but not in the Western Pacific. The Western Pacific lacks of a distinct yearly seasonal cycle in both the near-surface air temperature and SST, which may not generate the same periodic diurnal variation as in the other two locations.

Overall, the near-surface air temperature and SST hourly anomalies resemble the findings of the diurnal cycle analysis. Indeed, the coolest hours are regularly those situated between 00 and 06 for the near-surface air temperature and between 06 and 12 for the SST. The warmest hours are constantly found in the 12-18 interval for both the air temperature and the SST.

The evolutions of the relative humidity hourly time series display a similar fluctuation as the near-surface air temperature and the SST. Indeed, Figure 3.39 illustrates a larger diurnal variation in phase with regimes of higher relative humidity occurring in the boreal spring. This pattern characterises only the Eastern and Central Pacific in the first years of records. The Western Pacific does not exhibit the same variation, probably due to the absence of a clear seasonal cycle. The higher diurnal variation of the relative humidity are likely due to the correspondent air temperature's fluctuation and not to a particular process, since, as observed in section 4.1, the relative humidity is strictly related to the air temperature.

The near-surface air temperature and SST are characterised by a periodic increase in the diurnal temperature range. This periodicity is in phase with the yearly seasonal cycle of the two variables; in particular, larger diurnal amplitudes are associated with warmer temperatures. The periodic increase in the diurnal ranges of the two variables can be explained by considering the long-term evolution of the two main factors affecting air and sea-surface temperature, i.e. solar radiation and wind speed. As evidenced in section 4.3, large amounts of incoming solar radiation and low wind speeds generate a great diurnal range in the near-surface air temperature and SST. However, Figure 3.2 reveals a lack of a yearly seasonal cycle in the incoming radiation in the Eastern and Central Pacific. Therefore, solar radiation appears to be unrelated with the periodic change of the amplitude of the diurnal temperature. Instead, wind velocity is characterised by a noticeable yearly seasonal cycle in the Eastern and Central Pacific, as illustrated in Figure 3.8. Moreover, periods of average weak winds occur in phase with periods of warmer temperatures, i.e. during boreal spring. The wind speed may be the factor causing the periodic increase in the diurnal amplitudes of the near-surface air temperature and SST. To test this hypothesis, the average temporal evolution of the wind speed is displayed together with the average evolutions of the diurnal amplitudes of air temperature and SST. The three time series are smoothed according to the method described in sub-section 2.2.6.

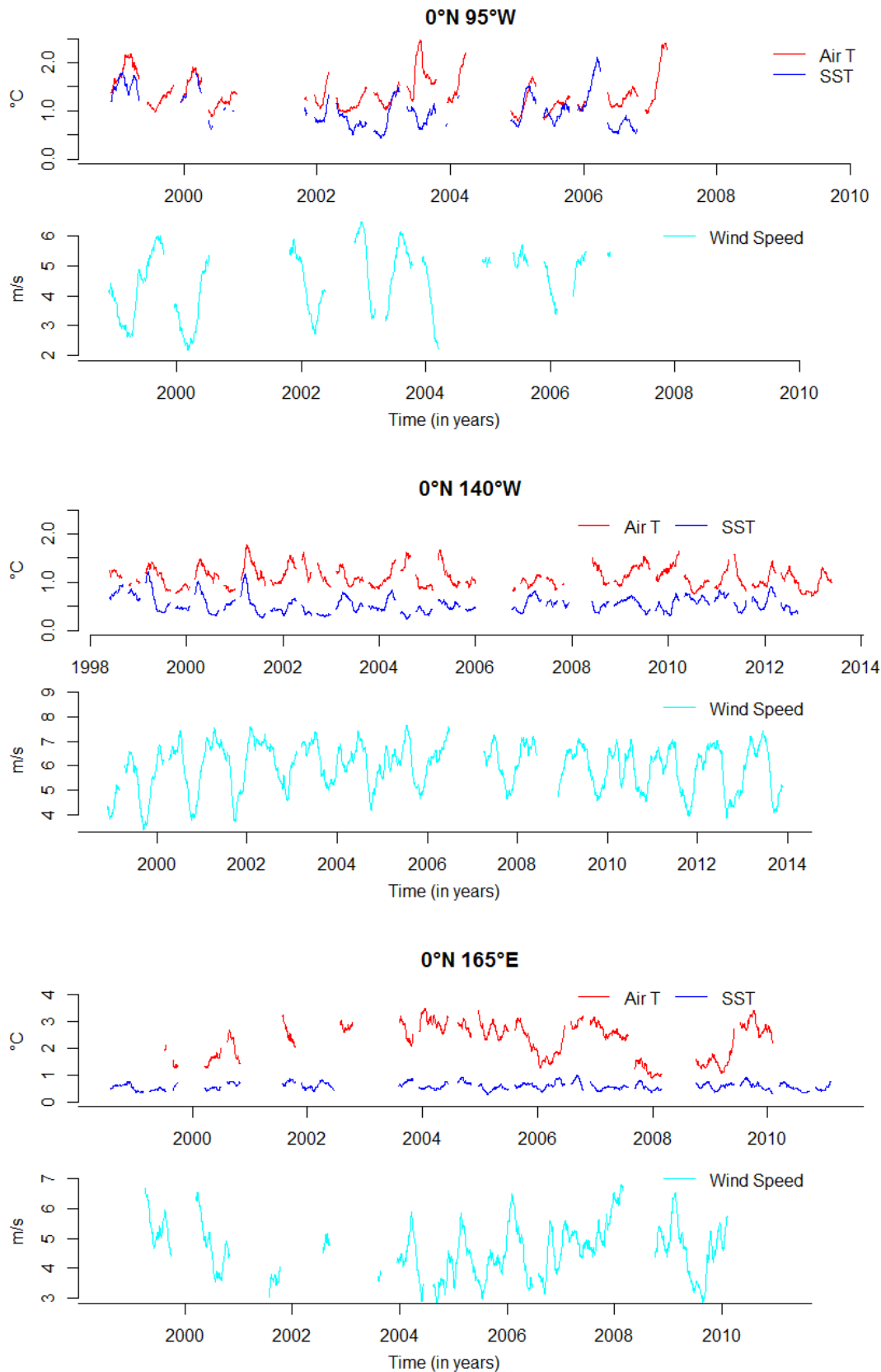


Figure 4.9: Comparison between the average diurnal amplitude evolutions of near-surface air temperature, SST and the average wind speed for the three locations. The upper graph reports the smoothed evolutions of the diurnal amplitudes of the air temperature (red line and SST (blue line) . The lower graph reports the wind speed smoothed evolution (light blue line).

The evolution of the diurnal amplitudes appears to be related with the average wind speed. Indeed, strong winds often reduce the diurnal range of near-surface air temperature and SST, whereas weak winds are associated to growing diurnal amplitudes. As regards the Central Pacific, this behaviour can be easily observed over the whole recorded period. Instead, the Eastern and Western Pacific do not display regularly this pattern, due also to the presence of frequent unrecorded periods. Besides the diurnal range, the average wind speed is correlated also with the long-term evolution of these three variables. Indeed, strong winds feature cooler temperatures, whereas weak winds are linked to warmer temperatures, as highlighted in Figures 3.24, 3.31 and 3.38. Overall, the wind speed yearly fluctuation appears to drive both the variation of the diurnal amplitude and the yearly seasonality of near-surface air temperature and SST in the Equatorial Pacific Ocean.

## 4.5 Relations between variables

The assessment of the relations existing between the different variables is performed through the cross-correlation function. The significant correlations assessed in section 3.9 are summarised in Figure 4.10. The single points identify the value of the maximum correlation coefficients among two variables and its specific lag. The significant correlations are reported separately for each location.

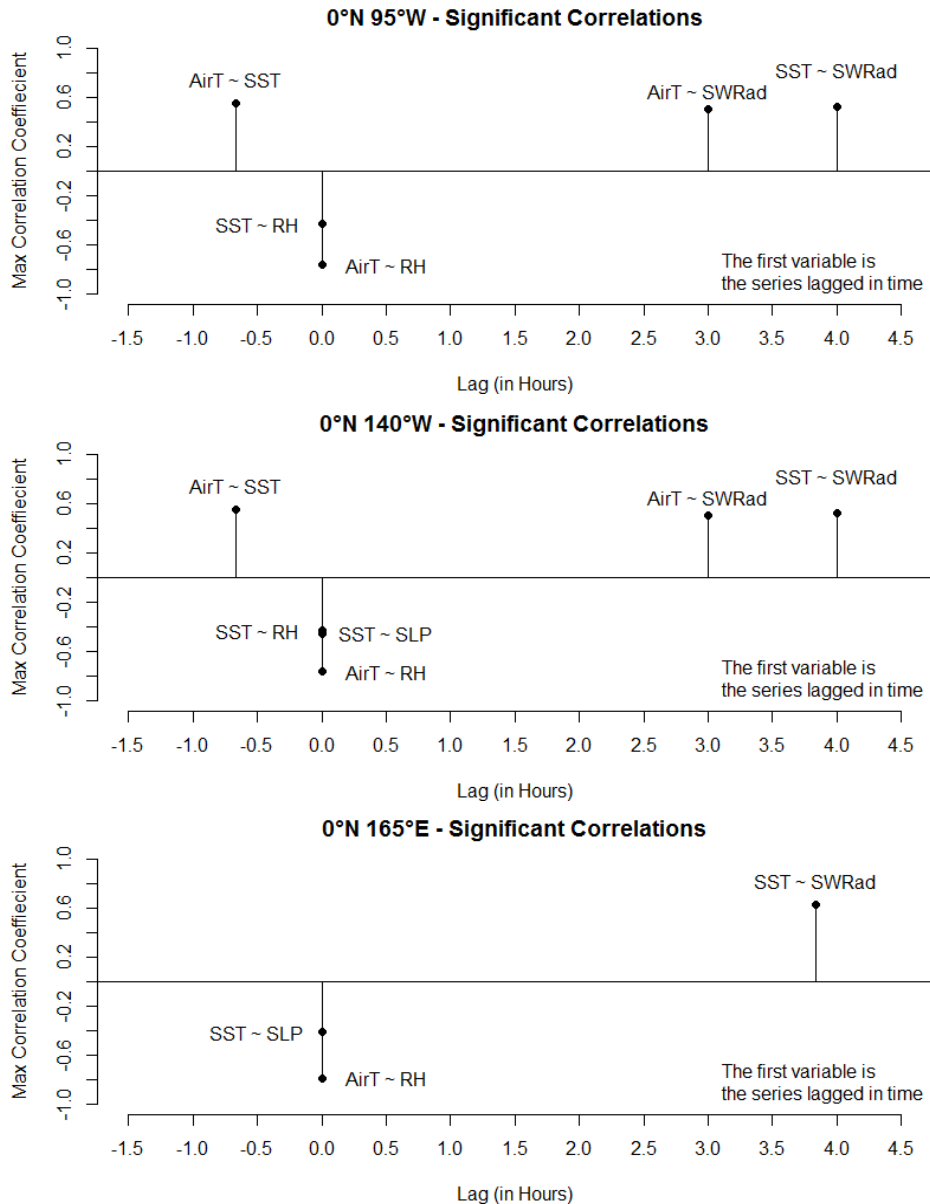


Figure 4.10: Summary of significant relations for each location. Correlation coefficients greater than 0.4 are assumed to indicate a significant correlation.

Overall, the cross-correlation analysis confirms the findings of the assessment of the diurnal cycles. The near-surface air temperature and the SST show a significant positive correlation in the Eastern and Central Pacific. The correlation coefficient is maximum as the SST is lagged by 40/50 minutes and reaches 0.5. The presence of the radiative heating error probably lowers the maximum correlation coefficient since, as

explained in sub-section 1.3.2, the near-surface air temperature measurements should nearly follow the SST evolution. In the Western Equatorial Pacific, the two parameters do not show a significant correlation on a diurnal scale. The near-surface air temperature and the SST appear to be significantly correlated with the shortwave radiation in the Eastern and Central Pacific. The maximum correlation value, reaching 0.5, is linked to lagged near-surface air temperature and SST by, respectively, 3 and 4 hours. This finding is consistent with Ahrens (2012) indicating the lagged response of the near-surface air temperature and SST to solar forcing. The Western Pacific features only a significant correlation between the shortwave radiation and the SST lagged by 4 hours. The air temperature and the relative humidity feature a strong negative correlation at lag 0 in each location, confirming the previous observation that the relative humidity is almost totally dependent on air temperature.

## 4.6 Limitations and recommendations

This chapter addresses a critical discussion of different aspects of the presented work. First, the accuracy of the estimation of the diurnal cycle is evaluated. Then, the goodness of the analysis concerning the role of ENSO on the diurnal cycles is inspected. Furthermore, the method used in the analysis of the diurnal cycle under different local meteorological conditions is examined.

The diurnal cycle analysis is based on the computation of the diurnal anomalies for each day of the recorded 10-minutes time series. Then, the mean diurnal cycle is calculated by averaging the anomalies at each time step. Since the distribution of the anomalies at each time step may present some outliers, the mean may not be a robust estimator. However, the goodness of the arithmetic mean increases with the number of available observations. Hence, in this thesis work, the averages computed using a small number of days are the ones which may be noticeably altered by the presence of outliers. Specifically, the variables and the associated selection incorporating the smallest number of days are:

- Wind speed in *wind class 1* in the Central Pacific (16 days).
- Wind speed during the “warm” ENSO phase in the Eastern Pacific (30 days).
- Air temperature in *wind class 1* in the Central Pacific (32 days).
- SST in *wind class 1* in the Central Pacific (31 days).
- SLP during the “warm” ENSO phase in the Eastern Pacific (0 days).
- The SLP in *wind class 1* in the Eastern (25 days) and Central Pacific (11 days).
- Wind direction in *wind class 1* in the Central Pacific (38 days).
- Wind direction during the warm ENSO phase in the Eastern Pacific (31 days).
- Precipitation in *wind class 1* in the Central Pacific (36 days).

All the above selections incorporate less than 40 days i.e. less than 40 observations for each time step. Thus, results based on these selections should be interpreted cautiously.

This limitation motivates the search of possible modifications to the diurnal cycle analysis. Future works may assess the mean diurnal cycle by considering only those measurements lying in the interval between the 5<sup>th</sup> and 95<sup>th</sup> percentile of the data distribution of each time step. Thus, this method allows the computation of a more robust mean, as it would be less influenced by outliers.

As reported in section 4.1, the precipitation diurnal cycle is not clearly consistent with previous studies. This dissimilarity may be attributed to the approach used to analyse the data. Indeed, several studies cited in sub-section 1.3.7 (Augustine, 1984; Meisner et Arkin, 1987; Janowiak et al., 1994; Yang and Slingo, 2001; Serra and McPhaden, 2004; Bowman et al., 2005) utilised the so-called “Harmonic analysis”. This approach involves the estimation of the sinusoidal function that accounts for most of the variance in the data. The best combination of the sinus amplitude and phase is utilised to infer strength and the timing of the diurnal cycle. However, this approach is valid almost only for diurnal cycles resembling a sinusoidal evolution, thus featuring a regular increase (decrease) after the minimum (maximum) point.

The method used for the assessment of the diurnal cycles occurring during ENSO’s warm and cold phases may be influenced by some possible limitations. The analysis is conducted utilising the Southern Oscillation Index (SOI) values for every month from 1998 to 2017. Days belonging to the different parameters are selected considering the SOI value of the associated month. As reported in sub-section 2.1.3, the TAO time series are composed by different missing data periods, sometimes occurring during an ENSO event. Therefore, regardless of the number of selected months, the number of selected days varies independently leading sometimes to a lack of data for an ENSO event in a particular location. For example, the number of days recorded during El Niño events in the Eastern Pacific is close to 30 for many variables. As a

consequence, the observed diurnal cycle may not represent the true daily cycle occurring over the different months associated to an ENSO event.

The selection approach utilised to distinguish between the warm and cold ENSO phases is limited also by the presence of a yearly seasonal cycle throughout the entire time series. In particular, the analysed diurnal cycles may be more deeply influenced by the yearly periodicity and less by the occurrence of an ENSO event. One of the possible influencing seasonal variations is the yearly evolution of the Inter-Tropical Convergence Zone (ITCZ) and the South Pacific Convergence Zone (SPCZ). As highlighted in section 1.2, the different regions of the Pacific Ocean experience periods of both developed convective phenomena and limited convective activity. However, results concerning the analysis of near-surface air temperature and SST oppose partly this hypothesis. As reported in Tables 2.8-2.9, the selected months linked to both events are often January and February. However, both variables exhibit different mean amplitudes associated to the two ENSO phases. Hence, this variation is likely caused by ENSO and not by the yearly seasonality, since the mean amplitudes are observed in the same months of different years. On the other hand, if the selected months were only interested by the yearly seasonal variation, the amplitudes difference should be small and negligible.

Future studies should consider also the strongest events to determine the possible influence of “background” climatic conditions in the diurnal cycles. The strongest El Niño events could be evaluated by means of other ENSO-related indexes. A list of all ENSO-related indexes is provided by Barnston (2015), which includes the Oceanic Niño index (ONI), Equatorial Southern Oscillation Index, SST indexes (namely Niño1, Niño2, Niño3 and Niño4), outgoing longwave radiation indexes and wind indexes.

The assessment of the diurnal cycles under different local insolation conditions has been performed through the definition of different classes, i.e. *sunny*, *moderate-sunny*, *moderate-cloudy* and *cloudy*. This differentiation is performed through the sum of the shortwave radiation values characterising each day. Days featuring sums lower than the 20<sup>th</sup> percentile of the sums’ distribution are defined as *cloudy*, whereas those with sums larger than the 80<sup>th</sup> percentile are distinguished as *sunny*. Accordingly, this approach assumes that 20% of all the recorded days presents sky-covered conditions, while another 20% exhibits fully cloud-free conditions. This assumption may not be valid in each location. For instance, as examined in section 4.1 and 4.3, the Central Pacific displays a very limited range of the sums’ distribution and a restricted variation of the shortwave radiation diurnal cycle among *sunny* and *cloudy* days. Thus, in this location, the percentage of cloud-covered days over the total number of recorded days may be not as high as the 20%, but smaller. Another limitation of this approach is linked to the potential variability of local insolation conditions over the day. Indeed, cloudy conditions may turn into sunny during the course of the day. The procedure based on the shortwave radiation sums is not able to discriminate between days featuring cloudy or sunny conditions occurring throughout the entire day. In section 4.3, an alternative method to distinguish days receiving the smallest amounts of solar radiation is performed to discriminate a diurnal cycle of air temperature not affected by the radiative heating error. This method selects days characterised by diurnal shortwave radiation values smaller than a certain threshold. This procedure permits the recognition of those days receiving the lowest solar radiation over the entire recorded period. However, it selects a small number of days, thus presenting again the problem linked to the examination of small amounts of data.

The assessment of the diurnal cycles of the different variables under different meteorological conditions may be enriched by focusing on days featuring rainfall events. A new class should be created (*rainy days*), which incorporates days featuring precipitation intensities greater than 0.5 mm/hr during the entire day or, more realistically, just during a defined time interval. This approach shall reveal the influence of convective phenomena on the diurnal evolution of different variables. In particular, it could be interesting to examine the variation between *sunny* and *rainy* days in the near-surface air temperature, SST, wind speed and relative humidity.

## 5. Conclusions

This thesis aimed to characterise the diurnal cycles of different near-surface atmospheric and oceanographic parameters in the Eastern, Central and Western Equatorial Pacific. In addition, the diurnal cycles are differentiated according to the local meteorological conditions and the variations in the general “background” climate state.

The solar radiation features a diurnal evolution characterised by the presence of one peak, occurring at noon. The wind speed displays a mid-day peak in the Eastern Pacific, while it shows the highest values in the morning around 8 in the Western and Central Pacific. However, the diurnal variation of wind speed in the Western and Central Pacific is practically negligible. Days characterised by the presence of strong and moderate winds follow precisely these patterns, while calm days do not exhibit a significant diurnal variation.

The near-surface air temperature exhibits a similar diurnal cycle in the different oceanic regions. This cycle is composed by one mid-morning peak and one mid-afternoon peak. Although this diurnal evolution may suggest the occurrence of convective phenomena acting as a thermal regulator for the lower atmosphere, it proves the presence of a radiative heating error affecting the air temperature measurements. An extended analysis confirmed that the error affects the air temperature measurements of all TAO equatorial mooring. This thesis further showed that the magnitude of the radiative heating error varies accordingly to the local meteorological conditions. In particular, the error is smaller under cloudy and windy conditions, whereas it grows with increasing solar radiation and decreasing wind speeds. Cloudy conditions, i.e. a damped solar radiation, are more efficient in limiting the growth of the error than windy conditions. Therefore, the error appears to be more sensitive to the incoming solar radiation and the associated warming of the naturally ventilated shield than to the wind speed and the correlated convective cooling of the shield. Overall, the air temperature increases from sunrise to a few hours before sunset, and decreases from evening to dawn. However, it remains approximately stable during the latter hours of the night between 03 and 06, indicating the presence of a warming process that balances the radiative cooling. This observation does not agree with previous studies, indicating a constant reduction of the air temperature during night.

The diurnal cycle of sea-surface temperature (SST) is consistent among the three locations and features a sinusoidal shape, peaking in the mid-afternoon and with minimum values located in the morning near 07-08. The shape of the SST diurnal evolution is directly related to the diurnal cycle of shortwave radiation, which warms the superficial layers of the ocean in the morning and early afternoon. However, the diurnal SST range ( $\Delta$ SST) is primarily dependent on the strength of the wind. Indeed,  $\Delta$ SST is lowered by strong winds, whereas it is enhanced by weak winds. The diurnal  $\Delta$ SST is found to be maximum in the Eastern Pacific. Strong winds in the Eastern Pacific appear to constantly cool the SST over the day, thus suggesting the idea that winds may control even the long-term variation of the superficial temperature of the ocean in this region. The SST shows different cooling rates over the 24-hours period: it decreases faster after reaching the diurnal maximum, and then declines slowly approximately after 18. This evidence, which was not identified in previous studies, suggests the existence of a warming process reducing the SST cooling during night-time hours, and thus limiting the diurnal  $\Delta$ SST. Possibly, the two “unknown” warming processes reducing the night-time cooling of SST and air temperature are probably correlated and may be part of a feedback loop. Future works should further assess this conclusion and examine its entity and functioning.

The relative humidity features a diurnal cycle that is principally dependent on the near-surface air temperature diurnal cycle over the whole recorded period, even under different background climatic and local meteorological conditions. Thus, the relative humidity appears to be strictly dependent on the same processes affecting the air temperature.

The SLP shows a regular diurnal cycle, which does not modify in response to different local meteorological and climatic conditions. The SLP diurnal cycle is consistent among the three locations and features a

sinusoidal shape with two maxima and two minima. The primary maximum and minimum are encountered at 09-10 and at 15-16, respectively. The secondary maximum and minimum develop at 22-23 and at 03-04, respectively. The amplitude of the observed mean SLP diurnal cycles is regularly above 3 hPa in the different locations.

The diurnal evolution of the wind direction is steady and characterised by a large variability in each of the three analysed locations. The wind blows constantly toward the same direction over the day, even during different local meteorological and climatic conditions. Overall, the air moves predominantly toward north in the Eastern Equatorial Pacific and toward west in the Central and Western Equatorial Pacific. The only notable feature is that the variability of wind direction is maximum during weak winds and minimum during strong winds.

Unlike previous findings, the analysis of precipitation data does not exhibit a clear dominance of early morning rainfalls. In particular, light rainfalls (0.5-3 mm/hr) occur more frequently during early morning, whereas medium (3-10 mm/hr) and heavy (>10 mm/hr) rainfalls apparently occur randomly throughout the day. All the equatorial TAO buoys exhibit the presence of an error, identified as a dominant peak in light rainfalls in one specific hour. However, averaging the 10-minutes precipitation data into hourly intensities removes these single dominant peaks, suggesting the occurrence of an anomalous routine activity of the precipitation sensor.

The assessment of the diurnal cycles during the two phases of ENSO, i.e. El Niño and La Niña, reveals the general insensitivity of several variables, such as wind speed and direction, precipitation, relative humidity and SLP. However, the SST and air temperature present a noteworthy characteristic: the diurnal amplitudes of these two variables are the largest during the “cold” ENSO phase in the Eastern Pacific, even though the presence of strong winds related La Niña should lower the diurnal range in SST and air temperature. Thus, this finding is not consistent with the general characteristics of La Niña events.

The near-surface air temperature and SST share common aspects regarding the variation of their diurnal cycle. These variables exhibit an enhanced diurnal variation in phase with the annual regime of warmer temperatures occurring between boreal winter and spring. Often, the wind speed appears to influence considerably these two periodicities since periods of greater velocities are linked to both lowered diurnal amplitudes and low temperatures, whereas periods of weak winds are associated to increased daily amplitudes and warmer temperatures. Hence, the wind speed is found to control both the diurnal and annual variability of air temperature and SST mostly in the Equatorial Eastern and Central Pacific Ocean.

The examination of the relations existing between different variables on a diurnal scale partly confirms the results of the diurnal cycle assessment. Indeed, the air temperature and SST exhibit a maximum correlation as the air temperature is delayed in time by almost 40/50 minutes. In addition, the shortwave radiation reveals the maximum correlation with the air temperature and SST as the first variable is lagged by 3 hours and the second one by 4 hours.

This thesis work determined the diurnal cycle of different near-surface atmospheric and oceanographic parameters in the Equatorial Pacific Ocean and their variability under different meteorological and climatic conditions as well as over the long term. The results of this assessment are mostly consistent with previous studies. However, findings outline the presence of few interesting aspects, which may stimulate further research works. The TAO air temperature measurements are affected by a radiative heating error, which overestimates the oceanic ambient air temperature. This error may have altered various derived data products and the results of several research works, since the TAO data are broadly utilised for different purposes. The night-time “warming” effect on the air temperature and SST implies the presence of another recursive heating forcing, other than the solar radiation, acting in the 24-hours period. The wind, by controlling the diurnal and annual variations in air and sea-surface temperature, replaces the solar radiation as the most influencing factor over equatorial regions, where, indeed, the incoming radiation is almost steady over the whole year.

## 6. References

- Ahrens, C. D. (2012). *Meteorology today: an introduction to weather, climate, and the environment*. Cengage Learning.
- Anderson, S. P., & Baumgartner, M. F. (1998). Radiative heating errors in naturally ventilated air temperature measurements made from buoys. *Journal of Atmospheric and Oceanic Technology*, 15(1), 157-173.
- Augustine, J. A. (1984). The diurnal variation of large-scale inferred rainfall over the tropical Pacific Ocean during August 1979. *Monthly weather review*, 112(9), 1745-1751.
- Barnston, A. (2015, January 29). Why are there so many ENSO indexes, instead of just one? Retrieved from: <https://www.climate.gov/news-features/blogs/enso/why-are-there-so-many-enso-indexes-instead-just-one>. Accessed: 27/01/2018.
- Barry, R. G., & Chorley, R. J. (2009). *Atmosphere, weather and climate*. Routledge.
- Bergman, J. W., & Salby, M. L. (1996). Diurnal variations of cloud cover and their relationship to climatological conditions. *Journal of climate*, 9(11), 2802-2820.
- Bigg, G. R., Jickells, T. D., Liss, P. S., & Osborn, T. J. (2003). The role of the oceans in climate. *International Journal of Climatology*, 23(10), 1127-1159.
- Campbell Scientific, Inc. (2018), 41002 12-Plate Gill Radiation Shield. Retrieved from: <https://www.campbellsci.com/p41002>. Accessed: 15/02/2018.
- Chapman, S., & Lindzen, R. S. (1970). *Atmospheric Tides: Thermal and Gravitational*, 200 pp. Gordon and Breach, New York.
- Clayson, C. A., & Weitlich, D. (2005). Diurnal warming in the tropical Pacific and its interannual variability. *Geophysical research letters*, 32(21).
- Clayson, C. A., & Weitlich, D. (2007). Variability of tropical diurnal sea surface temperature. *Journal of climate*, 20(2), 334-352.
- Chen, S. S., & Houze, R. A. (1997). Diurnal variation and life-cycle of deep convective systems over the tropical Pacific warm pool. *Quarterly Journal of the Royal Meteorological Society*, 123(538), 357-388.
- Cooper, N. S. (1982). Inferring solar UV variability from the atmospheric tide. *Nature*, 296(5853), 131-132.
- Cronin, M. F. and W. S. Kessler (2002): Seasonal and interannual modulation of mixed layer variability at 0°, 110°W. *Deep-Sea Res. I*, 49, 1–17.
- Cubasch, U., D. Wuebbles, D. Chen, M.C. Facchini, D. Frame, N. Mahowald, and J.-G. Winther, 2013: Introduction. In: *Climate Change 2013: The Physical Science Basis. Contribution of Working Group I to the Fifth Assessment Report of the Intergovernmental Panel on Climate Change* [Stocker, T.F., D. Qin, G.-K.

Plattner, M. Tignor, S.K. Allen, J. Boschung, A. Nauels, Y. Xia, V. Bex and P.M. Midgley (eds.)). Cambridge University Press, Cambridge, United Kingdom and New York, NY, USA.

Dai, A., & Trenberth, K. E. (2004). The diurnal cycle and its depiction in the Community Climate System Model. *Journal of Climate*, 17(5), 930-951.

Deser, C. (1994). Daily surface wind variations over the equatorial Pacific Ocean. *Journal of Geophysical Research: Atmospheres*, 99(D11), 23071-23078.

Deser, C., & Smith, C. A. (1998). Diurnal and semidiurnal variations of the surface wind field over the tropical Pacific Ocean. *Journal of Climate*, 11(7), 1730-1748.

Deschamps, P. Y., & Frouin, R. (1984). Large diurnal heating of the sea surface observed by the HCMR experiment. *Journal of physical oceanography*, 14(1), 177-184.

Encyclopædia Britannica, (2017). Pacific Ocean. Retrieved from: <https://www.britannica.com/place/Pacific-Ocean>. Accessed: 14/11/2017

Fairall, C. W., Bradley, E. F., Godfrey, J. S., Wick, G. A., Edson, J. B., & Young, G. S. (1996). Cool-skin and warm-layer effects on sea surface temperature. *Journal of Geophysical Research: Oceans*, 101(C1), 1295-1308.

Fu, R., Del Genio, A. D., & Rossow, W. B. (1994). Influence of ocean surface conditions on atmospheric vertical thermodynamic structure and deep convection. *Journal of climate*, 7(7), 1092-1108.

Gentemann, C. L., Donlon, C. J., Stuart-Menteth, A., & Wentz, F. J. (2003). Diurnal signals in satellite sea surface temperature measurements. *Geophysical Research Letters*, 30(3).

Graham, N. E., & Barnett, T. P. (1987). Sea surface temperature, surface wind divergence, and convection over tropical oceans. *Science*, 238(4827), 657-659.

Gray, W. M., & Jacobson Jr, R. W. (1977). Diurnal variation of deep cumulus convection. *Monthly Weather Review*, 105(9), 1171-1188.

Halpern, D., & Reed, R. K. (1976). Heat budget of the upper ocean under light winds. *Journal of Physical Oceanography*, 6(6), 972-975.

Haurwitz, B., & Cowley, A. D. (1973). The diurnal and semidiurnal barometric oscillations global distribution and annual variation. *pure and applied geophysics*, 102(1), 193-222.

Hayes, S. P., Mangum, L. J., Picaut, J., Sumi, A., & Takeuchi, K. (1991). TOGA-TAO: A moored array for real-time measurements in the tropical Pacific Ocean. *Bulletin of the American Meteorological Society*, 72(3), 339-347.

Kawai, Y., & Kawamura, H. (2005). Spatial and temporal variations of model-derived diurnal amplitude of sea surface temperature in the western Pacific Ocean. *Journal of Geophysical Research: Oceans*, 110(C8).

Kawai, Y., & Wada, A. (2007). Diurnal sea surface temperature variation and its impact on the atmosphere and ocean: A review. *Journal of oceanography*, 63(5), 721-744.

- Kraus, E. B. (1963). The diurnal precipitation change over the sea. *Journal of the Atmospheric Sciences*, 20(6), 551-556.
- Le Blancq, F. (2011). Diurnal pressure variation: the atmospheric tide. *Weather*, 66(11), 306-307.
- NASA. Goddard Space Flight Center. (2017). Tropical Rainfall Measurement Mission. Retrieved from: <https://trmm.gsfc.nasa.gov/>. Accessed: 11/11/2017.
- National Data Buoy Center (NDBC). (2016a). Data Telemetry. Retrieved from: [http://tao.ndbc.noaa.gov/proj\\_overview/tel\\_ndbc.shtml](http://tao.ndbc.noaa.gov/proj_overview/tel_ndbc.shtml). Accessed: 04/02/2018.
- National Data Buoy Center (NDBC). (2016b). Mooring Information. Retrieved from: [http://tao.ndbc.noaa.gov/proj\\_overview/mooring\\_ndbc.shtml](http://tao.ndbc.noaa.gov/proj_overview/mooring_ndbc.shtml). Accessed: 18/10/2017.
- National Oceanic and Atmospheric Administration (NOAA). (2009). Relative Humidity. Retrieved from: <http://www.nws.noaa.gov/glossary/index.php?word=relative+humidity>. Accessed: 03/01/2017.
- National Oceanic and Atmospheric Administration (NOAA). (2017a). El Niño & La Niña (El Niño-Southern Oscillation). Retrieved from: <https://www.climate.gov/enso>. Accessed: 07/12/2017.
- National Oceanic and Atmospheric Administration (NOAA). (2017b). GOES Data Collection System. Retrieved from: <http://www.noaasis.noaa.gov/DCS/>. Accessed: 11/11/2017
- National Oceanic and Atmospheric Administration (NOAA). (2017c). Southern Oscillation Index (SOI). Retrieved from: <https://www.ncdc.noaa.gov/teleconnections/enso/indicators/soi/>. Accessed: 07/12/2017.
- McPhaden, M. (1995). The tropical atmosphere and ocean (TAO) array is completed. *Bull. American Meteorol. Soc.*, 76, 731-739.
- McPhaden, M. J., Busalacchi, A. J., Cheney, R., Donguy, J. R., Gage, K. S., Halpern, D., ... & Niiler, P. P. (1998). The Tropical Ocean-Global Atmosphere observing system: A decade of progress. *Journal of Geophysical Research: Oceans*, 103(C7), 14169-14240.
- Morak-Bozzo, S., Merchant, C. J., Kent, E. C., Berry, D. I., & Carella, G. (2016). Climatological diurnal variability in sea surface temperature characterized from drifting buoy data. *Geoscience Data Journal*, 3(1), 20-28.
- Pacific Marine Environmental Laboratory (PMEL). (2017). Global Tropical Moored Buoy Array. Retrieved from: <https://www.pmel.noaa.gov/gtmmba/>. Accessed: 16/10/2017.
- Price, J. F., Weller, R. A., & Pinkel, R. (1986). Diurnal cycling: Observations and models of the upper ocean response to diurnal heating, cooling, and wind mixing. *Journal of Geophysical Research: Oceans*, 91(C7), 8411-8427.
- Pugh, D. T. (1987). *Tides, surges and mean sea-level: a handbook for engineers and scientists*, 472 pp.
- Randall, D. A., & Dazlich, D. A. (1991). Diurnal variability of the hydrologic cycle in a general circulation model. *Journal of the atmospheric sciences*, 48(1), 40-62.

- Ruprecht, E., & Gray, W. M. (1976). Analysis of satellite-observed tropical cloud clusters. I. Wind and dynamic fields. *Tellus*, 28(5), 391-413.
- Schneider, T., Bischoff, T., & Haug, G. H. (2014). Migrations and dynamics of the intertropical convergence zone. *Nature*, 513(7516), 45-53.
- Serra, Y. L., A'hearn, P., Freitag, H. P., & McPhaden, M. J. (2001). ATLAS self-siphoning rain gauge error estimates. *Journal of Atmospheric and Oceanic Technology*, 18(12), 1989-2002.
- Soloviev, A., & Lukas, R. (1997). Observation of large diurnal warming events in the near-surface layer of the western equatorial Pacific warm pool. *Deep Sea Research Part I: Oceanographic Research Papers*, 44(6), 1055-1076.
- Stocker, T. F., Qin, D., Plattner, G. K., Tignor, M., Allen, S. K., Boschung, J., ... & Midgley, P. M. (2013). IPCC, 2013: summary for policymakers in climate change 2013: the physical science basis, contribution of working group I to the fifth assessment report of the intergovernmental panel on climate change.
- Stommel, H., Saunders, K., Simmons, W., & Cooper, J. (1969). Observations of diurnal thermocline. *Deep-Sea Research*, 269.
- Stramma, L., Cornillon, P., Weller, R. A., Price, J. F., & Briscoe, M. G. (1986). Large diurnal sea surface temperature variability: Satellite and in situ measurements. *Journal of Physical Oceanography*, 16(5), 827-837.
- Tanahashi, S., Kawamura, H., Takahashi, T., & Yusa, H. (2003). Diurnal variations of sea surface temperature over the wide-ranging ocean using VISSR on board GMS. *Journal of Geophysical Research: Oceans*, 108(C7).
- Trent, E. M., & Gathman, S. G. (1972). Oceanic thunderstorms. *pure and applied geophysics*, 100(1), 60-69.
- Trenberth, K. E., Dai, A., Rasmussen, R. M., & Parsons, D. B. (2003). The changing character of precipitation. *Bulletin of the American Meteorological Society*, 84(9), 1205-1217.
- Ueyama, R., & Deser, C. (2008). A climatology of diurnal and semidiurnal surface wind variations over the tropical Pacific Ocean based on the tropical atmosphere ocean moored buoy array. *Journal of Climate*, 21(4), 593-607.
- Waliser, D. E., & Gautier, C. (1993). A satellite-derived climatology of the ITCZ. *Journal of Climate*, 6(11), 2162-2174.
- Wilks, D. S. (2011). *Statistical methods in the atmospheric sciences*(Vol. 100). Academic press.
- Zhang, G. J., Ramanathan, V., & McPhaden, M. J. (1995). Convection-evaporation feedback in the equatorial Pacific. *Journal of Climate*, 8(12), 3040-3051.

## Appendix A

This appendix reports the specifications of the sensors installed on the moorings. The information, retrieved from NBDC (2016), are reported in Table A.1 and pertains those parameters examined in this study and measured by the Next Generation ATLAS Moorings.

Measurement	Sensor type	Manufacturer Model	Resolution	Range	Accuracy	Comments
Wind speed	Propeller	R. M. Young: 05103	0.2 m s <sup>-1</sup>	1-20 m s <sup>-1</sup> (0.4 – 36 m s <sup>-1</sup> )	±0.3 m s <sup>-1</sup> or 3%	[7]
Wind direction	Vane	R. M. Young: 05103	1.4°	0-355°	5° - 7.8°	[7] See also footnote to [7]
	Fluxgate compass	E.G.and G. 63764 or KVH LP101-5	1.4°	0-359°		
Air temperature	Pt-100 RTD (Resistance Temperature Recorder)	Rotronic Instrument Corp.: MP-101	0.01°C	14-32°C (0-40°C)	±0.2°C	[12]
Relative humidity	Capacitance		0.4 %RH realtime 0.02 %RH delay mode	55-95 %RH (0-100 %RH)	±2.7 %RH	[12]
Rainfall	Capacitance	R. M. Young: 50203-34	0.2 mm hr <sup>-1</sup>	0-50 mm	±0.4 mm hr <sup>-1</sup> on 10 min filtered data	[6]
Downwelling shortwave radiation	Pyranometer	Eppley Laboratory: PSP- TAO, Delrin case	0.4 W m <sup>-2</sup>	200-1000 W m <sup>-2</sup> (0-1600 W m <sup>-2</sup> )	±2%	[15]
Downwelling longwave radiation	Pyrgeometer	Eppley Laboratory: PIR- TAO, Delrin case, 3-output (1)	0.1 W m <sup>-2</sup> 0.03°C	200 W m <sup>-2</sup> @ 20°C (thermopile only)	±1%	[M] Nominal calibration values used for case and dome thermistors
Barometric pressure	Pressure transducer	Paroscientific: MET1-2	0.1 hPa	800-1100 hPa	±0.01% of reading	[M]
Sea surface and subsurface temperature	Thermistor	PMEL electronics using YSI (Yellow Springs Instruments) thermistor 46006	0.001°C	6-32°C (0-40°C)	±0.02°C	[14], [9]
Sea surface and subsurface temperature	Thermistor	Sea Bird Electronics: SBE16, SBE37	0.001°C	1-31°C (-5-35°C)	±0.003°C	[3]

Table A.1: Sensors specifications. Source: NBDC (2016).

## References linked to the comments

[3] Freitag, H.P., M.E. McCarty, C. Nosse, R. Lukas, M.J. McPhaden, and M.F. Cronin, 1999: COARE Seacat data: Calibrations and quality control procedures. *NOAA Tech. Memo. ERL PMEL-115*, 89 pp.

[6] Serra, Y.L., P.A'Hearn, H.P. Freitag, and M.J. McPhaden, 2001: ATLAS self-siphoning rain gauge error estimates. *J. Atmos. Ocean. Tech.*, 18, 1989-2002.

[7] Freitag, H.P., M. O'Haleck, G.C. Thomas, and M.J. McPhaden, 2001: Calibration procedures and instrumental accuracies for ATLAS wind measurements. NOAA. Tech. Memo. OAR PMEL-119, NOAA/Pacific Marine Environmental Laboratory, Seattle, Washington, 20 pp.

**Footnote:** *This study discovered a systematic error in standard and NextGeneration ATLAS wind directions of approximately 6.8° in the counterclockwise direction. This error was present possibly as far back as 1984. Modifications were made to the NextGeneration ATLAS system in 2000 to correct this error in subsequent deployments, and archived NextGeneration ATLAS wind directions were corrected (both daily averages and high resolution datasets) on 28 March 2002. For corrected Next\_generation Atlas Wind Directions see <https://www.pmel.noaa.gov/gtmba/corrected-next-generation-atlas-wind-directions>. Standard ATLAS wind directions have not been corrected in the archives since the exact time when the error began to affect the measurements is unknown. Standard ATLAS were used exclusively between 1984 and 1996 when NextGeneration ATLAS moorings began to replace them. By November 2001, the standard ATLAS had been phased out and the array was comprised entirely of NextGeneration systems. Expected RMS error for standard ATLAS wind direction is 7.8° (of which 6.8° is a bias) while expected RMS error for NextGeneration ATLAS wind directions is about ±5° with no appreciable bias.*

[9] A'Hearn, P.N., H.P. Freitag, and M.J. McPhaden, 2002: ATLAS module temperature bias due to solar heating. NOAA Tech. Memo OAR PMEL-121, NOAA/Pacific Marine Environmental Laboratory, Seattle, WA, 24 pp.

[12] Lake, B.J., S.M. Noor, H.P. Freitag, and M.J. McPhaden, 2003: Calibration procedures and instrumental accuracy estimates of ATLAS air temperature and relative humidity measurements. NOAA Tech. Memo. OAR PMEL-123, NOAA/Pacific Marine Environmental Laboratory, Seattle, WA, 23 pp.

[14] Freitag, H.P., T.A. Sawatzky, K.B. Ronnholm, and M.J. McPhaden, 2005: Calibration procedures and instrumental accuracy estimates of next generation ATLAS water temperature and pressure measurements. NOAA Tech. Memo. OAR PMEL-128, NTIS: PB2008-101764, NOAA/Pacific Marine Environmental Laboratory, Seattle, WA, 22 pp.

[15] Cronin, M.F. and M.J. McPhaden, 1997: The upper ocean heat balance in the western equatorial Pacific warm pool during September-December 1992. *J. Geophys. Res.*, 102, 8533-8553.

## References

National Data Buoy Center (NDBC). (2016). Sensors Specifications. Retrieved from: [http://tao.ndbc.noaa.gov/proj\\_overview/sensors\\_ndbc.shtml](http://tao.ndbc.noaa.gov/proj_overview/sensors_ndbc.shtml). Accessed: 01/02/2018.

## Appendix B

The R code written to accomplish the data elaborations described in Section 2.2 and produce the graphics reported in Chapter 3 is presented in this Appendix. Section B.I describes the creation of a dataset composed by measurements of one variable from a NetCDF file, whereas Section B.II introduces the data pre-processing. Section B.III delineates the representation of the complete time series in time as well as the implementation of the spectral analysis. Section B.IV reports the computation and the depiction of the diurnal cycles. Section B.V and B.VI describes the distinction according to “background” climatic conditions and to the local meteorological conditions, respectively. Section B.VII reports the code utilised in the assessment of the variation of the diurnal cycle over the long period. Section B.VIII presents the assessment of the relations between variables. Section B.IX shows the code utilised to produce the graphics reported in Chapter 4 (Discussion) and Chapter 6 (Conclusions).

Some comments helps to understand the usage and meaning of the written R code. The comments are preceded by “#”.

### B.I Create dataset from NetCDF file

The following code creates a dataset with 2 columns: time and observations of the variable. The dataset is created from a NetCDF file, reporting the observations of one variable of one buoy and the associated UTC time.

```
data = open.nc("reference_variable.nc")    # create connection with NetCDF file
variable = var.get.nc(data, variable = "AT_21")    # extract the variable vector from NC file
variable[variable>1e+35] = NA# convert Missing Data
time = convertDateNcdf2R(data)            # create time vector
dataset = data.frame(time, variable)# bind time and data
```

The time vector extracted from the NetCDF file is in the “UTC” format. Thus, a new vector is created indicating the local time of the observations.

```
# The following function removes data acquired before the true 00:00 of the first recorded day.
# The final measurements of the dataset are removed to produce a dataset with complete daily
# observations.
# Description of the function inputs:
# data = input dataset
# index.start = number of the measurement observed at the true 00:00
# period = total measurements composing one day i.e. 144

cut.boundaries = function(data, index.start, period){
  dataset = dataset[index.start : (((floor(nrow(data) / period) * period) - (length(index.start :
period))))),]
}
```

```

# create a function which gathers the starting date of a dataset and creates a new time vector
from midnight of the starting date

create.date.time.vector = function(dataset, time.column){
  data.time = dataset[,time.column]

  # gather starting date
  sY = as.numeric(strftime(data.time[1], format = "%Y"))
  sM = as.numeric(strftime(data.time[1], format = "%m"))
  sD = as.numeric(strftime(data.time[1], format = "%d"))
  sH = 0
  sM.1 = 0
  sS = 0

  time = seq(ISOdatetime(sY,sM,sD,sH,sM.1,sS,tz = "UTC"), length.out =
((length(data.time)*10)),by = 'min')

  time = time[seq(1,length(time),10)] # select only 10 min
  return(time)
}

# substitute UTC time column with the Local Time column
dataset$time = create.date.time.vector(dataset,1)

```

## B.II Data pre-processing

The following code converts the hourly Sea Level Pressure time series into a 10-minutes time series.

```

# data.slp corresponds to the vector of data extracted from the NetCDF file
# The following function takes a hourly vector and computes 5 intermediate measurements every two
hourly measurements through linear interpolation.

fill.NA.slp = function(data.slp){

  # take values of slp and linearly interpolate
  i = 1
  d = data.slp[i]
  while(i < length(data.slp)){

    if(!is.na(data.slp[i]) & !is.na(data.slp[i+1])){
      a = seq(data.slp[i], data.slp[i+1], length.out=7)
      d = append(d, a[c(-1, -length(a))])
      d = append(d, data.slp[i+1])
      i = i+1
    }
    else{
      d = append(d, rep(NA, 6))
      i = i+1
    }
  }

  return(d)
}

# The associated time vector is created using the first "UTC" recorded date and, then, corrected
into "Local Time"

```

```

time = convertDateNcdf2R(data)      # create "UTC" time vector

# gather starting date and set time to 00:00:00
sY = as.numeric(strftime(time[1], format = "%Y"))
sM = as.numeric(strftime(time[1], format = "%m"))
sD = as.numeric(strftime(time[1], format = "%d"))
sH = 0
sM.1 = 0
sS = 0

# create the local time vector
time = seq(ISOdatetime(sY, sM, sD, sH, sM.1, sS, tz = "UTC"), length.out =
((length(data.time)*10)), by = 'min')
time = time[seq(1,length(time),10)]

```

The following code converts the 2-minutes Shortwave Radiation time series into a 10-minutes time series. The new time series is created by selecting those measurements observed at each 00, 10, 20, 30, 40 and 50 minutes of every hour.

```

# SWRad_2.minutes is a dataset created through the steps reported in B.I
SWRad_10.minutes = SWRad_2.minutes[seq(1,nrow(SWRad_2.minutes),5),]

```

The following code transforms the wind direction measurements. The procedure is explained in Sub-Section 2.2.1.

```

# wind direction are firstly imported as in B.I
y = (dataset$wind.direction)

# the "table" function builds a contingency table of the counts of each wind direction
measurement, i.e. from 0.0 to 359.9
w = table(y)
t = as.data.frame(w)

# find the angle which appears the most
t[which(t$Freq==max(t$Freq)),]

# data are converted through the following function
# description of the function inputs:
# data.vector = y
# add.to.who = direction which appears the most

add.to = function(data.vector, add.to.who){
  data.indexes = which(data.vector <= add.to.who)

  i = 1
  while (i <= length(data.indexes)){
    j = data.indexes[i]
    data.vector[j] = data.vector[j]+360
    i = i+1
  }

  return(data.vector)
}

```

The following code is utilised to correct precipitation data accounting for the error caused by wind undercatchment.

```
# First, the two variables, i.e. precipitation and wind speed, are imported according to the
# procedure in B.I

rain.fix = function(data.rain, data.wind){
  fixed.rain = NULL

  i = 1
  while(i <= length(data.rain)){
    if (!is.na(data.wind[i]) & !is.na(data.rain[i])){
      w = data.wind[i]
      p = -(0.0141)*(w^3) + 0.4409*(w^2) + 0.9927*w + 0.1010
      d = data.rain[i]+(p/100)*data.rain[i]
      fixed.rain = append(fixed.rain,d)
      i = i+1
    }
    else{
      fixed.rain = append(fixed.rain,data.rain[i])
      i = i+1
    }
  }

  return(fixed.rain)
}

# the "fixed.rain" vector replaces the uncorrected precipitation vector
```

### B.III Time series representation and spectral analysis

The following function plots the complete time series. In addition, it computes and superimpose the smoothing lines.

```
plot.data = function(variable, time, color.smooth, ylab1, title){
  plot(variable~(time), type='l', xlab='Time', ylab=ylab1, main=title)

  # define the weights for the smoothing
  p = 10*144
  weights = rep(1/(2*p+1),times = 2*p+1)
  smooth.line = filter(variable, sides = 2, filter = weights)
  lines(smooth.line ~ time, col=color.smooth)
}
```

The following code is utilised to perform the spectral analysis of a variable. In addition, the smoothed periodogram of each buoy is plotted in the same graph.

```
# a1, a2 and a3 are datasets reporting the 10-minutes observations of one variable for the three
# different buoys

a = spectrum(a1$variable,log='no',xlim=c(0,0.04),spans=c(10,10),plot=F)
```

```

b = spectrum(a2$variable,log='no',xlim=c(0,0.04),spans=c(10,10),plot=F)
c = spectrum(a3$variable,log='no',xlim=c(0,0.013),spans=c(10,10),ylim=c(0,300))
spectrum(a1$variable,log='no',xlim=c(0,0.013),spans=c(10,10),col=2,ylim=c(0,150000000),main='Smoothed periodogram')
lines(b$spec~b$freq,col=4)
lines(c$spec~c$freq,col=3)
abline(v=0.006944444,lty=3)
legend('topright',legend = c('0°N 95°W', '0°N 140°W', '0°N 165°E'), col=c(2,4,3), lty=1)

# compute which should be the daily periodicity given a particular amount of data
# a1, a2 and a3 are dataset without missing data
number.of.days = (nrow(a1)/144)
daily.frequency = 1/number.of.days
# add the vertical dashed line corresponding to the daily frequency
abline(v=daily.frequency,lty=2)

```

The spectral analysis is conducted on small amounts of data, composed approximately by 180 days of measurements, which must exclude missing data (called also NA). The following function is utilised to detect the starting and ending date of periods of missing data in one dataset. The output of this function allows to accurately select periods of recorded measurements. Since missing data are frequent, missing data periods smaller than 144 measurements (i.e. one day) are maintained in the selected dataset. A second function, i.e. “fill.NA”, replaces the missing observations in these small missing data periods with the average between the recorded measurements positioned at their extremes.

```

# description of the inputs for the function:
# dataset = dataset imported as in B.I
# VarNum = number of the column reporting the interested variable
# date.time_ColNum = number of the column reporting the local time
# threshold = only periods composed by a number consecutive missing data (NA) higher than the threshold are reported in the output. In this thesis, the threshold is 144 (i.e. one day).
# the output of the function is a list composed by three columns: number of NA composing the missing data period, starting date of the missing data period, ending date of the missing data period

```

```

Examine.NA.Periods = function (dataset, VarNum, date.time_ColNum, threshold){
  i=1
  file.res = NULL
  while (i <= nrow(dataset)){
    if (is.na(dataset[i,VarNum])){
      start = as.character(dataset[i,date.time_ColNum])
      i1 = i
      i = i+1
      count = count+1
      while(i <= nrow(data)){
        if (!is.na(dataset[i,VarNum])){
          end = as.character(data[i,date.time_ColNum])
          i2 = i
          interval = i2-i1
          if (interval >= threshold){
            line = c(interval, start, end)
            file.res = rbind(file.res, line)
          }
          i=i+1
          break
        }
      }
    }
  }
}

```

```

    }
    else{
      i=i+1
    }
  }
}
else{
  i=i+1
  free.period = free.period+1
}
}
return((file.res))
}

```

# As a correct period is identified, the eventual missing observations are replaced with the average value computed between the recorded observations positioned at the extremes of the missing data periods

# the following function is utilised for this purpose

```

fill.NA = function(data){
  i = 1
  d = 1
  while (i <= length(data)){
    if (is.na(data[i])){
      sta = data[(i-1)]
      start = i
      int = 1
      i = i+1
      while (i <=length(data)){
        if (is.na(data[i])){
          int = int+1
          i = i+1
        }
        else{
          int = int+2
          fin = data[i]
          end = i-1
          fe = seq(sta,fin,length.out = int)
          fe = fe[-length(fe)]
          fe = fe[-1]
          data[start:end]=(fe)

          #data[is.na(data[start:end])]=seq(sta,fin,length.out = int)
          break
        }
      }
    }
    else{
      i = i+1
    }
  }
  return(data)
}

```

## B.IV Representation of the diurnal cycle

The following code is utilised to represent each single diurnal cycle. The mean and the 5<sup>th</sup> and 95<sup>th</sup> percentiles, computed at each time step, are then added to the plot. All the variables are illustrated using this methods except the precipitation. The final part of this section is dedicated to the elaboration of the diurnal cycle of precipitation data.

```
# The "anomaly_period" function creates a new vector of daily anomalies, i.e. over each recorded day, from a dataset. The dataset should be created as in B.I. The new vector is added to the existing dataset as a new column.
# NumVar = column's number of the interested variable
# period = number of measurements composing one day i.e 144
```

```
anomaly_period = function(dataset, NumVar, period){
  i = 1
  ii = period
  d = NULL
  while (i <= (nrow(dataset))){
    dat = dataset[i:(i+ii-1), NumVar]
    if (length(dat[is.na(dat)]) > 0){
      d = append(d, rep(NA, period))
      i = i+ii
    }
    else{
      d = append(d, anomaly_vector(data[i:(i+ii-1), NumVar]))
      i = i+ii
    }
  }
  dataset = cbind(data[1:(length(d)+start.period-1),], d)
}
```

```
# The "return_mean" function computes the diurnal mean of a column (variable) of a dataset
# The output is a vector composed by the daily mean values
# description of the function inputs:
# NumVar = column's number of the interested variable
# period = number of measurements composing one day i.e 144
```

```
return_mean = function(dataset, NumVar, period){
  i = 1

  # create a vector reporting the absolute number of days within the dataset
  index = rep(c(1:period), length.out = nrow(dataset))

  dataset = cbind(index,dataset)
  d = NULL
  while (i <= period){
    res = subset(dataset, subset = index == i)
    d = append(d, mean(res[,NumVar+1], na.rm = TRUE))
    i = i+1
  }
  return(d)
}
```

```
# The "percentile_daily" function computes the 5th and 95th percentiles of the anomalies' distribution at each time step. The function operates on a variable composing a dataset
# The output is a dataset composed by two columns: the daily 5th and 95th percentiles
# description of the function inputs:
# VarNum = column's number of the interested variable
# period = number of measurements composing one day i.e 144
```

```

# probs.2 = a vector composed by the two interested quantiles i.e. 0.05 and 0.95

percentile_daily = function(data, VarNum, period, probs.2){
  d=NULL
  i=1
  j=1
  num = rep(c(1:period), length.out=nrow(data))
  num1 = c(1:period)
  data1 = cbind(num, data)
  while(i <= length(num1)){

    dat = data1[data1$num == num1[i], VarNum+1]
    di = quantile(dat, na.rm = T, probs = probs.2)
    r = c(di[[1]], di[[2]])
    d = rbind(d, r)
    i = i+1
  }
  d = data.frame(d)
  colnames(d) = c(as.character(probs.2[1]), probs.2[2])
  return(d)
}

# The "plotting_daily" function plots each daily cycle, the mean cycle and the 5th and 95th
# percentiles' cycles. The function takes as input a variable composing a dataset
# description of the function inputs:
# VarNum = column's number of the interested variable
# period = number of measurements composing one day i.e 144
# margins = margins of the y-axys (depending on each variable)

plotting_variable = function(data, VarNum, period, margins){
  # define start, stop, frequency
  sta = 0; sto = 24;fre = 6

  i = 1
  f = period
  plot(ts(data[(i:f), VarNum],sta,sto,fre),ylim=margins,ylab='',xlab='',type='l')
  i = i+period
  f = f+period
  while (I <= (nrow(data))){
    lines(ts(data[i:f,VarNum],sta,sto,fre))
    i = i + period
    f = f + period
  }

  lines(ts(return_mean(data,VarNum,1,period),sta,sto,fre),col=2,lwd=2)
  lines(ts(percentile_daily(data,VarNum,period)[,1],sta,sto,fre),col=3,lwd=2)
  lines(ts(percentile_daily(data,VarNum,period)[,2],sta,sto,fre),col=3,lwd=2)

}

# draw the axis of the plot
axis(1,at=seq(0,24,2))
axis(2)
mtext(side = 1,text = "Local Time", line = 2.3)
mtext(side = 2,text = "unit of measurement", line = 2.5)
title(main = "Title of the plot")
# x-axys
# y-axys
# x-axys text
# y-axys text
# title of the plot

```

The following code compute the occurrences of rainfall events over the day and the occurrences of each rainfall category. Then, the occurrences are drawn to illustrate the precipitation diurnal cycle. Finally, the frequency of rainfall events is computed and the axis is drawn in the same plot.

```

# Precipitation data should be imported and pre-processed as in B.I and B.II
rain.hr = dataset$fixed.rain

# create a vector of hours which should be associated to rain.hr in a new dataset
hr = rep(c(0:23),each=6,length.out=length(rain.hr))
new.dataset = data.frame(hr, rain.hr)

# select only precipitation intensities greater than 0.5 mm/hr
new.dataset = new.dataset[new.dataset$rain.hr > 0.5,]

# exclude missing data from the new dataset
new.dataset = new.dataset[which(!is.na(new.dataset$rain.hr)),]

# create a function which examines the occurrences of rainfall event for a given hour
# examined.hr = vector of hours to be examined i.e. from 0 to 23
# int.thr.down = lower intensity threshold
# int.thr.up = upper intensity threshold
group.occurrences = function(dataset, PrecVar, hr.Var, examined.hr, int.thr.down, int.thr.up){
  d = NULL
  prec = dataset[,PrecVar]
  hr.1 = dataset[,hr.Var]
  data.new = data.frame(hr.1, prec)

  # select intensity range
  data1 = data.new[ data.new$prec > int.thr.down & data.new$prec < int.thr.up, ]

  # create a vector of the occurrences
  i = 1
  while(i <= length(examined.hr)){
    p = nrow(data1[(data1$hr == examined.hr[i]),])
    d = append(d, p)
    i = i+1
  }

  return(d)
}

# find the occurrence of rainfall events for each hour using the "group.occurrences" function
# the MaxPrec threshold refers to the highest observed intensity
d1 = group.occurrences(new.dataset,2,1,c(0:23),0.5,MaxPrec) # rainfall events
d2 = group.occurrences(new.dataset,2,1,c(0:23),0.5,2.99) # light rain
d3 = group.occurrences(new.dataset,2,1,c(0:23),3,9.99) # medium rain
d4 = group.occurrences(new.dataset,2,1,c(0:23),10,MaxPrec) # heavy rain

# find the frequencies associated to the counts
{
  i = 1
  d1.tot = NULL
  hr1 = c(0:23)
  while (i <= length(hr1)){

# find the number recorded intensities for each hour
  a = nrow(new.dataset[hr==hr1[i] & !is.na(new.dataset$rain.hr),])
  d1.tot = append(d1.tot,a)
  i = i+1
}
}
d2 = d1/d1.tot

# plot the precipitation diurnal cycle
plot(d1 ~ c(0:23), type='b', ylab='', xlab='', axes=F, ylim=c(0,max(d)))
lines(d2 ~ c(0:23), type='b', col=2)
lines(d3 ~ c(0:23), type='b', col=3)
lines(d4 ~ c(0:23), type='b', col=4)

```

```

# draw axis and legend
axis(1, at=seq(0,24,2))
axis(2)
mtext(side = 1, text = 'Local Time', 2.3)
mtext(2, text = 'Counts', 2.5)
title(main = "title")
legend('topleft', legend = c('>0.5 mm/hr', '0.5-3 mm/hr', '3-10 mm/hr', '>10 mm/hr'), col =
c(1,2,3,4), lty=1)
# draw the frequency axis on the right
par(new = T)
plot(d2~c(0:23), type='n', ylab='', xlab='', axes=F, ylim=c(0,max(d2)))
axis(4)
mtext("Frequency", 4, 2.5)

```

The following code displays the diurnal cycle of extreme rainfalls.

```

# Precipitation data should be imported and pre-processed as in B.I and B.II
rain.hr = dataset$fixed.rain

# create a vector of hours which should be associated to rain.hr in a new dataset
hr = rep(c(0:23),each=6,length.out=length(rain.hr))
new.dataset = data.frame(hr, rain.hr)

# select only precipitation intensities greater than 0.5 mm/hr
new.dataset = new.dataset[new.dataset$rain.hr > 0.5,]

# exclude missing data from the new dataset
new.dataset = new.dataset[which(!is.na(new.dataset$rain.hr)),]

# find the 98th percentile
p.98 = quantile(new.dataset$rain.hr,0.98)[[1]]

# use the function "group.occurrences" to examine the timing of rainfall intensities greater than
the 98th percentile
a1 = group.occurrences(new.dataset,2,1,c(0:23),p.98,MaxPrec)

# plot the diurnal cycle of extreme rainfalls for one buoy
plot(ts(a1,0,24), type='b', axes=F, xlab='', ylab='', col=2, ylim=c(0,30))
# draw the axis and title
axis(1,at=seq(0,24,2))
axis(2)
mtext(side = 1,text = 'Local Time',2.3)
mtext(2,text = 'Counts',2.5)
title(main = "Extreme rainfall occurrences")

# draw the diurnal cycle of extreme rainfalls for the other two buoys
# a2 and a3 are computed as a1
lines(ts(a2,0,24), type='b', col=3)
lines(ts(a3,0,24), type='b', col=4)

# draw the legend
legend("topright", legend = c("0°N 95°W", "0°N 140°W", "0°N 165°E"), col=c(2,3,4), lty=1)

```

## B.V Select days according to the “background” climatic conditions

The following code is utilised to select those days occurring during the warm and cold ENSO phases. This distinction is performed by means of the Southern Oscillation Index (SOI) values for each month from 1998 to 2017.

```

# import a csv file reporting the SOI values of the each month
SOI <- read.csv("folder/file", ";",header = T)
# the SOI file is composed by three columns: "Year", "Month" and "SOI.Value"

# select the desired months
warm.SOI = SOI[SOI$SOI.Value < (-1.25),]
cold.SOI = SOI[SOI.in$SOI.Value > (1.5),]

# import the variable's data as in B.I and, eventually, pre-process the data as in B.II

# select the time column of the dataset
data.time = dataset$time

# select either the warm or the cold ENSO phase
data.SOI = warm.SOI          # or cold.SOI

# the following code select those days occurring during either the warm or cold ENSO phase
v = data.frame(as.numeric(strftime(data.time, format="%Y")), as.numeric(strftime(data.time,
format = "%m")))
colnames(v) = c('yr','month')
m = data.frame(as.numeric(data.SOI$Year), as.numeric(data.SOI$Month))
i = 1
d = NULL
while (i <= nrow(m)){
  a = which(v[,1] == m[i,1] & v[,2] == m[i,2])
  i = i+1
  d = append(d, a)
}
}
ENSOdata = dataset[d,]

```

#### B.VI Select days according to the local meteorological conditions

The following functions create different classes according to the local meteorological conditions. The first function differentiates *cloudy*, *moderate-cloudy*, *moderate-sunny* and *sunny days*. The second function distinguishes *wind class 1*, *wind class 2* and *wind class 3*.

# The two following functions ("select\_days\_sum" and "select\_days\_ws") take as input a dataset with 3 columns: time, the selector variable (shortwave radiation or wind speed) and variable to analyse (Air Temperature, SST etc.)

```

# "select_days_sum" select days according to summed values in a certain hour
# description of the function inputs:
# NumVar = number of column of the shortwave radiation variable
# index.start = starting shortwave radiation measurement of day i.e. 36 (06 am)
# index.interval = interval of measurements to consider i.e. 37 (from 06 am to 13 am)
# period = amount of measurements taken in one day i.e. 144
# probs.2 = the two quantiles of reference, 0 and 0.2 for cloudy days, and 0.8 and 1 for sunny
days

select_days_sum = function(data,NumVar,index.start,index.interval,period,probs.2){

  # Compute the sum for each day
  i = index.start
  d = NULL
  dayNum = NULL
  Sum = NULL
  j = 1
  while (i <= nrow(data)){

```

```

    sam = sum(data[i:(i+index.interval-1),NumVar])
    dayNum = append(dayNum,j)
    Sum = append(Sum,sam)
    i = i + period
    j = j+1
}

d = data.frame(dayNum,Sum)
colnames(d) = c('DayNum', 'Sum')

# remove days with missing data
a1 = d[which(!is.na(d$Sum)),]

# compute the two percentiles of interest
qs = quantile(a1$Sum, na.rm = T, probs = probs.2)
q = c(qs[[1]], qs[[2]])

# select sums in between the two percentiles
selection = a1[a1$Sum > q[1] & a1$Sum <= q[2],1]

# find days
DayNum = rep(c(1:(nrow(data)/(period))+1), each = period, length.out = (nrow(data)))
data.tt = cbind(DayNum, data)
i = 1
result = NULL
while ( i <= length(selection)){
  day = data.tt[data.tt$DayNum == selection[i],]
  result = rbind(result, day)
  i = i+1
}

return(result)
}

# The outcome of the function is a dataset composed by days responding to the queried
characteristics

# The following function select days according to how many values in a certain time period lie in
between a specific interval
# Description of the function inputs:
# NumVar = number of column of the wind speed variable
# index.start = starting wind speed measurement of day i.e. 36 (06 am)
# interval = interval of measurements to consider i.e. 37 (from 06 am to 13 am)
# period = total number of measurements gathered in one day i.e. 144
# ThrDown = lower threshold of the analysed wind class i.e. 0 for wind class 1, 3 for wind class
2 and 6 for wind class 3
# ThrUp = upper threshold of the analysed wind class i.e. 2.99 for wind class 1, 5.99 for wind
class 2 and the maximum observed wind speed (referred to as "WSMax") for wind class 3
# min.occ = minimum number of wind speed measurements observed in the interested time interval
lying which should lie in between the lower and upper threshold of the wind class

select_days_ws = function(dataset, NumVar, index.start, interval, ThrDown, ThrUp, min.occ){

  # give a number for each day of the data
  dayNum = rep(c(1:(nrow(dataset)/period)),each=period,length.out=nrow(dataset))
  data = cbind(dayNum,dataset)

  # create a list of selected dayNum satisfying the selective condition
  i = index.start
  dN = NULL
  while (i <= nrow(data)){
    dat = data[i:(i+interval-1), NumVar+1]
    if (length(dat) == length(dat[!is.na(dat)])){
      if (length((dat[dat >= ThrDown & dat <= ThrUp])) >= min.occ){
        dN = append(dN, data[i,1])
      }
    }
  }
}

```

```

    }
    i = i+period
  }

# find days
d = NULL
i = 1
while (i <= length(dN)){
  d = rbind(d, data[data$dayNum == dN[i],])
  i = i+1
}
d = data.frame(d)
return(d)}

```

The following function is utilised to create the input dataset for the previous two functions.

```

# First of all, two different datasets should be created as in B.I, one associated to the
selector variable (shortwave radiation or wind speed) and the other related to the variable to
analyse. If necessary, data should be pre-processed as in B.II
# Then, the following function is utilised to merge the two different datasets
# Description of the function inputs:
# data1 and data2 = the two datasets created as before
# time.col1 = number of the time column in data1
# time.col2 = number of the time column in data2
# coltobindfrom2 = number of the column to bind from two; in case of multiple columns, a vector
reporting the number of columns should be created
merging.dataset = function(data1,time.col1,data2,time.col2,coltobindfrom2){
  start1 = strftime(data1[1,time.col1], tz = "UTC")
  start2 = strftime(data2[1,time.col2], tz = "UTC")
  end1 = strftime(data1[nrow(data1),time.col1], tz = "UTC")
  end2 = strftime(data2[nrow(data2),time.col2], tz = "UTC")

  if (start1 > start2){
    s2 = which(strftime(data2[,time.col2], tz = "UTC") == start1)
    s1 = 1
  }
  if (start1 < start2){
    s1 = which(strftime(data1[,time.col1], tz = "UTC") == start2)
    s2 = 1
  }
  if (start1 == start2){
    s1 = 1
    s2 = 1
  }
}

  if (end1 > end2){
    e1 = which(strftime(data1[,time.col1], tz = "UTC") == end2)
    e2 = nrow(data2)
  }
  if (end2 > end1){
    e2 = which(strftime(data2[,time.col2], tz = "UTC") == end1)
    e1 = nrow(data1)
  }
  if (end1 == end2){
    e1 = nrow(data1)
    e2 = nrow(data2)
  }
}

  data = data.frame(data1[s1:e1,], data2[s2:e2,(coltobindfrom2)])
  return(data)
}

```

The following code utilises the functions presented before and creates the different meteorological classes.

```
# Variables' datasets should be created as in B.I and, if needed, pre-processed as in B.II
# Here, we take as reference datasets data1 and data2
# data1 contains measurements of the selector variable
# data2 contains measurements of the variable to analyse

# First, merge the datasets
data = merging.dataset(data1,1,data2,1,2)
colnames(data) = c('time','Variable to analyse','Selector Variable')

result = select_days_sum(data,3,36,36,144,c(0,0.2))           # Cloudy days
result = select_days_sum(data,3,36,36,144,c(0.2,0.5))       # Moderate-cloudy days
result = select_days_sum(data,3,36,36,144,c(0.5,0.8))       # Moderate-Sunny days
result = select_days_sum(data,3,36,36,144,c(0.8,1))         # Sunny days
result = select_days_ws(data,3,37,36,0,3,36)                 # Wind class 1
result = select_days_ws(data,3,37,36,3,6,36)                 # Wind class 2
result = select_days_ws(data,3,37,36,6,WSMax,36)             # Wind class 3

# Data are then analysed as in B.IV
```

## B.VII Assessment of the variation of the diurnal cycle during the entire recorded periods

The following code is utilized in the assessment of the variation of the diurnal cycle during the entire recorded period. First, the daily anomalies of 10-minutes data are computed over the entire dataset. Then, the 10-minutes anomalies are averaged to form hourly data. Finally, the hourly data are smoothed with a running filter.

```
# First, the "dataset" should be created and, if necessary, pre-processed as in B.I and B.II

# Compute the daily anomalies over the entire dataset
data = anomaly_period(dataset, 2, 1, 144)

# Gather the time vector and select only one string per day
time = data$time
time.1 = time[seq(1,length(time),144)]
# time.1 will be use below to format the length for the hourly anomalies vector.

# Assign a reference hour to the variables' measurements
hour = rep(c(0:23), each=6, length.out = nrow(data))
data = cbind(hour,data)

# create a function which computes the mean over a selected amount of measurements
# interval = number of measurements to be averaged
step.mean = function(data, interval){
  i = 1
  d = NULL
  while (i < length(data)){
    m = mean(data[i:(i+interval-1)], na.rm = T)
    d = append(d, m)
    i = i+interval
  }
  return(d)
}
```

```

# select the number of the column reporting the 10-minutes anomaly in "dataset"
varnum = 4
# compute the hourly mean of 10-minutes data for each hour
{
  hour.0 = step.mean(data[hour==0, varnum], 6)[1:length(time.1)]
  hour.1 = step.mean(data[hour==1, varnum], 6)[1:length(time.1)]
  hour.2 = step.mean(data[hour==2, varnum], 6)[1:length(time.1)]
  hour.3 = step.mean(data[hour==3, varnum], 6)[1:length(time.1)]
  hour.4 = step.mean(data[hour==4, varnum], 6)[1:length(time.1)]
  hour.5 = step.mean(data[hour==5, varnum], 6)[1:length(time.1)]
  hour.6 = step.mean(data[hour==6, varnum], 6)[1:length(time.1)]
  hour.7 = step.mean(data[hour==7, varnum], 6)[1:length(time.1)]
  hour.8 = step.mean(data[hour==8, varnum], 6)[1:length(time.1)]
  hour.9 = step.mean(data[hour==9, varnum], 6)[1:length(time.1)]
  hour.10 = step.mean(data[hour==10, varnum], 6)[1:length(time.1)]
  hour.11 = step.mean(data[hour==11, varnum], 6)[1:length(time.1)]
  hour.12 = step.mean(data[hour==12, varnum], 6)[1:length(time.1)]
  hour.13 = step.mean(data[hour==13, varnum], 6)[1:length(time.1)]
  hour.14 = step.mean(data[hour==14, varnum], 6)[1:length(time.1)]
  hour.15 = step.mean(data[hour==15, varnum], 6)[1:length(time.1)]
  hour.16 = step.mean(data[hour==16, varnum], 6)[1:length(time.1)]
  hour.17 = step.mean(data[hour==17, varnum], 6)[1:length(time.1)]
  hour.18 = step.mean(data[hour==18, varnum], 6)[1:length(time.1)]
  hour.19 = step.mean(data[hour==19, varnum], 6)[1:length(time.1)]
  hour.20 = step.mean(data[hour==20, varnum], 6)[1:length(time.1)]
  hour.21 = step.mean(data[hour==21, varnum], 6)[1:length(time.1)]
  hour.22 = step.mean(data[hour==22, varnum], 6)[1:length(time.1)]
  hour.23 = step.mean(data[hour==23, varnum], 6)[1:length(time.1)]
}

# smooth the hourly anomalies
{
  p = 10
  weights = rep(1/(2*p+1), times = 2*p+1)
  smoo.0 = filter(hour.0, sides = 2, filter = weights)
  smoo.1 = filter(hour.1, sides = 2, filter = weights)
  smoo.2 = filter(hour.2, sides = 2, filter = weights)
  smoo.3 = filter(hour.3, sides = 2, filter = weights)
  smoo.4 = filter(hour.4, sides = 2, filter = weights)
  smoo.5 = filter(hour.5, sides = 2, filter = weights)
  smoo.6 = filter(hour.6, sides = 2, filter = weights)
  smoo.7 = filter(hour.7, sides = 2, filter = weights)
  smoo.8 = filter(hour.8, sides = 2, filter = weights)
  smoo.9 = filter(hour.9, sides = 2, filter = weights)
  smoo.10 = filter(hour.10, sides = 2, filter = weights)
  smoo.11 = filter(hour.11, sides = 2, filter = weights)
  smoo.12 = filter(hour.12, sides = 2, filter = weights)
  smoo.13 = filter(hour.13, sides = 2, filter = weights)
  smoo.14 = filter(hour.14, sides = 2, filter = weights)
  smoo.15 = filter(hour.15, sides = 2, filter = weights)
  smoo.16 = filter(hour.16, sides = 2, filter = weights)
  smoo.17 = filter(hour.17, sides = 2, filter = weights)
  smoo.18 = filter(hour.18, sides = 2, filter = weights)
  smoo.19 = filter(hour.19, sides = 2, filter = weights)
  smoo.20 = filter(hour.20, sides = 2, filter = weights)
  smoo.21 = filter(hour.21, sides = 2, filter = weights)
  smoo.22 = filter(hour.22, sides = 2, filter = weights)
  smoo.23 = filter(hour.23, sides = 2, filter = weights)
}

# plot the smoothed hourly anomalies with different colors according to the specific time period
of the day

# gather the starting year and number of day for defining the time-series objects

```

```

sY = as.numeric(strftime(time[1], format = "%Y"))
sD = as.numeric(strftime(time[1], format = "%j"))
eY = as.numeric(strftime(time[length(time)],format = "%Y"))
{
  plot(ts(smoo.0, start = c(sY, sD), frequency = 365), col=2, axes=F, xlab='', ylab='')
  lines(ts(smoo.1, start = c(sY, sD), frequency = 365), axes=F, col=2)
  lines(ts(smoo.2, start = c(sY, sD), frequency = 365), axes=F, col=2)
  lines(ts(smoo.3, start = c(sY, sD), frequency = 365), axes=F, col=2)
  lines(ts(smoo.4, start = c(sY, sD), frequency = 365), axes=F, col=2)
  lines(ts(smoo.5, start = c(sY, sD), frequency = 365), axes=F, col=2)
  lines(ts(smoo.6, start = c(sY, sD), frequency = 365), axes=F, col=3)
  lines(ts(smoo.7, start = c(sY, sD), frequency = 365), axes=F, col=3)
  lines(ts(smoo.8, start = c(sY, sD), frequency = 365), axes=F, col=3)
  lines(ts(smoo.9, start = c(sY, sD), frequency = 365), axes=F, col=3)
  lines(ts(smoo.10, start = c(sY, sD), frequency = 365), axes=F, col=3)
  lines(ts(smoo.11, start = c(sY, sD), frequency = 365), axes=F, col=3)
  lines(ts(smoo.12, start = c(sY, sD), frequency = 365), axes=F, col=4)
  lines(ts(smoo.13, start = c(sY, sD), frequency = 365), axes=F, col=4)
  lines(ts(smoo.14, start = c(sY, sD), frequency = 365), axes=F, col=4)
  lines(ts(smoo.15, start = c(sY, sD), frequency = 365), axes=F, col=4)
  lines(ts(smoo.16, start = c(sY, sD), frequency = 365), axes=F, col=4)
  lines(ts(smoo.17, start = c(sY, sD), frequency = 365), axes=F, col=4)
  lines(ts(smoo.18, start = c(sY, sD), frequency = 365), axes=F, col=5)
  lines(ts(smoo.19, start = c(sY, sD), frequency = 365), axes=F, col=5)
  lines(ts(smoo.20, start = c(sY, sD), frequency = 365), axes=F, col=5)
  lines(ts(smoo.21, start = c(sY, sD), frequency = 365), axes=F, col=5)
  lines(ts(smoo.22, start = c(sY, sD), frequency = 365), axes=F, col=5)
  lines(ts(smoo.23, start = c(sY, sD), frequency = 365), axes=F, col=5)
}

# draw the axis, legend and title
axis(1,at=c(sY:eY))
axis(2)
mtext(text = "unit of measurement",2,2.5)
title(main="title")
legend('topright',legend = c('0-5 LT', '6-11 LT', '12-17 LT', '18-23 LT'), col=c(2,3,4,5), lty=1,
lwd=2)

# the following code compute and draws the smoothed absolute time series
dat = step.mean(dataset$variable, interval = 144)
p = 10
weights = rep(1/(2*p+1), times = 2*p+1)
var = filter(dat, sides = 2,filter = weights)
plot(ts(var, start = c(sY, sD), frequency = 365), type='l', xlab='', ylab='', axes=F)
axis(1,at=c(sY:eY))
axis(2)
mtext(text = "unit of measurement",2,2.5)
mtext(text = "Time",1,2)

```

## B.VIII Assessment of the relations between the different variables

The following code examines the relations between the different variables by the means of the cross correlation function.

```

# First, the two "dataset" should be imported as in B.I and, if necessary, pre-processed as in
B.II

# compute the daily anomaly (for each dataset)

```

```

data1 = anomaly_period(dataset1, 2, 1, 144)
data2 = anomaly_period(dataset2, 2, 1, 144)

# compute the cross correlation function and display the cross-correlogram
a1 = ccf(data1$var.anomaly, data2$var.anomaly, na.action = na.pass, lag.max = 72, main='')

```

## B.IX Distinction of days characterized by low shortwave radiation values in chapter 4 (Discussion)

This section describes the code utilized in chapter 4 to select those days with daily shortwave radiation values lower than a certain threshold.

```

# shortwave radiation and air temperature data should be imported as in B.I, pre-processed as in
# B.II and merged together as in B.VI
# the resulting "dataset" should have 3 columns: time, air temperature and shortwave radiation

# First, calculate the interested percentiles (i.e. 0.2) for the shortwave radiation measurements
# acquired at each time step.

perc = percentile_daily(dataset, 3, 144, 0.2)

# create a function with compares the daily shortwave radiation measurements of an input dataset
# with the reference shortwave radiation daily cycle. Only those days with at least 130 values of
# 144 shortwave radiation daily measurements below the reference threshold are selected.
compare = function(data, NumVar, period, thres.vector){
  i = 1
  j = period
  d = NULL
  while (i <= nrow(data)){
    int.data = data[i:j,NumVar]
    if (length(int.data) == length(int.data[!is.na(int.data)])){
      b = int.data <= thres.vector
      if ((length(int.data)-14) <= length(which(b==TRUE))){
        d = rbind(d,data[i:j,])
      }
    }
    i = i+period
    j = j+period
  }

  print(nrow(d)/144)
  return(d)
}

# select days
res = compare(data, 3, 144, perc[,1])

# the air temperature diurnal cycle is illustrated as in B.IV

```